

VAN DER WAALS HETEROSTRUCTURES:
FABRICATION AND NANOSCALE
ELECTRONIC AND THERMAL
CHARACTERISATION VIA SPM METHODS

Elisa Castanon Garcia-Roves



THESIS SUBMITTED FOR THE DEGREE OF
DOCTOR OF PHILOSOPHY

APRIL 2021

*“The tower isn’t the structure itself. It is all of us, and the wisdom we share. It grows
ever upward, a stone for every new arrival”*

Reliquary tower, Archmage Vintra (Magic: The Gathering™)

In loving memory of **Jesus**, who has been always by my side;

and of **Diego Antonio**, who taught me to love books.

Also dedicated to **Nacho Guerra**, the best physics
teacher and friend that I could have ever had.

一期一会

ABSTRACT

Since the dawn of two-dimensional (2D) era, graphene and the plethora of other atomically thin layered materials cousins, including their combinations in heterostructures, have revolutionized material science and established themselves as promising candidates for the next-generation of nanoscale devices. However, the landscape of opportunities and possible combinations is so vast, that many promising research topics remain widely unexplored. The aim of this work is to address some of these questions, contributing to the progress and understanding in three different areas: fabrication of novel 2D materials and their heterostructures; electronic properties and doping mechanisms in these at the nanoscale; and characterization of the nanoscale thermal and thermoelectric properties of 2D materials.

Starting with the fabrication procedures, different techniques for mechanical exfoliation and polymeric dry transfer of 2D materials and heterostructures were explored. This research route led to the establishment of a new fabrication facility at the National Physical laboratory (NPL), and to the production of a wide variety of samples, from exfoliated flakes to complex heterostructures and devices. A selection of the produced samples was employed during this thesis to investigate the electronic and thermal properties of 2D materials via spectroscopic and advanced scanning probe microscopy (SPM) techniques. Regarding the electronic response of graphene, two routes were undertaken: first, the electronic response of different types of graphene towards humidity acting as a p-dopant was studied for the first time using Raman spectroscopy. Second, a procedure improving current methods of quantitative probe calibration in Kelvin probe force microscopy (KPFM) was developed, establishing the determination of reliable and consistent work-function values with high-resolution. This method was then employed to study the electronic properties and doping of encapsulated graphene heterostructures, providing quantitative values of the work-function of the system, as well as demonstrating the capability of KPFM as an excellent visualisation and characterisation technique for buried layers otherwise inaccessible by other methods. Finally, various thermal properties of 2D materials were studied via advanced SPM techniques: Scanning thermal microscopy (SThM) that was used for the determination of the thickness dependence of the thermal conductance of exfoliated InSe, and scanning thermal gate microscopy (STGM) that was employed to explore the thermovoltage, and thus Seebeck coefficient, variation in encapsulated graphene heterostructures with patterned constrictions.

The main highlights of the work developed during this thesis are: (1) the formulated need and subsequent realisation of various approaches towards the fabrication of 2D materials and heterostructures. For this, shared expertise with other researchers and institutions, and access to different fabrication facilities were essential; and (2) the exploitation of the potential of spectroscopic and advanced SPM methods in providing reliable characterisation of the 2D material and heterostructure's properties with nanoscale resolution. The findings of this thesis have provided new insights in a varied number of areas, and hold promise for different future applications: from single material thermocouples to graphene-gas sensors, including improved fabrication procedures for 2D materials, or even, probe-calibration and characterisation methods.

STATEMENT OF AUTHORSHIP

I declare that this PhD thesis is a result of the author's original work.

However, it is important to highlight that as a consequence of the diversity of the work carried out during these past years, collaboration has been an essential foundation to reach the successful completion of this thesis. For this reason, an acknowledgment section has been included at the beginning of each experimental chapter in which the main contributions from other authors related to the pertinent work have been clearly stated.

I further declare that this thesis has not been submitted elsewhere in the pursuit of the award of a higher degree. The work presented here has been carried out between November 2016 and April 2021 both at the National Physical Laboratory (NPL) in London, United Kingdom, and at Lancaster University, UK, under the supervision of Dr Olga Kazakova, Prof. Oleg V. Kolosov, and Dr Benjamin J. Robinson. This work has been equally funded by NPL and Lancaster University.

Eli Castanon

April 2021

ACKNOWLEDGEMENTS

This PhD has been an incredible journey, full of ups and downs, new discoveries and failures. This experience has changed my perspective of life completely, and has filled my book of memories with very precious moments. Completing this journey was only possible with the support and guidance offered by all the people that I met during these years.

To start, I would like to thank my three supervisors as their help has been fundamental for the development and completion of this PhD thesis: I would like to express my gratitude to my supervisor Dr Olga Kazakova from the National Physical Laboratory in London (UK), for all her support and encouragement. I am especially grateful for all the hours spent together, where she provided me with extensive personal and professional guidance, as well as with precious scientific knowledge, opportunities and resources. Without her guidance and constant feedback, this PhD would not have been achievable. I feel especially grateful with my supervisor Prof. Oleg Kolosov from Lancaster University (UK) for providing hours of insightful discussions and mentorship, always accompanied by a comforting hot chocolate. I am deeply grateful for all his patience, motivation and care, and for sharing with me all his immense knowledge. His guidance helped me to carry out this research, to write the thesis and, more importantly, to be brave enough to pursue my own ideas. Last but not least, I would like to express my sincere gratitude to my supervisor Dr Benjamin J. Robinson for being there to help me in the moments in which I most needed him. Thank you.

I would like to acknowledge as well the Lancaster University Physics department and the National Physical Laboratory for the provision of a studentship.

Besides my supervisors, I am deeply indebted to all the people that I met walking this path of science, including senior scientists, post-doctoral researchers, PhD students, laboratory technicians, and many more. In particular, I would like to give my most special thanks to all the people in my group at NPL, which I feel is like a small family. To Dr Cristina Giusca for all her patience, guidance, and especially for all the *¿Qué pasa, bruja?*, laughs and funny stories that we shared. Thanks to Dr Christos Melios for teaching me his AFM secrets, and for his continuous smile. To Dr Craig Barton, even being from the nanomagnetism group, for always listening and for sharing all his knowledge unreservedly. To Dr David Buckley for all his support, for his tenacious spirit and for always pushing his own limits, serving as an inspiration. To Dr Nathaniel Huang, the whisperer, for running faster than the wind back to his homeland, for his delicate taste in transparent mugs and for always making me smile regardless of the circumstances. Not to forget, Alex Browning, and Dimitrios Sagkovits, always ready for either a good session of 2D material's fabrication, some Raman characterisation or for a Spotify music lounge. My most special thanks go to Tom Vincent, for being the best workmate and friend possible, for all the fruitful discussions and the jokes we shared, and for teaching me all the secrets of English language. I would also like to dedicate special

thanks to Dr Miriam Ferrer Huerta, for the endless talks and the occasional collisions. And finally, to Dr Héctor Corte-León, who has been by my side for many years, sharing his immense physics knowledge, his taste for retro-technology and his awful jokes.

From NPL, I would like to also dedicate few lines to my dear colleague Dr Alessandro Catanzaro, who sadly passed away the 1st of October of 2020. I will never forget your smile. Your enthusiasm and passion were contagious. You departed too soon, while you were still full of dreams and full of life, my friend. *Per aspera ad astra*.

I cannot forget, for obvious reasons, to thank here all my mates from Lancaster University, whom have been providing me with all their nano-support, always accompanied by a very comforting nano-pint. First, I would like to thank the best '*partners in crime*', Dr Denise and Dr Eva, always ready for the action, purely like rock stars. To follow, my gratitude goes to our lovely Italian mafia, Dr Lamanita, Sebi and Cinzia, who never taught us to cook any Italian dish. Among all the Italians, I am especially grateful to Mr Romeo, the professional powder-eater man and music-taster, source of endless cultural facts, intense discussions, and good hugs. Forza, my friend! The next on my list are the members of the crew of the 'Kolosov group: the next generation'. A bunch of lovely people all together, from Dr Yue to Dr Kushboo, Sergi and Andy. Thanks for your support, folks! Also, Sophie, and Saba, we spent very little time together but it was always extremely nice, you are truly lovely. Thanks to the experienced crew Chara, Ramon and Juanito, for being there and for helping us filtering and focusing continuously. Finally, my biggest thanks goes to Dr Martaja, the best Spartan Vallisoletana that I have ever met. I couldn't have survived without our cooking sessions, house hashtags, siiiiri, killing gym tortures and golden lion classic pints.

I am also deeply thankful to the collaborators that made possible the completion of this work. Being able to work alongside so many different people has been a very enriching experience. I would especially like to mention the colleagues working at Technical University of Denmark (DTU): Peter Bøggild, Tim Booth, Jose Caridad and Xiaojing Zhao, for all the discussions and the interesting experiments performed together. I would like to also thank the scientists at the National Graphene Institute (NGI): Roman V. Gorbachev, Vladimir Falko, Daniel J. Terry, Matthew J. Hamer, Astrid Weston, Tom H. Boynton and Johanna Zultak, for their warm welcome, for dedicating to me all their time and effort, for the fruitful discussions and teachings, always full of patience and care. Finally, from Lancaster University, I am extremely thankful to Dr Sergey Kafanov and Dr Leonid Ponomarenko, whom helped me unreservedly during my last set of experiments.

Outside the scientific environment, nobody has been more important for me in the completion of this thesis than my family. I would like to thank my mother, Elisa Garcia-Roves Suarez, a truly great woman always following her heart. You are the greatest, mum; to my father, Felix 'Briatore' Castañón, always quoting brand slogans to cheer me up when I have been down, and to my little brother, Marcos Castañón

Antón, for being adorable, always playful and for lecturing me for hours in the history of SEGA, Nintendo and all the other relevant 'classics'. The best group of all deserves few words as well: 'La tierrina manda', shouting out loud 'Puxa Asturias', the presence of these ladies has been fundamental not only during this period, but for much longer. Now, after 10 years together, I have the opportunity to thank Dr Yurema 'Amísima' Teijeiro, for the endless talks, the laughs and the 'cachopadas'; Ana for the intense philosophical discussions, always finding a bright side on the simplest aspects of life; and Dr Marina 'the finer' for leading the way of science and for having enough trees in the garden to talk to during the lockdown period. Although we don't see each other as often as I would like to, I couldn't have gone far without you, ladies. Special mention to all the other friends that have been also present in my life giving their best support and caring: Fran (Percha), Serrucho, Carme, Estela, Oscar, Nao-chan, Yuriko-chan, Rosalba, Luis, Chloe, Ester, Panchis,... and the list goes on. Please, don't be offended if you are not here, you are with me anyway, and I owe you a pint to compensate for not being in the acknowledgments!

Finally, I would also like to dedicate a very special thank you to all the Kendo community that has supported me throughout these years. I am extremely thankful to all the amazing *kenshi* that I have met while practising around the UK, and to the Spanish national team members, for the warm welcome and the unconditional friendship. I cannot forget my most beloved 'Vinegar Girls' group: Silvia 'capi senpaya' Romeral, always a colourful inspiration; Lau 'Rubia' Palau, full of energy and good vibes; Concha, happy and dedicated like no-one else; Miri 'the girliest Hollow Knight', and Mila 'the unstoppable'. We are unavoidably moving forward step by step. Check!

THANK YOU EVERYBODY!

LIST OF PUBLICATIONS

ORCID ID: <https://orcid.org/0000-0003-4316-4796>

- *"Frontiers of graphene and 2D material-based gas sensors for environmental monitoring"*, D.J. Buckley, N.C.G. Black, **E.G. Castanon**, C. Melios, M. Hardman, O. Kazakova. *2D materials* 7 032002 (2019), DOI: [10.1088/2053-1583/ab7bc5](https://doi.org/10.1088/2053-1583/ab7bc5)
- *"In-situ Raman spectroscopy of graphene in controlled humidity environment"*, K. Brown, T. Vincent, **E.G. Castanon**, F.S. Rus, C. Melios, O. Kazakova, C.E. Giusca. *Carbon*, vol. 163, pages 408-416 (2020), DOI: [10.1016/j.carbon.2020.03.037](https://doi.org/10.1016/j.carbon.2020.03.037)
- *"Calibrated Kelvin-probe force microscopy of 2D materials using Pt-coated probes"*, **E.G. Castanon**, A.F. Scarioni, H.W. Schumacher, S. Spencer, R. Perry, J. Vicary, C. Clifford, H. Corte-León. *Journal of Physics Communications* 4 095025 (2020), DOI: [10.1088/2399-6528/abb984](https://doi.org/10.1088/2399-6528/abb984)
- *"Anomalous low thermal conductivity of atomically thin InSe probed by scanning thermal microscopy"*, D.J. Buckley, Z.R. Kudrynskiy, N. Balakrishnan, T. Vincent, **E.G. Castanon**, Z.D. Kovalyuk, O. Kolosov, O. Kazakova, A. Tzalenchuk, A. Patané. *Advanced Functional Materials* (2021), DOI: <https://doi.org/10.1002/adfm.202008967>
- *"Opportunities in Electrically Tunable 2D Materials beyond Graphene: Recent Progress and Future Outlook"*, T.V. Vincent, J. Liang, S. Singh, **E.G. Castanon**, X. Zhang, A. McCreary, D.M. Jariwala, O. Kazakova, Zak Y. Al Balushi. Submitted to Applied Physics Review in March 2021.
- *"Investigating hBN-SiO₂ interface effects and ultra-thin transfer"*, A.R. Browning, **E.G. Castanon**, A. Catanzaro, O. Kazakova, J. Allam, C.E. Giusca. In preparation.

POSTERS, ORAL PRESENTATIONS AND OUTREACH

2017

- **PHYSICS MASTER-CLASS (March):** Astrophysics and cosmology featuring observational astrophysics, Lancaster University
- **PHYSICS MASTER-CLASS (March):** Particle physics featuring experimental particle physics research, Lancaster University
- **POSTER (July):** "*SThM characterisation of local thermal properties of semiconductors and insulators on the nanometer scale*", **E.G. Castanon**, C. Evangeli, J. Spièce, B.J. Robinson, S. Gomès, O. Kazakova, O.V. Kolosov. Microscience microscopy congress (Manchester, UK).

2018

- **POSTER (February):** "*Structural and electrical characterisation of vertical MoS₂ and graphene heterostructures*", **E.G. Castanon**, T. Vincent, C. Melios, V. Panchal, R. Chang, J. Warner, R. Yakimova, B.J. Robinson, O.V. Kolosov, O. Kazakova. Graphene winter conference (Innsbruck, Austria)
- **POSTER (July):** "*2D materials: Applications at NPL and future outlook*", **E.G. Castanon**, NPL Open day (London, UK)
- **WORKSHOP FOR KIDS (July):** "*Fabrication of 2D materials, magic scotch tape and the hidden layers*", **E.G. Castanon**, NPL Open Day (London, UK)
- **POSTER (September):** "*Precise method of assembly of 2D material heterostructures*", **E.G. Castanon**, H. Corte-Leon, B.J. Robinson, O. Kazakova, O.V. Kolosov, NPL graphene and 2D materials Conference. IOP prize: Best poster. (London, UK)

2019

- **TUTORING SUMMER SEPnet (June-September):** Lead a project towards automatization of optical inspection of 2D materials using python.
- **POSTER (September):** "*Effect of preferential sites in graphene on NO₂ adsorption*", **E.G. Castanon**, C.Melios, B.J. Robinson, O. Kazakova, O.V. Kolosov, Graphene Week conference (Helsinki, Finland)

2020

- **TALK (May):** "*Electrostatic characterization of 2D materials and heterostructures via KPFM*", Quantum Materials and Sensors conferences at National Physical Laboratory (London, UK)
- **INVITED TALK (May):** "*Fabrication of Van der Waals heterostructures: from exfoliation to devices*", Spintronics group at University of Central London (UCL, London, UK)

Table of contents

LIST OF FIGURES	xiii
LIST OF TABLES	xxviii
Glossary and abbreviations	xxix
List of symbols and constants	xxxii
1 Introduction	1
1.1 Scope of the thesis.	3
1.2 Thesis outline.....	6
LITERATURE REVIEW	9
2 Graphene foundation and literature review	9
2.1 Why carbon?.....	9
2.1.1 Electronic properties of graphene	11
2.2 Types of graphene	14
2.2.1 Exfoliated graphene	14
2.2.2 Epitaxial growth.....	16
2.2.3 Chemical vapour deposition	17
2.3 Other layered materials electronic properties	20
2.3.1 Hexagonal boron nitride (hBN).....	20
2.3.2 Indium selenide (InSe).....	21
2.4 Graphene Fermi level and doping mechanisms	23
2.4.1 Electrostatic doping	24
2.4.2 Chemical doping	25
2.4.3 Fermi level characterisation	26
2.4.4 Graphene for gas sensing applications.....	27
2.5 Nanoscale thermal conductivity	28
2.5.1 Thermal transport in 2D materials.....	28
2.5.2 Thermoelectricity of 2D materials	29
2.6 Concluding remarks.....	31

3	Review of characterization methods.....	32
3.1	Scanning probe microscopy (SPM).....	32
3.1.1	Atomic force microscopy (AFM)	33
3.1.2	Kelvin probe force microscopy (KPFM).....	36
3.1.3	Scanning thermal microscopy (SThM).....	39
3.2	Optical techniques	43
3.2.1	Bright field microscopy.....	43
3.2.2	Dark field microscopy	43
3.2.3	Raman spectroscopy.....	44
3.3	Electrical transport measurements: 2 point probe method.....	47
3.4	Conclusions.....	48
	EXPERIMENTAL METHODS.....	49
4	Fabrication of 2D heterostructures and devices	49
4.1	Introduction	50
4.2	Air effects on 2D materials: working in controlled environments	51
4.3	Substrate preparation	53
4.3.1	Silicon oxide substrate	53
4.3.2	Polymer substrate.....	55
4.4	Mechanical exfoliation	55
4.5	Optical identification	58
4.5.1	Edge detection algorithms for flake identification.....	62
4.6	Heterostructure assembly.....	65
4.6.1	Transfer system	66
4.6.2	PPC/PDMS transfer method	67
4.6.3	PMMA carrying layer method	73
4.6.4	Comparison between different transfer methods	79
4.7	Device fabrication.....	82
4.8	Example: InSe heterostructure for thermal studies	86
4.9	Conclusions.....	91

5	Understanding the effect of water adsorption on graphene doping via Raman spectroscopy in environments of controlled humidity.....	93
5.1	Introduction	94
5.2	Experimental methods.....	95
5.2.1	Sample description and characterisation.....	95
5.2.2	Environmental chamber and Raman system set-up.....	95
5.2.3	KPFM set-up	97
5.3	Humidity effects on different graphenes.....	97
5.3.1	Morphology studies of various types of graphene	97
5.3.2	Raman results in environments of varying humidity.....	99
5.3.3	Correlation of strain and doping.....	103
5.4	Conclusions.....	106
	108	
6	KPFM studies: calibration method and its application for the characterisation of GFET devices	108
6.1	Introduction	109
6.2	Experimental methods.....	110
6.2.1	KPFM set-up	110
6.3	KPFM calibration methodology.....	112
6.3.1	Ultraviolet photon spectroscopy (UPS)	113
6.3.2	KPFM parameters optimisation	115
6.3.3	Probe calibration and performance test.....	122
6.3.4	Characterisation of the KPFM spatial resolution.....	126
6.3.5	Example: work-function vs thickness dependence.....	127
6.4	KPFM studies of gate electrostatic on GFET devices.....	128
6.4.1	GFET device fabrication.....	130
6.4.2	KPFM measurements.....	132
6.5	Conclusions.....	141
7	Thermal nanoscale characterisation of 2D materials with advanced SPM	144
7.1	Introduction	145

7.2	Experimental methods.....	146
7.2.1	Custom microscope set-up	146
7.2.2	Scanning thermal microscopy (SThM) set-up.....	148
7.2.3	Scanning thermal gate microscopy (STGM) set-up.....	149
7.2.4	Electrical characterisation set-up.....	150
7.3	Study of the thermal properties of exfoliated InSe via SThM	151
7.3.1	InSe exfoliation.....	151
7.3.2	SThM measurements in ambient environment	152
7.3.3	SThM measurements in vacuum and the effect of the substrate.....	156
7.4	Local Seebeck coefficient variations in GFET devices with patterned constrictions.....	160
7.4.1	Graphene device fabrication.....	161
7.4.2	Graphene device characterisation.....	163
7.4.3	Probing TE response of encapsulated graphene nanostructures via STGM.....	166
7.5	Conclusions.....	172
8	Conclusions and perspectives	175
8.1	Conclusions and key results	175
8.2	Future work.....	179
A	Edge detection algorithms for 2D materials identification.....	184
A.1.	Edge detection GUI for 2D materials.....	184
A.2.	Python 3.0 code: LynxViewer v3.0.....	185
	References.....	199

LIST OF FIGURES

Figure 1.1. Effects of dimensionality on the density of states (DOS) for different systems: **(a)** 3D Bulk semiconductor, **(b)** 2D quantum well, **(c)** 1D quantum wire and **(d)** 0D quantum dot. Figure inspired by Rogers et al. [12] 3

Figure 1.2. Layered structure (top) and band structure (bottom) diagrams of some 2D materials with different electronic and optical properties. From left to right, insulating hBN, semiconducting *MoS2* and BP, and the semimetal, graphene. Adapted with permission from [23] 4

Figure 1.3. **(a)** Illustration of a van der Waals heterostructure composed of layers from different crystals. Adapted with permission from [35]. **(b)** Schematic of the fabrication of 1D edge contacts to hBN-encapsulated graphene device. Adapted with permission from [36] 5

Figure 2.1. Atomic models of different allotropes of carbon. **(a)** 0D fullerene (buckyball), **(b)** 1D carbon nanotubes, **(c)** diamond, **(d)** amorphous carbon and **(e)** 3D layered structure of graphite. Inset: The 2D dimensional form of graphite, graphene, is composed by just 1 isolated layer. Figures (a-e) are adapted from [3]. The inset is adapted from [4]. 10

Figure 2.2. **(a)** Electronic levels of a carbon atom showing the ground state and the sp^2 hybridization scheme. **(b)** Model of the localization of the orbitals in graphene, showing sp^2 hybridization. The sp^2 orbitals form σ bonds and the p_z -orbitals form π bonds..... 11

Figure 2.3. **(a)** Honeycomb lattice structure of graphene, made out of two interpenetrating triangular lattices, depicted in dark and light green. The lattice unit vectors are a_1 and a_2 , and δ_i , $i=1,2,3$ are the nearest-neighbour vectors. **(b)** The reciprocal lattice of graphene represented with the first Brillouin zone grey shaded. High symmetry points are highlighted with different colours. The Dirac cones are located at the K and K' points..... 12

Figure 2.4. Electronic dispersion relation for monolayer graphene. The conduction and valence bands touch at six discrete non-equivalent K and K' points located at the vertices of the hexagonal Brillouin zone. Inset: Linear dispersion relation around the Dirac point. Adapted with permission from [14]..... 13

Figure 2.5. **(a)** Graphene exfoliation on blue tape. **(b)** White light optical image of a graphene flake deposited on 300 nm *SiO2*. Areas of different thicknesses in the flake are shown as regions of different contrast. Monolayer graphene is indicated by a label (1LG)..... 15

Figure 2.6. Epitaxial graphene. **(a)** Schematics of the epitaxial growth of graphene on SiC. The interfacial layer (IFL) is covalently bonded to the SiC surface at certain locations, leaving dangling bonds that contribute to n-dope the graphene layer sitting on top. **(b)** Topography (Left) and electrostatic force microscopy (Right) maps of epitaxial graphene grown on the phase 4H-SiC(0001). The topography shows the characteristic terraces of SiC. The electrostatic force microscopy provides information of the number of layers present in the material, such as the interfacial layer (IFL), monolayer (1LG) and multilayer (MLG) regions. Scale bars: 2 μm . Adapted with permission from [34] **(c)** Low energy electron microscopy

(LEEM) of epitaxial graphene prepared on 6H-SiC(0001) showing regions of different thicknesses marked as (1)-(4). Field of view: $20 \mu m$. Electron energy: $E_{vac} = +1.6eV$. Adapted with permission from [39] **(d)** Prototype of *Rk200* quantum Hall array resistance standard fabricated with epitaxial graphene. Micrograph of the entire chip (Left) and a zoom-in covering an array of 100 Hall bars (Right). Adapted with permission from [38]..... 17

Figure 2.7. CVD graphene growth diagram. Precursor species introduced in the reaction chamber are adsorbed by the metallic surface. A proportion will be desorbed with no further effect, while others will react with the substrate. The thin film growth starts at nucleation spots and expands to form a uniform layer. The by-products of the reaction are evacuated from the chamber. Transport of the molecules and the desorption products is performed by an inert carrier gas..... 18

Figure 2.8. **(a)** SEM image of graphene on a copper foil with a growth time of 30 minutes (left) and an SEM image of the same graphene transferred on 285 nm *SiO2/Si*, showing wrinkles as well as two- and three-layer regions (right). Inset: Optical micrograph of the graphene film on top of a 285 nm *SiO2/Si* substrate. Reprinted with permission from [42] **(b)** False-color optical image of CVD graphene on copper after a first (top-left) and a second (bottom-left) growth cycle. On the right-side, a small section of graphene covered by transferred hBN (which will be reviewed in the next section). Adapted with permission from [53] **(c)** Schematic of the roll-based production of graphene films grown on a copper foil. The process includes adhesion of polymer supports, copper etching (rinsing) and dry transfer-printing on a target substrate. **(d)** A transparent ultra-large area graphene film transferred on a 35-inch PET sheet. Adapted with permission from [56]..... 19

Figure 2.9. **(a)** hBN crystalline structure top-view **(b)** Histogram of the height distribution (surface roughness) measured by AFM for *SiO2* (black triangles), hBN (red circles) and graphene-on-hBN (blue squares). The curves show that the roughness of graphene on hBN is three times smaller than that of *SiO2*. Solid lines are Gaussian fits to the distribution. Inset: high-resolution AFM image showing a comparison of graphene and hBN surfaces. Scale bar: $0.5 \mu m$. Figure reproduced with permission from [61] **(c)** Left: False colour optical image of a graphene flake sandwiched between hBN flakes, a process known as encapsulation, which protects the 2D material flake from any interaction with the environment. Right: High-resolution transmission electron microscope image of an encapsulated graphene(hBN/Graphene/hBN) stack. From this image, it is obvious that the interfaces are atomically sharp and free from impurities. The heterostructure was produced using the PPC/PDMS method further explained in chapter 4. Reproduced with permission from [71] 21

Figure 2.10. **(a)** Side view and **(b)** top view of InSe crystal structure. Figures modified with permission from [79] **(c)** DFT calculations of the band structure of InSe in the first Brillouin zone for 1L, 5L and 10L of atoms. Figure is reproduced with permission from [80]..... 22

Figure 2.11. **(a)** Schematic view of a GFET. The graphene channel (black) is located between the metallic electrodes (yellow), denominated drain and source. All the structure is located on

top of a silicon wafer (purple) with a top oxide layer (pink). (b) Resistivity of pristine graphene as a function of gate voltage. For $V_{BG} < 0 V$, graphene is p-doped, and for $V_{BG} > 0 V$, graphene is n-doped. Reproduced with permission from [96].	25
Figure 2.12. Schematic representation of the molecular doping of graphene considering: (a) p-doping and (b) n-doping. The direction of the electron transference is determine based on the difference between the graphene Fermi energy and the HOMO or LUMO energy levels of the adsorbate molecule.	26
Figure 2.13. Chemical doping of graphene via external molecules. Variations in the resistance of a graphene Hall bar as a consequence of its exposure to different molecules. Adsorbates such as CO, or NH_3 produce n-doping of graphene, whereas other molecules like NO_2 , or H_2O , produce p-doped behaviour on graphene. Image reproduced with permission from [100].	27
Figure 2.15. (a) Interdependent relation between the Seebeck coefficient, S , electrical conductivity, σ , thermal conductivity, κ , and power factor, for different carrier concentrations. Adapted with permission from [137] (b) Progress of future TE materials. Conventional bulk materials showing values from 0.01 to around 1. By using nanostructures, values between 0.1 to 2 have been reported. The solid blue arrow indicates already made progress, while the dotted red arrow the prospects for further increased ZT. (c) Schematic design of an SnS_2 device on a photo-TE measurement setup. Reproduced with permission from [138] (d) Design of a TE device based on 2D materials: InSe deposited on a hBN substrate. The micro-heater acts as a heat source of the system, while the temperature at different spots of the device is measured by thermometers 1 and 2. Lateral contacts are used to measure the variations in voltage, ΔV , along the device. Reproduced with permission from [139].	30
Figure 3.1. Structure of the characterisation methods covered in this chapter	32
Figure 3.2. Force vs tip-sample distance curve. The attractive and repulsive regimes are specified by vertical arrows coming out from the x-axis. The contact and non-contact regions are highlighted with a yellow and pink background, respectively. The different operational modes, namely contact, tapping and non-contact modes are depicted by red, green and purple dotted lines, respectively.	33
Figure 3.3. (a) Typical AFM set-up, with a feedback mechanism based on the laser-beam deflection method. (b) Scanning electron microscopy (SEM) image of a silicon cantilever with an integrated probing tip manufactured by Bruker©. (c) SEM detail of the pyramidal tip from (b)	35
Figure 3.4. (a) Topography map acquired in tapping mode of a heterostructure formed only by layers of hBN deposited on top of each other. (b) Extracted profile from the red line in (a). The thickness of the different layers can be clearly assessed. Other features like bubbles (blue), contamination or folds (green) are also distinguishable.	36
Figure 3.5. Schematics showing the origin of the V_{CPD} . (a) For two separated samples, their work-function would be defined as the distance between their Fermi levels and the vacuum level. (b) When the materials are brought into electrical contact, their Fermi levels, E_F , aligned. This happens as the electrons from the material with higher work-function flow to the	

material of lower work-function, leading to the formation of a contact potential difference <i>VCPD</i> . (c) The <i>VCPD</i> , and so the electrostatic force between both materials, can be minimised by applying an external bias voltage, $VDC = VCPD$	37
Figure 3.6. Schematic diagram of the KPFM set-up, with the electrostatic system represented in pink, and the force feedback loop represented in blue.....	38
Figure 3.7. Schematic diagram of the frequency spectrum of an example cantilever. The peak at the mechanical resonance is placed at $f_0 = 300\text{ kHz}$ and highlighted in yellow. Side-lobes appear at the sides of the resonance frequency as a consequence of the electrostatic force field with peaks at $f_0 \pm f_{mod}$ and $f_0 \pm 2f_{mod}$. The frequency of the oscillating excitation signal generating the electrostatic force is placed at $f_{mod} = 5\text{ kHz}$, and highlighted in blue. Figure inspired by Zerweck et al.[11]	39
Figure 3.8. Standard SThM experimental set-up for resistive probes employed as passive resistance thermometer. In red the thermal related circuit is shown, while the topography-feedback is shown in blue. The heat transfer between the sample and the thermal probe is evaluated using a Wheastone bridge and a lock-in amplifier that measures the variations of the thermal probe electrical resistance. The force between the probe and the sample is controlled by a standard force feedback loop.	40
Figure 3.9. (a) Microscopic tip-sample contact. Different contributions to the heat transfer are shown as arrows of different colours: pink and orange for the near-field and far-field radiative transfer, respectively; and blue for the gas conduction. Also, a water meniscus is shown as a light blue shadow around the tip and sample contact. In (b) , a closer detail on tip-sample contact is shown. The dotted line represents the ideal profile of the tip-apex, while the most likely rough real profile is shown as a continuous line.....	41
Figure 3.10. Set-up schematics of an optical system for brightfield (left) and darkfield (right) microscopy in reflection mode. On top of each schematic, a diagram showing an example flake imaged with each mode highlights the differences between the two.	44
Figure 3.11. Scattering process present in Raman interaction.	45
Figure 3.12. (a) Raman spectra of pristine(top) and defective(bottom) exfoliated graphene displaying the main features, i.e. the G(green), the D(blue) and the 2D(red) modes. Adapted with permission of [41] (b) Representative Raman spectra of epitaxial graphene grown on SiC(0001), On top, three different spectra are compared: the original spectrum for the SiC substrate in black, the monolayer graphene (1LG) in blue, and the bilayer (2LG) spectrum in red. On the bottom panel, the spectra after subtraction of the SiC signal for 1LG in blue and for 2LG in red are represented. Figure represented with permission of [42].	46
Figure 3.15. Schematics of the two-point probe(2PP) measurement configuration applied to a graphene device fabricated on top of $300\text{ nm SiO}_2/\text{Si}$	48
Figure 4.1. Example device formed by several layers of 2D materials, i.e. hBN, graphene and InSe. The device was fabricated using the methods described in this chapter. More details are provided later in Section 4.8.	49

Figure 4.2. Schematic example showing the building process a random heterostructure formed by bottom hBN, with InSe and graphene sitting on top. As indicated by the blue arrows, a final layer of hBN will be deposited as the cover of the structure, in order to produce a typical encapsulated device. Importantly, the aggregation of interlayer contaminants is depicted as dark blue conglomerates between graphene and InSe. It is important to highlight how the graphene surface conforms to the shape of this contamination as well as to the shape of the other layers of the structure (i.e. the InSe flake, for instance). On the top part of the figure, above the hBN cover layer, environmental species present in the air are also depicted, showing the variety of molecules that could interact with 2D materials. In the inset, an AFM image of a flake shows the formed bubbles and ripples with white contrast. This kind of features are common to all 2D materials, appearing as a result of the transfer process. A colour-coded legend has been placed at the bottom of the figure to provide visual guide of the type of materials used. Inset figure adapted with permission from [8] 51

Figure 4.3. Schematic flowchart describing the substrate preparation and the mechanical exfoliation as independent processes only interlinked at the very end. This connection between the two is shown by the dashed blue line joining the prepared substrate with the deposition of the materials. For the substrate preparation process (left side), the steps concerning silicon dioxide and polymers are described in red and grey, respectively. The parts in green at the bottom are common for both types of substrates. However, the plasma treatment square is highlighted by a dashed orange border as it can be skipped in certain cases. For the mechanical exfoliation process (right-side), the steps are described by yellow squares while the different options per step are shown inside the diamond shaped blocks. 54

Figure 4.4. Bulk crystals of graphite, hBN and InSe. Grain boundaries in graphite and InSe can be observed. Scale bar: 1 cm 56

Figure 4.5. Superposition exfoliation process, with hBN shown as an example. **(a)** Cut two squares of tape and peel off the backing side to expose the sticky surface of the tape. **(b)** Deposit a crystal on one of the tapes, bring both of them together and press them. **(c)** Peel the tapes off and bring them back together. Repeat this process until the surface of the tape is fully covered of material as shown in **(d)**. 57

Figure 4.6. Step by step exfoliation process, with graphene shown as an example. **(a)** A bulk crystal is deposited on top of the sticky side of the adhesive tape. **(b)** Then, the tape is folded on top of the crystal and pressed down. **(c)** When peeling the tape off, few layers of crystal have attached to it, leaving a mark on the surface. At this point, the crystal is removed. **(d)** The marked part of the tape is folded onto itself several times always on top of clean areas. **(e)** This leaves marks of thin 2D materials on different locations. **(f)** The substrate of choice is placed on top of the desired area and pressed down to enhance the transfer of material to its surface. 57

Figure 4.7. Optical contrast of graphene as a function of the wavelength and the silicon dioxide thickness. Different light wavelengths are represented with respect to the silicon oxide

thickness. The values of the graphene contrast are calculated using the Fresnel formalism. Figure represented with permission from [31]	59
Figure 4.8. Exfoliated hBN on PMMA for different magnification objectives: (a) x5, (b) x20, (c) x50 and (d) x100.	60
Figure 4.9. (a) Bright field image of hBN exfoliated on PMMA. (b) Dark field of the same hBN flake. In this mode, the folds and contamination appear bright.....	61
Figure 4.10. Optical images acquired with a x10 objective. (a) Bright field image of InSe with 10% Fe intercalated. (b) Optical image acquired under white light and using a U-AN360-3 Olympus rotatable analyser.....	62
Figure 4.11. (a) Optical image of graphene monolayer flakes exfoliated on top of a PMMA/PVA/Si substrate. The image has been processed with three different edge detection algorithms: (b) Sobel, (c) Laplacian filter and (d) Scharr.....	64
Figure 4.12. Transfer station system designed and built for this project. (a) Optical microscope for flake identification. (b) Copper sample holder able to reach high temperatures and with incorporated vacuum. (c) xy stage allowing with micrometric step control. (d) Glass slide holder. (e) Vacuum tube connecting the bottom of the sample holder with the vacuum pump. (f) xyz micromanipulator base allowing control of the glass slide position. (g) Current source providing temperature control of the sample by Joule heating.....	66
Figure 4.13. PPC/PDMS polymer blocks fabrication process. (a) PDMS cured in the Petri dish and cut into $\sim 1 \times 1 \text{ cm}^2$ squares. (b) Drop of PPC on top of the PDMS block prior to spin-coating. (c) Resulting PPC/PDMS block after spin coating and baking. (d) Process of cutting the PPC/PDMS into small cubes of $\sim 1 \text{ mm}^2$. (e) Once the polymer blocks are glued to the glass slide, these are baked at 110°C for 5 minutes to improve the adhesion between both polymers. (f) Schematic view of a glass slide with the PDMS and PPC attached to it.....	68
Figure 4.14. (a) Schematic diagram showing the PPC/PDMS block entering in contact with the sample. The position of the PPC frontline is highlighted by a blue dot. (b) Optical image obtained with a x5 magnification objective. The area in which the PPC has established contact with the sample (top-left corner) presents a different contrast, lighter, than the area in which the polymer is still away from the surface. The PPC moving frontline has been again highlighted in blue.....	70
Figure 4.15. Schematic depiction of the PPC/PDMS transfer. Pick-up steps start with: (a) the material of interest(hBN) exfoliated on the substrate of choicee. <i>g.</i> $300 \text{ nmSiO}_2\text{Si}$. (b) Then, the substrate is heated up to 55°C , and the PPC/PDMS is brought closer to the surface. (c) When the PPC is in contact covering the flake of interest, the temperature of the substrate is reduced to 40°C . (d) The polymer is then removed out of contact by doing a “snap” movement, picking-up the flake from the substrate. The next step in the heterostructure fabrication is the drop-down: (e) a suitable graphene flake is found on the substrate and aligned with the hBN on the polymer. The temperature of the sample stage is set up to $\sim 110^\circ\text{C}$. (f) Both flakes are	

brought into contact. At this point, the temperature of the sample holder is reduced to 70°C, and the tape is removed as slowly as possible, so the flakes remain on the surface of the substrate. **(g)** The chip is then baked on a hotplate at 170°C for 30 minutes to enhanced the adhesion between the layers and avoid future delamination..... 72

Figure 4.16. Schematic depiction of the PMMA carrying layer method. **Step 1.** Wafer substrate preparation. **(a)**Initial test Si wafer. **(b)**PVA spin coated on top of the test Si wafer. The PVA is a water-soluble polymer **(c)**PMMA spin coated as a final cover layer. **Step 2.** Cutting the substrate. **(d)**Picture of the final PMMA/PVA/Si substrate. **(e)**Cutting the substrate with diamond scribe. **(f)**Final chips ready for exfoliation. **Step 3.** **(g)**Exfoliation of the 2D materials on the PMMA. **(h)**Find a suitable flake on the surface via optical microscopy. **Step 4.** **(i)**Scribing of the PMMA (purple) leaving the PVA exposed (green). **(j-k)** Process of hydration of the PVA. **(l)**Optical micrograph of the PMMA membrane. **Step 5.** **(m)** Fishing the membrane on the water using the plectrum. **(n)** Plectrum with membrane attached. As shown in the detail, ideally, the flake should sit on top of the membrane. 75

Figure 4.17. Membrane drop-down and deposition method. **(a)** Membrane on the plectrum observed with the x10 objective before contact. **(b)** Membrane in contact with the substrate. **(c-f)** Sequential process of membrane retraction 77

Figure 4.18:NGI transfer station placed inside a glovebox. **(a)** Motorised transfer system. The sample stage (orange) has a vacuum chuck to hold the substrates in place, heating and rotating capabilities. The transfer arm (green) is formed by a dedicated plectrum holder arm with a vacuum chuck and two micromanipulators to control the tilt of the plectrum. The microscope (blue) allows the optical identification of flakes and alignment. **(b)** Glovebox system **(c)** Micromanipulator controllers, optical zoom adjustment and computer for the control of the motorised transfer system. 78

Figure 4.19. Example of encapsulated graphene heterostructures fabricated using the methods discussed here: **(a)**PPC/PDMS transfer method was used to produce this heterostructure that was finally employed by Vincent et al.[56]. Scale bar: 10 μm. **(b)**On the other hand, this heterostructure was fabricated using the PMMA carrying layer method. It was patterned into a device and used for thermal measurements with SThM, further discussed in chapter 7. Scale bar is: 20 μm. **(c)**Lateral view of the layers forming the heterostructures discussed on (a) and (b). The colour legend on the right helps differentiating the layers. 81

Figure 4.20. Simplified schematics of common steps undertaken to transform a 2D material based heterostructure into a device. It is important to highlight that the order of the steps and the number of repetitions might vary depending on the complexity of the device. 82

Figure 4.21. Schematic of 1D contacts created on: **(a)**an encapsulated graphene device, and **(b)**an InSe device with overlapping graphene. For the contacts, the metal used is represented in yellow, while the adhesion layer is represented as a dark brown line. 84

Figure 4.22. **(a)**Optical image of an encapsulated InSe Hall bar device fabricated on top of a 300 nm SiO₂/Si wafer (purple-black). The whole chip was mounted on top of an insulating

mica spacer (white) to avoid direct contact between the Si bottom layer and the conducting Au layer of the chip carrier. Gold wires connect the Au pads from the device with the Au wires on the chip carrier, using silver epoxy (grey blobs) as bonding contact. In **(b)** an optical micrograph shows the detail on the bonding of the pads performed on the device. 86

Figure 4.23. Flowchart of the fabrication steps followed to produce an encapsulated InSe heterostructure with graphene finger contacts, employing the PMMA stamp transfer method. **(a)** Bottom hBN exfoliated on 300 nm *SiO₂/Si*. **(b)** Graphene fingers exfoliated onto PVA/PMMA, and surrounded by a white dotted line. **(c)** Transferred graphene fingers onto the bottom hBN layer using the PMMA carrying layer method. **(d)** Top hBN layer exfoliated onto PMMA/PVA and surrounded by a dark blue line. Final result of the heterostructure shown in **(e)** bright field, and **(f)** dark field. The scale bar in both images is 20 μm. **(g)** A schematic lateral view of the layers conforming the heterostructure following the colour legend at the bottom for the different materials. 87

Figure 4.24. Flowchart of the steps followed to transform the heterostructure presented in the previous figure into a finalised device. **(a)** AFM scan over the device area showing wrinkles and bubbles. Scale bar: 5 μm **(b)** AFM image after brooming. The area scanned appears clean with the dirtiness accumulated at the sides. **(c)** Alignment marks (surrounded by yellow circles) created around the heterostructure. **(d)** Layout editor design of the device, later exported to .gds format compatible with EBL. **(e)** EBL and metallisation of the big contact pads. **(f)** Detail showing the untouched heterostructure and the Cr/Au contacts deposited around it. **(g)** Final device produced after few cycles of resist, EBL, etching and metallisation. The final device consisted of a Hall bar of 6 arms, with two thermometers and a gold heater. Scale bar: 20 μm..... 90

Figure 5.1. Scheme of the Raman humidity measurements experimental set-up. The Raman scan parameters are controlled directly from the computer. The different values of humidity within the LinKam THMS600 environmental stage are achieved via a constant flow of water drops (blue) produced by a LinKam RH95 humidifier with nitrogen used as carrier gas (red). As shown in the inset, both gases are connected to the inlet of the chamber, where the sample is placed. The resulting gas is expelled from the outlet. The flow of gases and the temperature are controlled via the LinKam RH95 system. 96

Figure 5.2. **(a)** Optical image of the exfoliated flake on 300 nm *SiO₂/Si*. The region of interest (ROI) surrounded by a red square presents mainly two distinct regions with a very light contrast with respect to the bright blue substrate, corresponding to monolayer (1LG) and bilayer (2LG) areas. **(b)** The thickness of the flakes in the ROI is confirmed by AFM topography using profiles from the substrate to 1LG (yellow dotted line), and from the 1LG to 2LG (blue dashed line). **(c)** Profile following the yellow dotted line from (b) giving a total thickness of 1LG with respect to the substrate of $t \sim 0.34 \text{ nm}$ **(d)** Profile following the blue dashed line from (b) giving a total thickness of 2LG with respect to 1LG of $t \sim 0.37 \text{ nm}$, and thus a total thickness with respect to the substrate of $t \sim 0.71 \text{ nm}$ 98

Figure 5.3. **(a)** Topography and **(b)** surface potential images of the CVD sample. The KPFM map shows a homogeneous area mostly 1LG (dark contrast), with higher contrast areas corresponding to 2LG (green) and 3LG (blue). **(c)** Topography of the epitaxial graphene sample displaying the typical terraced surface, and **(d)** contact potential difference map showing 1LG (dark contrast), and stripes of higher contrast areas corresponding to 2LG, typically located at the edges of the terraces 99

Figure 5.4. Raman maps representing the G-peak integrated intensity for **(a)** exfoliated, **(b)** CVD-grown and **(c)** epitaxial graphene using 532 nm excitation wavelength. The regions corresponding to 1LG and 2LG are indicated in each image. The measurements were carried out in ambient. 100

Figure 5.5. Representative Raman spectra for **(a)** exfoliated, **(b)** CVD-grown, and **(c)** epitaxial graphene at varying humidity levels from 0% to 60% RH. In all cases, results corresponding to 1LG are represented at the top, and results for 2LG at the bottom. Spectra are shifted vertically for clarity. In **(d)** and **(e)** a summary of the peak position variation with humidity is shown for the of the G and 2D peaks, respectively. 102

Figure 5.6. Example of the application of the vector decomposition method. Figure representing the relation between the 2D frequency versus the G frequency, in which the data is obtained from fitting the graphene Raman peaks using Lorentzian curves. The position of the green dot corresponds to free-standing graphene, not affected by strain or doping. Displacement up or down on the black dotted line results in undoped graphene with an increase of compressive or tensile strain, respectively. Increases in doping are slightly more complex: movement along the pink dotted line towards higher frequencies results in strain-free graphene with higher p-doping, as denoted by the pink arrow; while the n-doping is determined by the curved trajectory in solid blue, also highlighted with a blue arrow. Inset: decomposition of the effects of hole doping and strain using a vector model. Any point in the map can be represented as a vector, OP , which can be further decomposed into two directions: along the OH 'strain-free' with hole doping, and along the OT 'charge-neutral' for tensile strain. These two lines divide the space into four quadrants (Q1-Q4). (Note that the data reported here is just an example, and it is not related to the discussion of the Raman) Adapted with permission from [44] . 104

Figure 5.7. **Top panel - Exfoliated graphene sample.** **(a)** Raman intensity map of the 2D peak at 0% R.H. This map was employed to distinguish the areas of mono- and bi-layer graphene, as well as the substrate regions. The red lines show the threshold value of 300 counts used to discriminate between the graphene region, and the substrate. The white dashed rectangle indicates the area of interest containing 1LG, and focused on in detail in the maps (c-h). **(b)** Raman map of the FWHM of the 2D peak at 0% R.H. This map was used to distinguish between areas of 2LG and 1LG. The red lines show the threshold value of 40 cm^{-1} , above which the graphene was judged to be 2LG. The size of the map in (a-b) is shown..... 105

Figure 5.8. Variation of the holes carrier concentration with respect to varying humidity levels from 0%RH up to 60%RH for **(a)** exfoliated and **(b)** CVD graphene. **(c)** Schematic diagram of how the relative humidity affects the work-function of graphene resulting in p-doping. 106

Figure 6.1. **(a)** Custom made sample holder for electrical measurements in the NT-MDT AURA system, allowing measurements in different environmental conditions. **(b)** Custom made TO-8 ceramic header. As shown in the image, the samples were fit in the centre of the holder and then connected via 12 Au pads. 111

Figure 6.2. Ultraviolet photon spectroscopy diagram of the intensity versus the binding energy extracted and modified from experimental data taken from our Au reference sample. The valence band electrons area is surrounded by a dashed black circle. The area corresponding to secondary electron cascade emission is highlighted by a green background. The cut-off energy is extracted by fitting the sharp region on the curve with a straight line, represented here as a dashed dark blue line. The Fermi level is represented by a dashed yellow line. ... 114

Figure 6.3. **(a)** Optical image of one of the calibration samples acquired with the camera of the Aura NT-MDT SPM system prior to a measurement. The wire bonds performed to the pads for grounding are visible in the image, as well as the AFM probe with the back reflected laser. **(b)** UPS spectra for Au (green) and Pt (blue), representing the intensity versus the binding energy. 114

Figure 6.4. Calibration sample maps acquired using single pass FM-KPFM providing simultaneous imaging of the **(a)** topography and the **(c)** surface potential *VCPD*. **(b)** Profiles extracted from the blue line in the topography showing a step of ~ 25 nm height, and **(d)** *VCPD* distribution map over the sample area showing two differentiated regions corresponding to the substrate (green) and the metal pad (brown). Scale bar: $1 \mu m$ 116

Figure 6.5. Trace and retrace profiles for the topography (blue) and the surface potential (red) acquired over the step between the metal pad and the substrate on the calibration sample. 117

Figure 6.6. **(a)** 3D representation of the measured contact potential difference superimposed on the topography of the calibration sample. The substrate is shown in green, the bond pad in brown and the edge is shown in yellow. The black dashed arrows represent the trajectory followed by the probe during the measurement. Point-measurements are performed at the locations highlighted by blue dots. Temporal response of the **(b)** PFQNE-Al and **(d)** NSG03-Pt probes represented by a black line, with the profiles followed by the X and Y scan directions represented by full and dotted red lines, respectively. Detail of the response during the first seconds of measurement for the **(c)** PFQNE-Al and the **(e)** NSG03-Pt probes. 119

Figure 6.7. Effect of varying the **(a)** amplitude and **(b)** the frequency of the AC modulation applied to the probe on the *VCPD*. As seen in **(a)**, the variation of the *VCPD* with respect to the *VAC* has been tested for both contacts Pt and Au, showing a difference on the contact potential difference of around 450 mV, similar to the separation between the work-functions obtained with UPS measurements (~ 490 mV). In **(b)**, The variations of the frequency have been only measured for the Au contact, however the contact potential difference changes only ~ 15 mV for the total range of frequencies tested (1 – 10 kHz). 122

Figure 6.8. **(a)** Contact potential difference *VCPD* measured using Pt-coated probes for all the reference samples: Pt (black), Ti (pink), Au (red) and Ta (blue) as a function of the bias voltage

applied to the metal pads. The value of the V_{CPD} at $V_{BG} = 0$ is highlighted in yellow **(b)** Comparison of the KPFM work-function results against the UPS measured values for the different metallic reference thin films (same as in **(a)**) including HOPG, measured in air and in vacuum **(c)** Measurement of Pt and Au work-function using SPARK-350 NuNano probes with different Pt coating thickness **(d)** Distribution of work function values for a batch of 20 nominally identical probes (SPARK-350 NuNano, 40 nm coating).123

Figure 6.9. SEM images of the NSG-03 probes acquired **(a)** before and **(b)** after performing KPFM measurements. From the image in **(b)**, it is obvious that some damage has been induced to the coating of the probe, most probably affecting the surface potential values obtained. It is not possible either to rule out the presence of contamination. Scale bar: $10 \mu m$125

Figure 6.10. Maps of the **(a)** topography and **(c)** surface potential of an area with graphene fingers. Scale bar is $2 \mu m$, and both images present the same aspect-ratio. Profiles extracted from the black line are represented for the **(b)** topography and the **(d)** surface potential.126

Figure 6.11. **(a)** Optical image of exfoliated flakes deposited on SiO_2 substrates with pre – patterned gold contacts. Scale bar: $10 \mu m$. **(b)** Schematic depiction of the hand-made TO-8 headers, with the exfoliated sample placed in the centre, ready to perform bonding to the Au contact pads, depicted in gold colour. **(c)** 3D topographic view of a graphite flake sitting on top of two Au electrodes, with the work-function map superimposed. **(d)** Evolution of the work-function with respect to the graphite thickness. The results were obtained for 3 different probes, calibrated following the proposed method. The arrows indicate that graphene work-function tends to $\sim 4.64 eV$ for monolayer, and to $\sim 4.38 eV$ for bulk.127

Figure 6.12. Schematic design for the narrow channel GFET encapsulated devices. The bottom hBN is signalled as light green background, the top hBN with a blue square and the graphene is shown as a grey stripe.129

Figure 6.13. Selective etching process of the encapsulated graphene heterostructure shown in **(a)**. **(b)** hBN etching with SF_6 **(c)** Graphene etching with O_2 and **(d)** Final device after etching 130

Figure 6.14. Optical images of the devices after the fabrication process with magnification **(a)** x20 and **(b)** x5.131

Figure 6.15. **(a)** Electrical schematics of the KPFM experiment with a back-gate voltage applied. The compensation voltage, V_{DC} , was applied to the tip. The work-function of the sample can be locally calculated by using the already known work-function of the tip and the measured V_{DC} . **(b)** Optical micrograph of the device. Four different devices fabricated in the same heterostructure are highlighted by orange rectangular shapes. The approaching direction of the probe with respect to the devices is shown. The electrical connections are represented by black lines.133

Figure 6.16. **(a)** Topography of the device showing the different layers: the bottom hBN (black sign), the graphene buried layer (yellow outline) and the top hBN (Blue dotted outline). The contacts are located in pairs on the sides, showing a dark green contrast. **(b)** Surface potential maps of the narrow graphene channel from **(c)**. Two different SP maps are presented for two

different applied backgate voltages, 0 V (top) and +5 V (bottom). The voltage colour scale has been normalised for both measurements. Scale bar: 1 μm	133
Figure 6.17. (a) Schematic lateral view of the device, showing the substrate formed of Si (light purple) and 300 nm of SiO_2 (dark purple), with a graphene layer (black) encapsulated between hBN layers (green) on top. (b) VCPD line profiles represented for different VBG and acquired following the white dashed line in figure 6.16(b).....	135
Figure 6.18. Graphene specific potential profile across a 100 nm wide graphene strip for a VBG = +10V. The downturned brims at the edges originate from quantum capacitance effects characteristic for graphene. Image adapted with permission from [71]	135
Figure 6.19. Schematic drawing showing: (a) the concept of AFM brooming, and (b) the effect of removing the PMMA layers with the consequent accumulation of debris on the sides of the scan. At the end of the process the PMMA in the central area is fully removed and accumulated at the sides. (c) Deflection signal showing the effect of the removal of the PMMA layer from the surface through time. Scale bar: 2 μm (d) Larger topography map including the area that has been broomed, showing the accumulation of the polymer at the edges of the square. Scale bar: 5 μm (e) Deflection detail taken around the dashed green square after the cleaning has been finished. Scale bar: 2 μm	136
Figure 6.20. KPFM work-function maps of the sample for different back gate voltages. The work-function of the sample was calculated by using $\Phi_{\text{sample}} = \Phi_{\text{tip}} - eV_{\text{DC}}$. The value of the backgate voltage applied in each case is specified by the blue labels placed inside the images. The scale has been normalised and it is common to all work-function maps. On the bottom left corner, an image of the topography is shown in green with the different layers highlighted: bottom hBN in red, graphene in yellow, and top hBN in dark blue. Scale bar: 1 μm	139
Figure 6.21 (a) Measured work function of SLG encapsulated samples as a function of VBG. The point of VBG = 0V is highlighted in light grey.	140
Figure 7.1. (a) System set-up. 1-The electronics rack used to perform the measurements. 2- Connection box. 3-Vacuum pumps, a rotary, a turbo and an ion pump used to achieve different vacuum environments. Surrounded by a red squared: the main head of the microscope. 4- Glass bell to hold the vacuum in the system. 5-Thermal reservoir. (b) Detail of the microscope in which we can see the 6- NT-MDT head of the microscope and 7-the camera. (c) Detail of the microscope head in which we can see 8-the sample holder and 9-the suspended base using springs.	147
Figure 7.2. (a) SEM image of a KNT Pd coated probe. Figure reproduced with permission of [17]. (b) SEM image of a doped-Si probe from Anasys AN2-200. Figure reproduced with permission of [16].....	149
Figure 7.3. Schematic set-up employed for all the measurements in the chapter: SThM, STGM and electrical measurements.....	150
Figure 7.4. InSe exfoliated on (a) 300 nm SiO_2/Si and (b) Si	151
Figure 7.5. (a) Topography and (b) SThM response maps of an area on the sample showing a large collection of InSe flakes of varying thicknesses on top of a SiO_2 substrate. Scale bar: 20 μm .	

(c) SThM voltage response, where V_{out} is the voltage on the inner area of the flake, and V_{SiO2} the voltage of the probe measured on the substrate, as a function of the number of layers. Note that the study only considers flakes with $area > 4\mu m^2$. Inset: Optical image showing another area of the sample with a collection of InSe flakes of different thicknesses exfoliated on top of SiO_2 . Scale bar: $100\ \mu m$. The maps and optical images were acquired with the microscope of the nanoIR2 system. The KNT probe can be seen in the image with the laser spot placed almost at its base. Reproduced with permission from [1].....152

Figure 7.6. Schematic diagram of the thermal resistances present in the system: **(a)** When the probe is out-of-contact, only the thermal resistance of the probe has an effect on the heat propagation. **(b)** However, when the probe is in-contact with the surface, a set of resistances appear, including: R_{tip} , $R_{contact}$ and $R_{spread - sub}$, corresponding to the thermal resistance of the tip itself, the detail of the contact and the heat spreading ability of the substrate, respectively. All these resistances are summed together in series under one term, R_x , which is then added in parallel to the original R_p . **(c)** Zoom-in detail to the resistances that conform $R_{contact}$, including $R_{Int, tip - InSe}$, the thermal interfacial resistance of the tip and the material; $R_{spread - InSe}$ the thermal resistance of the heat spread inside the InSe flakes, and $R_{Int, InSe - subs}$, the thermal interfacial resistance between the InSe and the substrate. Note that for (a-b), the heating of the probe is represented as temperature gradient established between the colder base of the cantilever T_{cold} , and the hotter part at the tip region T_{hot}154

Figure 7.7. Representative example of the measurements acquired for exfoliated InSe in vacuum $\sim 10 - 7\ mbar$. In the left column, measurements of the InSe exfoliated on SiO_2 showing in **(a)** the topography, **(b)** the SThM response and in **(c)** the profiles of the topography and the SThM response depicted together and acquired over the dotted white line in (b). On the right column, measurements of the InSe exfoliated on Si showing in **(d)** the topography, **(e)** the SThM response and in **(f)** the profiles of the topography and the SThM response depicted together and acquired over the dotted white line in (e).....157

Figure 7.8. SThM response measured in vacuum ($\sim 10 - 6\ mbar$) as a function of the number of layers for InSe exfoliated on **(a)** SiO_2 and **(b)** Si substrates.....158

Figure 7.9. **(a)** Topography of the graphene encapsulated device (Scale bar: $1\ \mu m$) with different patterned constrictions: **(b)** half bow-tie-flat junction top, **(c)** rectangular flat-narrow-flat central and **(d)** half bow-tie-flat junction bottom constriction. **(e)** Schematic of the experimental set-up for STGM. The probe acts as a local heater, while the thermovoltage generated on the graphene layer is measured through the Au contacts, highlighted in yellow in the figure.....161

Figure 7.10. Fabrication process of the encapsulated graphene device. In **(a)**, the top panel shows a bright field image with the bottom hBN, 1LG and top hBN surrounded by light green, grey and dark blue lines, respectively. In the bottom panel, a schematic lateral view of the layers is displayed following the same colour convention, with a legend for guidance. In **(b)**, the dark field microscopy image shows more clearly the contours of the different layers. The scale bar

both in (a) and (b) images is $20 \mu m$. In (c) the design of the device is performed in Layout Editor. In the left panel, an overview of the whole heterostructure with the design placed on top is presented, while the right panel shows a more detailed view of the constrictions. (d) Sample containing the device mounted on a gold chip carrier and wire bonded by hand. (e) Detail of the bonding on the contact pads of the device. (f) Close zoom-in of the device on the chip with three alignment marks. The area in which the rest of the heterostructure was placed is clearly visible as it presents a different contrast than the rest of the surface of the 300 nm SiO_2 chip. Scale bar: $50 \mu m$163

Figure 7.11. (a) AFM topography of the encapsulated device. Scale bar: $2 \mu m$. The contact pads have been named as top(T) and bottom(B), establishing a reference notation for the following sections. Profiles of the contact and the device are acquired following the red and yellow lines, and are shown in (b) and (c), respectively. (d) Raman spectrum showing the characteristic hBN peak (highlighted in orange) and the G and 2D graphene peaks (highlighted in grey). Inset: Intensity map obtained using the G-peak of graphene. The spectrum was acquired at the black dot position in the inset (e) Channel resistance versus backgate voltage measured at room temperature and $P = 10 - 7 \text{ mbar}$. The measurements were performed using a 2 point-probe set-up ($V_{DSLIA} = 0.1 \text{ V}$, which resulted in $I_{DS} \sim 0.1 \mu A$).....164

Figure 7.12. (a) SThM map of hBN encapsulated graphene test device. Darker contrast corresponds to higher thermal conductivity as expected from the hBN and graphene stack. Scale bar: $1 \mu m$. (b) Comparison of the profiles acquired for the topography (black) and the SThM response (red) signals.....165

Figure 7.13 Thermovoltage measurements performed in vacuum ($\sim 10 - 7 \text{ mbar}$), with the sample at room temperature ($T_s \sim 293 \text{ K}$), and an excess temperature on the tip of $\sim 50 \text{ K}$. Measurements were performed for different backgate voltages: (a) $V_{BG} = -6.8 \text{ V}$, therefore showing p-doped behaviour, and at (b) $V_{BG} 5.7 \text{ V}$, with an n-doped behaviour. In (c) profiles acquired across grey dotted line in (a) are compared for both p (orange) and n (green) type doping behaviours. In (d), the p-doped image was inverted, and the n-type (orange) and inverted p-type (green) profiles were compared in order to assess the symmetry of the response for opposite charge doping in the device.168

Figure 7.14. Thermovoltage measurements performed in vacuum ($\sim 10 - 7 \text{ mbar}$) and low sample temperatures ($T_s \sim 170 \text{ K}$). Almost opposite Seebeck domains can be observed for (a) p-doped graphene ($V_{BG} = -3 \text{ V}$) and (b) n-doped graphene ($V_{BG} = 3 \text{ V}$). (c) Profiles of the p-doped (green) and the n-doped (orange) maps are compared. The profiles were acquired along the dotted grey line in (a). The contacts have been labelled as S (source) and D (drain) corresponding to the top and bottom contacts, respectively.....170

Figure 7.15. Tip gating effect studied by comparing the signal profiles obtained along the line shown in the inset. Two heating voltages are depicted, namely $V_{DC} = 3 \text{ V}$ (black) and $V_{DC} = -3 \text{ V}$ (red) for (a) p-doped graphene ($V_{BG} = -6.8 \text{ V}$), and (b) n-doped graphene ($V_{BG} = -5.7 \text{ V}$).....171

Figure 8.1. Schematic of beam-exist cross-section polishing (BEXP), in which the Ar ions are attacking the surface at an angle of 5° , etching the top material and creating a gradient surface suitable for SPM studies. Image reproduce with permission from [15].....181

Figure 8.2. Encapsulated InSe Hall bar devices. The contacts connecting the heater are highlighted by a green square. Two micro-thermometers were patterned onto the InSe structure and their contacts are surrounded by red and orange, for the one closest to the heater and for the furthest one, respectively. Finally, the contacts connecting the Hall bar are surrounding the InSe are shown in light blue.....182

Figure A.1. Graphical user interface (GUI) developed for the application of edge detection algorithms to 2D materials. Using the controls in the left section, an image can be opened from folder. Images will open on the bottom-left corner. On the right side of the menu, options to modify the values of the filters are available.....184

LIST OF TABLES

Table 4-1. Tapes used for exfoliation for different 2D materials and substrates	56
Table 4-2. Spin coating recipes for PVA and PMMA fabrication	73
Table 4-3. Comparison between the PMMA stamp method and the PPC/PDMS hot pick-up technique.	80
Table 5.1. Characteristic averaged values for the position and FWHM of the G and 2D peaks recorded in ambient $T = 21^{\circ}\text{C}$, $RH = 40\%$. The spectral resolution of the Raman spectrometer is specified in the table as $\pm 2 \text{ cm}^{-1}$	101
Table 6.1. List of the probes employed during the development of a KPFM calibration procedure	111
Table 6.2. Work-function values for the different selected metals obtained via UPS and from a tabulated reference[14].	115
Table 6.3. Data extracted from figure 6.8(a): the intercept from the linear fitting, its error, the work function measured using UPS, and the calculated probe work-function based on the KPFM measurements using eq.6.2.....	123
Table 6.4. Work-function measured values for the encapsulated graphene devices for $V_{BG} = 0$	141
Table 7.1. Thermal probes employed in the experiments described in this chapter	148
Table 7.2. Equations showing the resistor model for heat propagation when the probe is out-of-contact or in-contact with the sample	153

Glossary and abbreviations

1LG – Graphene monolayer	EFM – Electrostatic force microscopy
2LG – Graphene bilayer	EG – Epitaxial graphene
AC / DC – Alternating current / Direct current	EMFP – Electronic mean free path
AFE – Ambipolar field effect	FET – Field effect transistor
AFM – Atomic force microscopy	FOM – Figure of merit of thermoelectrics
AI – Artificial intelligence	FOV – Field of view
BEXP – Beam exit cross-sectional polishing	GFET – Graphene field effect transistor
BP – Black Phosphorous	H₂O – Water
C – Carbon	hBN – Hexagonal boron nitride
CAB – Cellulose acetate butyrate	HCOH – Formaldehyde
CB – Conduction band	HOMO – Highest occupied molecular orbital
CCD – Charge coupled device	HOPG – Highly oriented pyrolytic graphite
CL – Closed loop	HRTEM – High resolution transmission electron microscopy
CMOS – Complementary metal oxide semiconductor	IE – Ionization energy
CNP – Charge neutrality point	IFL – Interfacial layer
CNTs – Carbon nanotubes	InSe – Indium selenide
CVD – Chemical vapour deposition	IPA – Isopropyl alcohol
DF – Dark field	ITO – Indium tin oxide
DI WATER – Deionised water	KPFM – Kelvin probe force microscopy
DOS – Density of states	FM-KPFM – Frequency modulated Kelvin probe force microscopy
DTU – Technical University of Denmark	
EBL – Electron beam lithography	

AM-KPFM – Amplitude modulated Kelvin probe force microscopy

LD – Low-dimensional

LEEM – Low-energy electron microscopy

LIA – Lock-in Amplifier

LT – Low-temperature

LUMO – Lowest unoccupied molecular orbital

MFM – Magnetic force microscopy

MLG – Multilayer graphene

MO – Molecular orbital

NH₃ – Ammonia

NN – Neural network

NO₂ – Nitrogen dioxide

NPL – National Physical Laboratory

PDMS – Polydimethylsiloxane

PID – Proportional, integral and derivative.

PMMA – Poly(methyl methacrylate)

ppm – Parts per million

ppb – Parts per billion

PPC – Poly(propylene carbonate)

PTB – Physikalisch-Technische Bundesanstalt

RGB – Red, green and blue channels

RH – Relative Humidity

RIE – Reactive ion etching

RT – Room temperature

SEM – Scanning electron microscopy

SPM – Scanning probe microscopy

Si – Silicon

SiC – Silicon carbide

SiO₂ – Silicon

STM – Scanning tunnelling microscopy

STGM – Scanning thermal gate microscopy

SThM – Scanning thermal microscopy

TDTR – Time-domain thermo-reflectance

TE – Thermoelectric

TMCs – Transition metal chalcogenides

TMDCs – Transition metal dichalcogenides

UFM – Ultrasonic force microscopy

UPS – Ultraviolet photon spectroscopy

VB – Valence band

vdW – Van der Waals

List of symbols and constants

α – Temperature coefficient of the electrical resistance [K^{-1}]

C – Capacitance [F]

e – Electron charge [C]

E_a – Activation energy [eV]

E_b – Binding energy [eV]

E_{vac} – Vacuum energy [eV]

E_F – Fermi level [eV]

E_F^{Gr} – Fermi energy of graphene [eV]

f – Frequency [Hz]

G – Thermal conductance [$W \cdot K^{-1}$];

\hbar – Reduced Planck's constant [$J \cdot s$]

I – Current [A]

κ – Thermal conductivity [$W \cdot m^{-1} \cdot K^{-1}$];

κ_{\parallel} – In-plane thermal conductivity; κ_{\perp} – Out-of-plane thermal conductivity.

k_B – Boltzmann constant [$m^2 \cdot Kg \cdot s^{-2} \cdot K^{-1}$]

Q – Heat flux [$W \cdot m^{-2}$]

R_{Gr} – Graphene resistance [Ω]

σ – Electrical conductivity [$S \cdot m^{-1}$]

S – Seebeck coefficient [$V \cdot K^{-1}$]

T – Temperature [K]

V – Voltage [V]; V_{AC} – AC Voltage [V]; V_{DC} – DC Voltage [V]. V_{BG} – Backgate Voltage [V].

x, y, z – Cartesian coordinates. Displacement in the lateral, forward and vertical directions, respectively. [m]

v_F – Fermi velocity [$m \cdot s^{-1}$];

ZT – Figure of merit of thermoelectrics

ω – Angular frequency [$rad \cdot s^{-1}$]; NOTE: $\omega = 2\pi f$

Φ – Work-function [eV]

Introduction

“Our modern technology builds on an ancient tradition” [1]

From the rudimentary stone tools used by our ancestors to our modern silicon-based electronic era, it is undeniable that materials have shaped the evolution of human history. It is so, that even early ages of civilization are classified by the key material used at the time, i.e. Stone Age, Bronze Age and Iron Age. However, hundreds, even thousands of years, were spent in order to improve the properties of the materials, compounds and alloys, structures and processing recipes, as most of the knowledge was based on empirical observation, with very little understanding of the chemistry or physics playing in the background.

It was in the latest decades of the 19th century when several scientists, such as A. Matthiessen, G. Wiedmann, E. Hall and P. Drude among others, took the first steps towards unravelling the secrets behind the atomic structure and material’s behaviour, building the foundations for the modern solid-state physics and material science. The 20th century was thus a very exciting era in this regard. Notably, the attention of the scientific community during this century shifted its focus from the attainable macroscopic world to its very small constituents. The development of quantum mechanics and the crystalline theory of solids allowed us to finally start understanding how the atoms are arranged together, why its different crystalline structures could have such a huge impact in the properties of solids and what was the behaviour of these small pieces holding the machinery together at the very core of matter.

However, looking deeper into matter was not an effortless path. When did it happen that our understanding and capability was able to overcome the micron scale? For many, 1959 is the revolutionary year in which finally, the seeds that would give birth to nanotechnology were first sowed. In this year the words that needed to be heard were finally pronounced. In the extremely broadly cited lecture, *“There is plenty of room at the bottom”* [2], R. P. Feynman discussed the

possibilities and challenges of working at reduced scales, even achieving atomic precision. At that time, the ideas presented in the lecture were still either under development or far from even being achieved, as all belong to a field that was not even named yet, but that was to flourish soon like no other.

In 1974, Norio Taniguchi employed for the first time the term nanotechnology in his paper “*On the basic concepts of Nanotechnology*” [3]. Since the 1980s, atomic precision and dimensionality entered the horizons of condensed matter physics. The development of tools such as scanning tunnelling microscopy (STM) [4] and atomic force microscopy (AFM) [5], together with the improvement of previously existing techniques like scanning electron microscopy (SEM) or lithography, opened the path to explore matter at its very core, even achieving atomic resolution. All these advances combined led to the discovery of low-dimensional (LD) materials, from the fullerenes in 1985 by Kroto et al. [6], to carbon nanotubes (CNTs) in 1991 by Ijima et al. [7], to finally, the material covered in this thesis, graphene, reported in 2004 by Novoselov and Geim with co-authors [8], together with other 2D materials.

The main questions to understand prior to dive in more within the realm of nanotechnology are: Why these systems are so interesting? What is driving the scientific community to keep investing time and money on this research? In contrast with the familiar 3D systems, low-dimensional materials are characterised for having nanoscale size in at least one of their dimensions. Normally, this reduction in size is quite dramatic, reaching values that are comparable with the de Broglie wavelength of the system, and thus leading to unique quantum behaviours, produced by the so-called quantum confinement effect. Depending on how many dimensions are confined, LD materials can be divided in three categories:

- Two-dimensional (2D), having only 1 dimension reduced to the nanoscale (e.g. graphene).
- One-dimensional (1D), with 2 of their dimensions reduced (e.g. carbon nanotubes).
- Zero-dimensional (0D), with all of their dimensions in the nanoscale (e.g. fullerenes).

One of the most striking consequences of this confinement, as shown in *figure 1.1*, is the discretization of the density of states of the system creating “droplets” of isolated electrons, which contrast with the continuous density of states of bulk materials. The more the dimensions are confined, the more the density of states function resembles like that of an atom. Therefore, these systems with discrete charge states and quantized energy are a perfect testbed for scientist to play and experiment with all the quantum effects that become important at these scales, such as electron tunnelling or coulomb blockade, for instance, or the effect of intermolecular like Van der Waals (vdW) forces [9–11].

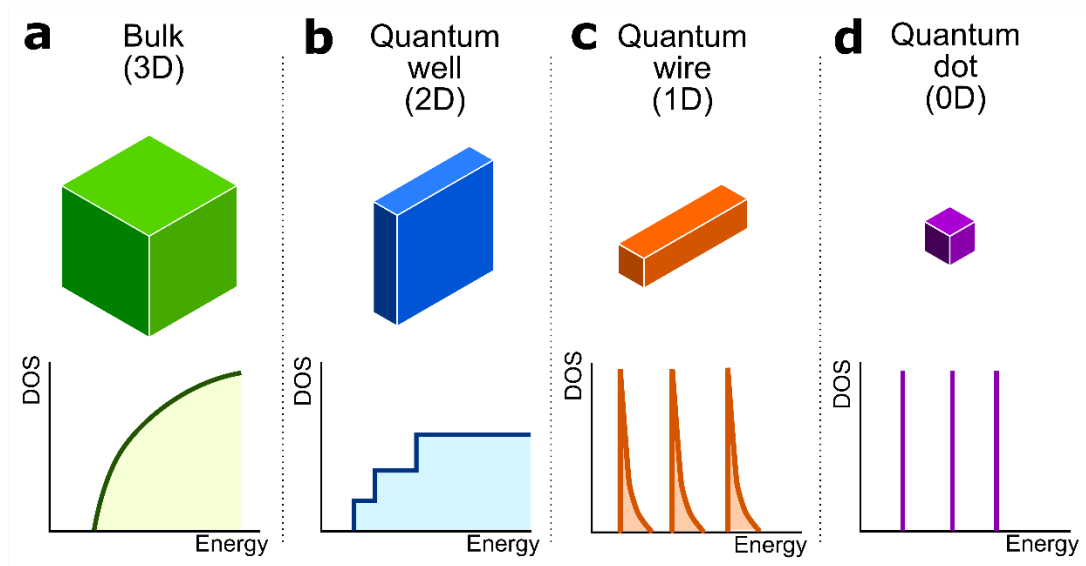


Figure 1.1. Effects of dimensionality on the density of states (DOS) for different systems: (a) 3D Bulk semiconductor, (b) 2D quantum well, (c) 1D quantum wire and (d) 0D quantum dot. Figure inspired by Rogers et al. [12]

From the technological point of view, the possibility to design and tailor the size and shape of quantum structures opens the path to new applications and possibilities. Following Moore's law and the continuous race to miniaturization, the challenge is to do more with less. Using the established silicon technology, this will be extremely challenging, because of the scale: at some point the thickness of the transistor's channel will become greater than the channel length, ultimately leading to difficulties in the electrostatic control via the transistor gate [13, 14]. Low-dimensional materials are a perfect fit for this role, due to their atomic thickness, they can fit in the next steps of miniaturisation without the scaling constraints that silicon technology is facing. Also, it is important to consider that a 100-fold reduction on the linear size scale translates into 100^2 by area and 100^3 by volume, meaning that up to one million times more circuitry could be stuffed into the same volume. Besides that, the reduced size of these kind of systems is also a huge advantage with respect to conventional electronics, as they allow for more portable and smaller devices, with improved heat dissipation. Therefore, for all these reasons, the prospects for technological applications based on LD are extremely exciting [12, 15].

1.1 Scope of the thesis.

Quoting A. Castellanos-Gomez the question that needs to be answered at the starting point of a doctoral thesis related with 2D materials is: 'Why all the fuss about 2D semiconductors (and graphene)?' [16]. It is undeniable that the experimental and theoretical study of 2D systems, consisting of individual sheets of atomic thickness, has been one of the main hot-topics in the condensed matter scenario during the last twenty years. This uppermost interest shown by the

community regarding these materials is due to the unusual physical effects presented by them as a result of the quantum confinement effect, and the promising technological applications.

The discovery of the existence of 2D materials, starting with graphene, was remarkable as these systems have been predicted to be thermodynamically unstable at room temperature [17, 18]. In short, 2D materials are the atomically thin versions of the well-known layered crystals which are held together by weak out-of-plane Van der Waals forces [19, 20]. Graphene, a semimetal made out of carbon atoms arranged on a honeycomb structure, was the first material of this kind to be isolated from a piece of bulk graphite in 2004, by Andre Geim, Kostya Novoselov and their group in Manchester University [8]. Since then, graphene has been widely investigated showing outstanding properties, exceeding those obtained for all studied previous materials, and even reaching some fundamental theoretical limits. Many interesting ideas have been tested so far in different laboratories around the world, and huge efforts are dedicated to develop technologies allowing for industrial scale graphene-based products to be commercially available in the near future. The prospects are wide, with promising applications in many different fields, including transparent and flexible electronics [21, 22], solar cells and optoelectronics [23, 24], gas sensors [25, 26] and composite materials [27, 28], among others.

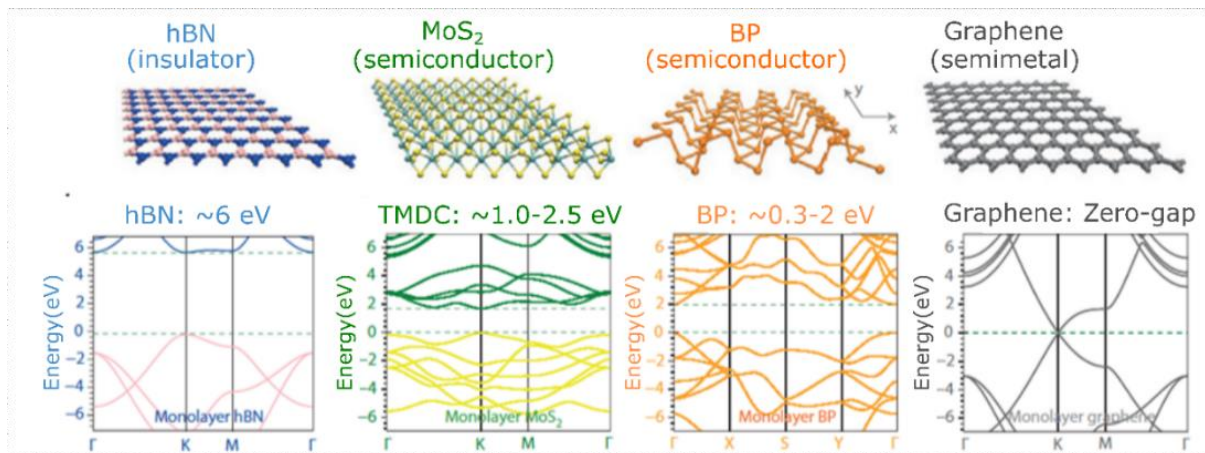


Figure 1.2. Layered structure (top) and band structure (bottom) diagrams of some 2D materials with different electronic and optical properties. From left to right, insulating hBN, semiconducting MoS₂ and BP, and the semimetal, graphene. Adapted with permission from [23]

Although graphene stood out from the beginning as an extremely promising material, its lack of natural bandgap was an inherent limit for the development of transistors or photonic devices [29, 30]. Luckily, other 2D materials were also isolated presenting a variety of different atomic arrangements and bandgaps. Inter alia, it is possible to find insulators as hexagonal boron nitride (hBN) [31], and wide variety of semiconductors as the transition metal dichalcogenides (TMDCs) [32], black phosphorous (BP) [33] or indium selenide (InSe) [34]. The atomic arrangement and the band structure of some of these materials are depicted in *figure 1.2*.

The expanding family of 2D materials not only allows studying the properties of these exciting systems in an isolated way, but also their combinations. As represented in *figure 1.3(a)*, the different layers can be stuck together taking advantage of the vdW interactions between them, giving rise to the so called vdW heterostructures. The design of complex devices is achievable by combining materials with different thickness, stacking order or position, and with varied physical and chemical properties. Furthermore, the combination of new fabrication techniques with standard processes already developed for the semiconductor industry, have granted access to the physical properties of these heterostructures via device patterning and contact deposition, as shown in *figure 1.3(b)*. It is like a whole new materials' playground, and the possibilities are endless.

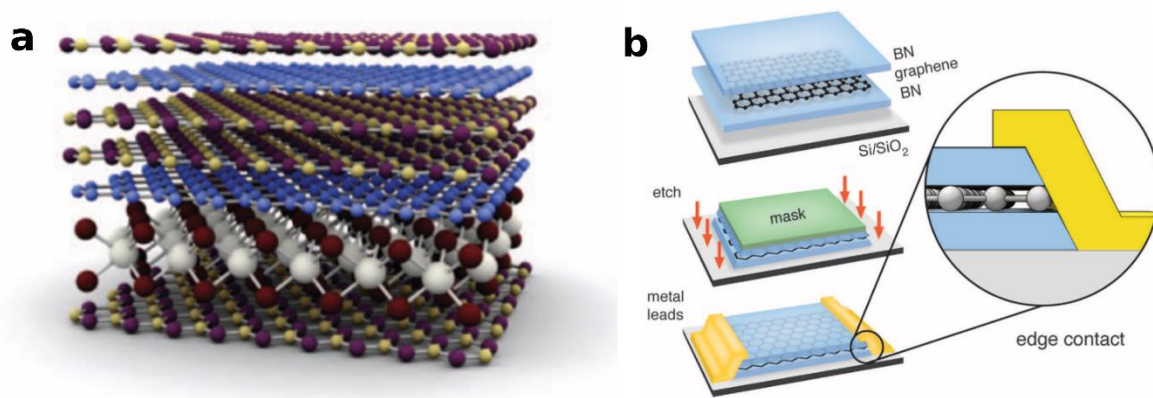


Figure 1.3. (a) Illustration of a van der Waals heterostructure composed of layers from different crystals. Adapted with permission from [35]. (b) Schematic of the fabrication of 1D edge contacts to hBN-encapsulated graphene device. Adapted with permission from [36]

However, the two-dimensional materials world, full of technological promises is also full of major challenges. With an estimated number of ~ 1000 stable 2D materials, plus their possible combinations into heterostructures, the amount of research areas that remain unexplored is vast. With the ultimate purpose of bringing 2D materials out of the laboratories into real-world reliable applications, further understanding of their physical and chemical behaviour is required, even for graphene [15, 37]. The scope of this thesis is to help the advancement of the field by providing new insights on the properties and behaviour of graphene and other 2D materials, as well as on their fabrication and characterisation techniques. Because graphene has proven to have many characteristics that make it suitable for a wide range of applications, thus by focusing on it, every new information gathered has the potential of impacting many areas. Special emphasis has been placed on exploring the electronic behaviour of graphene and its sensing capabilities, as it has demonstrated to be extremely sensitive to a wide range of environmental molecules. At the same time, because by creating heterostructures is possible to expand the functionalities of 2D materials in general, and graphene in particular, the scope is not limited to graphene, but also to

other 2D materials and their combinations (potentially with graphene to expand its capabilities). To work towards this scope, three different objectives were set:

- The first objective of this thesis is to explore the fabrication techniques for 2D materials and heterostructures based on mechanical exfoliation and dry transfer methods, respectively. This is of uttermost importance in order to be able to access new samples, with minimal contamination, and new 2D materials systems to investigate. To further develop this topic, another goal is the setup of a facility either at Lancaster University or at the National Physical Laboratory (NPL) for the reliable production of complex heterostructures of new vdW materials for which protocols have not yet been established.
- The second objective is the characterisation of the electronic properties of graphene nanostructures. In particular, two topics will be studied:
 - As graphene has demonstrated to be a highly sensitive system to its environment due to its exposed π electrons, the doping effects of varying levels of relative humidity will be studied for different types of graphene. For this, a novel approach will be undertaken, employing Raman spectroscopy as a characterisation tool, looking to provide useful information for future graphene-based gas sensors.
 - Application of advanced scanning probe microscopy (SPM) methods, in particular, calibrated Kelvin probe force microscopy (KPFM) to reliably characterise and quantify the electronic properties of exfoliated and encapsulated graphene at the nanoscale.
- The third and final objective of this thesis consists in the characterisation of the thermophysical properties of layered materials using SPM techniques: scanning thermal probe microscopy (SThM) and scanning thermal gate microscopy (STGM). The thermal properties of 2D materials are widely unexplored, here our attention will be focus on materials with highly promising thermoelectrical properties, such as patterned graphene and exfoliated InSe.

The specific order and further details on how this research will be structured is provided in the next section.

1.2 Thesis outline

Here, a brief overview of each chapter is presented in order to give a general idea of the structure of the thesis and the main topics that will be covered:

Chapter 1 (current chapter) includes an introduction section in which the research topic of this thesis is developed. Then the research area is narrowed down in the *scope of the thesis* section. Finally, the content of the different chapters is outlined in the current section.

Chapter 2 reviews the existing literature regarding the fundamentals of the topics covered in this thesis. With respect to the materials, the properties and types of graphene, hBN and InSe are discussed in detail. As for the physics, different doping mechanisms for graphene are reviewed, together with thermal properties and thermoelectric opportunities in 2D systems. The chapter is closed with a concluding remarks section in which the main challenges lying ahead of us are briefly overviewed.

Chapter 3 details the foundations of the experimental methods used to characterise and measure the samples studied in this project. It includes the basics of scanning probe microscopy (SPM) techniques, and some advanced modes like KPFM and SThM. Optical techniques such as bright field and dark field microscopy are explained, together with Raman spectroscopy. Finally, transport measurements, specifically 2-point probe methods, are described.

Chapter 4 describes all the experimental techniques modified and developed in this thesis that relate to the fabrication of 2D materials and heterostructures on the course of this work. The chapter has been detailed as a recipe so anyone could follow it to fabricate 2D materials and complex heterostructures if having the correct equipment. Firstly, the selection of suitable substrates and the main exfoliation methods are described in depth, providing plenty of figures and examples. Secondly, optical identification techniques allowing the selection of suitable flakes are discussed, including also the use of novel edge detection algorithms. Thirdly, two types of transfer techniques, the *PPC/PDMS transfer* and the *PMMA carrying layer* methods are described and compared, allowing manufacturing of complex nanostructures including 2D materials of differing properties, such as graphene, hBN and γ -InSe. Examples and figures explaining how to perform both processes are provided throughout the whole text. Then, an example of the fabrication of a complex heterostructure is provided. Fourthly, a short overview of the developed device production methods is outlined. To finalise, the main achievements, conclusions and future prospects are detailed.

Chapter 5 studies the interactions between graphene and environmental dopant molecules, specifically H₂O. Raman spectroscopy is employed to evaluate the effect of suspended water molecules on different types of graphene in controlled environments of varying levels of relative humidity (R.H.). This systematic study compares the response of graphene grown by different methods, namely exfoliation, chemical vapour deposition and epitaxial growth, and with different thicknesses, mono- and bi-layer graphene, when the R.H. changes from 0% up to 80%. Then

charge densities are calculated employing a vector decomposition method, and finally, the main conclusions and future prospects are discussed.

Chapter 6 shows the results obtained using KPFM to characterise complex 2D materials heterostructures. The chapter is divided in 2 sections. The first one covers the development and implementation of a KPFM tip calibration procedure, essential to obtain effective and reproducible measurements. The fabrication and characterisation of the calibration samples is discussed first, followed by the revision and further optimisation of the KPFM operational parameters. Then the KPFM calibration procedure is demonstrated using platinum coated probes and tested against graphene. For the second part of the chapter, the spatial distribution of the surface potential of encapsulated graphene field effect transistors (GFET) is studied via KPFM. The potential of this technique to provide sub-surface imaging of buried layers and reliable work-function values is then discussed. The chapter is then concluded with final remarks, challenges and directions for future improvements.

Chapter 7 is dedicated to the study of thermal effects in 2D materials at the nanoscale. Two different experiments are discussed: In the first section, the dependence of the thermal conductance of exfoliated γ -InSe with respect to its thickness is investigated. This is performed using SThM in different environmental conditions of pressure and thermal conductivity of the environment (i.e. ambient and vacuum). In the second part of the chapter, the variations of the local Seebeck coefficient on encapsulated graphene devices with patterned constrictions are investigated via STGM. The challenges in this area, conclusions and future perspectives are discussed to finalise the chapter.

Chapter 8 provides a summary of the results presented in this thesis, highlighting the main achievements and the biggest challenges encountered so far. To finish, possible future work paths are discussed.

LITERATURE REVIEW

CHAPTER 2

Graphene foundation and literature review

This chapter presents a short literature review of the fundamental concepts related to graphene, including its electronic structure and physical properties. The various fabrication procedures developed for graphene are discussed, making special emphasis on the difference in the final sample quality and sizes achieved. Furthermore, another section is dedicated to outline the properties of other 2D material systems that are of interest in this thesis, i.e. hBN and InSe. The unique electronic properties of graphene, together with its main doping mechanisms (i.e. chemical and electrical) are then briefly discussed. Finally, a short section is dedicated to thermal properties at the nanoscale and thermoelectricity of 2D materials.

2.1 Why carbon?

Carbon is the 4th most abundant element in the universe and forms the basis of life and organic chemistry as we know it. This element was first named by Antoine Lavoisier in his textbook ‘*Traité Élémentaire de Chimie*’ published in 1789 [38]. However, carbon has been known since ancient times in many distinct forms or allotropes, such as soot, graphite, charcoal or diamond, all of them presenting different appearance and physical properties. This incredible variety of structures emerges as a direct consequence of the bonding flexibility of carbon-based systems, being able to bind itself to nearly all elements in almost limitless variety of ways. Some of these forms are depicted in *figure 2.1*, including low-dimensional systems as the fullerenes or carbon nanotubes (CNTs), together with the familiar 3D structures, diamond or graphite.

In its atomic ground state, carbon has six electrons in the configuration $1s^2 2s^2 2p^2$. The two electrons in the 1s orbital, located at $E = -285$ eV, fill the inner shell and are strongly bound to

the nucleus, thus they do not participate in any bonding reactions. On the other hand, the electrons located in the second shell ($n = 2$), the valence electrons, play an important role in the final hybridization of the system. The $2p$ orbitals ($2p_x$, $2p_y$ and $2p_z$) are roughly 4 eV higher than the $2s$ orbital, so in principle, it is energetically favourable to locate two electrons in the $2s$ orbital and the remaining 2 electrons in the $2p$ orbitals, conforming carbon's ground state, as shown in *figure 2.2(a)*. However, in the presence of other atoms, it results more favourable energetically to excite one electron from the $2s$ orbital to the third $2p$ orbital, in order to form covalent bonds[39].

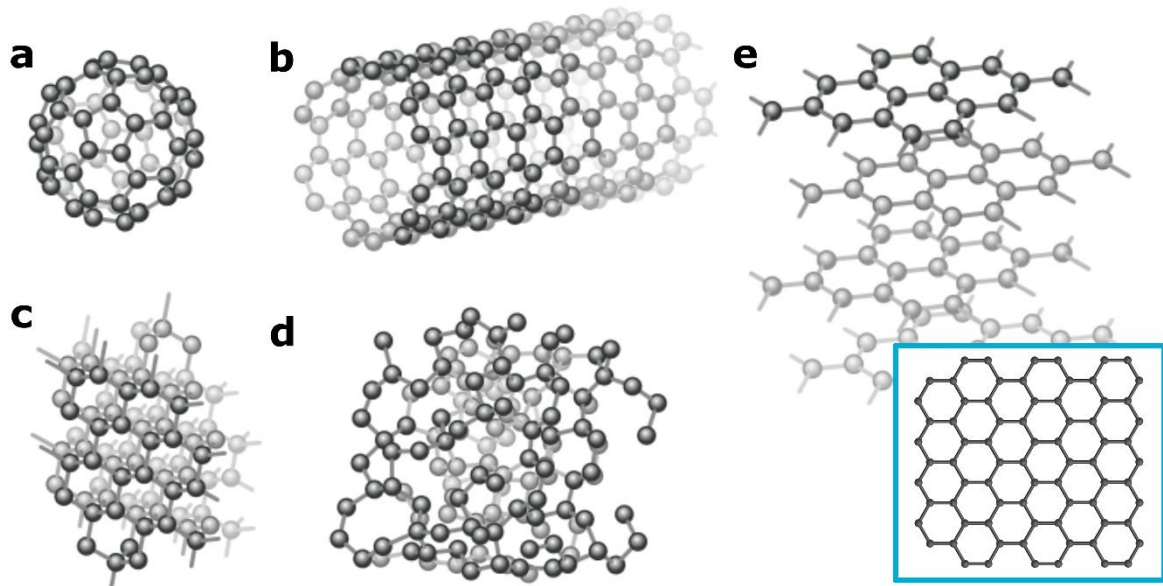


Figure 2.1. Atomic models of different allotropes of carbon. (a) 0D fullerene (buckyball), (b) 1D carbon nanotubes, (c) diamond, (d) amorphous carbon and (e) 3D layered structure of graphite. Inset: The 2D dimensional form of graphite, graphene, is composed by just 1 isolated layer. Figures (a-e) are adapted from [40]. The inset is adapted from [41].

Graphene, as depicted in *figure 2.2(b)*, has sp^2 hybridization¹. In this electronic scheme, the $2s$ -orbital overlaps with two $2p$ -orbital, $|2p_x\rangle$ and $|2p_y\rangle$, leading to a trigonal planar structure in the x - y plane, conformed by three hybridized orbitals each having one electron. The carbon atoms are held together by strong covalent σ (bonding) and σ^* (antibonding) bonds, making graphene the thinnest, and yet the strongest material ever measured [42, 43]. On the contrary, the remaining un-hybridised $2p_z$ orbital is perpendicular to the plane and binds with other $2p_z$ orbitals from neighbouring carbon atoms forming the π and π^* bands. The electrons on the half-filled π bands are decoupled from the others, and hence to a great extent, they define and dominate the electronic transport properties of graphene through the lattice. These properties will be further discussed in the next section.

¹ sp^n hybridisation is a quantum-mechanical superposition of the wavefunctions associated with the state $|2s\rangle$, with the $n|2p_j\rangle$ states

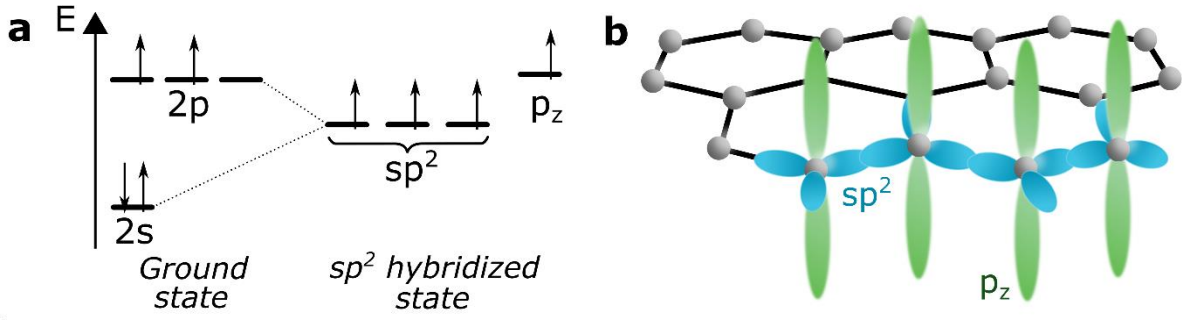


Figure 2.2. **(a)** Electronic levels of a carbon atom showing the ground state and the sp^2 hybridization scheme. **(b)** Model of the localization of the orbitals in graphene, showing sp^2 hybridization. The sp^2 orbitals form σ bonds and the p_z -orbitals form π bonds.

2.1.1 Electronic properties of graphene

As described in the previous section, graphene is a one atom thick system composed by sp^2 -hybridized carbon atoms arrange in a honeycomb lattice that extends on the same x-y plane. The hexagonal lattice is formed by the interpenetration of two different triangular Bravais lattices, hence, its basis is formed of 2 atoms A and B, where A is surrounded by 3 atoms of the sublattice B, and vice versa, as shown in *figure 2.3(a)*. In Cartesian coordinates, the real space lattice vectors \mathbf{a}_1 and \mathbf{a}_2 can be written as:

$$\mathbf{a}_1 = \frac{a}{2}(3, \sqrt{3}), \quad \mathbf{a}_2 = \frac{a}{2}(3, -\sqrt{3}) \quad (1)$$

where $a = 1.42 \text{ \AA}$ is the nearest neighbour distance², being the principal vector length or lattice constant, $a = |\mathbf{a}_1| = |\mathbf{a}_2| = 1.42 \cdot \sqrt{3} = 2.46 \text{ \AA}$. The three vectors connecting the nearest-neighbour atoms in the basis, A and B, are:

$$\boldsymbol{\delta}_1 = \frac{a}{2}(1, \sqrt{3}), \quad \boldsymbol{\delta}_2 = \frac{a}{2}(1, -\sqrt{3}), \quad \boldsymbol{\delta}_3 = -a(1, 0) \quad (2)$$

The reciprocal lattice of the triangular lattice is also triangular, with its vectors given by:

$$\mathbf{b}_1 = \frac{2\pi}{3a}(1, \sqrt{3}), \quad \mathbf{b}_2 = \frac{2\pi}{3a}(1, -\sqrt{3}) \quad (3)$$

With a reciprocal space lattice constant equal to $\frac{4\pi}{\sqrt{3}a}$ [44].

² The nearest neighbour distance $a = 1.42 \text{ \AA}$ is an average between the single (C – C) and the double (C = C) covalent bonds present in graphene, in the same fashion as in benzene.

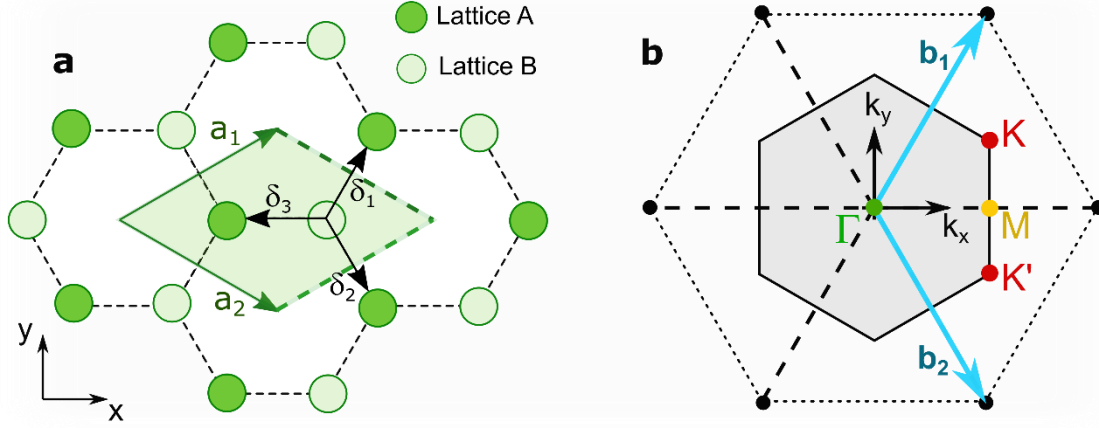


Figure 2.3. **(a)** Honeycomb lattice structure of graphene, made out of two interpenetrating triangular lattices, depicted in dark and light green. The lattice unit vectors are a_1 and a_2 , and δ_i , $i=1,2,3$ are the nearest-neighbour vectors. **(b)** The reciprocal lattice of graphene represented with the first Brillouin zone grey shaded. High symmetry points are highlighted with different colours. The Dirac cones are located at the K and K' points.

In the first Brillouin zone, shown in *figure 2.3(b)*, the Γ and M points are located at the centre of the hexagon and at the mid-point of the edge, respectively. At the corners, there are six high symmetry K points, reduced to inequivalent pairs, K and K' , commonly referred to as Dirac points, with their coordinates given by:

$$\mathbf{K} = \left(\frac{2\pi}{3a}, \frac{2\pi}{3\sqrt{3}a} \right), \quad \mathbf{K}' = \left(\frac{2\pi}{3a}, -\frac{2\pi}{3\sqrt{3}a} \right) \quad (4)$$

The Dirac points are of high importance as at these discrete locations the π -bands meet, resulting in a vanishing density of electronic states (DOS). The energy dispersion relation of the π -bands is shown in *figure 2.4*. This relationship was first calculated by P. R. Wallace in 1947 using a tight-binding model including nearest- and next nearest-neighbour hopping. A detailed calculation is out of the scope of this thesis and it can be found elsewhere [45, 46]. However, it is of interest to mention that close to the Dirac points, the dispersion relation is simplified to³:

$$E_{\pm}(\mathbf{k}) \approx \pm \hbar v_F |\mathbf{k}| \quad (5)$$

where \hbar is the Planck's constant, $v_F \approx 10^6$ m/s is the Fermi velocity and \mathbf{q} is the wavevector measured at the Dirac points. Therefore, the charge carriers in graphene behave as massless relativistic-like particles, Dirac fermions, moving at the Fermi velocity, 300 times smaller than the speed of light ($c = 3 \cdot 10^8$ m/s). Furthermore, the energy is linear with the wave-vector direction and there is no energy dependence with the mass of the charge carriers, unlike other semiconductors. This makes graphene a semimetal with zero bandgap [47]. All these properties

³ Note that the linear dispersion of graphene is only valid for low energies.

opened the path to study quantum-relativistic phenomena in graphene, such as the half-integer quantum Hall effect [48, 49] or Klein tunnelling [50], among others.

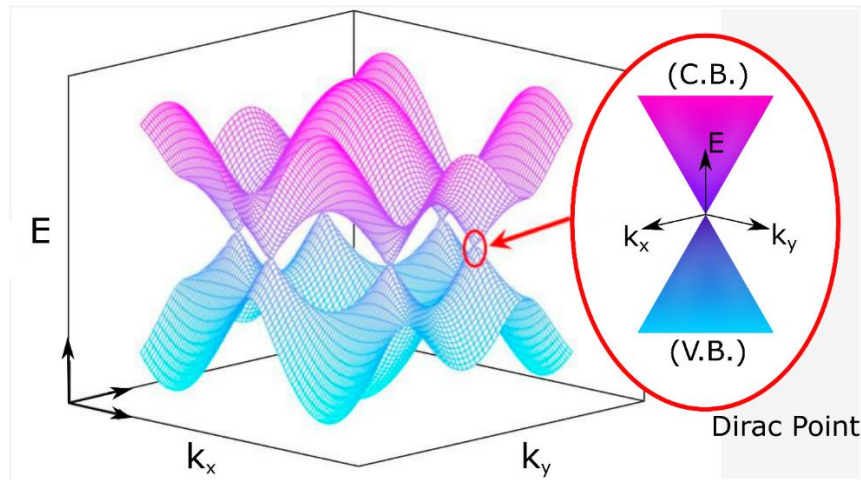


Figure 2.4. Electronic dispersion relation for monolayer graphene. The conduction and valence bands touch at six discrete non-equivalent K and K' points located at the vertices of the hexagonal Brillouin zone. Inset: Linear dispersion relation around the Dirac point. Adapted with permission from [51]

As well as the properties discussed above, there are other characteristics that contribute in making graphene such a remarkable system. To start, graphene presents high carrier electron mobilities over a whole range of temperatures, being specially outstanding at room temperature, where it reaches values of $2.5 \cdot 10^5 \text{ cm}^2 \text{ V}^{-1} \text{ s}^{-1}$ [52], even exceeding that of InSb, the semiconductor with the highest known mobility, $\mu_{\text{InSb}} \sim 7.7 \cdot 10^4 \text{ cm}^2 \text{ V}^{-1} \text{ s}^{-1}$ [53]. The optical properties of this monolayer of carbon atoms are also interesting, having a visible light absorption defined solely by fundamental constants, $\pi\alpha < 2.3\%$ (in the infrared limit, where α is the fine structure constant) [54]. However, it is important to highlight that the transparency is reduced with the increasing number of layers. Furthermore, it is one of the strongest materials ever measured, with a Young's modulus of 1 TPa and intrinsic strength of 130 GPa [42]. Its thermal conductivity is also very high, and it has been measured to be above $3,000 \text{ W m} \cdot \text{K}^{-1}$ [55], making graphene a good candidate as a heat sink material. To top this cocktail of outstanding properties ambipolar field effect (AFE) has been demonstrated in graphene, meaning that the carriers can be tuned from electrons to holes by different strategies such as electrostatic or chemical doping as will be discussed further in *section 2.4*.

Thanks to all the properties held by graphene, this material has the potential to be utilised in a whole range of applications: from energy harvesting [56, 57] and optoelectronics [58], to composite materials [59], gas sensing [60] or medical applications [61, 62], among others. However, the jump from fundamental properties to the exploitation in different applications, requires robust fabrication protocols and device mass production.

2.2 Types of graphene

Graphene synthesis methods can be split into two main approaches: top-down exfoliation and bottom-up-based growth.

- Top-down approaches rely in separating the stacked sheets comprising graphite by overcoming the van der Waals forces that hold the layers together. By doing so, single graphene layers can be produced, together with flakes of different thicknesses. Mechanical exfoliation, that will be reviewed in the following section, is a prominent example of this approach. However, despite of the relatively low interlayer bonding energy characteristic of layered materials, key challenges such as the low repeatability and the long times needed to produce the samples, make this approach unsuitable for mass production of devices.
- On the other hand, bottom-up methods involve synthesising graphene from alternative carbon containing sources. High levels of graphitisation must be promoted in order to produce high quality material, therefore high temperatures are required. These methods offer the possibility to grow large area thin films, although minimising the presence of defects such as vacancies or grain boundaries is still challenging. Epitaxial growth and chemical vapour deposition (CVD) reviewed below are examples of this approach.

The quality and size of the final graphene is highly dependent on the method followed for its production.

2.2.1 Exfoliated graphene

Mechanical cleavage is a top-down procedure, also known as ‘Scotch tape’, ‘peel-off method’ or ‘exfoliation’, consisting on the direct detach of layers from bulk graphite crystals by means of an adhesive tape. This technique was firstly employed by Geim and Novoselov in 2004, allowing them to isolate graphene flakes by peeling-off layers from highly oriented pyrolytic graphite (HOPG), with Scotch® Magic™ tape [8, 63]. In order to perform the exfoliation, a bulk crystal is pressed onto the adhesive tape, which is later peeled off. Some superficial layers of the material remain attached to the tape. As depicted in *figure 2.5(a)*, this process is repeated until achieving a homogeneous cover of the material on top of the tape, approximately of the same size as the chosen substrate. Then, the graphene covered tape is firmly pressed onto a freshly cleaned substrate. Typically, silicon substrates with an oxide layer of certain thickness are employed for this purpose. Due to light interference effects, the

thickness of the oxide layer plays a major role in the optical contrast of the 2D materials under study. Thus, this parameter is carefully selected. In the case of graphene substrates with oxide layers of 90 nm or 300 nm oxide layers are normally chosen as shown in *figure 2.5(b)*. More details about optical identification of 2D materials and enhancing the optical contrast are provided later in *chapter 4, section 4.5*. Finally, the tape is removed either by peeling it manually or by dissolving it with a chemical treatment. After the removal of the tape, flakes of different thicknesses remain attached to the surface of the substrate. Further investigation of the substrate by optical microscopy, Raman spectroscopy or AFM, allows the confirmation of the flake thicknesses. An optical micrograph of a flake with different areas of varying thickness is shown in *figure 2.5(b)*.

Exfoliated graphene samples present the highest crystalline quality among all the fabrication methods. However, although the process can be optimised for certain crystals and substrates, its stochastic nature, results in a random distribution of flakes of different thickness that varies each time, resulting in a low production yield. Furthermore, the size of the flakes produced by mechanical exfoliation is typically on the order of $\sim\mu\text{m}^2$, which makes this technique practically unsuitable for large-scale production. For these reasons, it is mainly confined to research institutions with the purpose of performing fundamental studies. Further technical details on exfoliation are provided in *chapter 4*.

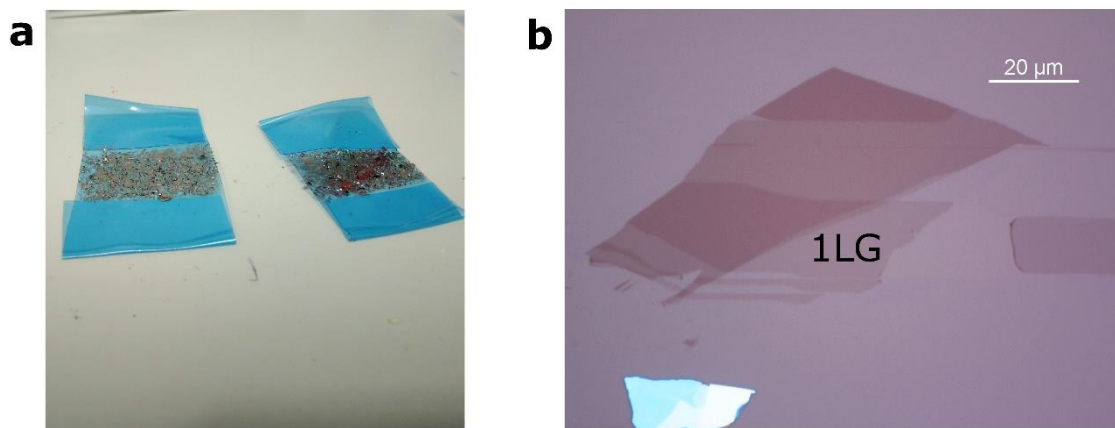


Figure 2.5. (a) Graphene exfoliation on blue tape. (b) White light optical image of a graphene flake deposited on 300 nm SiO_2 . Areas of different thicknesses in the flake are shown as regions of different contrast. Monolayer graphene is indicated by a label (1LG).

This technique can also be used to exfoliate other layered materials such as hexagonal boron nitride (hBN), transition metal dichalcogenides (TMDCs) or indium selenide (InSe), among others.

2.2.2 Epitaxial growth

The word epitaxy comes from the Greek roots: *epi* which means ‘above’, and *taxis* meaning ‘an ordered manner’. Epitaxial growth is a bottom-up fabrication method that produces high quality graphene from SiC crystals. The graphitization of the SiC surface has been widely studied since 1965, although it was in 2006 when the Dirac nature of the charge carriers in the top carbon layer was first demonstrated by Walt de Heer group [64]. Epitaxial growth occurs through the sublimation at high temperatures ($> 1000\text{ }^{\circ}\text{C}$) of the top layers of Si atoms from both of the inequivalent polar surfaces present in SiC (i.e. the Si-face(0001) and the C-face(000 $\bar{1}$)), resulting in a carbon rich environment that nucleates in epitaxial graphene layers [65]. The growth mechanism for the Si-face and the C-face is the same, however, the surface reconstruction and growth kinetics are different for both surfaces, resulting in different graphene growth rates, morphology and electronic properties [66, 67]. The Si-face presents a slower growth rate, which provides better control of the graphene thickness and homogeneity, resulting in large uniform monolayer regions with small bilayer and trilayer graphene islands. In this case, graphene reconstructs with $(6\sqrt{3} \times 6\sqrt{3})R30^{\circ}$, typically denominated as $6\sqrt{3}$ for short, forming a first graphene-like atomic arrangement of C atoms, aligned with the substrate in a manner so that the primitive translation vectors and SiC enclose an angle of 30° . This first top layer of carbon atoms, also known as interfacial layer (IFL) or buffer layer, shows a strong interaction with the substrate and remains partially bonded ($\sim 30\%$) to the SiC surface, as shown in *figure 2.6(a)*. The presence of these covalent bonds modifies the electronic structure, deviating it from that of graphene in the region of the π -bands. As a consequence, the IFL does not exhibit graphene-like electronic properties. The latter are obtained for the second and further layers only, which are bound by weak dispersion forces to the IFL [68]. Monolayer and multilayer graphene are formed on top of the IFL after further heating at higher temperatures (1,300-2,000 $^{\circ}\text{C}$). On the other hand, graphene on the C-face grows much faster, but it generally leads to multilayer graphene with a significant amount of rotational disorder and defects.

Characterisation of the fractional coverage of a SiC surface, and quantification of the number of layers can be performed by different techniques such as low energy electron microscopy (LEEM) [69], electrostatic force microscopy [70], Kelvin probe force microscopy [71] or Raman spectroscopy [72], among others [73]. Some examples are shown in *figure 2.6(b)* and *(c)*. The main advantages of graphene growth on SiC is that the size of the graphene sheet can be as large as the substrate and that devices can be processed on the same fabrication chip, with no need of transfer [74]. On the other hand, although this technique is able to produce large

monolayer areas, multilayer regions, such as bilayer or trilayer, are commonly found in the prepared samples. One of the main reasons is the miscut angle of the SiC wafer, which results in a substrate governed by terraces, in which the steps act as nucleation centres for graphene layers, giving formation to 2LG or MLG along them [67].

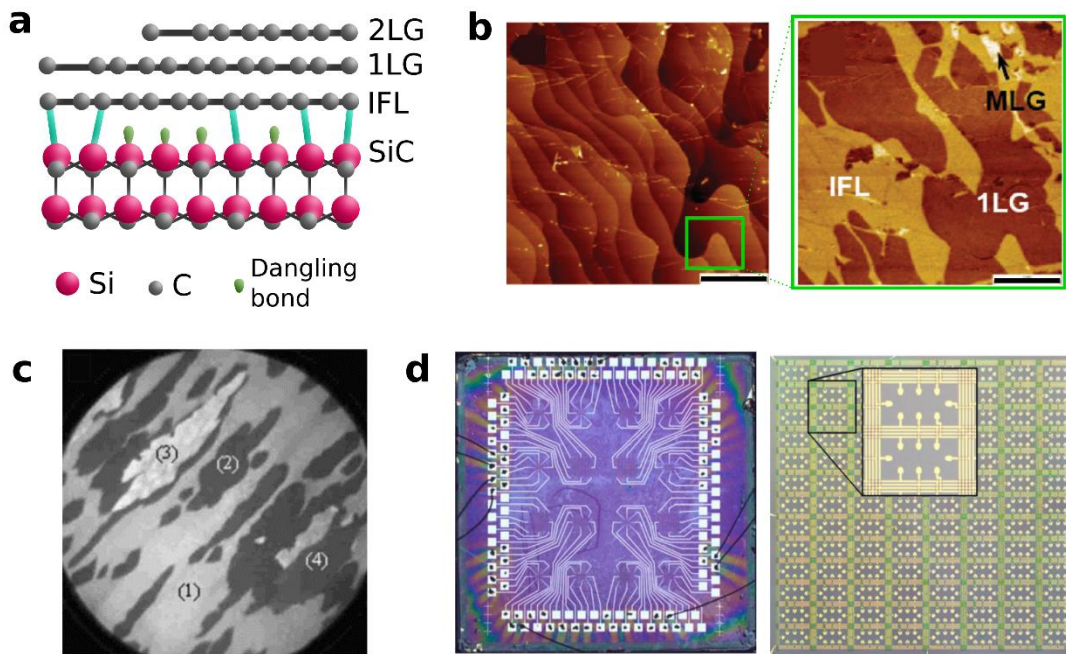


Figure 2.6. Epitaxial graphene. **(a)** Schematics of the epitaxial growth of graphene on SiC. The interfacial layer (IFL) is covalently bonded to the SiC surface at certain locations, leaving dangling bonds that contribute to n-dope the graphene layer sitting on top. **(b)** Topography (Left) and electrostatic force microscopy (Right) maps of epitaxial graphene grown on the phase 4H-SiC(0001). The topography shows the characteristic terraces of SiC. The electrostatic force microscopy provides information of the number of layers present in the material, such as the interfacial layer (IFL), monolayer (1LG) and multilayer (MLG) regions. Scale bars: 2 μm . Adapted with permission from [70] **(c)** Low energy electron microscopy (LEEM) of epitaxial graphene prepared on 6H-SiC(0001) showing regions of different thicknesses marked as (1)-(4). Field of view: 20 μm . Electron energy: $E_{vac} = +1.6\text{eV}$. Adapted with permission from [75] **(d)** Prototype of $R_K/200$ quantum Hall array resistance standard fabricated with epitaxial graphene. Micrograph of the entire chip (Left) and a zoom-in covering an array of 100 Hall bars (Right). Adapted with permission from [74]

2.2.3 Chemical vapour deposition

Chemical vapour deposition (CVD) is another bottom-up fabrication approach used to produce large-area graphene uniform films. A schematic illustration describing the main steps in the growth process is depicted in *figure 2.7*. Firstly, the target substrate is placed within the reaction chamber and annealed at a high temperature ($\sim 1000^\circ\text{C}$), typically in Ar or H_2 atmosphere. For graphene growth, copper (Cu) and nickel (Ni) are commonly used as substrates, acting both as catalytic material for the reaction and as the platform to hold the thin film [76–78]. This initial annealing is critical as it removes the cover oxide layer and leads to grain growth and annihilation of most of the surface defects that might be present. Secondly, precursor species in vapour phase are introduced in the chamber carried by an inert gas. The most typical carbon sources used are

methane (CH_4) or hexane (C_6H_{14}) [79, 80]. Thirdly, when the carbon source comes into contact with the hot surface of the substrate, thermal dissociation takes place, breaking down the source into C atoms and H_2 molecules. Depending on the carbon solubility of the substrate, the C atoms will deposit on the surface at specific nucleation sites, without further penetrating the material. The deposited atoms combine to form graphene islands. Further processing enlarges the size of these graphene islands finally producing a continuous graphene layer. The H_2 molecules are evacuated from the chamber as desorption by-products of the reaction, together with the desorbed precursors that did not react with the substrate [81].

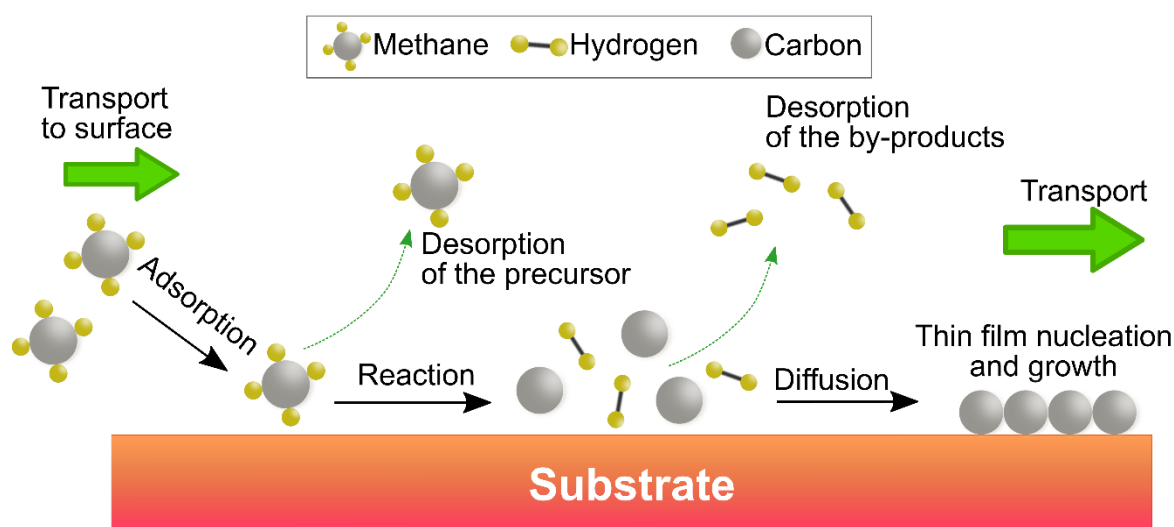


Figure 2.7. CVD graphene growth diagram. Precursor species introduced in the reaction chamber are adsorbed by the metallic surface. A proportion will be desorbed with no further effect, while others will react with the substrate. The thin film growth starts at nucleation spots and expands to form a uniform layer. The by-products of the reaction are evacuated from the chamber. Transport of the molecules and the desorption products is performed by an inert carrier gas.

The as-grown graphene can be characterised by scanning electron microscopy (SEM) or angle-resolved photo-emission spectroscopy (ARPES), as it is grown on a metallic substrate. For certain applications, such as for GFETs, CVD grown layers are usually transferred to insulating substrates, such as SiO_2/Si , as shown in figure 2.8(a) [82–85].

The number of layers, their size, morphology, orientation, and the introduction of any dopants or defects are dependent on a wide range of growth parameters such as temperature, chamber pressure, carrier gas flow-rate, precursor and substrate purity and composition, and source–substrate distance [86–88]. In general, the CVD growth technique is highly versatile, allowing to tailor and produce large area thin films of different characteristics. However, there are also disadvantages to this method. One of the main problems found is that the thin films are generally polycrystalline presenting a significant number of atomic defects. Although this can be minimised by developing and modifying the recipes, the posterior transfer process may also result in cracks and ripples in the sample [84]. Consequently, the quality of the samples obtained by this method has been generally lower than the exfoliated materials, presenting comparatively

higher doping levels and reduced carrier mobility. Furthermore, metal substrates are generally expensive, making this procedure cost-ineffective.

Besides these disadvantages, CVD growth remains as one of the most promising techniques to produce large area thin films for electronics and optoelectronics based on 2D materials. Recent advances in the transfer process by Banszerus et al. [89], have produced high quality hBN encapsulated CVD graphene heterostructures with mobilities as high as $350,000 \text{ cm}^2\text{V}^{-1}\text{s}^{-1}$, comparable with the ones obtained for exfoliated graphene. Although this method is only suitable for transferring small flakes with lateral size on the micrometer scale, as shown in *figure 2.8(b)*, it allows the reuse the copper substrate, reducing the total cost of the production. More details on hBN are provided in the next section. Additionally, some groups have demonstrated that 30-inch graphene films can be grown on Cu and transferred onto a flexible substrate by a roll-to-roll process, presenting a sheet resistance as low as $125 \Omega\text{sq}^{-1}$ and 97.4% optical transmittance, very promising to replace indium tin oxide (ITO) as transparent and flexible electrodes [89]. An example of the roll-to-roll process and the final product is depicted in *figure 2.8(c)* and *(d)*.

Apart from graphene, other 2D materials such as transition metal dichalcogenides (TMDCs) can be also grown by CVD methods, showing great potential for the fabrication of semiconducting thin films, but also, for large-area vertical and lateral heterostructures based on 2D materials [90, 91].

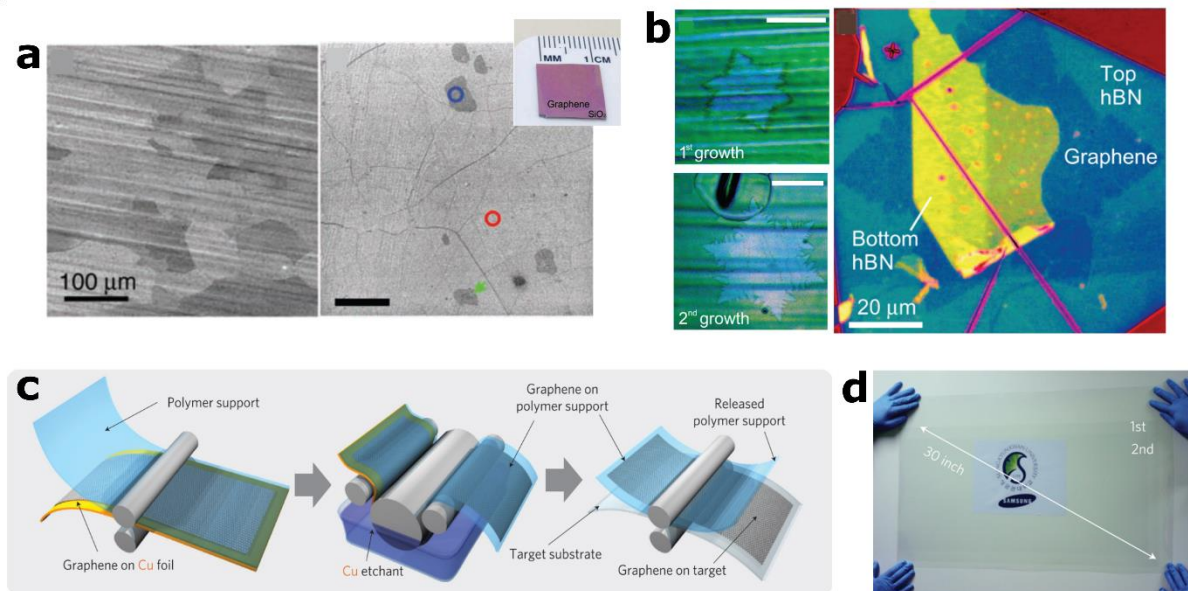


Figure 2.8. (a) SEM image of graphene on a copper foil with a growth time of 30 minutes (left) and an SEM image of the same graphene transferred on 285 nm SiO₂/Si, showing wrinkles as well as two- and three-layer regions (right). Inset: Optical micrograph of the graphene film on top of a 285 nm SiO₂/Si substrate. Reprinted with permission from [78] (b) False-color optical image of CVD graphene on copper after a first (top-left) and a second (bottom-left) growth cycle. On the right-side, a small section of graphene covered by transferred hBN (which will be reviewed in the next section). Adapted with permission from [89] (c) Schematic of the roll-based production of graphene films grown on a copper foil. The process includes adhesion of polymer supports, copper etching (rinsing) and dry transfer-printing on a target substrate. (d) A transparent ultra-large area graphene film transferred on a 35-inch PET sheet. Adapted with permission from [22]

2.3 Other layered materials electronic properties

In this section, the other materials besides graphene, i.e. hBN and InSe, that will be used in posterior chapters of the thesis are reviewed.

2.3.1 Hexagonal boron nitride (hBN)

Hexagonal boron nitride (hBN) is a III-V insulator with a wide bandgap of ~ 6 eV [92, 93]. Its crystalline structure, analogous to graphene, is formed by layers of nitrogen and boron atoms occupying the inequivalent A and B sublattices of a honeycomb structure, as shown in *figure 2.9(a)*. In the same manner as graphene, weak out-of-plane van der Waals forces hold the different layers together, which are covalently bonded within the basal planes. It is important to mention that even before the advent of 2D materials, boron nitride has been widely used in the past in its own right, as a lubricant and as an additive to cosmetic products, amongst other things [94]. As described in *section 2.2.1*, hBN can be exfoliated from bulk crystals by mechanical cleavage to obtain flakes of varying thickness. However, as a result of its large bandgap, hBN exhibits little contrast ($< 1.5\%$) under white light in most of the substrates. As it will be further discussed in *chapter 4* [95]. Besides this, hBN has also become one of the most popular 2D materials together with graphene, mainly for three reasons:

First, because it makes an excellent substrate for other 2D materials. Its low roughness, consequence of its atomically planar surface (*figure 2.9(b)*), suppresses rippling from 2D materials, which tend to mechanically conform to the surface holding them. This fact was initially highlighted by Dean et al. [31] in 2010, demonstrating a three-fold increase in the carrier mobility for graphene devices deposited on top of hBN with respect to SiO_2 . Since then, hBN has been widely employed as the substrate of choice for 2D material-based devices [96]. Second, because it is an ideal gate dielectric material presenting optical phonon modes with energies two times higher than those in SiO_2 , nice dielectric characteristics ($\epsilon_{\text{hBN}} \approx 3 - 4$), high breakdown field ($V_{\text{hBN}}^{\text{Br}} \approx 0.7 \text{ Vnm}^{-1}$), and excellent thermal conductivity up to six times higher than that of SiO_2 [97]. Third and last, because its lack of dangling bonds makes of it a good passivation layer. The lack of dangling bonds or surface charge traps in this material, together with its excellent impermeability and superior chemical and thermal stability, makes hBN a relatively inert material to its environment. As it will be further discussed in *chapter 4*, some 2D materials are sensitive to their environment, suffering from oxidation, doping or corrosion, which leads consequently to the degradation of their intrinsic properties. As a consequence of all the reasons stated above, encapsulation of 2D materials between layers of hBN, creating a sandwich like structure as shown in *figure 2.9(c)*, has become a common practice in the community. Therefore,

hBN is almost ubiquitous in heterostructure fabrication, as it helps maintaining clean interfaces as shown in the right panel of *figure 2.9(c)*, as well as preserving the intrinsic electronic properties of materials and extending the sample's lifetime [20, 92, 98].

So far, hexagonal boron nitride has been almost ubiquitous in 2D materials research and published papers, employed to fabricate field effect tunnelling transistors [99, 100], optoelectronic emitters in the deep ultraviolet (UV) regime [101], as well as, single photon emitters from localised defects in the hBN lattice working in the UV and IR regimes [102, 103].

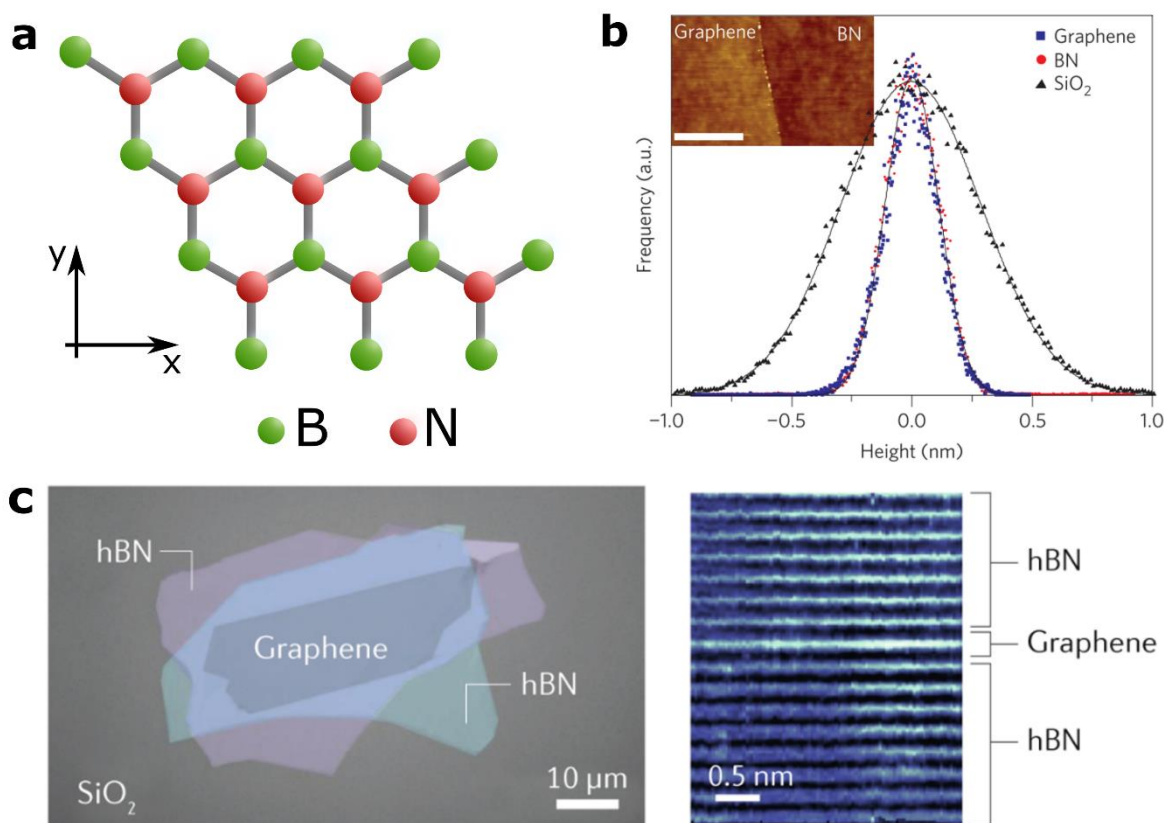


Figure 2.9. (a) hBN crystalline structure top-view (b) Histogram of the height distribution (surface roughness) measured by AFM for SiO₂ (black triangles), hBN (red circles) and graphene-on-hBN (blue squares). The curves show that the roughness of graphene on hBN is three times smaller than that of SiO₂. Solid lines are Gaussian fits to the distribution. Inset: high-resolution AFM image showing a comparison of graphene and hBN surfaces. Scale bar: 0.5 μm. Figure reproduced with permission from [31] (c) Left: False colour optical image of a graphene flake sandwiched between hBN flakes, a process known as encapsulation, which protects the 2D material flake from any interaction with the environment. Right: High-resolution transmission electron microscope image of an encapsulated graphene(hBN/Graphene/hBN) stack. From this image, it is obvious that the interfaces are atomically sharp and free from impurities. The heterostructure was produced using the PPC/PDMS method further explained in chapter 4. Reproduced with permission from [104]

2.3.2 Indium selenide (InSe)

Indium selenide (InSe) is a layered IIIA-VIA monochalcogenide semiconductor, with MX (M = In, X = Se) stoichiometry. As depicted in *figure 2.10(a-b)*, the crystal structure of InSe consists of In-Se-Se-In covalently bonded layers with an in-plane hexagonal structure held together by out-of-plane van der Waals forces. Bulk InSe can be found in different polytype forms: β , ϵ , γ , defining

its crystalline structure and physical properties [105]. The InSe crystals used in this thesis were grown by the *Institute for Problems of Materials Sciences* (Chernivtsi, Ukraine) using the Bridgman method from a polycrystalline melt of $\text{In}_{1.03}\text{Se}_{0.97}$ [106, 107], resulting in γ -phase bulk crystals. The extraction of thinner layers of InSe is performed by direct mechanical exfoliation from bulk crystals [108], as it will be detailed in *chapter 4*.

As shown in *figure 2.10(c)*, the InSe band structure is strongly dependent on the number of atomic layers, presenting a thickness dependent tuneable bandgap. In contrast with other materials such as the well-known TMDCs, it undergoes a transition from direct bandgap in its bulk form to indirect bandgap when its layer thickness is reduced to ≤ 6 nm, as the valence band maximum (VB_{max}) moves away from the Γ towards the K symmetry point [109, 110]. Another interesting feature highlighted by the band structure is that the conduction band minimum (CB_{min}) remains at the Γ symmetry point, although it shifts to higher energies as the number of layers is reduced from 10L to 1L, while the VB_{max} remains at almost the same energy for all the thicknesses, which results in an increasing of the bandgap as the number of layers is reduced. Therefore, the bandgap increases from around ~ 1.24 eV for 10L, to 2.39 eV for monolayer [111].

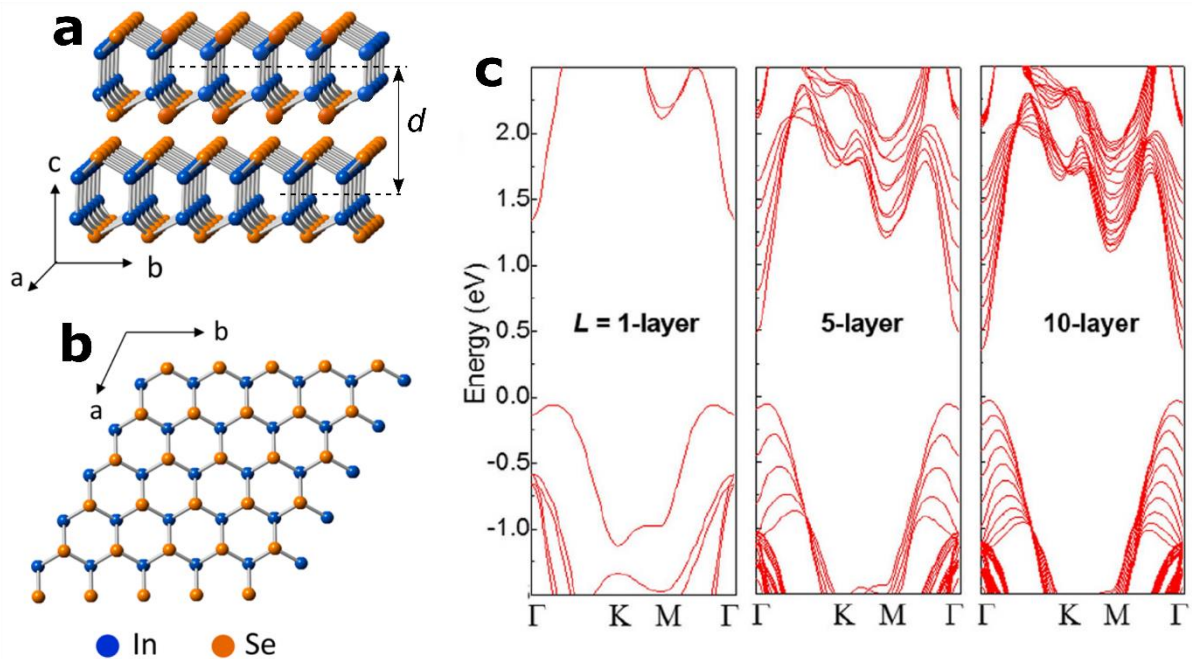


Figure 2.10. (a) Side view and (b) top view of InSe crystal structure. Figures modified with permission from [112] (c) DFT calculations of the band structure of InSe in the first Brillouin zone for 1L, 5L and 10L of atoms. Figure is reproduced with permission from [113]

It is not surprising then that InSe has created a lot of interest in the 2D materials community in recent years due to its unique set of physical properties including high broad-photoresponsivity from the infrared to the ultra-violet range [114–116], or high mechanical strength [117, 118]. Also, the relatively small electron effective masses in the layer plane give rise in this material, to

high electron mobility at room temperature, with values over $1000 \text{ cm}^2\text{V}^{-1}\text{s}^{-1}$ reported in few layer InSe devices [119, 120]. The combination of these properties makes InSe an ideal material for the development of innovative device applications in photonics and optoelectronics, as successfully demonstrated in few-layer photodetectors and field effect devices [112, 116, 120].

Besides its high prospects for optical devices, InSe has also shown promise for thermal applications, however this topic remains widely unexplored. Earlier experimental works performed in bulk InSe have demonstrated low thermal conductivity values down to $\kappa < 1.2 \text{ Wm}^{-1}\text{K}^{-1}$ [121], and more recent theoretical papers have explored the thermal properties of thinner InSe showing values of $27.60 \text{ Wm}^{-1}\text{K}^{-1}$ at room temperature for 1L InSe [122]. These low thermal conductivities, together with its high carrier mobility, make of InSe an interesting candidate for thermoelectric applications, as it will be further highlighted in *section 2.5.2*. The lack of experimental research in this area was noted, and initial experiments using scanning thermal microscopy (SThM) were performed during the development of this thesis. These results will be discussed further in *chapter 7*.

It is important to note that, one of the main limitations of InSe is that the performance of the material can be heavily affected by the presence of impurities or by the exposure to air, light and/or moisture, eventually oxidising it to In_2O_3 [105]. Although theoretically perfect InSe crystals are inert, presenting even more stability (i.e. much lower oxygen affinity) than MoS_2 or phosphorene, the unavoidable presence of Se vacancies in the lattice dramatically lowers the adsorption energy towards oxygen, promoting oxidation even at room temperature [123, 124]. To avoid these issues and prevent electronic degradation of the material, encapsulation in inert environments is generally performed [125, 126], as it will be further discussed in *chapter 4* of this thesis.

2.4 Graphene Fermi level and doping mechanisms

Theoretically, for undoped graphene the Fermi level lies at the Dirac point, where the conduction and valence bands meet. As previously described in *section 2.1.1*, at the Dirac point, the carrier concentration is very low (theoretically, it is zero) as the DOS vanishes. Consequently, the resistance (conductance) tends to infinity (minimum), creating a characteristic inverted V-shaped curve, as shown in *figure 2.11(b)*. Experimentally, reaching the Dirac point alongside the whole surface of a device is unlikely to happen due to the presence of local inhomogeneities, such as crystal disorder, boundaries, or chemical doping. More commonly, undoped graphene is divided into electron-hole puddles close to the Dirac point, in the so-called charge neutrality point

(CNP). In this realistic scenario, the characteristic maximum of resistance is usually found shifted from its ideal zero position [127, 128].

Fortunately, the electrical properties of graphene, such as its carrier concentration, and thus, its conductance, can be easily tuned by shifting the position of the Fermi level. Furthermore, the ambipolar behaviour of graphene allows accessing both the electrons and holes regimes. The most common doping strategies, electrostatic gating and chemical doping, will be reviewed in the following sections.

2.4.1 Electrostatic doping

Electrostatic gating is a very common strategy applied to manipulate the carrier concentration of graphene devices, and thus the electronic properties [129]. For this, graphene is commonly deposited in substrates covered with thin dielectric films in a GFET configuration as shown in *figure 2.11(a)*. This architecture acts as a parallel plate capacitor, therefore when a voltage is applied to the gate (V_{BG}), it induces charges of opposite sign in the graphene device, achieving n-type ($V_{BG} > 0$) or p-type ($V_{BG} < 0$) doping behaviour by shifting the Fermi energy level towards the conduction or valence band, respectively. The relation between the displacement of the Fermi energy level (from the charge neutrality point) and the carrier concentration follows a unique linear trend for monolayer graphene:

$$\mathcal{E}_F = \sqrt{n\pi}\hbar v_F \quad (6)$$

where \hbar is the reduced Planck constant, and v_F is the Fermi velocity in graphene which is $\sim 10^6 \text{ m} \cdot \text{s}^{-1}$. Using the model of a parallel plate capacitor, the number of charge carriers induced in the device channel can be described as:

$$n \approx \frac{CV_{BG}}{e} = \frac{\epsilon_0 \epsilon_r V_{BG}}{d e} \quad (7)$$

where e is the fundamental electron charge, V_{BG} is the backgate voltage, and C is the capacitance defined as $C = \epsilon_0 \epsilon_r / d$, having ϵ_0 the vacuum permittivity, ϵ_r the relative permittivity and, d , the thickness of the dielectric layer.

Experimentally, these changes on the Fermi energy, and therefore in the charge carrier concentration, are typically characterised by measuring the resistance of the device channel while applying a bias voltage as shown in *figure 2.11(b)*. Also, by doing this, information about the intrinsic doping of the sample can be obtained by looking at the crossover of the curve with $V_{BG} = 0V$. The main advantages of this method is that it is fast, easy to implement and also, that it allows the modification of the main charge carriers without introducing defects or disorder in the

channel [130]. In this thesis, electrostatic doping will be employed in *chapter 6* to study the effect of back-gate in the charge distribution of narrow channel GFET devices, and in *chapter 7* to study the effect of doping in the local variations of the Seebeck coefficient in GFET devices with patterned constrictions.

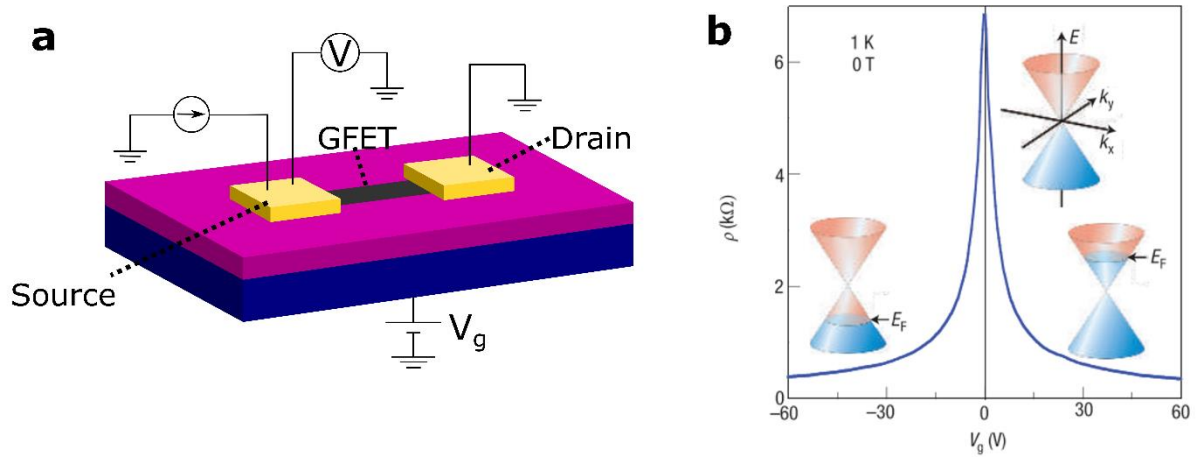


Figure 2.11. **(a)** Schematic view of a GFET. The graphene channel (black) is located between the metallic electrodes (yellow), denominated drain and source. All the structure is located on top of a silicon wafer (purple) with a top oxide layer (pink). **(b)** Resistivity of pristine graphene as a function of gate voltage. For $V_{BG} < 0$ V, graphene is p-doped, and for $V_{BG} > 0$ V, graphene is n-doped. Reproduced with permission from [129]

2.4.2 Chemical doping

Another doping method is the chemical doping, which mainly comprises two mechanisms: i) substitutional doping with heteroatoms and ii) molecular doping. In the first one, some of the carbon atoms in the graphene lattice are substituted by other species, disrupting the sp^2 hybridization scheme and therefore, modifying the chemical properties of the material. This type of doping will not be further discussed as it is out of the scope of this thesis. More information can be found elsewhere [131, 132].

Molecular doping, or in the case of 2D materials also called surface transfer doping, is realised as the transfer of charges between graphene and a certain external adsorbate. This effect was first demonstrated experimentally by Schedin et al. [25], employing molecular doping, based on NO_2 , to modulate the carrier concentration and therefore the resistance of a graphene device. Using the molecular orbitals (MO) description, the direction of the charge transfer can be determined by the relative positions between the Fermi level of graphene, E_F^{Gr} , and the DOS of the highest occupied molecular orbital (HOMO) and the lowest unoccupied molecular orbital (LUMO). The positions of these levels can be imagined as delta-peaks in the DOS and need to be compared to the electronic band-structure of graphene.

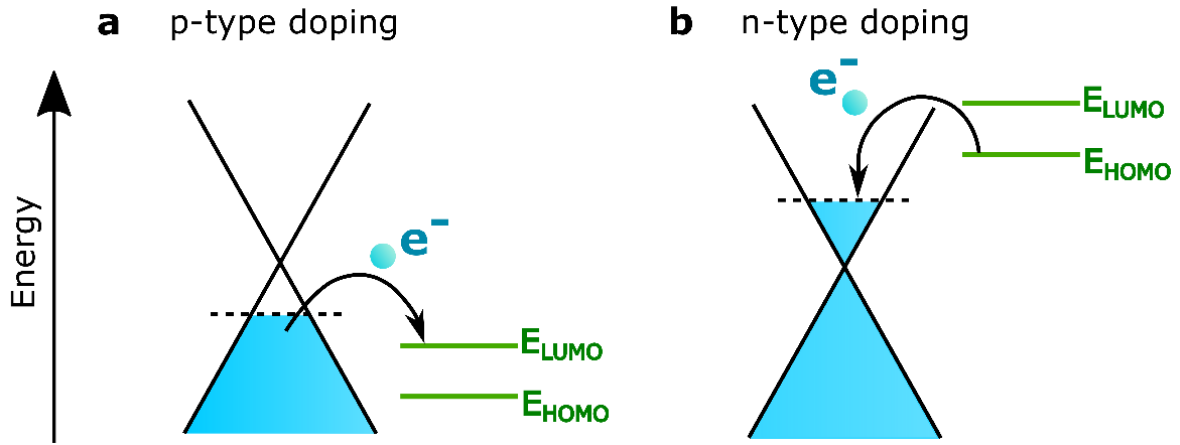


Figure 2.12. Schematic representation of the molecular doping of graphene considering: (a) p-doping and (b) n-doping. The direction of the electron transference is determine based on the difference between the graphene Fermi energy and the HOMO or LUMO energy levels of the adsorbate molecule.

Thus, as schematically illustrated in figure 2.12, if the HOMO of a dopant is located above E_F^{Gr} , the adsorbate will ionize, acting as a donor and transferring electrons to graphene, and thus increasing its Fermi energy. On the contrary, if the LUMO is placed below E_F^{Gr} , then the charge is transferred from the graphene layer to the dopant, which in this case becomes ionised acting as an acceptor. Besides this, it is important to remember that molecular adsorption is a dynamic process happening continuously between individual molecules and the graphene surface, thus it is a process that evolves in time, and that highly depends on the instantaneous energy state of the system. Generally, successful adsorption also depends on the molecule having sufficient kinetic energy to overcome the adsorption energy barrier:

$$E_a = E_{(molecule+Gr)} - E_{Gr} - E_{molecule} \quad (8)$$

where E_a , $E_{(molecule+Gr)}$, E_{Gr} and $E_{molecule}$ are the total energies of the adsorption process, the relaxed molecule on the graphene system, graphene and the molecule, respectively. For an adsorption event to occur, $E_a > 0$ must happen. More formal description than the one provided here is out of the scope of this thesis, however, more information can be found elsewhere[133–135].

2.4.3 Fermi level characterisation

Changes in the doping levels of graphene, or in other words, in its Fermi level, can be probed by different techniques such as: Raman spectroscopy [136], FET characteristics [25] (shown in **Error! Reference source not found.(d)**) and Kelvin probe microscopy (KPFM) [137], among others. Some of these techniques are employed in this thesis for the purpose of characterising the doping levels of the material under study as it will be discussed in following chapters.

2.4.4 Graphene for gas sensing applications

Improving current gas sensing technologies is essential for a wide range of areas such as environmental monitoring, R&D, safety in industrial processes and Earth observation, among others. This diverse range of applications has led to a need for sensors operating with different parameters such as limits of detection, concentration ranges and response/recovery times. Current technologies, like metal Oxide semiconductors (MOS) or optical-based methods, present a different set of challenges such as the requirement of high-temperatures for operation, slow response, poor limits of detection or bulky equipment[138–140]. In this regard, graphene has shown potential as a future alternative route with improved capabilities, such as its outstanding

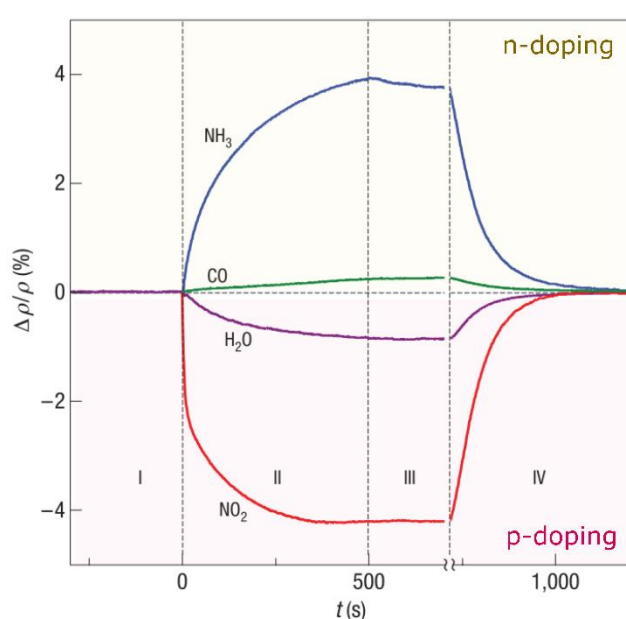


Figure 2.13. Chemical doping of graphene via external molecules. Variations in the resistance of a graphene Hall bar as a consequence of its exposure to different molecules. Adsorbates such as CO, or NH₃ produce n-doping of graphene, whereas other molecules like NO₂, or H₂O, produce p-doped behaviour on graphene. Image reproduced with permission from [25]

or p-doping), as shown in figure 2.13 Since then, several experimental studies have been performed to understand the interaction of graphene with several gaseous environmental dopants, and to prove its capability as a powerful sensor towards NO₂[26, 142], NH₃ [143, 144], and H₂O [145, 146], among many others.

In this thesis, the focus will be stressed in exploring the capability of Raman spectroscopy to study the interactions of graphene and the environmental dopants. In particular, the effect of H₂O on different types of graphene in environments of controlled humidity levels. This topic will be further discussed in chapter 5.

sensitivity to external adsorbates, fast response and recovery times, small size and its ability for operation at room temperature[60, 141].

As mentioned above, the first experimental result confirming the suitability of graphene as a gas sensor was performed by Schedin et al.[25], whom not only demonstrated the extreme sensitivity of graphene towards NO₂ down to the single-molecule level, but also to other gases such as NH₃, CO and H₂O, by measuring the variations of resistance in a graphene Hall bar. This group also demonstrated that different molecules produced different types of doping in graphene (i.e. n-doping

2.5 Nanoscale thermal conductivity

2.5.1 Thermal transport in 2D materials

Thermal conductivity is a measure of the ability of a material to transfer heat spatially. At the macroscopic scale, the heat flux from the hotter side of a material to its colder side is proportional to the temperature gradient and the negative thermal conductivity as expressed by Fourier's law:

$$Q(\vec{r}, t) = -\kappa_c A \nabla T(\vec{r}, t) \quad (9)$$

where $Q(\vec{r}, t)$ is the heat flux density vector, κ_c is the thermal conductivity of the material, A is the cross-sectional area and $T(\vec{r}, t)$ is the temperature gradient established within the material. Within solids, heat energy is mostly transferred by electrons and phonons (i.e. quantised modes of vibration), however the individual contribution of each carrier depends on the type of material considered [147, 148]. Regardless of the carrier type, the determination of the thermal conductivity in materials, specifically for electronic and optoelectronic applications is crucial to understand energy dissipation and heat management in devices [149].

In the case of 2D materials, current measurement techniques struggle to provide accurate values of the thermal conductivity mainly due to two reasons: (1) their small lateral sizes, and (2) their anisotropy. For the first point, techniques with nanoscale resolution are required in order to provide accurate values of the thermal conductivity. In this regard, scanning thermal microscopy (SThM), able of achieving sub- μm thermal resolution, presents itself as one of the main candidates to obtain thermal information of nanoscale materials [150, 151]. More details on SThM that I deployed in this thesis will be provided in *chapter 3* and *chapter 7*. As for the second reason, as explained previously, in 2D materials covalent bonds hold the atoms in-plane, while out-of-plane, the layers are held by weak vdW forces. This leads to phonons and electrons traveling easier in-plane than out of plane, and thus generating anisotropic heat transport, being in general heat conduction worse across the plane than in-plane [152], and producing a thickness dependent thermal conductivity [149].

So far, due to the stated above reasons, most of the studies on thermal conductivity of 2D materials are theoretical, with very few experimental works, mainly focused on graphene[153], hBN [154], MoS₂ [155, 156] or InSe [122]. Therefore, more research is required to better characterise the thermal conductivity of layered materials, which will be of use for thermal applications, such as thermoelectricity reviewed in the next section. In this thesis, experimental studies of the thermal properties using SThM have been performed and are discussed in *chapter 7*.

2.5.2 Thermoelectricity of 2D materials.

Thermoelectric (TE) devices are energy transducers converting heat to electricity, and viceversa. Many electrical devices in our everyday lives are powered using thermoelectricity, from solid-state power generators and refrigerators, to thermal management or energy harvesting systems, among others. The appeal of TE devices is obvious since they are simple to operate, do not produce undesirable vibrations or waste, and have long operating lifespans. However, the main problem shared by current TE materials is that they suffer from poor efficiency [157–159]. The efficiency of a material to be used as a thermoelectric generator is given by the ratio between the energy provided to the load (when a load closes the electrical circuit), and the heat energy absorbed at a hot junction. However, because the efficiency varies depending on the temperature and its gradient, usually when comparing devices, the maximum value of the efficiency, called figure of merit, ZT , is given. This quantity can be calculated using:

$$ZT = \frac{\sigma S^2}{\kappa} T \quad (10)$$

where σ is the electrical conductivity, S is the Seebeck coefficient, T is the temperature and κ the thermal conductivity of the heat carriers. Optimisation of the figure of merit is non-trivial due to the interdependence of the parameters coming into play (σ, κ, S), as shown in *figure 2.14(a)*. As a rule of thumb, good TE materials need to have a high electrical conductivity in order to carry as much heat-bearing current as possible, while preventing Joule heating, and a low thermal conductivity in order to minimise the heat dissipation, keeping this way the temperature gradient, and therefore the movement of carriers.

Although theoretically ZT could take infinite value (i.e. Carnot efficiency), the highest performance that materials available nowadays have achieved for devices that operate near room temperature reach ZT of about 2.5, like in the case of SnSe (see the timeline of maximum ZT in 2D materials in [160]). However, normally, the values are around 1 [161–164], and achieving a ZT of 4 has been the goal to reach for many years. This would be equivalent to achieve a 30% Carnot efficiency (e.g. comparable to home refrigeration) [165]

Luckily, there are theoretical grounds for some optimism in order to overcome this formidable challenge: In 1993, Hicks and Dresselhaus [166, 167] predicted that the future of improved Seebeck coefficients and TE responses lied in low-dimensional (LD) materials as shown in *figure 2.14(b)*, mainly as a consequence of two factors:

- (i) **Quantum confinement** (discussed in *chapter 1*): Contrasting with the smooth DOS presented by bulk materials, 2D materials often exhibit sharp peaks (i.e. high $dDOS/dE$). When tuning the Fermi level to these positions, the large asymmetry

established between hot ($E > E_F$) and cold ($E < E_F$) electrons leads to a higher Seebeck coefficient without a large sacrifice of the electrical conductivity. Furthermore, the Fermi level of the layered materials can be accessed much more easily than bulk materials, by simply applying an external electric field, as reviewed in section 2.4.1.

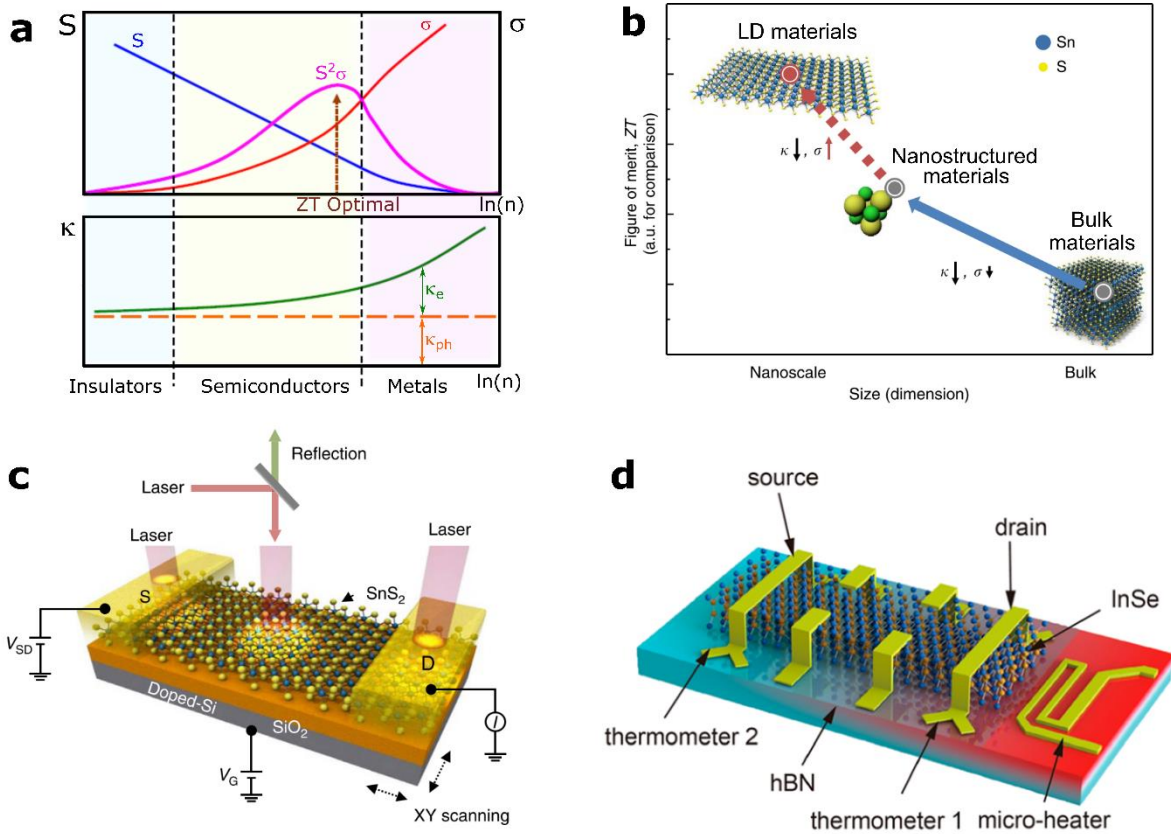


Figure 2.14. (a) Interdependent relation between the Seebeck coefficient, S , electrical conductivity, σ , thermal conductivity, κ , and power factor, for different carrier concentrations. Adapted with permission from [168] (b) Progress of future TE materials. Conventional bulk materials showing values from 0.01 to around 1. By using nanostructures, values between 0.1 to 2 have been reported. The solid blue arrow indicates already made progress, while the dotted red arrow the prospects for further increased ZT. (c) Schematic design of an SnS_2 device on a photo-TE measurement setup. Reproduced with permission from [169] (d) Design of a TE device based on 2D materials: InSe deposited on a hBN substrate. The micro-heater acts as a heat source of the system, while the temperature at different spots of the device is measured by thermometers 1 and 2. Lateral contacts are used to measure the variations in voltage, ΔV , along the device. Reproduced with permission from [170].

- (i) **Scattering control:** The mean free-path (MFP) of certain carriers can be modified by engineering the geometry of the devices or controlling feature sizes. In general, phonons have a MFP of around an order of magnitude larger than the MFP of electrons in semiconductors (of the order of 100 nm vs 10 nm). But in 2D materials it is possible to reduce the size of a system below the MFP of phonons, while staying above the MFP of electrons, allowing for much more tuneability of properties than traditional semiconductors.

Based on these prospects, theoretical and experimental studies have been performed in different systems such as graphene [171–173], twisted bilayer graphene [174], MoS₂ [175], SnS₂ [169], InSe [169, 170] or BP [176], among others, revealing in some cases unprecedented values of ZT, higher than any bulk material. Unfortunately, because of the difficulty on fabricating large areas of certain 2D materials, many studies has to be performed in nanostructures, such as the devices shown in *figure 2.14(c)* and *(d)* and heat gradients have to be produced by light-matter interaction (*figure 2.14(c)*), nanosized heaters (*figure 2.14(d)*), or using special atomic force microscope probes that incorporate heaters (as it will be discussed in this thesis on *chapter 7*).

2.6 Concluding remarks

This chapter intends to provide the background knowledge needed for the experimental chapters of the thesis. First, the fundamental properties of graphene were reviewed, followed by the main fabrication methodologies (i.e. mechanical exfoliation, CVD and epitaxial routes). Then, other materials of interest, such as hBN and InSe, were analysed covering their main properties, and applications. To continue, mechanisms of electrostatic and chemical doping of graphene were studied. Finally, a short description of the nanoscale thermal conductivity and the prospects of 2D materials for thermoelectric applications were discussed. All the concepts covered here will provide a foundation for understanding all the experimental work presented in the following chapters.

Review of characterization methods

This chapter presents an overview of the fundamental aspects related to the different experimental techniques that will be employed in this thesis.

The first section covers scanning probe microscopy (SPM) techniques, which allow obtaining topographic information, as well as local material properties mapping at the nanoscale. To start, atomic force microscopy (AFM) working principle will be described, setting up the basics upon which all the other techniques rely on. Following this, Kelvin probe force microscopy (KPFM) and scanning thermal microscopy (SThM), will be introduced in this order. Then, optical methods will be also described, including bright and dark field microscopy, and Raman spectroscopy. Finally, a short description of electrical methods, specifically two- and four-point probe techniques, is included.

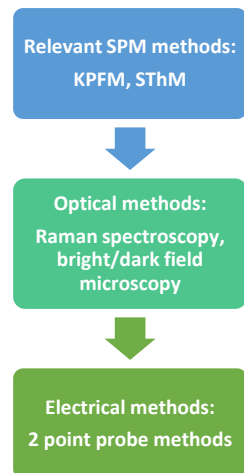


Figure 3.1. Structure of the characterisation methods covered in this chapter

3.1 Scanning probe microscopy (SPM)

Scanning probe microscopy (SPM) is the name received by a family of techniques in which a sharp tip is used to raster scan the surface of materials, in the same fashion as a gramophone [177], providing topographic mapping and information of different physical and chemical properties at the nanoscale [178, 179]. These revolutionary methods allowed overcoming the light diffraction limit imposed by Abbe's condition to all optical techniques. In this section, atomic force microscopy (AFM) is covered, together with other advanced modes, namely Kelvin probe force microscopy (KPFM), scanning thermal microscopy (SThM), and scanning thermal gate microscopy (STGM).

3.1.1 Atomic force microscopy (AFM)

An AFM cantilever is essentially a force sensor; however, it is important to highlight that no forces are measured directly by it. Instead, the normal force exerted by the cantilever is typically calculated in first approximation using Hooke's law by:

$$F_N = -k \cdot \Delta z \quad (11)$$

where k is the stiffness of the cantilever, and Δz the total normal bending. This approximated force results from the sum of all the interactions occurring at the tip-sample system, which are varied in nature and range. The equilibrium is usually reached as a compromise between long-range attractive and the short-repulsive forces. A variety of scanning modes have been developed so far by exploiting the tip-sample interactions. Thus, depending on the dominant forces acting on the tip-sample distance, different AFM modes are considered: contact, tapping and non-contact modes, as shown in *figure 3.2*. In this thesis, only contact and tapping mode will be employed, and will be discussed in the following paragraphs.

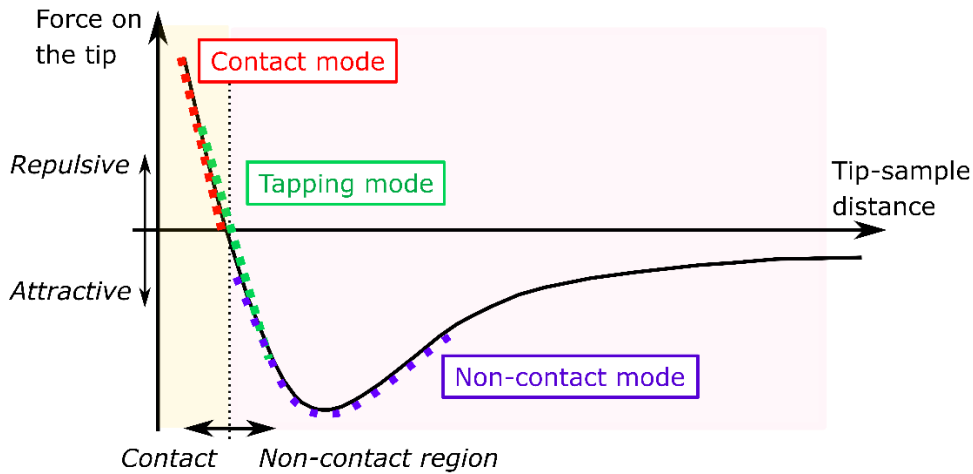


Figure 3.2. Force vs tip-sample distance curve. The attractive and repulsive regimes are specified by vertical arrows coming out from the x-axis. The contact and non-contact regions are highlighted with a yellow and pink background, respectively. The different operational modes, namely contact, tapping and non-contact modes are depicted by red, green and purple dotted lines, respectively.

A typical diagram of an AFM set-up is represented in *figure 3.3(a)* [180], with the AFM probe formed by a sharp tip mounted at the end of a flexible cantilever, as shown in *figure 3.3(b)* and *figure 3.3(c)*. For the AFM operation, the probe displacement over the sample's surface in all three perpendicular directions, x , y and z , is achieved by a piezoelectric actuator, also known as tube scanner. These changes in the z -position are tracked using the beam-deflection method and a closed feedback-loop: a laser beam is reflected at the back end of the cantilever, which is typically coated with a reflective material, into a four-quadrant photodiode. The changes in the position of

the laser on the surface of the detector produces an electrical current proportional to the displacement, which provides information about both the normal bending and the torsion of the cantilever. This current is then converted into a voltage bias signal which is compared to a fixed setpoint value via a proportional-integral-derivative (PID) control system. The result of this comparison dictates if any adjustment the Z-direction piezo is needed (i.e. by elongating or compressing it) in order to maintain a constant interaction force between the tip and the sample. This operation is repeated for each point in the sample, generating a pixel-by-pixel image of the surface topography.

The signal that is measured by the photodiode is different for each of the measuring modes, as the tip-sample interaction is different:

- **Contact mode:** In this mode, the tip-sample distance is kept in the range where repulsive forces dominate as shown in *figure 3.2*. The force between both systems is kept constant via the feedback mechanism: As the tip encounters surface features, the deflection signal on the photodetector varies and is fed as the error signal to the feedback control, which then compares it with the setpoint value selected by the user, and re-adjusts the distance between the probe and sample to keep the force constant. The cantilevers used for contact mode are rather soft with spring constants typically ranging between 0.01 N/m and 5 N/m. Contact mode is normally used for SPM methods like scanning thermal microscopy (S_{Th}M). It is also commonly employed on its own to obtain the topography of certain samples, and also to remove dirt or resist from the surface of 2D materials and vdW heterostructures [181]. Nevertheless, it is important to remark that this mode can sometimes lead to scratches or damage of the samples, especially if the feedback parameters are not optimised or if the force set point is selected to be too high. This occurs due to high normal forces acting on the sample, but also due to the presence of high frictional and adhesive forces.

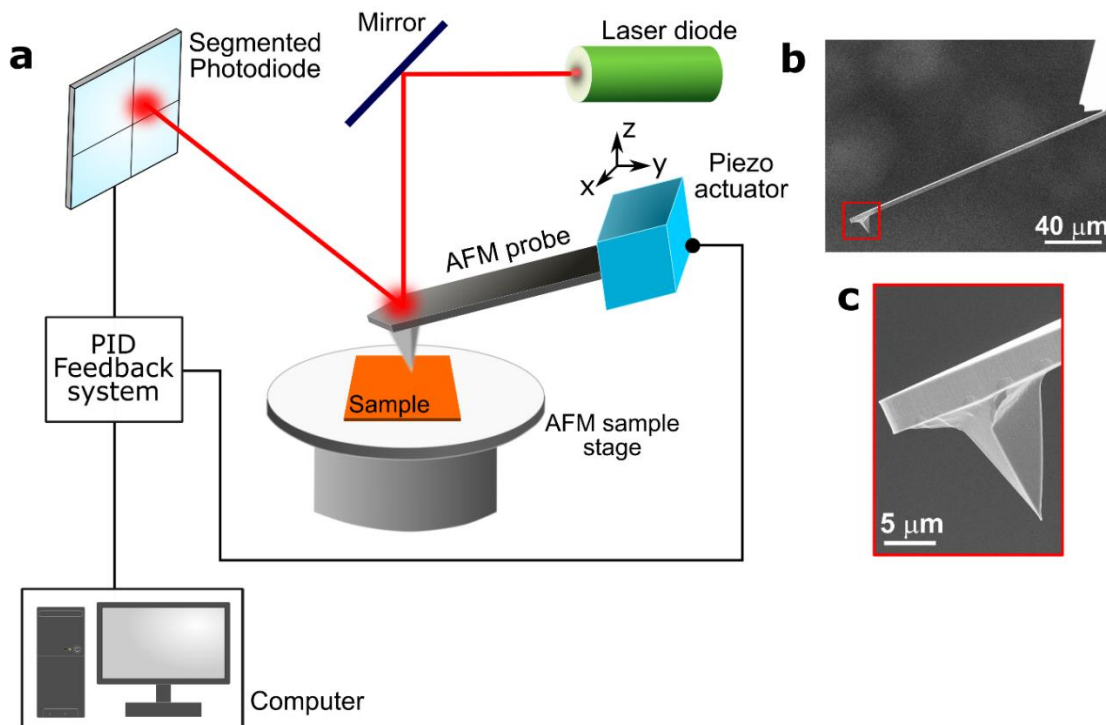


Figure 3.3. **(a)** Typical AFM set-up, with a feedback mechanism based on the laser-beam deflection method. **(b)** Scanning electron microscopy (SEM) image of a silicon cantilever with an integrated probing tip manufactured by Bruker©. **(c)** SEM detail of the pyramidal tip from **(b)**

- **Tapping mode:** in this mode, the cantilever is driven to oscillate at a fixed frequency, typically near or at its resonance frequency, while in close proximity to the surface, causing it to continuously “tap” (i.e. intermittently contact) the sample’s surface. A lock-in amplifier (or a phase lock loop (PLL)) connected to the photodiode and operating at the frequency and phase used for the mechanical excitation is used to monitor changes in cantilever’s vibrational parameters, being these the amplitude or phase, of the oscillating probe (or frequency if using the PLL). The image contrast in this case is the extension of the z piezo, which is varied by a feedback loop that uses the lock-in/PLL output (i.e. amplitude, frequency shift, or phase) to raise or lower the probe in order to keep a constant force on the surface. This mode has the advantage of still providing good resolution with reduced lateral forces due to the intermittent contact, thus reducing the possibility of damaging or scratching the surface, which makes it ideal for imaging soft and fragile samples [182]. Note that through this thesis PLL is not used as part of the tracking mechanism, hence it is only mentioned here as another possibility for operation of the tapping mode without adding further details.

The main advantages of AFM methods are its robustness, allowing the performance of measurements in different environmental conditions (i.e. from room conditions to ultra-high

vacuum or low temperatures), and its versatility, as different nanoscale properties can be studied with small adjustments to the presented set-up.

AFM is widely employed to study 2D materials and their related heterostructures. One of the most common applications of AFM is extracting high resolution topographical information such as the shape and the thickness of the flakes, which is of extreme importance, as 2D materials generally present thickness dependent physical properties. Additionally, AFM is typically used to assess the number of fabrication related defects, such as bubbles, cracks or folds (see figure 3.4) that might be present in the sample of interest, as well as the possible contamination deposited on the surface, which typically affects the optical and electronic properties of the materials, undermining device performance. In the next sections we will discuss electrical and thermal AFM modes, less common AFM modes, that nevertheless can add additional important information when studying 2D materials.

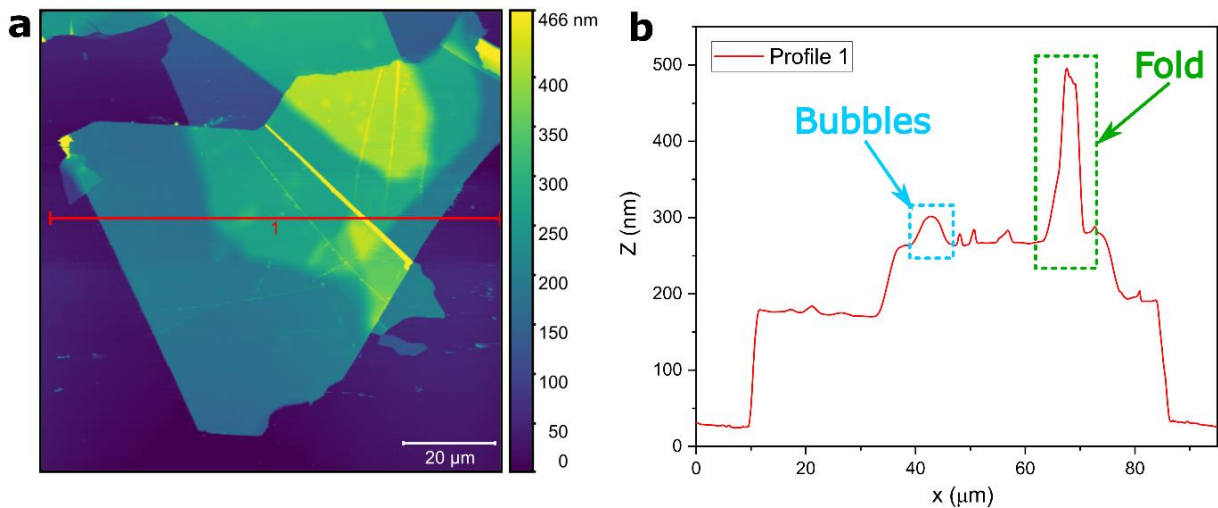


Figure 3.4. **(a)** Topography map acquired in tapping mode of a heterostructure formed only by layers of hBN deposited on top of each other. **(b)** Extracted profile from the red line in (a). The thickness of the different layers can be clearly assessed. Other features like bubbles (blue), contamination or folds (green) are also distinguishable.

3.1.2 Kelvin probe force microscopy (KPFM)

Tip-sample interaction are composed of several forces that are varied in nature and range, including short-range such as chemical or vdW forces, and long-range such as electrostatic or magnetic forces. Kelvin probe force microscopy (KPFM), first developed by Nonnemacher et al. [183] in 1991, is a dynamic AFM-based technique which measures the contact potential difference (V_{CPD}) of a sample's surface alongside with its topography [184]. The V_{CPD} arises from the work-function difference between two conductive materials in electrical contact, as shown in figure 3.5(b). In KPFM a conductive probe and a sample are brought into electrical contact and the V_{CPD} that arises is nullified by applying a V_{DC} , as illustrated in figure 3.5(c). There are different

strategies to detect when the V_{CPD} is nullified by the applied V_{DC} , namely, amplitude sensitive methods (AM-KPFM), or frequency modulated methods (FM-KPFM). In this thesis, only single-pass FM-KPFM will be employed, however, more information about the other techniques can be found in other sources [185–187].

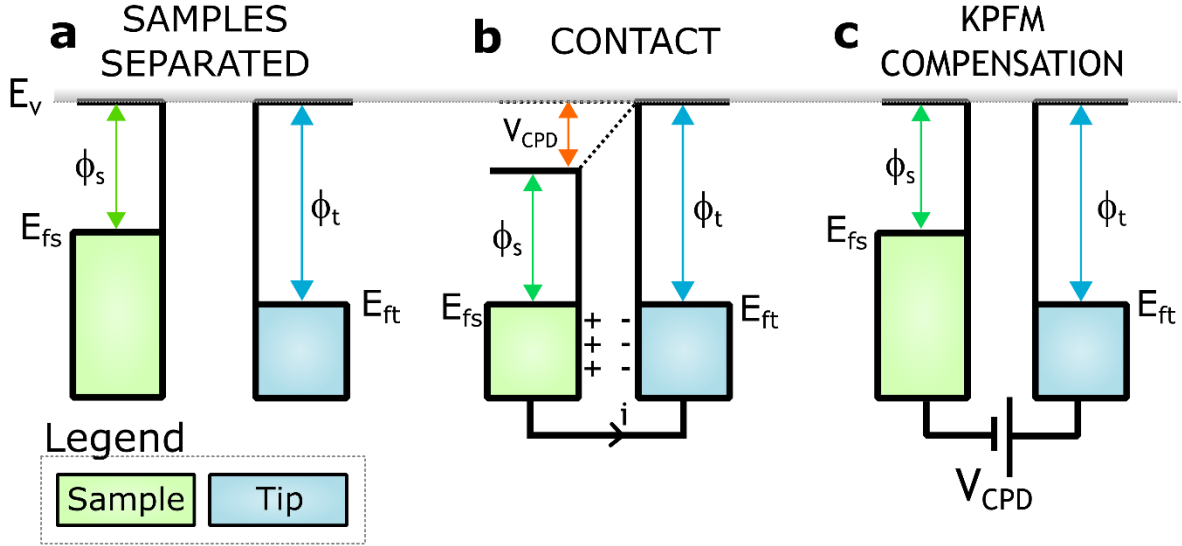


Figure 3.5. Schematics showing the origin of the V_{CPD} . **(a)** For two separated samples, their work-function would be defined as the distance between their Fermi levels and the vacuum level. **(b)** When the materials are brought into electrical contact, their Fermi levels, E_F , aligned. This happens as the electrons from the material with higher work-function flow to the material of lower work-function, leading to the formation of a contact potential difference V_{CPD} . **(c)** The V_{CPD} , and so the electrostatic force between both materials, can be minimised by applying an external bias voltage, $V_{DC} = V_{CPD}$.

Details of the working set-up used for KPFM are shown in *figure 3.6*. It is based on tapping mode imaging as per discussed in the previous section, with an electrical signal applied to the probe with its own feedback control to null the electrostatic forces between the tip and the sample. More details are provided in the following:

1. On the tapping mode part, the probe is mechanically oscillated at, or close to, its resonance frequency, f_0 , which translates into a tapping motion of the tip over the sample. This is used by a feedback loop to track the distance between probe and surface, lowering or raising the probe to track the topography of the surface and produce a height map.
2. The surface potential is obtained applying an AC + DC voltage, V_{app} , to the probe. The AC part, V_{AC} , has a frequency f_{mod} , which modulates the total electrostatic force field between the sample and the probe, $F_{el} = \frac{1}{2} \frac{\partial C}{\partial z} V_{app}^2$, where C is the capacitance of the system, z is the normal to the plane formed by the sample. The modulation allows using a lock-in technique (if it is amplitude or phase modulated), or a PLL (if it is frequency modulated) to track the electrostatic force, and decide if to raise or low the applied DC voltage to null that force. When the force is nullified, the obtained DC voltage, V_{DC} , maps the surface potential of the sample. Note that typically, the frequency of the electrical

excitation is chosen to be much lower than the mechanical excitation frequency, $f_{\text{mod}} \ll f_0$, to avoid any coupling between both signals.

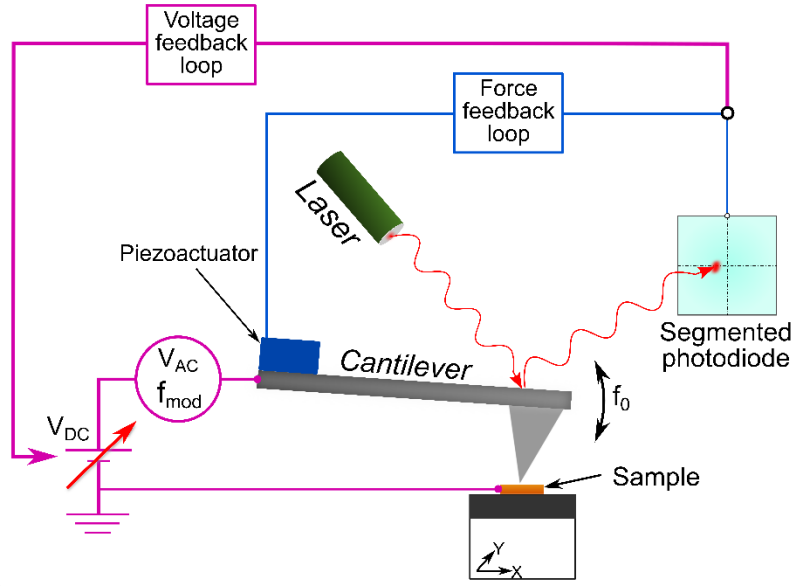


Figure 3.6. Schematic diagram of the KPFM set-up, with the electrostatic system represented in pink, and the force feedback loop represented in blue.

In single-pass FM-KPFM maps of the topography and the V_{CPD} are acquired at the same time in tapping mode, and changes in the oscillation frequency provide information about the interactions between the tip and the sample. The changes in oscillation frequency are dependent on the force gradient established between the two, as expressed by:

$$f'_0 = \frac{1}{2\pi} \sqrt{\frac{k - \partial F_{el}/\partial z}{m^*}} \approx f_0 \left(1 - \frac{1}{2k} \frac{\partial F_{el}}{\partial z} \right) \quad (12)$$

where k and m^* are the spring constant and the effective mass of the cantilever, and $\partial F_{el}/\partial z$ the gradient of the electrostatic force in the normal direction with respect to the sample's surface. More details on the physical meaning and mathematical development of eq 3.2 can be found in [182].

The applied AC voltage modulates the electrostatic force between the tip and the sample, F_{el} , and with it, $\partial F_{el}/\partial z$ as well. It also interacts with the mechanical excitation of the probe, originating several new peaks in the frequency spectrum of the probe when imaging in tapping mode, which can be seen on a frequency spectrum of the probe while imaging (as shown in figure 3.7). Figure 3.7 shows the peak due to the AC excitation at f_{mod} , its second harmonic at twice the frequency, and the pure mechanical excitation peak at f_0 . The additional peaks are the sidebands that appear when the mechanical excitation and the AC excitation are mixed. Because these sidebands only appear when there is an electrostatic force, they can be used to monitor the electrostatic interaction. The newly created peaks at $f_0 + f_{\text{mod}}$ are monitored by a PID feedback loop, and the

DC voltage is then applied to compensate them. The value of the voltage at which the lobes are annihilated corresponds to the contact potential difference, V_{CPD} .

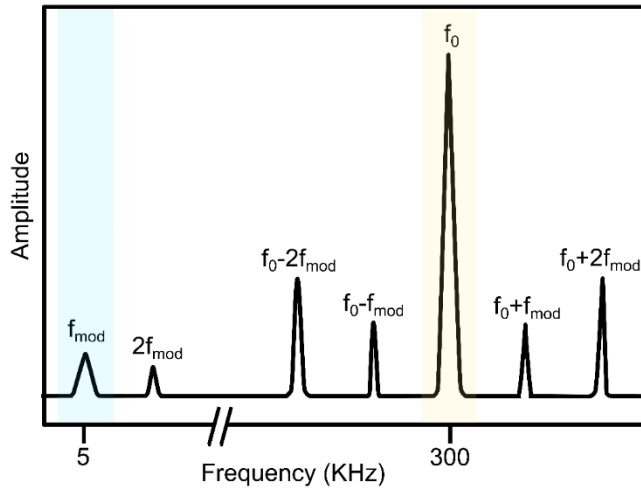


Figure 3.7. Schematic diagram of the frequency spectrum of an example cantilever. The peak at the mechanical resonance is placed at $f_0 = 300$ kHz and highlighted in yellow. Side-lobes appear at the sides of the resonance frequency as a consequence of the electrostatic force field with peaks at $f_0 \pm f_{mod}$ and $f_0 \pm 2f_{mod}$. The frequency of the oscillating excitation signal generating the electrostatic force is placed at $f_{mod} = 5$ kHz, and highlighted in blue. Figure inspired by Zerweck et al.[187]

One of the advantages of using FM-KPFM is that as the gradient of the force is much more confined to the tip front end than the force, resulting in higher lateral resolution than AM-KPFM. Also, it is important to note that the contact potential difference (V_{CPD}) between two materials is affected by several parameters such as their respective work-functions, the presence of adsorption or oxide layers, or the dopant concentration in semiconductor, among others. Thus, regardless of the method employed, the measurement of the V_{CPD} can be used to obtain information concerning these parameters, but these have to be also considered when interpreting the data [188–192].

Finally, one of the most important applications of KPFM is that it allows to obtain quantitative values of the work function of the material ($\Phi_{surface}$) with nanoscale resolution. For this however, the work-function of the tip (Φ_{tip}) has to be known as expressed by:

$$V_{CPD} = \frac{\Delta\Phi}{e} = \frac{1}{e}(\Phi_{surface} - \Phi_{tip}) \quad (13)$$

where e is the elementary charge of the electron. The calibration of the probe and the obtention of reliable values of the work-function will be discussed in detail in *chapter 6*.

3.1.3 Scanning thermal microscopy (SThM)

The Scanning thermal microscopy (SThM) technique, first envisioned and developed by Williams and Wickramasinghe et al. [193] in 1986 as a thermal profilometer, is nowadays a key method to study the thermal properties of materials with nanoscale resolution.

The operation of SThM, which is performed in contact mode, requires the addition of few modifications to a standard AFM system, as shown in *figure 3.8*. For instance, the probe, which is

the key part of the set-up, serves in the case of the work performed in this thesis, as a resistance thermometer as well as an AFM tip. While scanning across the sample, a closed feedback mechanism tracks the topographical features of the sample, using a beam-deflection method to detect the z variations, as explained in *section 0*. On the other hand, the SThM signal is measured directly using a Wheatstone bridge connected to a lock-in amplifier (LIA) [194]. The probe is mounted as part of the set of resistors of a Wheatstone bridge, R_{probe} , together with other two known fixed resistors, R_1 and R_2 , and a variable resistor R_3 . Initially, the probe is heated by means of the Joule effect when passing a very small electrical current, normally as a combination of AC and DC electrical signals. Before the measurements, and having the tip still millimeters above the sample surface, and therefore out of contact, the variable resistor is adjusted to null the voltage across the bridge, $V_{out} \sim 0V$.

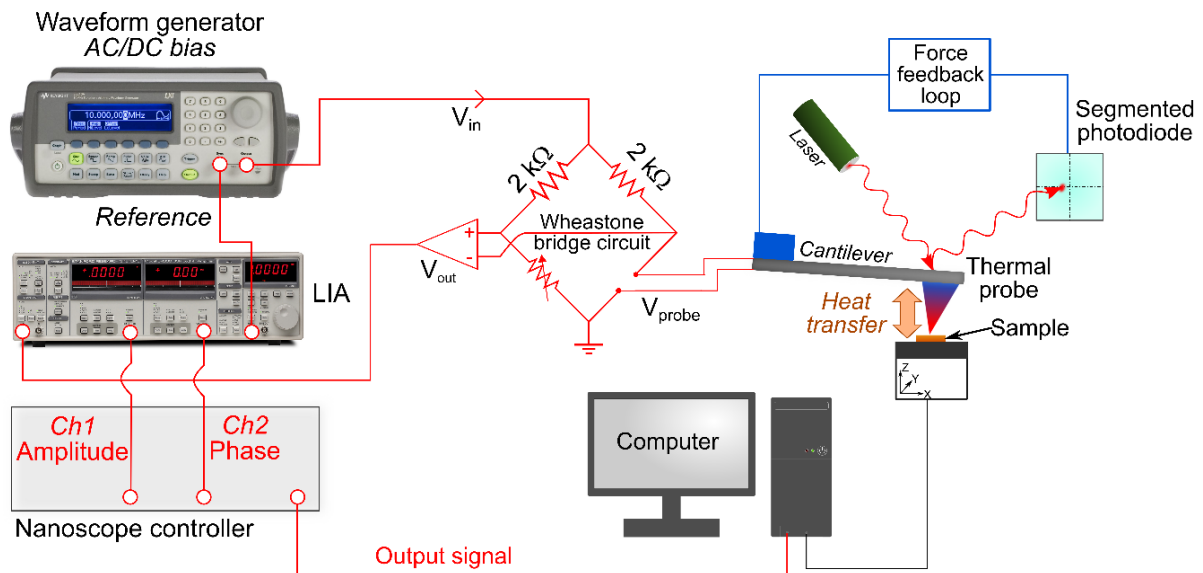


Figure 3.8. Standard SThM experimental set-up for resistive probes employed as passive resistance thermometer. In red the thermal related circuit is shown, while the topography-feedback is shown in blue. The heat transfer between the sample and the thermal probe is evaluated using a Wheatstone bridge and a lock-in amplifier that measures the variations of the thermal probe electrical resistance. The force between the probe and the sample is controlled by a standard force feedback loop.

Then, when the hot tip is brought into close contact with the surface of the sample, heat transfer occurs, decreasing the probe's temperature, and thus leading to a reduction of the probe's resistance, ΔR_p . This variation unbalances the bridge output voltage signal, V_{out} , that is continuously monitored by the LIA as shown in *figure 3.8* and fed into the microscope controller to create the thermal image map pixel by pixel.

The corresponding change of electrical power dissipated by the probe resistor, $\Delta P = R_{probe} \Delta V_{out}$, is proportional to the heat flux towards the sample and its thermal conductivity. However, it is also influenced by the heat loss from the cantilever with its environment. As shown

in figure 3.9(a-b), there are several tip-sample heat transfer mechanisms, which become more or less important depending on the measurement conditions [193, 195].

- The obvious **solid-solid conduction** through the tip-sample contact, is the most important heat transfer channel for SThM, as it can provide information of the thermal conductivity of the sample. It is present in all conditions.
- In ambient pressure, normally a water meniscus is formed around the tip-sample contact point due to the condensation of environmental humidity, also known as capillary condensation. This meniscus then becomes another heat transfer channel, with its size depending on several parameters such as the type of the materials involved, the relative humidity on the environment, and the temperature of the probe, among others. The contribution of the water meniscus to the thermal conductance depends on the type of probe employed, as demonstrated by Assy et al. [196, 197]. This **solid-liquid** contact is considered a parasitic contribution, but its influence can be eliminated by increasing the temperature of the probe above $T > 100^\circ\text{C}$, and also by measuring in vacuum conditions. Further details on the contributions of the water meniscus to SThM measurements can be found in the following references [195, 198].

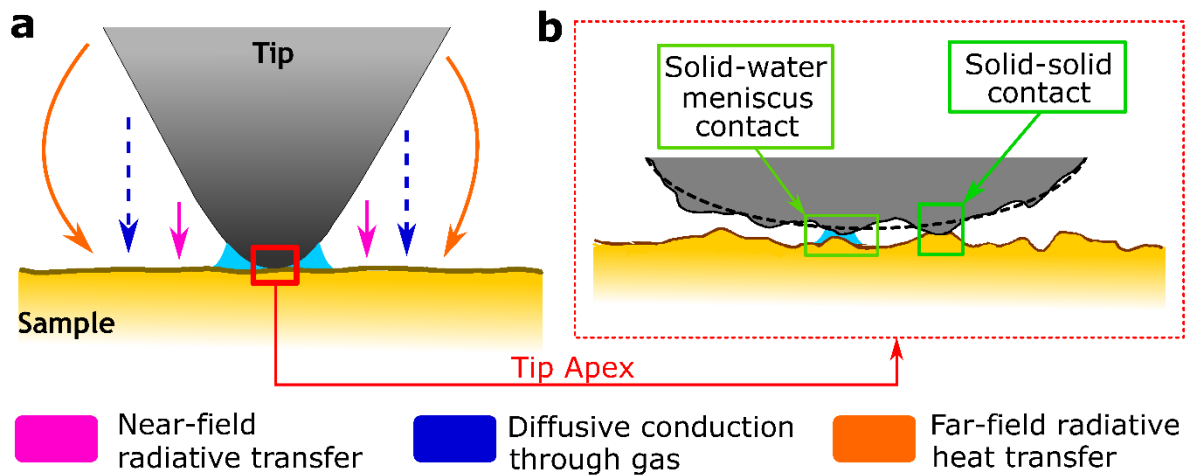


Figure 3.9. (a) Microscopic tip-sample contact. Different contributions to the heat transfer are shown as arrows of different colours: pink and orange for the near-field and far-field radiative transfer, respectively; and blue for the gas conduction. Also, a water meniscus is shown as a light blue shadow around the tip and sample contact. In (b), a closer detail on tip-sample contact is shown. The dotted line represents the ideal profile of the tip-apex, while the most likely rough real profile is shown as a continuous line.

- In dry conditions or when working with hydrophobic surfaces, **air conduction** becomes a major component of the tip sample system. Three mechanisms can occur depending on the heat-sample distance. When considering large distances, air convection transports heat by gas flow. At distances smaller than a few micrometers, heat diffusion becomes the dominant mechanism. Finally, when considering a few hundreds of nanometers, ballistic

conduction occurs as the carrier mean free path of air is around 70 nm It is also considered a spurious contribution

- **Radiation losses** are always present in the experiment due to the ubiquitous Planck's law. However, in ambient conditions, it is very difficult to assess how important is the contribution of the heat loss coming from thermal radiation, in comparison with other contributions, such as air convection or solid-liquid interface. Nevertheless, as the radiated energy is proportional to the fourth power of temperature, at ambient and lower temperatures the loss by radiation have been assumed to be negligible. When measuring in vacuum, near-field radiation is considered to possibly have an effect on the measurements, however, not much research has been dedicated to this, and it is a topic still open to debate and clarification in the SThM community. More details on the impact of radiation losses on SThM can be found elsewhere [198–200].

Therefore, in order to interpret properly and accurately the thermal signals, it is of high importance to consider the conditions in which the experiment is performed. To eliminate the parasitic contributions, measurements have to be done in vacuum, in which the solid-solid conduction and radiation losses are assumed to be the only contributions [195, 201, 202]. SThM can be a powerful tool to investigate heat transfer in nanostructures, such as thin films on different substrate or even 2D materials [192, 203, 204]. More on the later will be discussed on *chapter 7*.

3.1.3.1 Scanning thermal gate microscopy (STGM)

Scanning thermal gate microscopy (STGM) is a very recently established technique that uses the similar set-up to SThM. However, as explained in the previous section, SThM is capable of measuring variation of temperature in the sample by passing a small current through the probe, and using it as a thermal sensor. On the contrary, STGM could be seen as the other side of the coin, in which a larger electrical current is passed through the probe, resulting in a significant Joule heating, which is used to heat up the sample at the specific points of contact, creating local temperature gradients. This mode is especially useful for thermoelectric studies: by using contacts pre-patterned on a sample, and measuring in open-circuit configuration, the thermovoltage generated by the proximity of the heated probe, allows the characterisation of local variations of thermoelectric properties as the Seebeck coefficient [203]. This topic will be discussed in more detail in *chapter 7*.

3.2 Optical techniques

The optical methods covered in this section are widely employed in the 2D materials community to locate areas of interest present in the sample, as for example the presence of flakes after exfoliation, or specific features in CVD or epitaxial samples. These methods can be also employed to identify the number of layers of a material, and the presence of any possible contamination or defects, such as cracks, bubbles or wrinkles.

3.2.1 Bright field microscopy

Bright field microscopy is used for sample characterisation in general. However, it is heavily employed for flake search and thickness determination in mechanically exfoliated samples [95, 205, 206].

Bright field microscopy can be used either in reflection (also known as epi-illumination) or transmission mode. As thin layers of 2D materials generally show high transparency, choosing one mode or the other commonly depends on the optical properties of the sample's substrate. Typically, samples deposited on non-transparent substrates (e.g. silicon) are investigated in reflection mode as shown in the left panel in *figure 3.10*, while transmission mode is used for samples deposited on transparent substrates (e.g. polymer). In both cases, a built-in light source is used for imaging. The light is directed via a system of lenses towards the surface of the sample, where it can be absorbed, scattered or reflected, producing a variation on the light intensity. The reflected image contains information of the different optical (e.g. refractive index) and geometrical (e.g. thickness) properties of the sample at distinct points. The outgoing light, either reflected or transmitted, is collected by a sensor, typically a CCD or CMOS, and an image is reconstructed pixel-by-pixel based on the intensity variation in the different RGB channels. Further adaptations such as the incorporation of light filters or manipulation of the final image with specific software in real time, are easily included in the set-up, making this technique even more versatile. Although subjected to the diffraction limit, optical microscopy is still the first tool used in sample assessment after fabrication. This is mainly due to its capability of providing real-time imaging over large samples areas with a very simple set-up and with no prior sample preparation. Optical microscopy is often employed together with AFM as complementary methods, in order to obtain accurate information of the samples under study.

3.2.2 Dark field microscopy

Dark field (DF) microscopy is commonly applied to identify grain boundaries, defects and contamination in 2D materials samples, either exfoliated, CVD or epitaxially grown [207, 208].

For the implementation of DF microscopy, rather than illuminating the sample vertically with a filled cone of light as for bright field microscopy, a patch stop is placed into the filter holder of the condenser lens. This way, a hollow cone of light arrives to the sample forming extremely oblique angles with respect to it. As a result, only the light scattered from the sample is collected back at the sensor. A schematic set-up of DF microscopy is shown in the right panel in *figure 3.10*. This is advantageous in order to image defective areas as rougher elements such as edges, point defects, dust particles or grain boundaries, ubiquitous in 2D materials, which tend to scatter more light. In DF images, these elements typically shine bright over a dark background, while they could remain undetectable in bright field illumination.

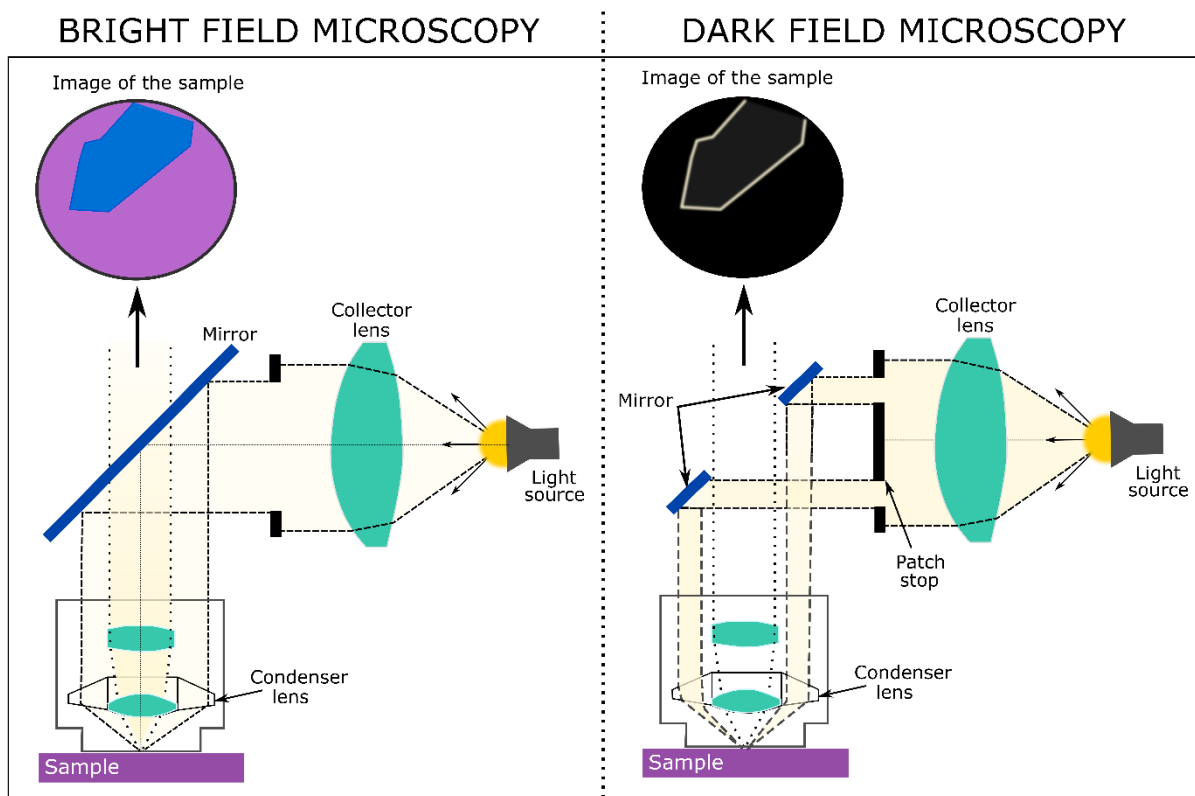


Figure 3.10. Set-up schematics of an optical system for brightfield (left) and darkfield (right) microscopy in reflection mode. On top of each schematic, a diagram showing an example flake imaged with each mode highlights the differences between the two.

The popularity of DF illumination for defect identification in 2D materials is mainly a consequence of its effectiveness, together with other advantages, such as the requirement of a very simple set-up, the production of images free of artefacts, and the possibility of real time operation.

3.2.3 Raman spectroscopy

Raman spectroscopy is a well established technique employed to non-destructively extract fundamental information about the 2D materials under study. This method permits the

differentiation of the number of layers and it is sensitive to defects, excess of charges (doping), strain, chemical composition, and even, to the atomic arrangement of the edges [209–212]. In this section, the fundamentals of Raman spectroscopy applied to graphene are briefly reviewed. For more information the book from A. Jorio et al. [213] is recommended.

In a Raman process, the sample is illuminated with a laser beam. The incident photons, with energy, $E_i = E_{laser}$ and momentum $k_i = k_{laser}$ reach the sample and interact with the vibrational modes (phonons and other excitations) via inelastic scattering. This interaction results in the generation (Stokes scattering) or annihilation (Anti-Stokes scattering) of a phonon, and in the emission of a photon of different energy, E_s , and momentum, k_s . The majority of the photons interacting with the sample undergo elastic scattering, i.e. Rayleigh scattering, however this signal is filtered out from the collected light. *Figure 3.11* displays schematically the scattering processes described above. The remaining scattered photons are dispersed using a grating that divides the light in its different components, and directs it to a

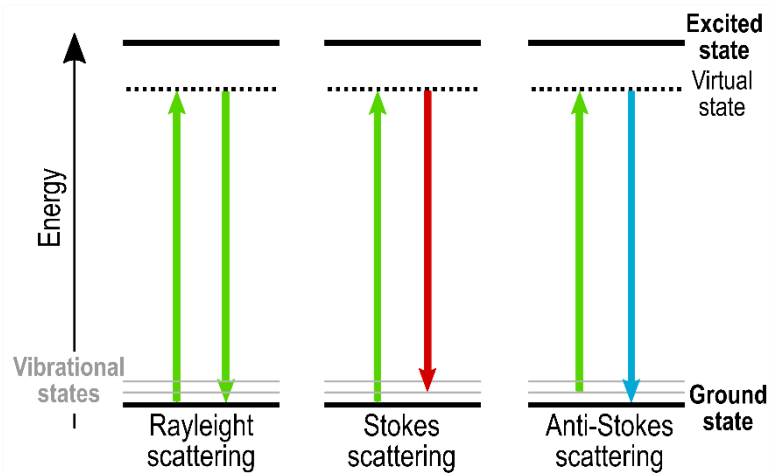


Figure 3.11. Scattering process present in Raman interaction.

photodetector. The energy shift of the scattered photons with respect to the incident photons is then measured and displayed as a characteristic spectrum of the material. Normally, these spectra are shown as graphs of intensity of counts or photons collected, versus the wavenumber (i.e. inverse of the wavelength) in cm^{-1} . The spectral resolution, i.e. how many features can be resolved, depend on the groove density of the grating, the laser wavelength and the detector.

Typical Raman spectra for different types of graphene are shown in *figure 3.12*. The position of the peaks that appear in the Raman spectrum, i.e. the energy shift measured, are independent of the laser wavelength. In the case of solids, which is what concerns the work presented here, the peaks are related to the in-plane and out-of-plane vibrations of the crystalline lattice, i.e. the phonon modes, thus they contain fundamental information of the composition, structure and behaviour of the sample. It is important to highlight that not all the vibrational modes present in a sample are always shown in the Raman spectra, some of them are not Raman active due to symmetry considerations. Further details on this are out of the scope of this thesis, but more information can be found elsewhere [214, 215]

In the case of pristine monolayer exfoliated graphene, the Raman spectrum contains prominent features like the G-mode and 2D-mode, as shown in the top panel of *figure 3.12(a)*. These peaks are commonly characterised by their position, full width at half maximum (FWHM), and their relative peak intensity (I) with respect to other features. Analysing these features, important information regarding the graphene samples such as the number of layers, strain, doping, or the presence of defects can be extracted.

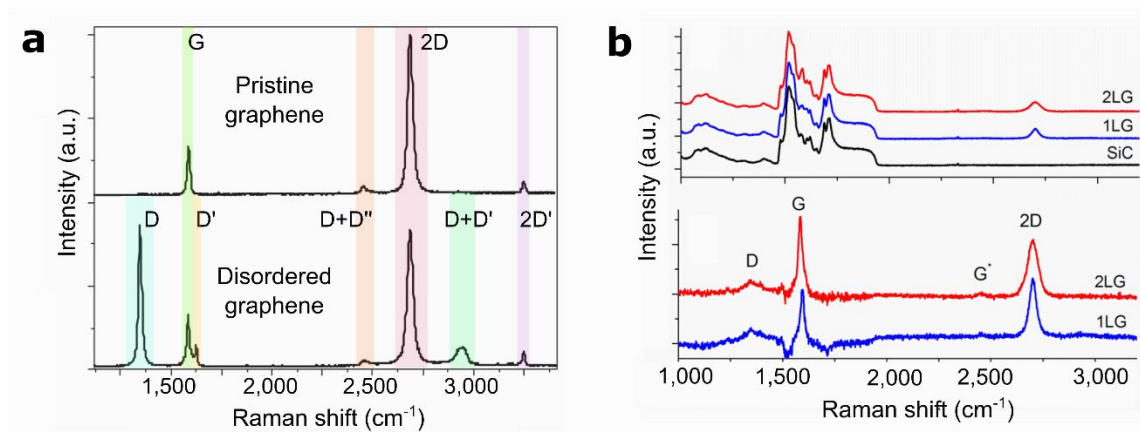


Figure 3.12. (a) Raman spectra of pristine (top) and defective (bottom) exfoliated graphene displaying the main features, i.e. the G (green), the D (blue) and the 2D (red) modes. Adapted with permission of [216] (b) Representative Raman spectra of epitaxial graphene grown on SiC(0001). On top, three different spectra are compared: the original spectrum for the SiC substrate in black, the monolayer graphene (1LG) in blue, and the bilayer (2LG) spectrum in red. On the bottom panel, the spectra after subtraction of the SiC signal for 1LG in blue and for 2LG in red are represented. Figure represented with permission of [217].

The most important Raman modes present and studied in graphene are discussed below:

- **G-mode:** The G-mode is a first order Raman peak located at $\sim 1585 \text{ cm}^{-1}$. This feature is common to all sp^2 hybridised carbon systems, produced by the stretching of the C-C bond. The intensity of this peak in the Raman spectrum is proportional to the number of layers. Furthermore, the position of the G peak is related to the doping level of the sample, blue shifting with increasing electron or hole concentration [136]. This last point will be further discussed in *chapter 5*.
- **D-mode:** The D-band is a second order mode located at $\sim 1350 \text{ cm}^{-1}$, as shown in *figure 3.12(a)*, bottom panel. It requires a defect for its activation, thus it commonly appears when measuring at the edge of graphene or in disordered graphene samples, i.e. graphene presenting some impurities, grain boundaries or vacancies. The intensity ratio between the D peak with respect to the G peak, $I(D)/I(G)$, is typically used as a reference to measure the defects in the lattice. Perfect crystalline lattices do not show this feature, although still preserve the 2D peak [218].
- **2D-mode:** The 2D-mode is another second order mode at $\sim 2700 \text{ cm}^{-1}$, corresponding to the overtone of the D peak ($\sim 1360 \text{ cm}^{-1}$). This is a single peak in monolayer graphene,

while it splits into four components in bilayer graphene. This mode does not need the presence of a defect for its activation, and thus it is always present. The FWHM and the position of the 2D peak are good indicators of the number of layers of the sample. As seen in *figure 3.12*, the 2D peak is distinctively large with respect to the G peak for monolayer graphene, and thus, the intensity ratio between the 2D and the G peaks, $I(2D)/I(G)$, is commonly employed as a reference to identify graphene monolayers [219–221].

When graphene is grown on different substrates, as for example epitaxial graphene on SiC, the peaks described above still appear on the Raman spectrum, and can be analysed to extract information of the layers. However, it is important to note that the position of the peaks or the line-shape of the spectra might vary due to doping. Also, they graphene common modes might be masked by the spectrum of the substrate, as shown in *figure 3.12(b)* for epitaxial graphene [222, 223]. In conclusion, besides giving a high amount of structural and electronic information, Raman spectroscopy presents several advantages, including its minimal sample preparation, fast data acquisition time, non-destructiveness and high reproducibility. For these reasons, Raman is one of the most exploited techniques for 2D materials characterisation

3.3 Electrical transport measurements: 2 point probe method

Electrical measurement techniques, specifically two-point probe (2PP) methods, will be briefly described here as they will be used in posterior chapters of the thesis. Two-point probe (2PP) is a method typically employed to determine the total resistance of a certain device under test (DUT). For its application, a set of two probes or electrical contacts are positioned at both ends of the DUT, while a controlled current is driven through the circuit. The voltage drop is then measured at the probes or at some point along the circuit, as depicted in *figure 3.13*. Then, the resistance of the DUT can be normally calculated following Ohms law:

$$R_T = \frac{V_{SD}}{I} = 2R_W + 2R_C + R_{DUT} \quad (14)$$

where V_{SD} and I are the voltage drop and current applied across the terminals; R_C is the contact resistance between the sample and the electrical probes, and R_W is the resistance of the wires. Normally, the resistance of the wires is so small in comparison with the rest of the values that it is not considered. However, it is not possible to determine the value of R_C , and thus the resistance of the DUT cannot be obtained from measuring R_T alone.

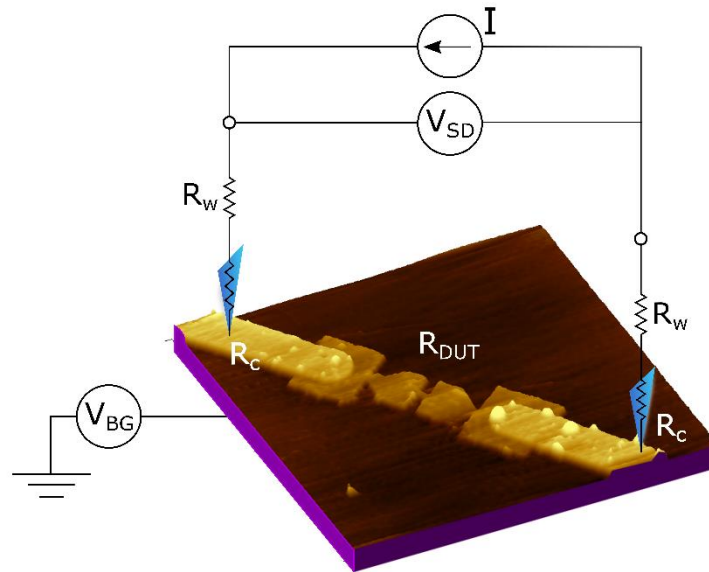


Figure 3.13. Schematics of the two-point probe(2PP) measurement configuration applied to a graphene device fabricated on top of 300 nm SiO_2/Si

Despite this limitation, one of the main advantages of this method is that its implementation is very simple and straightforward, and thus it is used in many situations. For example, like in the device depicted in *figure 3.13*, where some connections are reserved to be used for back-gating. To obtain the values of the contact resistance, R_C , together with the DUT resistance, R_{DUT} , other methods such as three-point probe (3PP) or preferably, four-point probe (4PP) are applied when possible. However, as they require more than two electrical connections to the device, and typically the devices studied through this thesis don't allow having so many connections on to them, they will not be described in detail here.

3.4 Conclusions

This chapter presented a description of the main experimental techniques that will be employed in the following sections of this thesis. The first part was dedicated to scanning probe microscopy methods. The section covered the essentials of AFM, plus two different advanced modes, KPFM and SThM, which are employed to obtain information of the electrostatic and thermal nanoscale interactions, respectively. Then, a section was devoted to optical techniques, from bright and dark field microscopy, widely employed during this project for fabrication of 2D materials, to Raman spectroscopy, which will be used for characterisation of the interactions between water and graphene later in *Chapter 5*, and also for the determination of the number of layers. Finally, the last section was dedicated to transport measurements, specifically 2-point probe methods, which were mainly employed to characterise graphene devices.

EXPERIMENTAL METHODS

CHAPTER 4

Fabrication of 2D heterostructures and devices

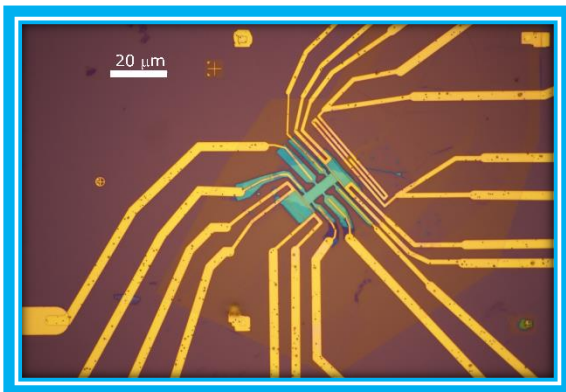


Figure 4.1. Example device formed by several layers of 2D materials, i.e. hBN, graphene and InSe. The device was fabricated using the methods described in this chapter. More details are provided later in Section 4.8.

This chapter presents the main experimental methods I employed and developed for 2D material's fabrication in this thesis. First, layered materials and van der Waals (vdW) heterostructures are shortly overviewed, together with the concept of air-sensitivity. To follow, the substrate selection and treatment, and the different exfoliation techniques are explained in extensive detail. Next, a description of how crystals with different thicknesses can be identified using optical contrast, and how this can be further enhanced using a selection of different tools (e.g. band-pass filters), is presented. Image processing algorithms applied to 2D material's detection will be also shortly discussed. Following this, the exciting prospect of stacking various 2D crystals to form van der Waals heterostructures will be explored. Then, a critical analysis comparing the two main stacking techniques used to fabricate heterostructure devices in this work will be performed. Finally, an overview of device fabrication is outlined, and a particular case study is shown.

Acknowledgments: All the processes presented in this chapter including flake exfoliation and heterostructure production, among others, have been performed by myself unless stated otherwise. However, I would like to acknowledge all the people that helped me along the way. Initial training on exfoliation was provided by Professor Oleg Kolosov and Dr Yameng Cao at Lancaster University.

Further training on heterostructure fabrication using the PPC/PDM dry stacking method was performed at the Technical University of Denmark (DTU). All the work involving the PMMA carrying layer method was performed at the National Graphene Institute (NGI), with the initial training on the technique provided by Dr Daniel J. Terry and Dr Matthew Hamer.

As a special mention, the project described in section 4.5.1 of this chapter, 'Edge detection algorithms for flake identification', started as part of a South-East Physics network (SEPnet) placement. This is a program in which a student in an organisation belonging to SEPnet works at NPL for three months during summer[224]. A first version of a code for image processing of 2D materials was developed by Catarina Areias(student) in python 2 under my guidance and supervision. Further updates to the code to python 3, the development of a new GUI and the addition of new features were done by me later on.

4.1 Introduction

Mechanical exfoliation is a technique that allows achieving mono- and multilayer flakes of high quality just by peeling off layers from a bulk crystal and depositing them on a new substrate. However, this method does not allow to deterministically create more complex structures such as stacks of different types of flakes. To produce such heterostructures in a controlled and reliable manner, it is necessary to use a completely new type of fabrication process known as '2D materials transfer'. In 2010, C. Dean et al. [31] presented the first demonstration of a vdW heterostructure formed by a monolayer of graphene transferred onto hexagonal boron nitride. This relatively simple device was a ground-breaking step forward, first corroborating the possibility to stack different materials together in a controlled manner, and second, highlighting the improved electronic quality of graphene deposited on hBN, which shown a 3-fold increase in electronic mobility with respect to graphene sitting on silicon oxide. Since then, the study of vdW heterostructures has rapidly expanded, allowing scientist to create complex structures and to explore intricate new physical phenomena. As briefly discussed in *chapter 1, section 2.2*, different methods for 2D materials and vdW heterostructures fabrication have been already explored, as for example the roll-to roll assembly of CVD grown materials for large scale applications. Nevertheless, in this work, the attention will be focused on deterministic methods based on polymeric stamps, which require the use of previously exfoliated flakes to build the stacks. These methods, typically generating $\sim\mu\text{m}^2$ area heterostructures, have demonstrated to be highly versatile, allowing to work with almost all known 2D materials, and providing an unprecedented level of control and accuracy in the manipulation of the individual layers. Clear examples of this are the intricate light emitting diode (LED) heterostructure produced by Withers et al. [225], with more than 10 stacked layers, or the elegant Moiré superlattices by Ribeiro-Palau et al. [226] in

which the twisting angle can be precisely aligned by rotating the top-most layer of hBN on top of the graphene channel.

Another important quality of these deterministic methods is their adaptability, low-cost and facile implementation. As for the basic equipment required, a microscope with long-working distance objectives, some micromanipulators, a polymeric matrix and the 2D materials of interest are sufficient. However, it is important to highlight that the transfer methods are not techniques carved in stone. The type of polymers employed, as well as the different methodologies used to transfer the flakes vary from place to place., presenting variations between research centres, and even between researchers working within the same laboratories [227–229]. In this thesis, two different dry transfer methods based on polypropylene carbonate (PPC) and polymethyl methacrylate (PMMA) were used, and will be described in detail later in *sections 4.6.2 and 4.6.3*, respectively.

4.2 Air effects on 2D materials: working in controlled environments

When considering the fabrication of 2D materials and their related heterostructures, it is important to keep in mind the two most important factors that can affect their performance (e.g. electrical or optical behaviour) negatively: (1) the presence of interlayer adsorbates, and (2) the environmental instability of certain 2D materials.

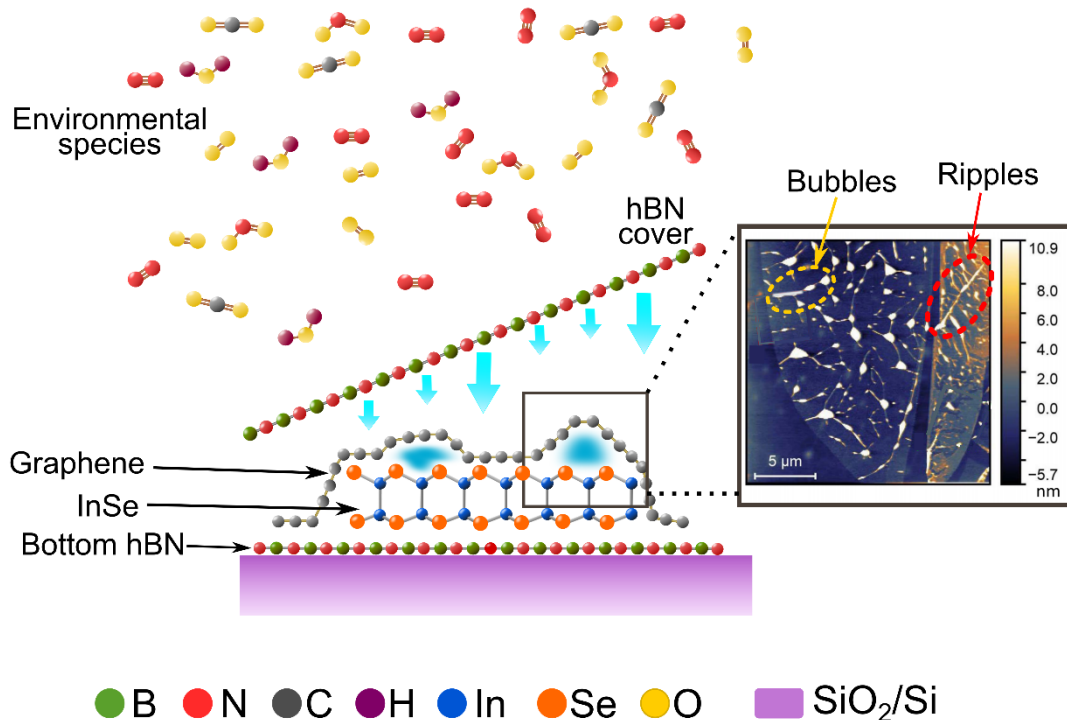


Figure 4.2. Schematic example showing the building process a random heterostructure formed by bottom hBN, with InSe and graphene sitting on top. As indicated by the blue arrows, a final layer of hBN will be deposited as the cover of the

structure, in order to produce a typical encapsulated device. Importantly, the aggregation of interlayer contaminants is depicted as dark blue conglomerates between graphene and InSe. It is important to highlight how the graphene surface conforms to the shape of this contamination as well as to the shape of the other layers of the structure (i.e. the InSe flake, for instance). On the top part of the figure, above the hBN cover layer, environmental species present in the air are also depicted, showing the variety of molecules that could interact with 2D materials. In the inset, an AFM image of a flake shows the formed bubbles and ripples with white contrast. This kind of features are common to all 2D materials, appearing as a result of the transfer process. A colour-coded legend has been placed at the bottom of the figure to provide visual guide of the type of materials used. Inset figure adapted with permission from [230]

First, interlayer contaminants appear as a result of the exfoliation process and the manipulation of flakes with polymeric stamps used to create the heterostructures. These residues, typically formed of hydrocarbon agglomerations, appear in the form of blisters, bubbles or ripples in between the vdW layers [231–233]. Such contaminants are one of the biggest limiting factors of the sample quality as they contribute to form an inhomogeneous surface potential, increasing the impurity scattering, and thus directly affecting the charge carrier mobility [234]. Although the PPC/PDMS and PMMA methods used in this work have demonstrated to be cleaner than others, finding interlayer contaminants is practically unavoidable [227]. Removal of the residual bubbles by contact AFM is a possible strategy, although it poses the risk of damaging the layers. This process is performed by slowly raster scanning the sample with the tip normal to the surface, and by increasing the applied force gradually. This way the contaminants are pushed out and accumulated at the sides of the scan. The force applied and the speed of the process highly depend on the material and probe employed. A practical example is shown later in *Chapter 6*[235].

Second, as a consequence of the very nature of 2D materials, composed only by superficial atoms, they are typically extremely sensitive to their environment. As shown in *figure 4.2*, our atmosphere is formed by several different molecules, such as oxygen (O_2), nitrogen (N_2), water vapour (H_2O), nitrogen dioxide (NO_2), carbon dioxide (CO_2) or carbon monoxide (CO), among others. These molecules tend to interact with 2D materials, doping them and modifying their electronic properties [236, 237]. Some of these changes will be discussed for graphene in more detail in *chapter 5*. However, the effect and amount of this modification varies depending on the material considered. Some cases are quite fast and dramatic, as for example, for black phosphorous (BP) [238–240], in which the changes are visible even with an optical microscope in just a matter of minutes after its exposure to air. Although, this is not the case for all 2D materials, in order to reduce the possible effects of atmospheric molecules to its bare minimum, all the steps of the fabrication, from exfoliation to deterministic transfer, are typically performed in cleanroom environments, where the air has been filtered, and the temperature and humidity levels are monitored, providing a clean, consistent and controlled working environment. Nevertheless, in order to implement functional devices that could be tested outside the cleanroom, an strategy that has been proved to work is to fully encapsulate thin layers with hBN, isolating this way the materials from their environment [241–243]. In this thesis, all the manipulation of 2D materials has been undertaken in cleanroom environments. In the case of InSe, which is highly

air-sensitive, exfoliation and transfer were performed in an argon filled glovebox (further discussed in *section 4.6.3.4*).

4.3 Substrate preparation

The selection of a proper substrate for 2D material's deposition is critical. As a consequence of the high surface to volume ratio presented by these materials, the interactions between the layers and the underlying substrates heavily affect their physical and chemical properties [244, 245]. In the following, the most common substrates for mechanical exfoliation used in this thesis are reviewed.

4.3.1 Silicon oxide substrate

Although several materials have been investigated so far to be used as a substrate, thermally grown silicon oxide on silicon wafers, typically 300 nm or 90nm SiO₂/Si, have become a standard substrate of choice for 2D materials deposition due to its advantageous properties: it can provide enhanced optical contrast for the thin layers (further discussed in *section 4.5*), it is pretty inert chemically, and it can serve as a good dielectric layer for back-gating devices [246].

Normally, prior to the 2D materials' deposition, a set of pre-treatment steps are applied to the substrates. First of all, as described in the left panel of *figure 4.3*, SiO₂/Si wafers are cut using a diamond scribe into smaller chips which are easier to work with. Normally, the wafers used in this thesis have either 3 or 4 inches in diameter.

Then, the substrates are cleaned. This step aims to avoid any kind of dust or contamination produced from the shipping, storage or cutting, to accumulate on the surface and therefore, affect the properties of the materials further deposited. Additionally, it increases the yield and size of the flakes, and minimises the amounts of trapped water and hydrocarbon species present between the flakes and the substrate [247]. The cleaning procedure employed in this thesis is based on the combination of ultrasonic cleaning with liquid rinse. The former is used to scrub the contaminants, while the latter is employed essentially to rinse away the residue and loosened particulate matter [248]. The process is performed as listed below:

1. Ultrasonic bath in acetone [249] at room temperature for 5-10 minutes.
2. Rinse with isopropyl alcohol (IPA) [250].
3. Ultrasonic bath in IPA at room temperature for 5-10 minutes.
4. Rinse with deionised water (DI water)
5. Dry with N₂ gas.

It is important to note that the transition between step 1 to step 2 should be done as fast as possible, avoiding the acetone to dry as that leads to the formation of chemical residues on top of the surface that are very difficult to remove.

If the surface contamination is bounded too strongly, the first step of the method is substituted by a bath of acetone at higher temperature ($\sim 55\text{ }^{\circ}\text{C}$) for 10 minutes, as rising the temperature of the solvents increases the effectiveness of the cleaning. These are standard procedures commonly applied in the semiconductor industry.

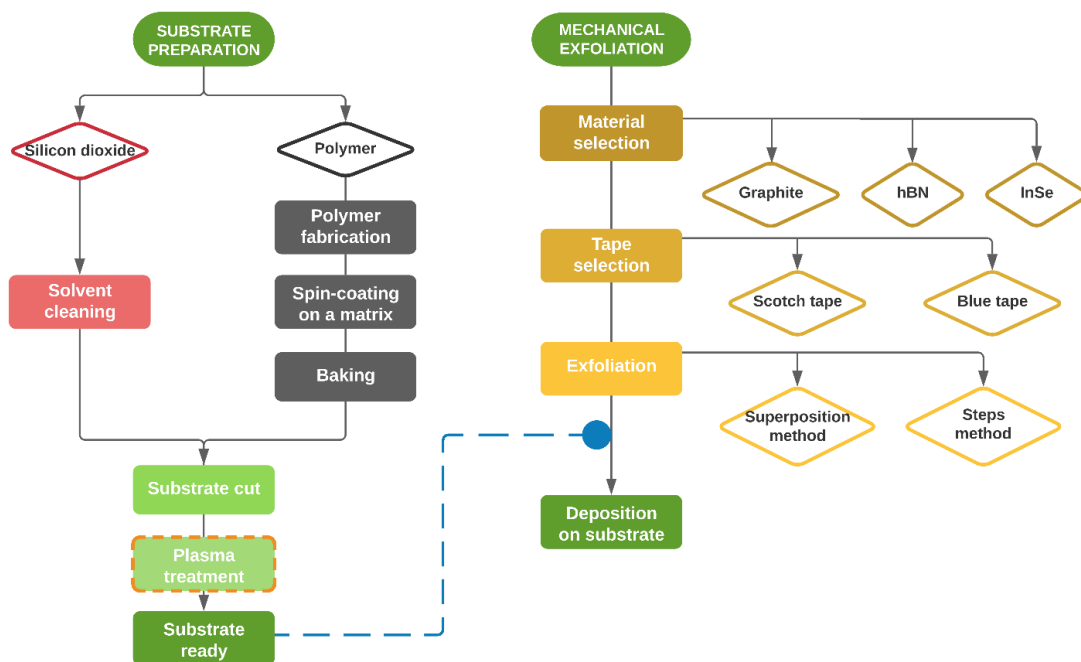


Figure 4.3. Schematic flowchart describing the substrate preparation and the mechanical exfoliation as independent processes only interlinked at the very end. This connection between the two is shown by the dashed blue line joining the prepared substrate with the deposition of the materials. For the substrate preparation process (left side), the steps concerning silicon dioxide and polymers are described in red and grey, respectively. The parts in green at the bottom are common for both types of substrates. However, the plasma treatment square is highlighted by a dashed orange border as it can be skipped in certain cases. For the mechanical exfoliation process (right-side), the steps are described by yellow squares while the different options per step are shown inside the diamond shaped blocks.

Following this solvent cleaning process, a plasma pre-treatment is applied to the chips with a Diener Electronics-FEMTO plasma asher model E [251], using a O_2 plasma at $\sim 100\text{W}$ for 5 minutes. This plasma treatment helps cleaning any extra contaminant that could remain on the substrate surface after applying the solvents, also increasing the adhesion between the materials and the substrate. The generated high-energy UV radiation splits any macromolecule (i.e. hydrocarbons) that could remain on the surface, and the oxygen radicals join the free chain ends of the polymers to form H_2O and CO_2 residues that are evacuated from the chamber. After the plasma treatment, the substrates are extracted from the chamber, and the previously prepared tapes are brought in contact with the exfoliated material facing the plasma treated surface. As the air normally carries tiny dust particles and other contaminants, it is advisable to bring the tape in

contact with the substrate as soon as possible, to avoid the re-deposition of contamination on the surface [252].

4.3.2 Polymer substrate

For certain applications, exfoliation can be also performed on polymeric substrates, especially if the final goal is to transfer the flakes to build heterostructures. The production of these substrates usually involves spin coating and baking the polymer on a matrix, typically silicon chips. As an advantage, exfoliation on polymer usually leads to a higher yield of thin flakes with respect to the exfoliation on silicon oxide. However, these flakes usually tend to be more contaminated. In this work, polymethyl methacrylate (PMMA) has been used as a substrate. This procedure will be further discussed in *section 4.6.3.1*.

4.4 Mechanical exfoliation

As described in *chapter 2, section 2.2*, mechanical exfoliation is one of the most widespread techniques for the production of 2D materials. In this work, graphene and other thin layered 2D materials (e.g. hBN, InSe, ...) were produced by micromechanical cleavage. However, although the main principle is the same, the exfoliation procedures vary slightly depending on the material and substrates considered, hence it is impossible to convey in a single description all the possible variations. The process used in this thesis, and summarized in *figure 4.3*, has been optimized for graphene and hBN, but covers most of the basic steps, and can be easily adapted to other materials. As it is stated in the figure, the full completion of the process can be divided in two differentiated parts: the substrate preparation, already discussed in the previous section, and the mechanical exfoliation of the flakes.

MATERIAL	SUBSTRATE	TAPE
hBN	90 or 300nm SiO_2/Si	<ul style="list-style-type: none"> • EPL-BT-150E-KL⁴ • ELP-BT-130E-SL • Ultron 1007R-6.0⁵
Graphene	300nm SiO_2/Si	<ul style="list-style-type: none"> • ELP-BT-130E-SL • 'Scotch tape'
Graphene	PMMA	ELP-BT-50E-FR

⁴ Tapes with reference starting as EPL are purchased from Nitto Denko

⁵ Ultron tapes are purchased from Ultron systems.

InSe	PMMA	EPL-BT-150E-KL
FeIn ₂ Se ₄	300 SiO ₂ /Si	ELP-BT-150P-LC

Table 4-1. Tapes used for exfoliation for different 2D materials and substrates

Below, the typical steps performed for exfoliation in this work are listed and described:

1. First, the material to be exfoliated is chosen.
2. Then, a suitable tape is selected considering mainly two factors: the relative adhesion strength and the amount of residue left on the surface. For this thesis, scotch tape and different types of 'blue tape' (as colloquially known) have been used as summarised in *table 4-1*. Specifically, 'blue tapes' adhesive films are common in Si industry for wafer dicing, and consist of a base polyvinyl chloride (PVC) film covered by a micron thick acrylic adhesive layer on top.
3. Once the desired tape is selected, two pieces of $\sim 2 \times 2$ cm² are cut. Their backing tape is peeled off to expose the adhesive surface.
4. A bulk crystal (see *figure 4.4*) is then positioned on top of the adhesive surface and pressed between the two pieces of tape.
5. After this, both tapes are peeled off from each other, cleaving the crystal approximately in half. To obtain thin crystals, this procedure is continuously repeated until the material has spread homogeneously on the tape, with the flakes being smaller and less shiny than the original bulk crystal. Depending on the material, two different procedures have been applied during this thesis to exfoliate the crystal, which will be referred from now on as superposition method and steps method.
 - **Superposition method:** The crystal is continuously exfoliated over areas in which the material has already been deposited, creating a concentrated area of flakes on the tape. This process is suitable for materials that do not tend to aggregate and overlap, such as hBN or graphene.



Figure 4.4. Bulk crystals of graphite, hBN and InSe. Grain boundaries in graphite and InSe can be observed. Scale bar: 1 cm

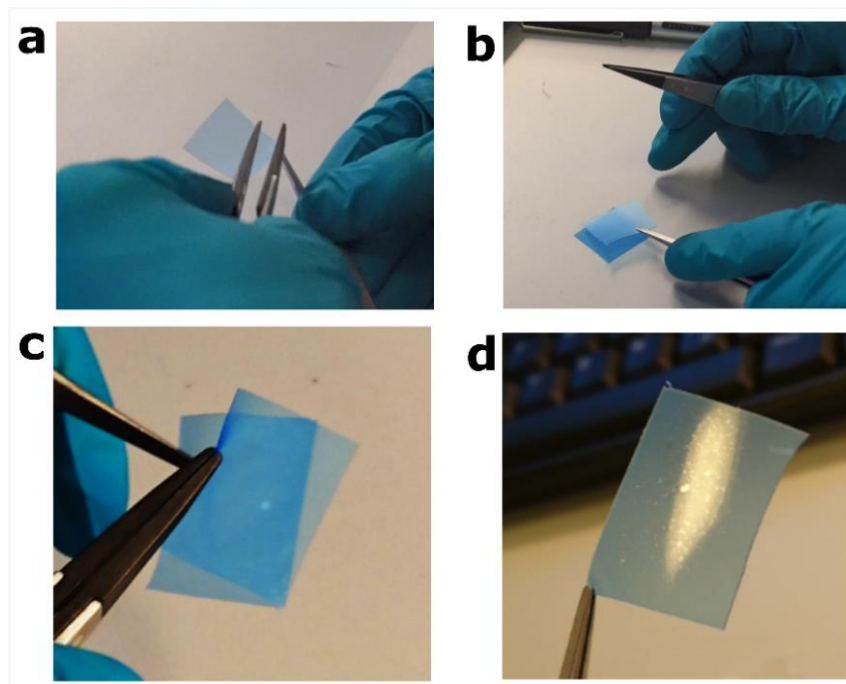


Figure 4.5. Superposition exfoliation process, with hBN shown as an example. **(a)** Cut two squares of tape and peel off the backing side to expose the sticky surface of the tape. **(b)** Deposit a crystal on one of the tapes, bring both of them together and press them. **(c)** Peel the tapes off and bring them back together. Repeat this process until the surface of the tape is fully covered of material as shown in **(d)**.

- **Steps method:** Each new exfoliation of the crystal is performed in a clean area of the tape, leaving localised patches with material around the surface. This avoids the excessive superposition of flakes and concentration of debris or small flakes on the substrate. This procedure is recommended specially for soft materials, such as InSe or its compounds, which tend to aggregate easily.

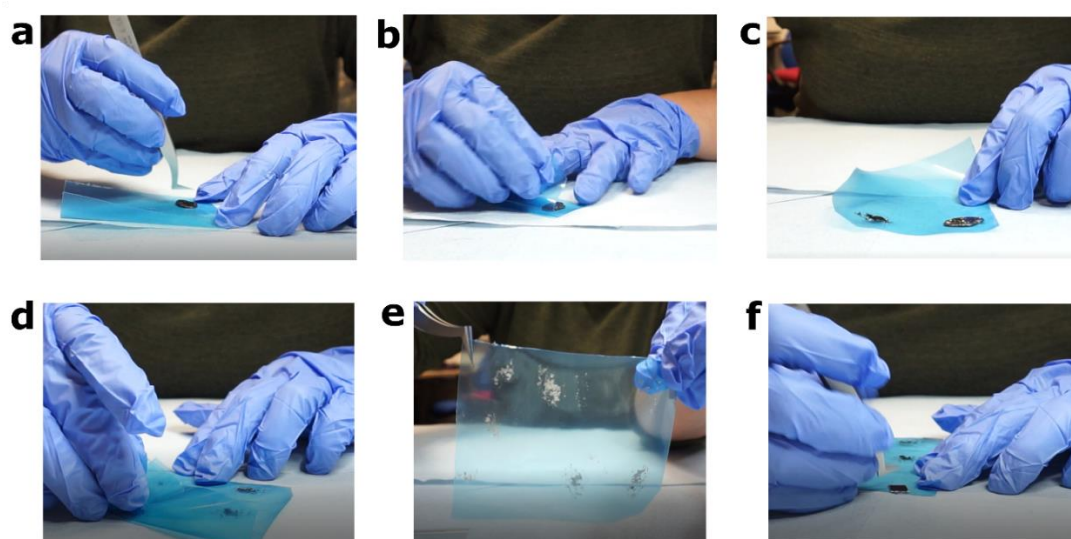


Figure 4.6. Step by step exfoliation process, with graphene shown as an example. **(a)** A bulk crystal is deposited on top of the sticky side of the adhesive tape. **(b)** Then, the tape is folded on top of the crystal and pressed down. **(c)** When peeling the tape off, few layers of crystal have attached to it, leaving a mark on the surface. At this point, the crystal is removed.

(d) The marked part of the tape is folded onto itself several times always on top of clean areas. (e) This leaves marks of thin 2D materials on different locations. (f) The substrate of choice is placed on top of the desired area and pressed down to enhance the transfer of material to its surface.

6. After exfoliation, the tape with the material is brought into contact with the substrate of interest, either a pre-treated silicon oxide chip or a polymeric substrate on silicon. Preparation of the substrate is described in *section 4.3*.
7. The transfer of materials from the tape to the substrate is enhanced by applying a vertical pressure downwards, just by pressing with the thumb or the palm of the hand, for approximately 1 minute. Lateral displacement of the tape during deposition does not lead to significant improvement in the number of deposited thin flakes. Increasing the vertical pressure leads to an increase in the total flake density but can damage the surface oxide layer and leave unwanted dust.
8. The tape is then left in contact with the substrate for several minutes (or even hours) to allow the materials to relax, increasing even further the adhesion with the substrate. Depending on the 2D material, tape and substrate considered, it is also possible to anneal the sample before removing the tape, as an additional strategy to increase the transfer yield of thin flakes on the surface of the substrate.
9. Finally, the tape is peeled off by pulling it very slowly, while forming an angle of $\sim 10 - 20^\circ$ with respect to the plane formed by the substrate.

This process usually leaves a random collection of flakes of different thicknesses and sizes, held to the surface by weak van der Waals forces. The thickness may vary from angstroms to few microns' thick crystals. The area of the deposited material is often on the order of few μm^2 , reaching exceptionally, sizes of mm^2 . The recipe for exfoliation can be tailored depending on the material, substrate and tapes considered, in order to increase the yield of thin materials deposited on the surface. However, it is worth noting that as a consequence of the random nature of mechanical exfoliation, the results are different for each attempt, and therefore, although samples can fit into certain statistics, they are not repeatable.

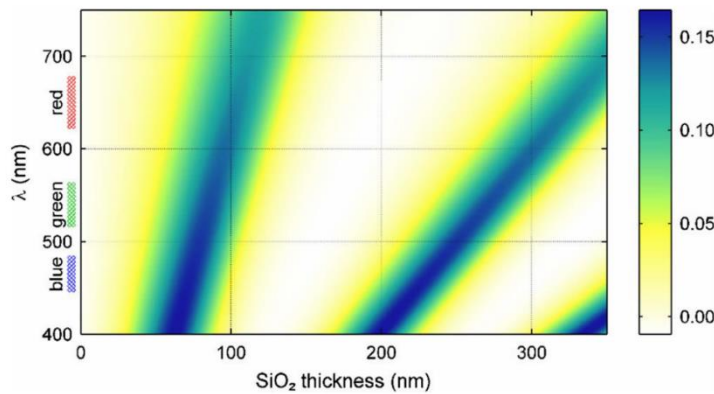
4.5 Optical identification

Optical microscopy in reflection mode is the most convenient way to find atomically thin flakes on a substrate. Other imaging techniques such as AFM or Raman spectroscopy, although being accurate at distinguishing thin layers from thicker ones, present a very low throughput and therefore they are rather unpractical and time-consuming for the task. In optical microscopy, crystals of different thickness can be distinctively identified based on contrast, by comparing the

light intensity reflected from the 2D layer, R_{2D} , with the intensity from the background substrate, R_{Sub} . This relationship is typically described with the equation:

$$C = \frac{(R_{Sub} - R_{2D})}{R_{Sub}} \quad (15)$$

The value of the contrast depends on several parameters, such as the substrate configuration (i.e. if it is a single or a multi-layered material), the refractive indices of the different materials, the wavelength of the incoming light, and the thickness of the conforming layers. The



interdependence of these parameters and the resulting contrast have been investigated

Figure 4.7. Optical contrast of graphene as a function of the wavelength and the silicon dioxide thickness. Different light wavelengths are represented with respect to the silicon oxide thickness. The values of the graphene contrast are calculated using the Fresnel formalism. Figure represented with permission from [253]

previously by different researchers using multiple interference theory based on Fresnel law. This formalism provides information on the intensity of the reflected light of a layered system (i.e. a 2D material layer deposited on top of SiO_2/Si wafers). A visual example of the interdependence between the flake contrast, the light colour and the SiO_2 layer thickness is shown in *figure 4.7*. Here, the optical contrast of graphene is represented by a colour scale, with blue being the maximum value, and yellow the minimum (i.e. invisible against the substrate). Based on this figure, the fact that 90 nm and 300 nm SiO_2/Si substrates have been so widely used can be better understood as these two thicknesses present maximum contrast for green light, which is also the peak of maximum sensitivity of the human vision. This reduces the tiredness of the eye during the time-consuming searching process [253]. The dependence of the contrast on the wavelength comes from the applied Fresnel formalism, which considers the refractive index of graphene to be a complex value, while the refractive indices of SiO_2 and Si are considered as wavelength dependent. More details on the mathematical formalism can be found in the following references: [253–255]. Just as a side note, due to the effectiveness of the Fresnel formalism in providing information about the contrast of the flakes in certain substrates, it has been widely applied to different materials besides graphene [95, 256, 257]. However, even in optimal conditions, the identification of certain thin flakes is still extremely difficult due to their low contrast. As an example, the wide bandgap insulator hBN, that is typically employed as dielectric substrate or as cover layer, shows $\sim 1\%$ contrast under white light when deposited on 300 nm SiO_2 substrates, making it undetectable under visual inspection [95]. As a reference, *figure 4.8* shows hBN

exfoliated on a multi-layered structure formed by PMMA/PVA/Si for different optical magnifications. The flake of interest, surrounded by a black circle in *figure 4.8(d)*, with a thickness of ~ 10 layers presents a very dim contrast, and it is barely visible for low magnifications. It can be safely assumed that thinner flakes will present even dimmer contrast and will require higher magnification objectives for their search, which results in increasing the time of exploration of a single substrate.

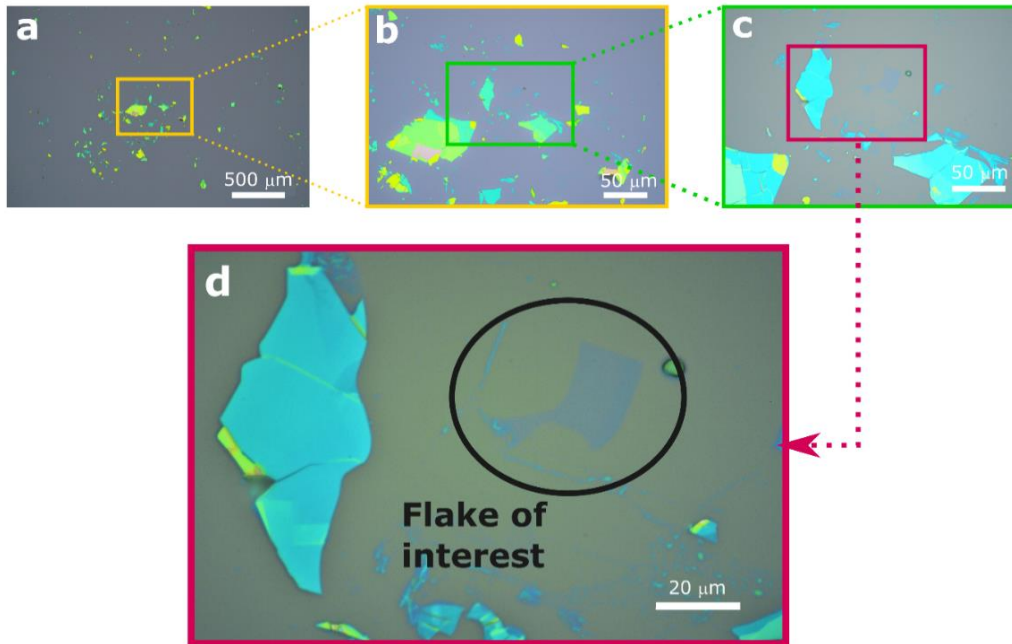


Figure 4.8. Exfoliated hBN on PMMA for different magnification objectives: (a) x5, (b) x20, (c) x50 and (d) x100.

In order to tackle these issues (i.e. the low contrast and the long exploration times), several strategies have been investigated to produce fast and in-situ solutions to increase the contrast:

- **Narrow bandpass filters** are typically incorporated right in front of the light source of the microscope. These optical elements absorb most of the incoming white light, allowing the transmission of only a small spectral region ($\sim 10 - 20$ nm) around a central wavelength specified by the manufacturer. Optical filter wheels or rails are commonly incorporated in dedicated microscopes for 2D material's inspection, providing access to different wavelengths. In this thesis, green bandpass filters (~ 550 nm) and blue bandpass filter (~ 470 nm) were used for graphene and hBN identification, respectively.
- **RGB channels:** This technique relies on the modification of the RGB values of specific pixels or areas within the image of a flake to enhance its contrast. Usually, digital images are composed of matrices of pixels containing spatial and intensity information. For colour images, the total intensity channel is divided in 3 components: red, blue and green. This technique can be done in-situ with a specialised software

while inspecting the substrate, using the Look-Up-Table (LUT), which employs a transfer function to map the RGB components. Also, it can be done after the image acquisition, although this last option is rather unpractical and rarely applied for fast identification.

- **Dark field (DF) imaging:** As explained in *chapter 3, section 3.2.2*, in dark field imaging only the light diffracted by the sample is collected to form an image. In the case of 2D materials, this technique is mainly employed to examine the contamination or cracks present on the surface of the sample, as any kind of defect emits light with respect to the main body of the crystal. During this thesis, DF imaging has been widely used with the purpose of assess the quality and cleaning level of exfoliated flakes as shown in *figure 4.9*, especially when these were going to be dedicated for heterostructure fabrication.

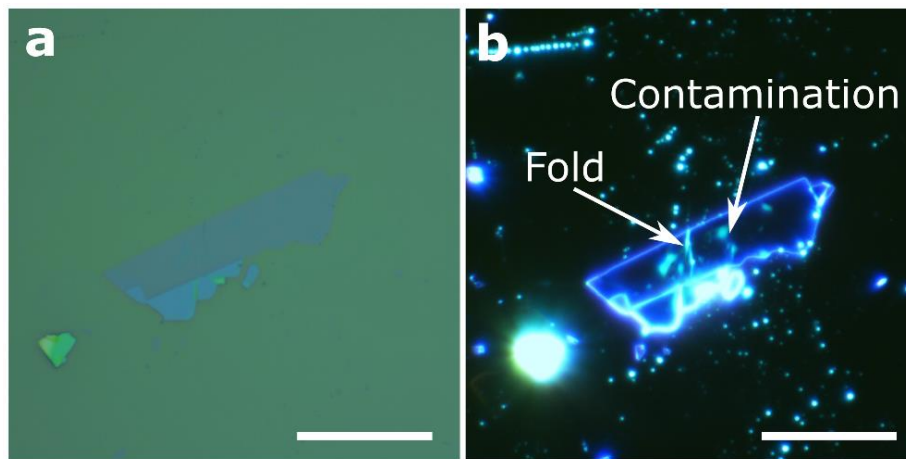


Figure 4.9. (a) Bright field image of hBN exfoliated on PMMA. (b) Dark field of the same hBN flake. In this mode, the folds and contamination appear bright

- **Polarised light:** In particular, InSe reflectance presents a response to out-of-plane polarised light that depends on the number of layers. This effect has to do with the the bandgap transition of few-layer InSe being inactive or extremely weak for in-plane polarized light. Further details are out of the scope of this thesis, but more information can be found in [258]. This method is not widely employed[259, 260], but in this thesis it has been used as shown in *figure 4.10*.for the identification of thin flakes of InSe, and other compound materials based on InSe.

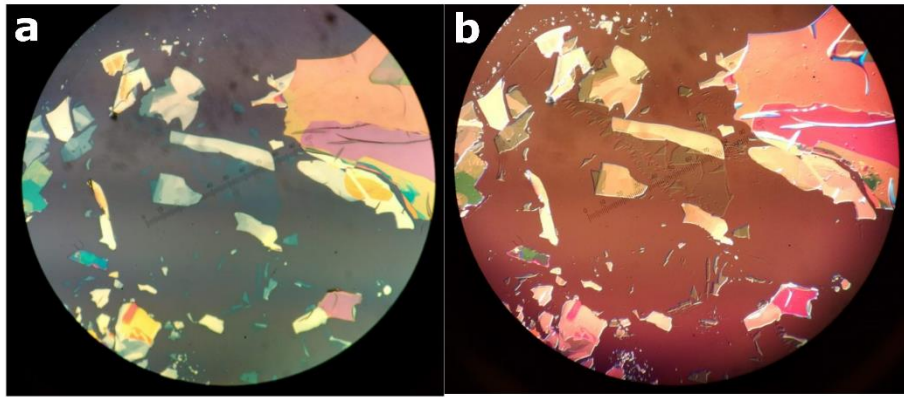


Figure 4.10. Optical images acquired with a $\times 10$ objective. **(a)** Bright field image of InSe with 10% Fe intercalated. **(b)** Optical image acquired under white light and using a U-AN360-3 Olympus rotatable analyser.

Following the initial optical identification, the number of layers of the flakes of interest can be confirmed by complementary techniques such as AFM, Raman spectroscopy or photoluminescence.

4.5.1 Edge detection algorithms for flake identification

As mentioned in the previous section, the process of 2D crystal ‘hunting’ under an optical microscope can be extremely time-consuming and challenging, especially if a flake with certain thickness or size characteristics is needed for an experiment. For these reasons, there has been a growing interest in achieving full automatization of the optical searching process. Part of the research has been dedicated to enhance the contrast of the 2D materials taking advantage of the digital imaging, specially focusing on the separation of the RGB contributions and the analysis of the intensity profiles [257, 260, 261]. On the other hand, other efforts were dedicated to the development of neural network systems, trained with thousands of images of exfoliated flakes, in order to implement a truly automated searching system [262, 263].

Inspired by some of these publications, a program was developed during this thesis for improved flake identification, based on the application of different edge detection algorithms to achieve better contrast of thin flakes of 2D materials. The program consists in a user graphical interface (GUI) that allows the user to upload an image, apply and tune different edge detection algorithms, and then save the resulting image. The rest of this section is a brief description of the edge detection algorithms, details of the Python code and its implementation in Visual Basic can be found in Appendix 1.

Edge detection algorithms are standard image processing tools, that have proven useful in different fields such as satellite [264, 265] or medical imaging [266], materials industry [267, 268] or object recognition [269]. Essentially, these algorithms detect the presence of boundaries or edges by comparing the values of the intensity of the different pixels composing an image, and

labelling any drastic change in the brightness as an edge. In order to do this, edge detection methods raster the image applying a specific mathematical transformation to each pixel. The mathematical transformation is normally a matrix, known as kernel, that is characteristic of the method employed.

In the case of this thesis, three algorithms (i.e. Sobel, Scharr and Laplacian) were used in the GUI, as shown in *figure 4.11*, where they appear together with the optical image of an example flake.

- Sobel operator: This operator rasters a double kernel, one for each direction: x ($Sobel_x$) and y ($Sobel_y$), as the ones shown below, along the image. As an effect, one of the kernels highlights the horizontal edges or gradients, while the other highlights the vertical. Combining both contributions using a certain weight function, w , produces a two-dimensional map of the intensity gradient at each point, as the one presented in *figure 4.11(b)*. This operation can be considered to be equivalent to the calculation of the partial first derivatives with respect to x and y.

$$Sobel_x = \begin{pmatrix} -1 & 0 & +1 \\ -2 & 0 & +2 \\ -1 & 0 & +1 \end{pmatrix}; \quad Sobel_y = \begin{pmatrix} +1 & +2 & +1 \\ 0 & 0 & 0 \\ -1 & -2 & -1 \end{pmatrix}$$

- Laplacian filter: this filter works by taking the second derivative of the image applying only one kernel, as shown below. In contrast with Sobel and Scharr, which have two kernels each this reduces the computing time significantly. When applying the Laplacian filter the edges are identified as areas of zero-crossing points. It provides very consistent results; however, it is much more noise sensitive than the other two methods.

$$Laplacian = \begin{pmatrix} 0 & -1 & 0 \\ -1 & 4 & -1 \\ 0 & -1 & 0 \end{pmatrix}$$

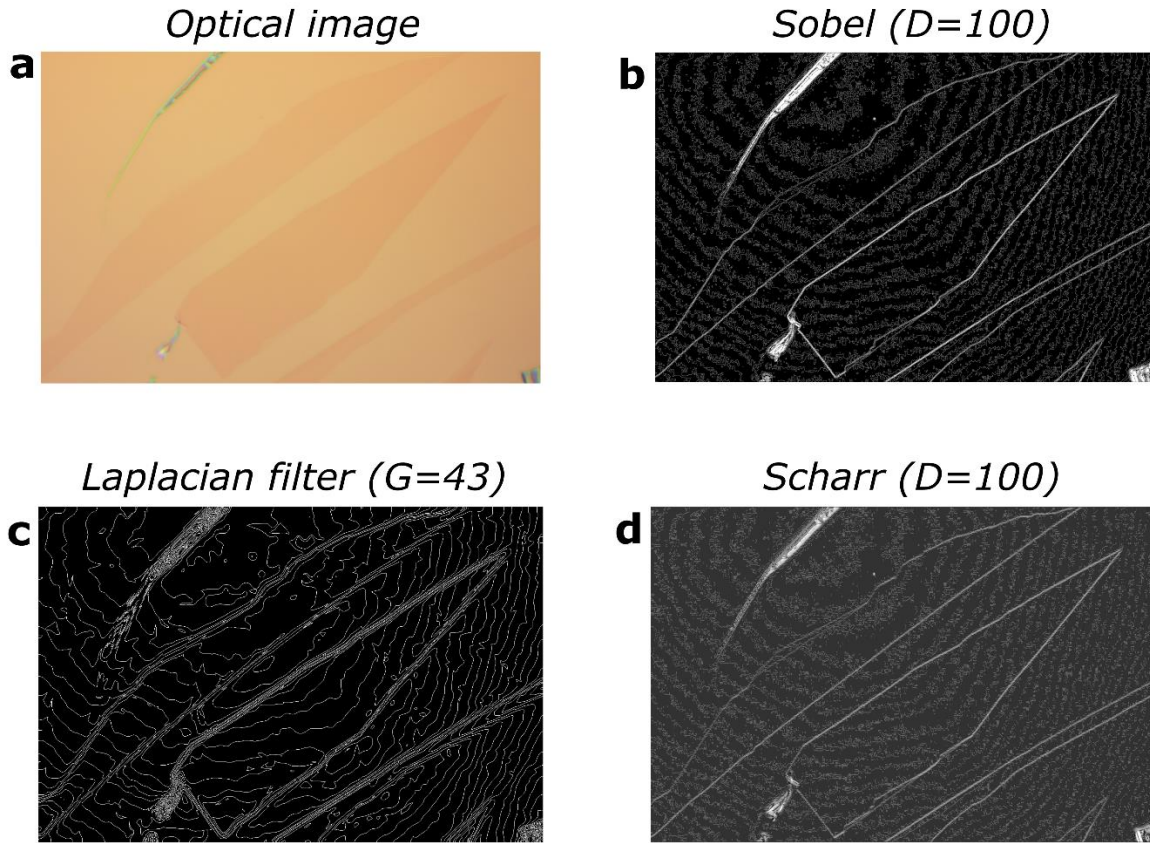


Figure 4.11. (a) Optical image of graphene monolayer flakes exfoliated on top of a PMMA/PVA/Si substrate. The image has been processed with three different edge detection algorithms: (b) Sobel, (c) Laplacian filter and (d) Scharr.

- Scharr operator: this operator works similarly to the Sobel operator. It also counts with a double kernel to scan both directions of the image, x ($Scharr_x$) and y ($Scharr_y$). In fact, as shown below, the kernel shape is exactly the same for both operators, however the difference lies in the coefficients and therefore in the sensitivity. The resulting images for each direction are combined with a certain weight after the operation, to produce a final image, as the one shown in figure 4.11(d). Mathematically, it can be understood as an approximation of the second derivatives of an image.

$$Scharr_x = \begin{pmatrix} +3 & 0 & -3 \\ +10 & 0 & -10 \\ +3 & 0 & -3 \end{pmatrix}; \quad Scharr_y = \begin{pmatrix} +3 & +10 & +3 \\ 0 & 0 & 0 \\ -3 & -10 & -3 \end{pmatrix}$$

These algorithms were tested by implementing a code in Python using Visual Studio. More details about the graphical user interface (GUI) and code produced can be found in *appendix 1*.

Regarding the results presented in *figure 4.11*, it is evident that all the algorithms did a good work identifying the boundaries of the flake. Similar results were obtained for almost all the images tested, which were mainly graphene and hBN flakes on two types of substrates: PMMA/PVA/Si

and 300 nm SiO₂/Si. These procedures should be extended to other materials in order to test their effectiveness. However, there are few common points to all the edge detection algorithms tested that require attention and further improvement: First, edge detection algorithms work with grey scale images, as only changes in intensity values are important for this kind of tasks. This implies that the images of 2D flakes had to be converted to grey scale, discarding the RGB channels, and therefore losing a lot of information in the process. It would be interesting to implement another section in the algorithm that could save the RGB values of the images to be applied for different processes. Second, as these methods work with derivatives, they are extremely sensitive to noise. This is more evident for the Laplacian operator, as it works with second order derivatives. One way to minimise this would be to include some pre-processing steps such as a Gaussian or a 2D median filter to smooth and clean the images prior to the application of the edge detection process [270, 271]. Third, the inhomogeneous illumination represents a problem for the application of all the filters, as shown by the concentric circles of varying intensity present in all the images in *figure 4.11(b-c)*. While writing this thesis, I found methods for correction of non-uniform illumination based on background subtraction, and this is the next improvement that would be implemented in the software [272].

4.6 Heterostructure assembly

Deterministic transfer techniques rely on the use of polymer stacks to manipulate thin flakes and build complex heterostructures based on 2D materials, via 'pick-up' and 'drop-down' procedures. Due to their relative simplicity, reduced levels of contamination and versatility, these transfer methods have become quite popular in recent years. Deterministic transfer techniques are typically employed for the production of vertical sandwich-like heterostructures, formed by layers of different materials, achieving yields up to 90%. Besides this high success rate in the production, this type of transfer is highly time consuming. It includes a significant number of steps covering from exfoliation to optical identification to the final transfer, that has to be performed independently for each of the layers. Furthermore, maybe more well-suited as an art than as a science, transferring of flakes and heterostructure building, typically requires highly skilled users fully dedicated to it, as each step requires precision, technique and patience. A small mistake in the transfer of one of the layers could lead to the total loss of the whole heterostructure, meaning that the whole process must be re-started. During this work, two different methods were used to fabricate heterostructures: the PPC/PDMS transfer method and the PMMA carrying layer method. Both procedures will be described in detail in the following sections.

4.6.1 Transfer system

Transfer station systems are used to stack 2D materials and produce heterostructures, providing high stability and accuracy through micrometric control during the building process. For this work, a dedicated transfer station was designed and built (see in *figure 4.12*)⁶. The system sits on the base of an Alicona Infinite Focus microscope (*figure 4.12(a)*) used for visualization of the flakes. Long-working distance objectives are required in order to leave some space, typically between 1-2 cm, between the objectives and the sample. This allows straight forward access for the transfer arm, and provides a large range of movement to perform any of operation.

The sample stage consists of a cylindrical copper piece (*figure 4.12(b)*), which is screwed into a micrometer manipulator (Mitutoyo, N° 148 – 205)[273] that provides movement range of the sample in the XY plane (*figure 4.12(c)*). A ceramic hotplate is built-in the Cu sample holder structure providing temperature control up to 150°C via a current source (*figure 4.12(g)*). The temperature of the sample holder is measured via a Pt-100 attached to the ceramic hotplate and connected to a current source. The sample is held in place thanks to a hole drilled in the centre of the copper cylinder which is directly connected to a vacuum pump.

Flakes are lifted (pick-up) and released (drop-down) with polymer blocks attached to glass slides. These procedures will be described in detail in the following sections. The glass slides are held by a by a clamp (*figure 4.12(d)*), which is mounted on a base with 3 attached micromanipulators (Mitutoyo, N° 148 – 801) [274] providing range of movement in the XYZ directions (*figure 4.12(f)*).

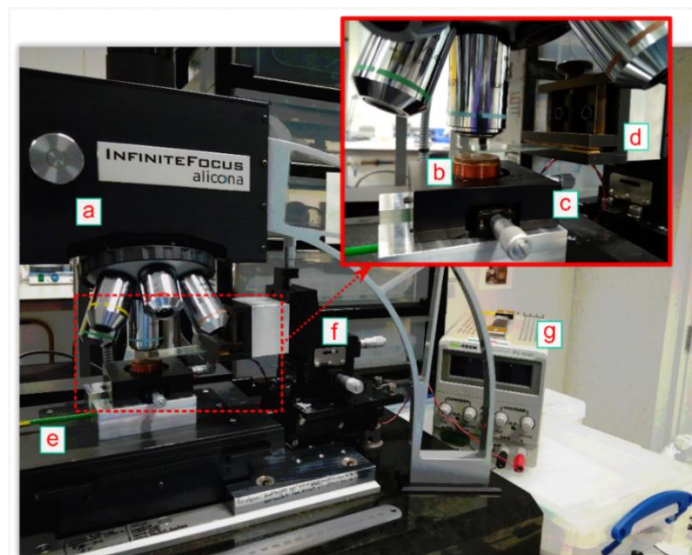


Figure 4.12. Transfer station system designed and built for this project. (a) Optical microscope for flake identification. (b) Copper sample holder able to reach high temperatures and with incorporated vacuum. (c) xy stage allowing with

⁶ The transfer station is in the cleanroom at the National Physical Laboratory (NPL), London

micrometric step control. **(d)** Glass slide holder. **(e)** Vacuum tube connecting the bottom of the sample holder with the vacuum pump. **(f)** xyz micromanipulator base allowing control of the glass slide position. **(g)** Current source providing temperature control of the sample by Joule heating

4.6.2 PPC/PDMS transfer method

In the PPC/PDMS transfer method, also known as vdW pick-up transfer method, flakes of different 2D materials are lifted (picked-up) and released (dropped-down) with the help of a top hBN layer held by a polypropylene carbonate (PPC) coated polydimethylsiloxane (PDMS) block, allowing to construct complex heterostructures[275]. PPC is used because it has a low glass transition temperature, typically between $\sim 25 - 40^\circ\text{C}$, allowing the PPC to flow as a viscous liquid when heated. Moreover, PPC also moulds itself to the surface when cooled down after heating as it is a thermoplastic, adapting to the shape of the flakes that is covering. This results in an increase of adhesion between the polymer and the 2D materials, which is highly advantageous for successful pick-up. The PDMS acts as a scaffolding, holding the PPC coating in place. The following sections review the fabrication process of the individual polymers, the PPC/PDMS block, and the transfer procedures.

4.6.2.1 Polydimethylsiloxane (PDMS) preparation

The PDMS is prepared from a two-part clear pack, Sylgard® 184 Silicone Elastomer Kit, purchased from Dow Corning. Both parts are mixed in a proportion 10:1 (Base:Curing agent). The thickness of the polymer block highly depends on the weight of the initial components in the mixture, and the size of the container used to cure it.⁷ Once both parts are accurately weighted, they are poured together into small beaker, and mix for 5 minutes using a plastic tool. The formation of undesired bubbles in the final polymer is avoided by mixing the components smoothly making circles at a constant speed. Following that, the mixture is degassed in a vacuum oven at $\sim 10^{-6}$ mbar for 10 minutes. This step allows the removal of any extra air trapped within the polymer. Then, the mixture is slowly poured into a Petri dish directly from its glassware container without the help of any extra tool to avoid the introduction of air in the mixture. Further degassing in vacuum is performed for 1 hour. Once the mixture is ready, it can be cured either at room temperature for 48 hours or within an oven at 150°C for 10 minutes. Both procedures were used during the development of this thesis giving similar results. Once the curing process is finished, a clear layer of PDMS sits at the bottom of the Petri dish. For further processing, the polymer is cut using a scalpel in $\sim 1 \times 1 \text{ cm}^2$ squares as shown in *figure 4.13(a)*.

⁷ For this work, 6.36 g of base and 0.64g of curing agent were mix together, giving a total of 7g. Pouring the final mixture in a 3.4 inch inner diameter dish gives as a result a polymer layer with thickness of $\sim 1-1.5$ mm.

4.6.2.2 Poly(propylene carbonate) (PPC) preparation

The PPC is purchased from Sigma Aldrich Chemistry with an average $M_n \sim 50,000$ [276]. The pack comes as a two-part solution containing anisole, a solvent, and the PPC. Both parts are poured together in a beaker in a proportion of 10:3 (Solvent:Polymer)⁸, and then mixed for 48 hours with a magnetic stirrer at room temperature. The stirring is performed inside a fume cupboard to evacuate the anisole that evaporates during the process. The resulting polymer is a highly viscous liquid, which is stored in UV protected bottles at $\sim 4^\circ\text{C}$.

4.6.2.3 PPC/PDMS polymer blocks

To start, one of the as-prepared PDMS squares is extracted from the matrix, placed in the centre a glass slide and subjected to an oxygen plasma treatment using a PVA TePLA plasma processing system, model IoN40, with 50 W for 10 minutes.

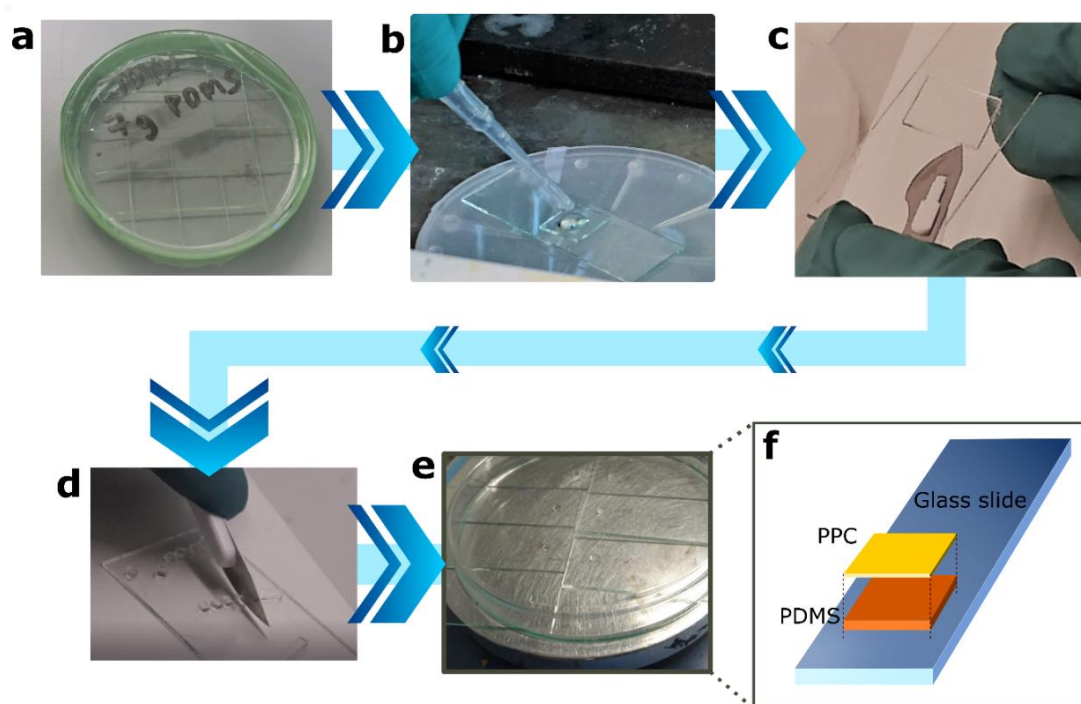


Figure 4.13. PPC/PDMS polymer blocks fabrication process. **(a)** PDMS cured in the Petri dish and cut into $\sim 1 \times 1 \text{ cm}^2$ squares. **(b)** Drop of PPC on top of the PDMS block prior to spin-coating. **(c)** Resulting PPC/PDMS block after spin coating and baking. **(d)** Process of cutting the PPC/PDMS into small cubes of $\sim 1 \text{ mm}^3$. **(e)** Once the polymer blocks are glued to the glass slide, these are baked at 110°C for 5 minutes to improve the adhesion between both polymers. **(f)** Schematic view of a glass slide with the PDMS and PPC attached to it.

This process will increase the adhesion between the two polymers, avoiding the PPC from delaminate during the posterior stacking of 2D materials. Immediately after extracting the PDMS from the plasma unit, a drop of liquid PPC is deposited on top of the PDMS square (see figure 4.13

⁸ For this thesis, 100 g of Anisole (the solvent) and 30g of PPC are weighted and mix together.

(b)), and spin coated at 1500 rpm for 1 minute. As a result, the liquid PPC spreads forming a flat layer that covers the PDMS block, which is then baked on a hot plate at 110 °C for ~90 minutes. This process must be undertaken inside a fume cupboard in order to safely evacuate all the remaining anisole vapours. Usually, the PPC not only covers the PDMS block but also spreads around the glass slide. This undesired extra material is removed with a scalpel, after the annealing process is finished and the sample is brought back to room temperature. The final PPC/PDMS block is cut in small cubes of ~1 mm² (*figure 4.13(d)*), which are then stuck into glass slides using a clear cyanoacrylate adhesive, which in the case of this work was Loctite superglue, purchased from RS components. The final glass slides are baked at 110 °C for 5 minutes (*figure 4.13(e)*). After the completion of this process, the polymer stamps are finally ready to pick-up and deposit 2D materials.

4.6.2.4 PPC/PDMS pick-up

Pick-up is the action of lifting a flake from the substrate in which it was exfoliated. With the PPC/PDMS transfer method, stacks are built from top to bottom, meaning that the first flake to be picked-up, is the top layer of the final stack, typically hBN. Below, the pick-up process for hBN deposited on SiO₂/Si substrate is described.⁹

1. The substrate with the exfoliated flakes is fixed on the sample holder via the vacuum chuck.
2. The glass slide with the PPC/PDMS block is loaded on the clamp of the transfer arm.
3. The flake of interest is placed in the centre of the field of view of the microscope using the xy micromanipulators controlling the sample stage. Then, the PPC/PDMS block is positioned on top of the substrate, almost parallel to it. A small tilt is beneficial for the transfer, as it helps controlling the process. Before starting the approach of the polymer block onto the surface, it is important to make sure that the area of the polymer that will enter in contact with the flake is clean of contamination and free of wrinkles or defects.
4. Once a clean area of polymer has been found, the micromanipulators controlling the clamp are used to slowly approach the glass slide to the substrate until the both surfaces enter in contact.
5. Due to the small tilt, one of the corners of the PPC will touch the surface first. The block is lowered further letting the PPC-sample contact area increase until the PPC front moves closer to the flake of interest. For this, it is advisable to use a x5 or x10 magnification objective, in order to visualise the whole area of the sample and the polymeric stamp

⁹ Note that for different materials the temperatures might vary.

while entering in contact. The contacted area is clearly visible under the optical microscope as there is a phase shift in the light passing through the polymer, which results in a different contrast (see *figure 4.14(b)*)

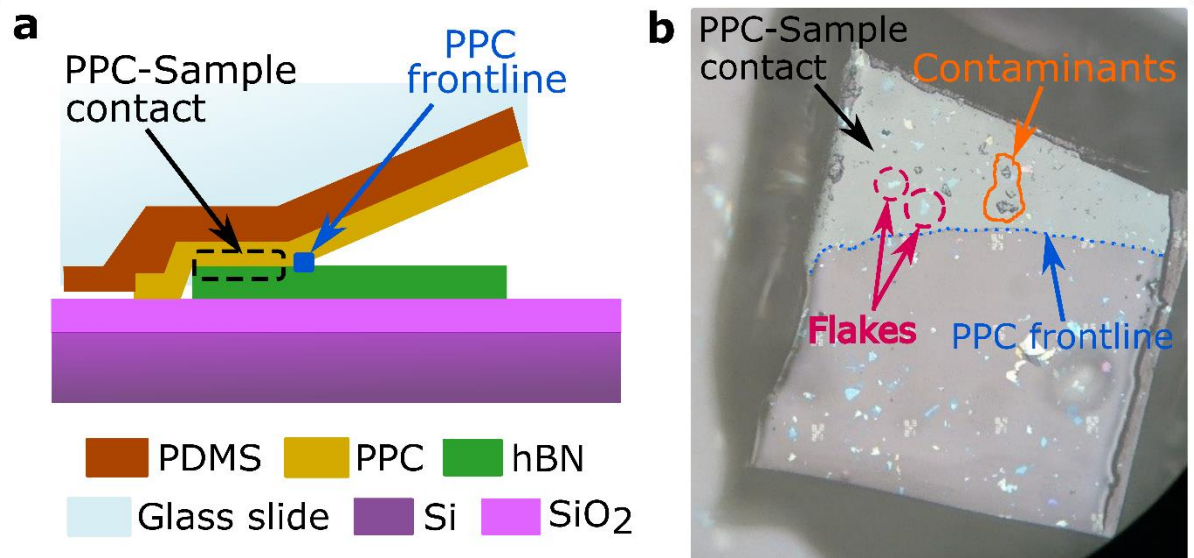


Figure 4.14. (a) Schematic diagram showing the PPC/PDMS block entering in contact with the sample. The position of the PPC frontline is highlighted by a blue dot. (b) Optical image obtained with a x5 magnification objective. The area in which the PPC has established contact with the sample (top-left corner) presents a different contrast, lighter, than the area in which the polymer is still away from the surface. The PPC moving frontline has been again highlighted in blue.

6. Then, the sample holder is heated up to 55°C to increase the adhesion between the flakes and the polymer block. As a result, the front line of polymer, shown as a dark blue dotted line in *figure 4.14(b)*, will move further by itself covering the flake.
7. Before pick-up, the area of the polymer in contact with the surface of the substrate is increased, until the polymer that is in contact with the surface covers an area of ~200µm around the flake. The contact process can be controlled by monitoring the movement of the frontline away from the flake of interest. It is important that the front-line moves smoothly as that would mean that the pressure and temperature of the system are homogeneous.
8. For the pick-up step, the heater is turned off, and when the temperature reaches ~40°C, the glass slide with the polymer is rapidly retracted using the Z-micromanipulator controller of the clamping stage (see *figure 4.12(f)*). It is important that the entire PPC contact area releases at once leading to a “snapping” motion.

As a result of this process the flake of interest is picked-up and remains on the PPC surface. The whole process is schematically depicted in *figure 4.15(a-d)*. However, there are certain points regarding the last step of the method that need to be considered.

Typically, if the whole PPC/PDMS block is brought into contact, it becomes very difficult to snap the PPC off the chip surface. Therefore, it is advisable to never surpass a contact area of ~50% of

the block as maximum. Another issue that might appear is that the PPC does not snap, but instead the front line of polymer retracts continuously or in small steps. When this happens, it is very likely that the flake is not going to be picked-up. This behaviour of the PPC appears often as a consequence of heating up the sample at an excessive temperature, moving the glass slide upwards too slow, or as a consequence of defective PPC, probably due to the fabrication process.

4.6.2.5 PPC/PDMS drop-down

Drop-down refers to the action of releasing a flake from the PPC/PDMS stamp onto a target flake or substrate. Typically, hBN is used as a top layer and deposited onto other materials, e.g. graphene, MoS₂, InSe, etc, covering and protecting them. Below, the process to release hBN on top of graphene is explained¹⁰.

1. The substrate with the exfoliated graphene sample is placed on the sample holder, fixed with the vacuum chuck and heated up to ~110°C.
2. Then, the glass slide with the cover hBN is loaded on the clamp and both flakes are aligned on top of each other using the xy movement of the stage and clamp without establishing contact. At this stage, the relative position of the crystals with respect to each other can be adjusted. A schematic representation of the process is shown in *figure 4.15(e)*. It is important to note that if the edges of the flakes are not aligned when entered in contact, it is not uncommon for the crystals to re-arrange themselves after the transfer into more energetically favourable positions, especially if the interfaces between them are clean. Contaminated interfaces tend to pin crystals in place.
3. The polymer stamp is brought closer to the substrate using the clamp micromanipulators until both surfaces enter in contact. As with the pick-up step, it is important to keep the glass slide slightly tilted at this stage, providing more control over the movement of the PPC front at high temperatures.
4. When both surfaces are in contact, the front of the PPC is brought close to the location of the hBN and graphene flakes by pressing down with the clamp micromanipulator. This step can be done relatively fast
5. However, the speed of the PPC front when progressing over the hBN and graphene has to be very slow. This avoids the formation of bubbles and helps squeezing out the contamination that can otherwise remain trapped between the hBN and graphene flakes

¹⁰ It is important to note that for different materials, the temperatures used might vary.

6. Once the flakes are both in contact, the area covered by the polymer is increased by pushing it down and moving its front-line (i.e. dark blue dotted line in *figure 4.14(b)*) further away, until the area covered by the polymer is $\sim 200 \mu\text{m}$ away from the flakes.
7. The stack is then left to rest at high temperature for $\sim 5 - 10$ min to ensure good adhesion between the layers.
8. Finally, the temperature is reduced to $\sim 70^\circ\text{C}$, as depicted in *figure 4.15(f)*, and the polymer is removed very slowly, especially when being retracted from the area in which the heterostructure is located. This process might take several minutes.

Once the polymer is retracted, the heterostructure remains on the surface of the substrate. To increase the adhesion between the layers, the chip is baked at 170°C for 30 minutes, either in environmental conditions or in vacuum, as shown in *figure 4.15(g)*. As a result of this annealing process, any contamination or air trapped between the layers will aggregate forming localised clusters and therefore, increasing the flat clean area of the heterostructure. Bubbles are generally unwanted as they deteriorate the electronic and optical properties of the heterostructures, compromise the van der Waals interlayer adhesion between the flakes, making further pick-up steps more complicated, and usually are filled with unknown contamination.

Once the baking process is finished, the pick-up and drop-down cycle is repeated sequentially in order to add more layers to the heterostructure until it is completed. However, the risk of failure is naturally increasing with the number of steps undertaken, especially due to unwanted folds or cracks that can appear on the flakes.

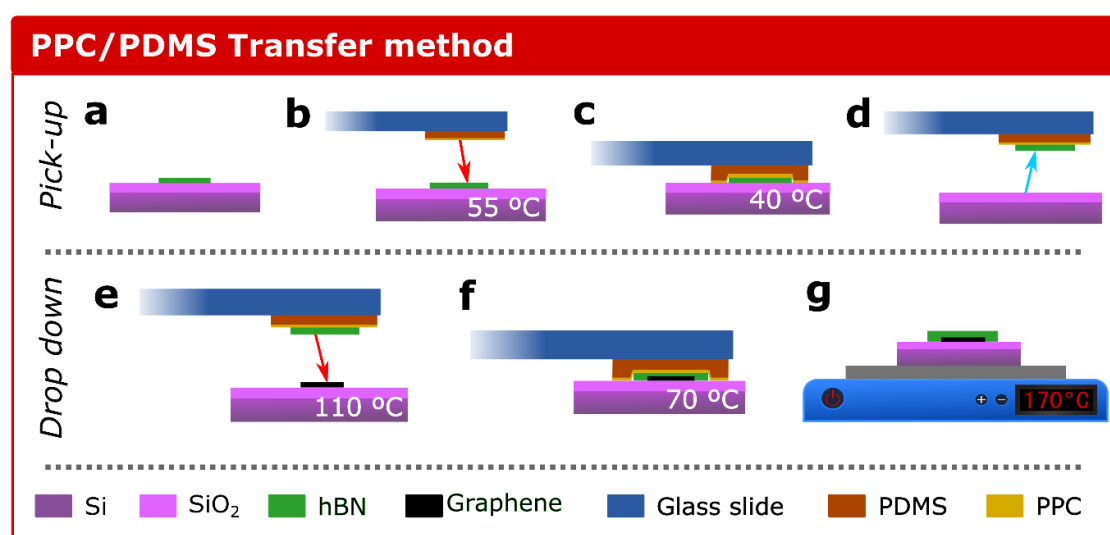


Figure 4.15. Schematic depiction of the PPC/PDMS transfer. Pick-up steps start with: (a) the material of interest (hBN) exfoliated on the substrate of choice (e.g. 300 nm SiO₂/Si). (b) Then, the substrate is heated up to 55°C, and the PPC/PDMS is brought closer to the surface. (c) When the PPC is in contact covering the flake of interest, the temperature of the substrate is reduced to 40°C. (d) The polymer is then removed out of contact by doing a “snap” movement, picking-up the flake from the substrate. The next step in the heterostructure fabrication is the drop-down: (e) a suitable graphene flake is found on the substrate and aligned with the hBN on the polymer. The temperature of the sample stage is set up to

~110°C. **(f)** Both flakes are brought into contact. At this point, the temperature of the sample holder is reduced to 70°C, and the tape is removed as slowly as possible, so the flakes remain on the surface of the substrate. **(g)** The chip is then baked on a hotplate at 170°C for 30 minutes to enhanced the adhesion between the layers and avoid future delamination.

4.6.3 PMMA carrying layer method

The PPC/PDMS transfer method is not applicable for thin and monolayer flakes, as thin flakes both are difficult to pick-up and tend to curl up on the PPC when heated. As an alternative method to overcome this issue, the PMMA carrying layer method [79] is a recommendable and robust technique of transfer suitable for flakes of all thicknesses. This method relies on polymer stacks formed by Polyvinyl acetate (PVA), a water-soluble polymer used as an adhesion layer, spin-coated on top of a silicon wafer, covered by polymethyl methacrylate (PMMA) as a top layer. The method, summarised in *figure 4.16*

4.6.3.1 PMMA/PVA/Si substrate preparation

To start, a 4-inch test silicon wafer is cleaned by rinsing it with acetone, IPA and DI water, in this order, and then dried with N₂. Once cleaned, a layer of 3% 50K PVA, dissolved in H₂O, is spin coated onto the wafer. This is followed by a baking process at 130°C for 5 minutes. After the wafer cools down back to room temperature, a layer of 8% 950K PMMA, dissolved in anisole, is then spun on top of the wafer, covering the PVA layer. Finally, the structure is again baked at 130°C for 5 minutes, and finally, left to cool down back to room temperature. The spin coating recipes are specified in *table 4-2* below, and the steps of the process are depicted in *figure 4.16-1(a-c)*.

POLYMER	SPIN SPEED (rpm)	SPIN ACCELERATION (rpm/s)	$t_{spin}(s)$
PVA	3,000	7,000	90
PMMA	4,400	7,000	120

Table 4-2. Spin coating recipes for PVA and PMMA fabrication

The thickness of the polymer layers was measured using a Bruker's DEKTAK® profilometer, resulting in a total value of ~640 nm, with individual values of the PVA and PMMA being ~54 nm and ~580 nm, respectively.

4.6.3.2 PMMA membrane fabrication

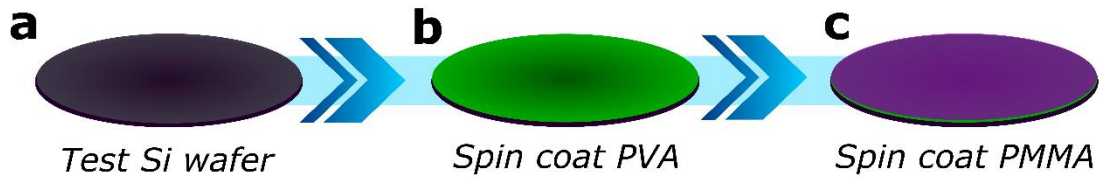
The PMMA/PVA/Si wafer is then cut into small chips of ~2 cm² using a diamond tipped hand scriber, as shown in as shown in *figure 4.16-2(d-f)*. Prior to mechanical exfoliation, the wafer is re-heated at 130°C for 1 minute to increase the adhesiveness of the PMMA surface. Immediately after the baking is finished, the tape containing the exfoliated material is pressed onto the PMMA

surface. For optimal results, follow the exfoliation steps from 6-8 as described in *section 4.4*. After the tape is removed, the wafer can be searched using optical microscopy. Identification of suitable flakes was done using a Nikon Eclipse LV100ND, with the aid of the software NIS-Elements BR. The exfoliation process is shown schematically in as shown in *figure 4.16-3(g-h)*. Once a flake with the correct size, shape and thickness has been identified, the polymers are processed in order to create a membrane.

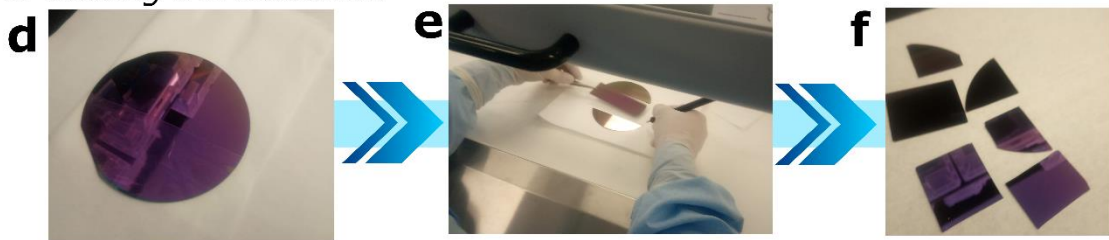
1. The chip is fixed on an optical microscope's specially designed sample holder with a vacuum chuck.
2. The flake of interests is placed in the centre of the field of view of a long working distance x5 magnification objective.
3. The surface of the PMMA is scratched following the contour of the x5 magnification objective, forming a circle of exposed PVA of ~5 mm of diameter around the flake, as shown in *figure 4.16-4(i)*. The scratching is performed using a sharp tool, such as a pair of tweezers.
4. Drops of DI water are then applied to the exposed PVA, which starts dissolving. As the hydration process continues, and therefore, the PVA dissolves, the water keeps propagating underneath the PMMA until a circular membrane is left floating freely. This step is depicted in as shown in *figure 4.16-4(j)*.
5. After the total detachment of the PMMA membrane from the PVA/Si substrate, the chip is carefully immersed in a beaker with DI water forming a shallow angle, as shown in *figure 4.16-5(m)*.
6. When the PMMA membrane comes into contact with the water surface, it comes off from the substrate and remains floating. The rest of the chip is then removed. At this stage, it is very important to avoid any contact of the water with the upper surface of the membrane, where the flake is located.
7. Meanwhile, a stainless-steel holder, known as 'plectrum', is pre-treated before being used to pick up the membrane from the water, as shown in *figure 4.16-5(n)*. The thin part of the plectrum, where the circular hole for holding the membrane is located, is immersed into liquid 3% 950K PMMA, and then baked on a hotplate at 150°C for 10 minutes to dry the PMMA. The purpose of this step is to enhance the adhesion between the membrane and the plectrum.
8. Finally, the membrane is carefully "fished out" using the circular open end of the plectrum and left to dry on a hotplate at 90°C for ~7 minutes. This helps evaporate any extra water remaining on the rear of the PMMA membrane, and causes it to tense.

PMMA Carrying layer method

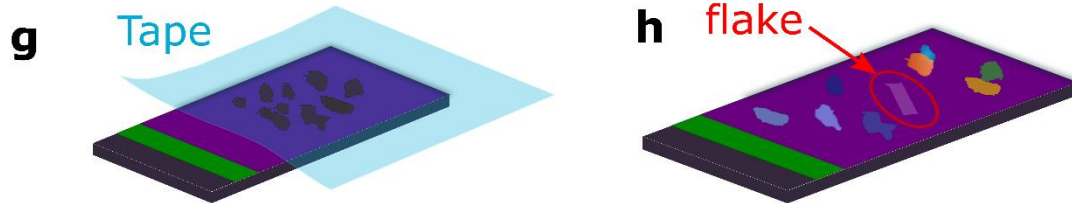
1. PVA/PMMA/Si substrate



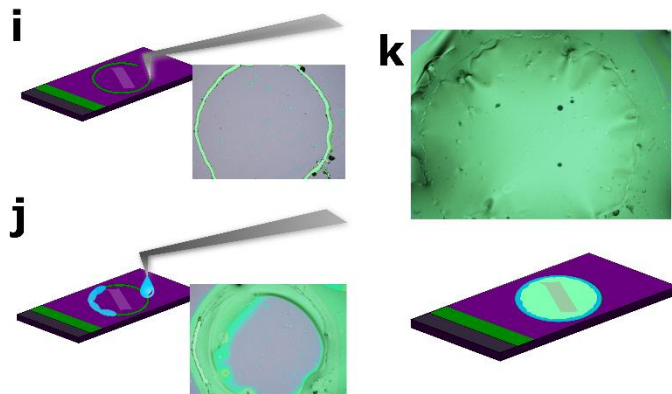
2. Cutting the substrate



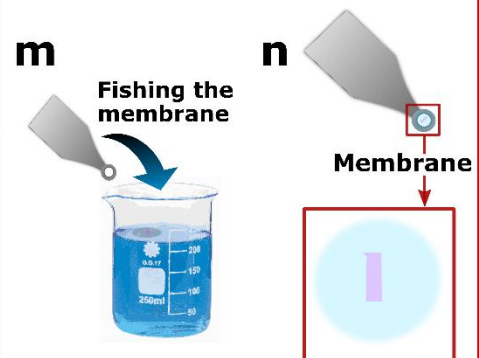
3. Exfoliation of 2D materials



4. PMMA membrane fabrication



5. Membrane fishing



Legend: PMMA PVA Test Si

Figure 4.16. Schematic depiction of the PMMA carrying layer method. **Step 1.** Wafer substrate preparation. **(a)** Initial test Si wafer. **(b)** PVA spin coated on top of the test Si wafer. The PVA is a water-soluble polymer **(c)** PMMA spin coated as a final cover layer. **Step 2.** Cutting the substrate. **(d)** Picture of the final PMMA/PVA/Si substrate. **(e)** Cutting the substrate with diamond scribe. **(f)** Final chips ready for exfoliation. **Step 3.** **(g)** Exfoliation of the 2D materials on the PMMA. **(h)** Find a suitable flake on the surface via optical microscopy. **Step 4.** **(i)** Scribing of the PMMA (purple) leaving the PVA exposed (green). **(j-k)** Process of hydration of the PVA. **(l)** Optical micrograph of the PMMA membrane. **Step 5.** **(m)** Fishing the membrane on the water using the plectrum. **(n)** Plectrum with membrane attached. As shown in the detail, ideally, the flake should sit on top of the membrane.

4.6.3.3 PMMA transfer

After the preparation of the membrane described in the previous section, the next stage is to transfer it onto a substrate or onto another crystal. As specified above at the beginning of the chapter, all the PMMA transfers were performed using the transfer station at the NGI.

1. The plectrum is attached to the specifically designed transfer arm and held via vacuum, parallel to the sample, and with the flake facing towards it. The tilting of the plectrum can be accurately adjusted using specifically designed micromanipulators connected to it.
2. The substrate is mounted below the membrane on the sample holder and fixed using the vacuum chuck.
3. The flakes of interest, both on the membrane and onto the substrate, are identified using the objectives and optical filters available on the microscope. Both crystals are then aligned using the XY-micromanipulators under the 50x objective. The sample holder also has the capability to rotate the substrate, providing more accurate alignment.
4. Furthermore, to help with the transfer process, the relative position of the flakes can be highlighted using the NIS-Elements BR software, which allows to trace lines around the contours of the flakes, which highlights any displacement from their initial positions when approaching and allows to carefully adjust before transferring.
5. After both flakes are aligned, the hotplate is turned on and the temperature is set to 60°C to soften the PMMA membrane and help it to stick smoothly to the substrate in a controlled way. Lower (< 40°C) and higher (> 80°C) temperatures are not recommended as they lead to jolting effects and melting issues, respectively.
6. After the system has reached the correct temperature, the plectrum is slowly lowered using the z-micromanipulator until the two crystals are brought closer, remaining few microns apart.
7. A blunt object is then used to gently tap the PMMA membrane down until it sticks to the substrate. Special care has to be taken on this step as it is fairly easy to break the membrane apart if there is any kind of shaking or sharp unexpected movement. The adhesion of the PMMA and the substrate can be clearly observed optically as there is a phase difference between the contact and out-of-contact areas, as clearly seen in *figure 4.17(a-b)*. Once the PMMA sticks to a specific spot of the surface, the contact area will expand slowly.
8. At this stage, there are two possible routes to perform the transfer:
 - a. The first and cleanest method is known as the “stamp transfer method”. In this procedure, the membrane is mechanically peeled away, leaving the transferred crystal on the wafer, in a similar fashion as with the “drop-down step” described

for the PPC/PDMS method in section 4.6.2. Alternatively, for complex devices, it might be of interest to pick-up several flakes with the substrate using the same PMMA membrane. This is performed in a similar fashion as the “pick-up step” described above, but with the temperature of the hotplate never exceeding 80°C. This latter option requires the top crystal to be laterally larger than the bottom crystal to increase the chances of successful pick-up.

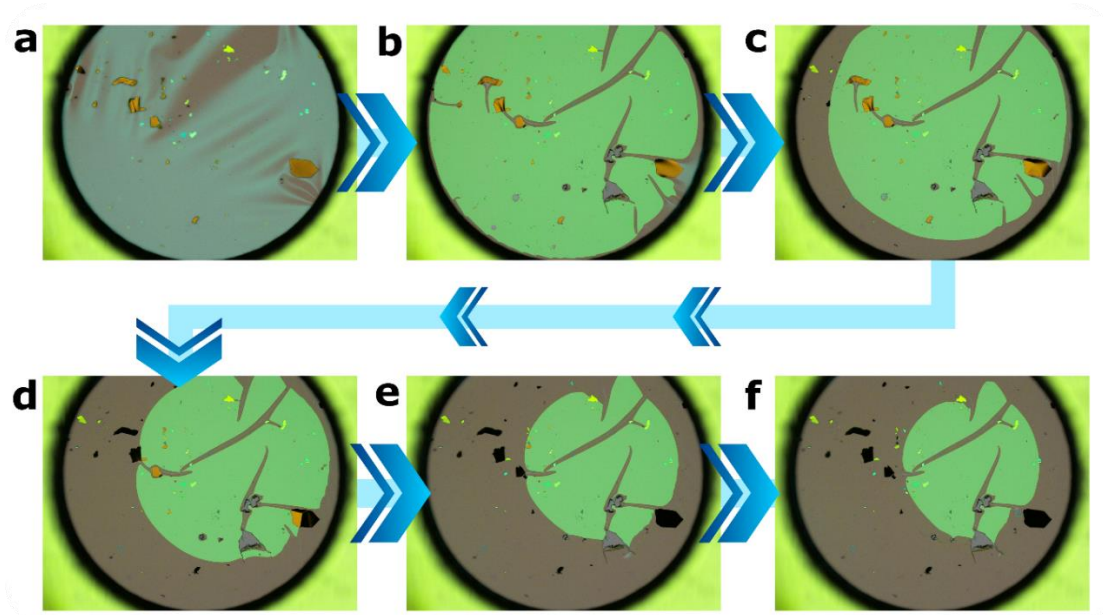


Figure 4.17. Membrane drop-down and deposition method. (a) Membrane on the plectrum observed with the x10 objective before contact. (b) Membrane in contact with the substrate. (c-f) Sequential process of membrane retraction

- b. The other option to produce heterostructures using this method is to essentially leave the membrane on the substrate once the flakes have entered in contact, and later remove the polymer using solvents. This method is not as clean as the first option presented, but it is convenient if there are some issues, i.e. if the membrane sticks too strongly to the surface of the substrate, if there are too many wrinkles or inhomogeneities or if the flakes are not transferring properly. Once the flakes have entered in contact and the membrane is attached to the surface, a pair of tweezers are used to cut the membrane forming a ring close to the edge of the plectrum, separating it from its holder. The sample is then beaked at 130°C for 30 seconds to encourage adhesion between the crystals and the substrate. Then, a thin layer of 3% 950K PMMA is spin-coated onto the surface. The purpose of this spun PMMA is to cover the curled edges of the PMMA membrane so that during the dissolving process, solvent doesn't rush underneath the cut membrane delaminating the crystals from the substrate. The sample is then placed in a beaker of acetone at room temperature for 30 minutes. This dissolves the PMMA

membrane leaving just the transferred crystal on the substrate wafer. The sample is then placed into IPA to remove the acetone and flash dried with nitrogen to remove any solvent residue.

4.6.3.4 Air effect on 2D-materials: Work in controlled environment.

In this project to address the problem of InSe degradation, an MBRAUN glovebox was used to exfoliate and transfer the material. The glovebox set-up, filled with argon, contains a transfer system (see *figure 4.18(a-b)*) and everything needed to mechanically exfoliate crystals including tapes and a hotplate. The environment within the boxes is continuously circulated through a gas purifier to remove oxygen and water. This purification keeps the levels of O₂ and H₂O below <0.1 parts per million (ppm), roughly equivalent to a vacuum of 10⁻⁴mbar.

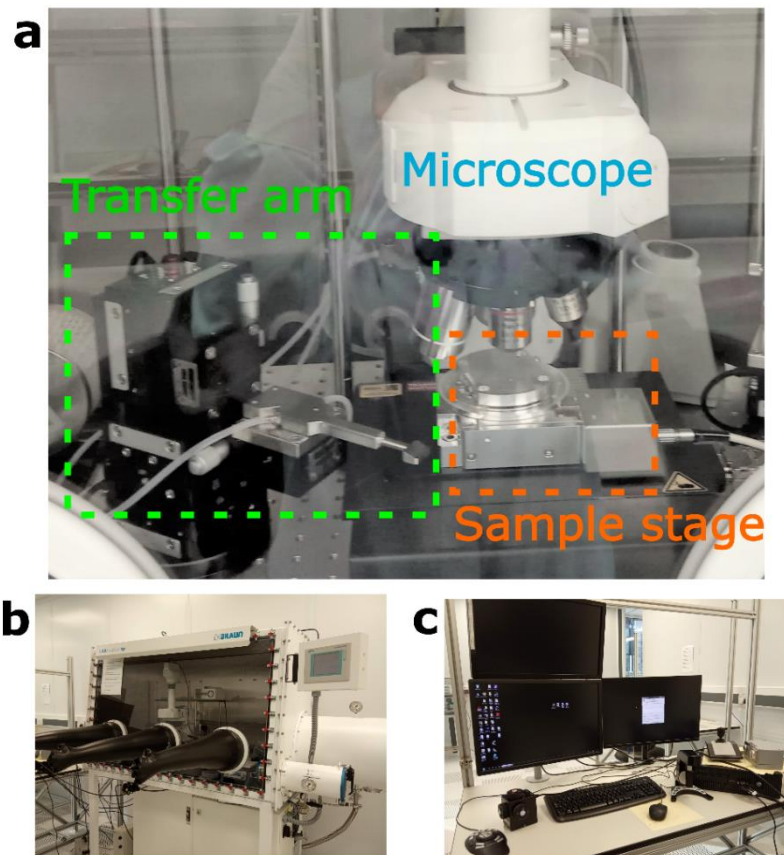


Figure 4.18:NGI transfer station placed inside a glovebox. (a) Motorised transfer system. The sample stage (orange) has a vacuum chuck to hold the substrates in place, heating and rotating capabilities. The transfer arm (green) is formed by a dedicated plectrum holder arm with a vacuum chuck and two micromanipulators to control the tilt of the plectrum. The microscope (blue) allows the optical identification of flakes and alignment. (b) Glovebox system (c) Micromanipulator controllers, optical zoom adjustment and computer for the control of the motorised transfer system.

One of the challenges of using a glovebox is that thick gloves (~1mm) are required to minimise gas diffusion, which highly complicates the manipulation of 2D materials. To overcome this issue, all the processes are remotely controlled using an external computer (see *figure 4.18(c)*), including the selection of optical objectives, the location of flakes and alignment, and finally the heterostructure stacking, which is done using the PMMA transfer method.

4.6.4 Comparison between different transfer methods

Both the PPC/PDMS transfer and the PMMA carrying layer methods described above present advantages and disadvantages. Normally, besides the equipment and resources available, selecting between one or the other is highly dependent on the characteristics of the final design of the heterostructure to be fabricated. It is rather difficult to produce a quantitative comparison, but in order to provide a clearer idea of the capabilities of each method, here a qualitative comparison is presented, considering different parameters, which are summarised below.

- In terms of difficulty, generally the PMMA carrying layer method requires higher skill in order to produce and manipulate the membrane throughout the whole transfer process. Failing in one of the steps could lead to the membrane destruction, meaning that the whole process from exfoliation, optical identification to membrane production, has to be re-started from scratch. On the contrary the PPC/PDMS procedure is much more straightforward. One of the most critical steps is the fabrication of the PPC/PDMS block, which can delaminate if the polymers are not properly attached. However, besides that, the technique does not involve higher risks of losing the whole heterostructure. If the user fails when picking-up or dropping-down flakes, the process can typically be repeated several times before the polymer degrades, leading to a much safer process and presenting a higher yield of success in building heterostructures.
- Regarding speed, the situation inverts. While the PMMA carrying layer method can be performed in a relatively short period of time for a trained user, the PPC/PDMS transfer drop-down step can take several minutes, even up to hours.
- Considering the cleanliness of the method, one of the main advantages of the PPC/PDMS transfer is that it can create large contamination free regions by pushing away all the contamination on the surface of the top hBN with the frontline of the PPC just by adjusting the speed. Furthermore, as only the first topmost layer enters in contact with the polymer, there is almost none intralayer polymeric contamination. As a counterpart, although the PMMA carrying layer is relatively clean, almost all the layers enter in contact with the PMMA, which could lead to intralayer residues. Additionally, the presence of residues on

the surface can be even higher, especially if the procedure described in *section 4.6.3.3-step 8b* is applied.



PARAMETERS	PMMA carrying layer	PPC/PDMS Transfer method	COMMENTS
Difficulty	High	Medium	The PMMA carrying layer method often requires high skill for the membrane production and manipulation.
Speed	Relatively fast	Fairly slow	Although both methods require to undertake several steps, the PMMA carrying layer turns out to be slightly faster for an experienced user point of view.
Contamination	Medium	Low	In the PPC/PDMS transfer method only the top hBN layer enters in contact with the polymer, leading to low intralayer residue.
Transfer of thin flakes (< 10 layers)			While the PMMA carrying layer allows the manipulation of flakes of any thickness, the PPC/PDMS transfer is constrained to work with relatively thick flakes.
Specific stack order	No	Yes	The PPC/PDMS transfer method requires to start the transfer always with an hBN top-layer, limiting the possible heterostructures to be performed.
Parallel work	No	Yes	Both methods allow the user to work in a modular way, saving time and effort.
Success rate	~70%	~78% ¹¹	

Table 4-3. Comparison between the PMMA stamp method and the PPC/PDMS hot pick-up technique.

- The versatility of the method is another important parameter to consider. It can be understood as the freedom that the technique gives the user in order to produce new heterostructures. Here, it is break down in three categories: the ability to manipulate thin flakes (< 10 layers), the restriction to a specific stack order and the possibility to work in parallel. In this sense, one of the main advantages of the PMMA carrying layer method is that it allows to transfer thin flakes (< 5 nm thickness), while with the PPC/PDMS based

¹¹ The percentages provided in the table account for the number of fully finished heterostructures and are based only in my own experience performing fabrication

procedure it is not possible to pick-up thin flakes from the substrate. An alternative could be to directly exfoliate the flakes onto the PPC/PDMS surface, however this often leads to undesired cracks or folds, and to additional contamination. So, if the future device application requires a thin layer of hBN or graphene, or any other material, the PMMA carrying layer transfer should be chosen over the PPC/PDMS method. Another limitation of the latter is that it requires the top layer to be always a relatively thick layer of hBN, therefore, limiting the production to encapsulated heterostructures. This is a consequence of the very nature in which the technique is based, which is taking advantage of the vdW interaction between the flakes. Finally, both methods are suitable for parallel work. It is possible for an experience user to prepare several PPC/PDMS blocks or plectrums with membranes and start transferring in series. In order to save even more time and effort, higher efficiency could be achieved by working in pairs or teams, with one of the users preparing the flakes and polymers, and the other just performing transfer.

- Finally, the success rate, as specified in *table 4-3*, accounts for the number of fully finished heterostructures fabricated using each of the methods. Note that this is just an estimation based on a personal experience, and only related to the transfer process. In those numbers it is not included the success rate on the polymer fabrication, the mechanical exfoliation, or the successful device fabrication using etching and contact deposition techniques.

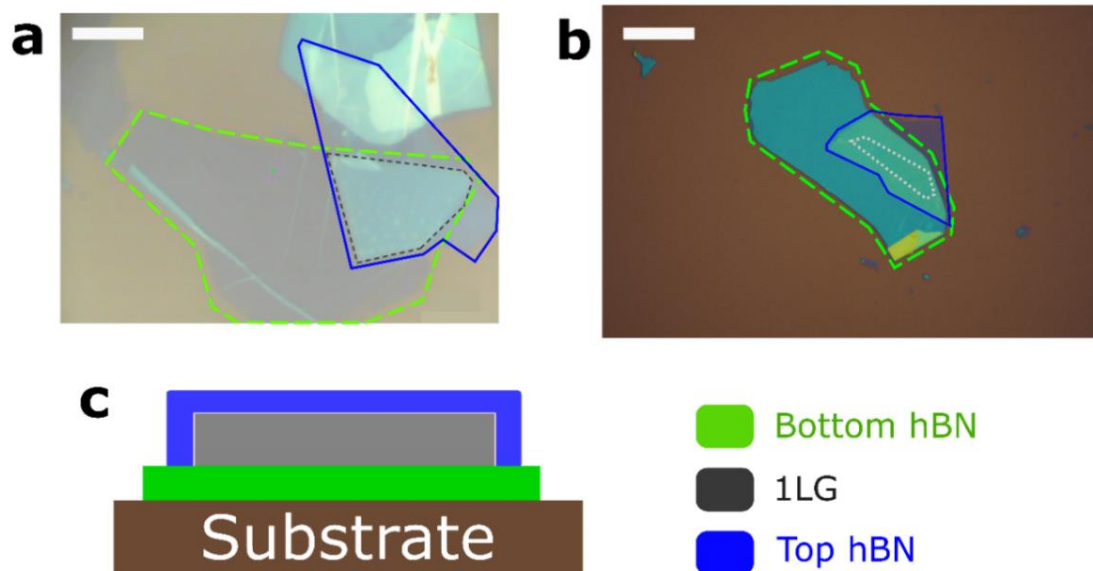


Figure 4.19. Example of encapsulated graphene heterostructures fabricated using the methods discussed here: **(a)** PPC/PDMS transfer method was used to produce this heterostructure that was finally employed by Vincent et al.[277]. Scale bar: 10 μm . **(b)** On the other hand, this heterostructure was fabricated using the PMMA carrying layer method. It was patterned into a device and used for thermal measurements with SThM, further discussed in chapter 7. Scale bar is: 20 μm . **(c)** Lateral view of the layers forming the heterostructures discussed on (a) and (b). The colour legend on the right helps differentiating the layers.

Two examples of encapsulated graphene heterostructures (i.e. hBN/Gr/hBN) produced during this thesis by the PPC/PDMS transfer and the PMMA carrying layer method are depicted in *figure*

4.19(a) and (b), respectively. It is possible to see there that while *figure 4.19(b)* is relatively clean, while *figure 4.19(a)* shows bubbles in the graphene area, and flakes adjacent to the heterostructure. Note that the encapsulated graphene heterostructure in *figure 4.19(a)* was successfully employed by Vincent et al.[277], to study strain in graphene and will not be discussed in this thesis; while the one in *figure 4.19(b)* was further processed into a device, and studied via SThM, and will be further discussed in *chapter 7*.

4.7 Device fabrication

The next step in terms of complexity is device fabrication from a heterostructure. Device fabrication consists of a series of techniques applied to achieve electrical connection to a certain heterostructure, which is also often shaped into a specific pattern or geometry. A simplified schematic of the steps and the order in which they are typically undertaken is depicted in *figure 4.20*.

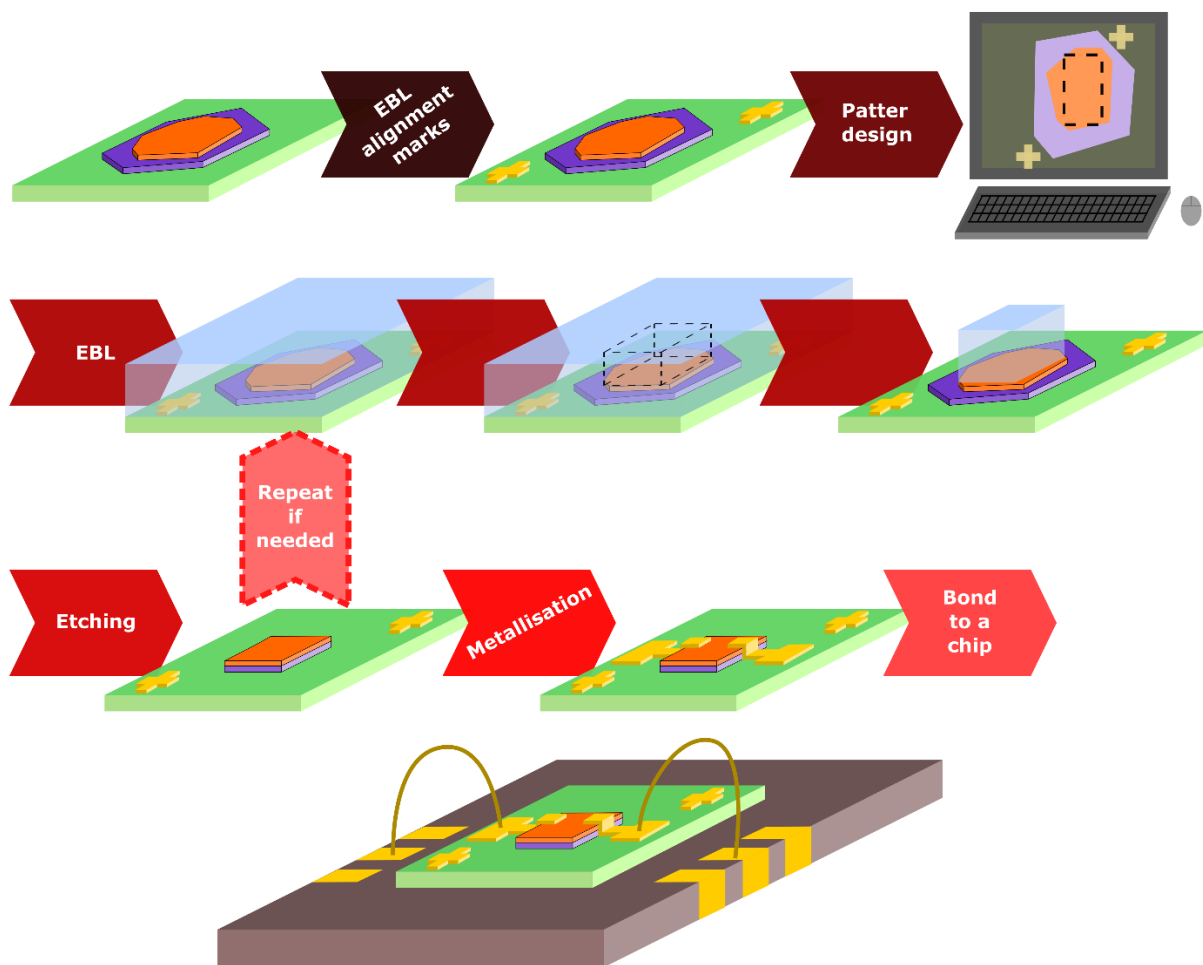


Figure 4.20. Simplified schematics of common steps undertaken to transform a 2D material based heterostructure into a device. It is important to highlight that the order of the steps and the number of repetitions might vary depending on the complexity of the device.

It is important to highlight that depending on the complexity of the device under fabrication, the steps might be repeated several times with certain adjustments, and not necessarily be performed just once. In fact, almost any microscale device or structure requires at least more than one masking step. A general description of the processes is given below:

- **e-beam lithography (EBL) Alignment marks:** In order to create a device, the exact position of the heterostructure features must be found and tracked through for each and every step of the fabrication process. For this purpose, small marks, called alignment marks, typically made of metal with a specific shape and size are written on the substrate chip. Normally, the marks are not isolated, but are formed of an array of crosses or circles around the structure of interest. The size and shape are selected considering the field of view (FOV) of the microscope on the lithography system used. The marks can be pre-written on the substrate of choice or can be placed on the substrate after the heterostructure has been fabricated on a preliminary EBL step. For the latter option, a .gds file must be created.
- **Pattern design:** to fabricate a device, the first step is to design its shape and draw the position of the contacts using a software program. There are many options for the latter and the selection of one of them is very much up to the researcher's preference. For this thesis, all the designs were .gds files made in Layout Editor [278]. To perform the design, also known as mask, a canvas is first created using a set of optical images of the flake or heterostructure with different magnifications. These images should include at least one alignment mark to allow aligning the images in the software, and later on, aligning the design with the flake during the lithography. Then, on top of the canvas, the design of the shape of the device and the contacts can be outlined, always taking into consideration the limitations imposed by the geometry needed and the posterior processing steps.
- **Electron beam lithography (EBL):** Initially, an electron sensitive resist is deposited on top of the chip containing the device. After finding the region of interest, the surface is exposed to irradiation by an electron beam following the pattern designed in the previous step. The exposure to the electron beam changes the chemical structure and therefore, the solubility, of the resist, which is then washed with organic solvents called *developers*. The resist can be either positive, which means that the regions exposed to the beam will be selectively removed by the developer, or negative, in which the exposed regions will remain, and the rest of the resist will be removed. In the case of this thesis, unless stated otherwise, all the devices have been fabricated using polymethyl methacrylate (PMMA), which is a positive resist. One of the main advantages of this technique is its resolution, with systems able to write patterns down to few nanometers. However, one important

point is that, EBL systems have the potential to damage 2D materials due to scattered electrons.

➤ **Etching:** This step serves to physically remove certain materials, finally shaping the device geometry needed by the experiment. For this, the etching mask is first created by EBL, and then the etching process is applied. As many of the processes described in previous sections, the type of etching employed is pretty much material dependent. In this thesis, two processes were employed to shape the devices:

- Reactive ion etching: this process is generally employed for graphene using a mixture of Ar and O₂, although for hBN, the Ar/O₂ plasma is not suitable, and instead CHF₃ and O₂ plasma should be used. Further details in RIE etching of encapsulated graphene heterostructures will be provided in *chapter 6*.
- Ion milling: this is a physical etching technique in which Ar ions generated in a plasma are accelerated towards a target, removing atoms from the surface of the sample upon impact. In this thesis, InSe was etched using ion milling due to the difficulty in etching it using RIE. More details are provided in *section 4.8* of this chapter.

➤ **Metallisation:** Metallisation is a technique used to deposit certain metals on a surface, allowing the creation of contacts, the definition of alignment marks, and top gates, among other applications.

In the case of this thesis, the focus will be set onto the creation of high quality 1D contacts to 2D interfaces, also known as edge contacts. This architecture, first presented by Wang et al. [279], has been widely

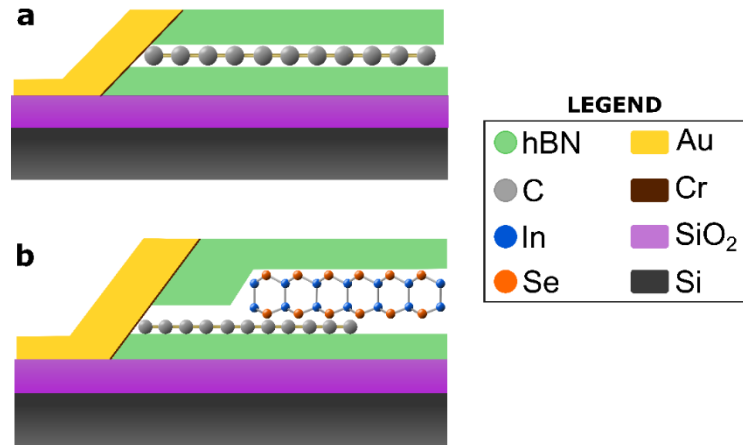


Figure 4.21. Schematic of 1D contacts created on: (a) an encapsulated graphene device, and (b) an InSe device with overlapping graphene. For the contacts, the metal used is represented in yellow, while the adhesion layer is represented as a dark brown line.

employed to achieve Ohmic contacts to graphene. For its fabrication, the sandwich formed by hBN/Graphene/hBN is etched on the side forming an angle with the normal to the surface, and the metal was deposited only contacting the edge of the graphene flake, but not its surface, as shown in **Error! Reference source not found.**(a). For other 2D materials, such as TMDCs or InSe, in which achieving Ohmic contacts has been a continuous challenge over the past years, this issue was overcome by overlapping

graphene together with the material of interest, and creating electrical connection directly to the graphene in an edge contact architecture as shown in **Error! Reference source not found.**(b) [280, 281]. However, regardless of the architecture chose, normally contacts in this thesis are formed by using gold, with a chromium adhesion layer. The latter is used to help the Au stick to the substrate, and it is typically very thin, as shown in **Error! Reference source not found.**. The specific thickness of the contact layers will be specified in posterior chapters when discussing the devices under study.

- Bonding to a chip: The final stage of the fabrication procedure consists in bonding the gold contact pads of the newly created device to the ones on the chip carrier, normally using gold wires. In this thesis, two different techniques were used to bond samples:
 - For the first method a wire-bonding machine was used. Essentially, this technique presses a gold wire into the surface of the contact pad applying a short ultra-sonic pulse with enough force to cause the wire and pad to adhere. One of the main advantages of this method is its precision, allowing the bonding of contacts with separations as small as $< 100\mu\text{m}$. However, one of the main risks offered by this technique is breaking the oxide insulating layer at the moment of contact, due to excessive pressure and a very small contact area of the needle. This can often inevitably lead to the creation of a short circuit between the contact on the surface and the usually conductive substrate, which leads to high leakage currents between contacts or the substrate (which can be grounded or act as a backgate electrode), and essentially kills the device. Due to this risk, bonding by hand is the preferred method used in this thesis unless otherwise stated.

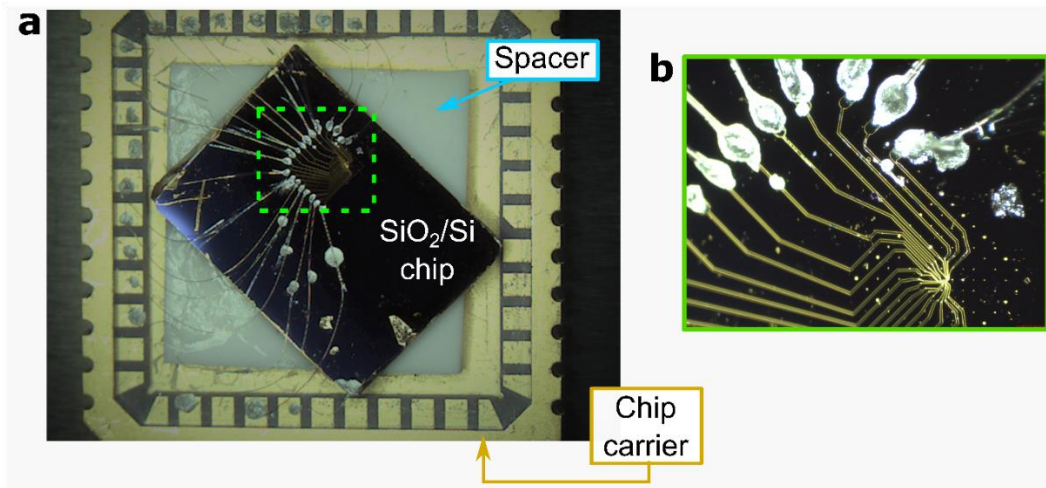


Figure 4.22. (a) Optical image of an encapsulated InSe Hall bar device fabricated on top of a 300 nm SiO₂/Si wafer (purple-black). The whole chip was mounted on top of an insulating mica spacer (white) to avoid direct contact between the Si bottom layer and the conducting Au layer of the chip carrier. Gold wires connect the Au pads from the device with the Au wires on the chip carrier, using silver epoxy (grey blobs) as bonding contact. In (b) an optical micrograph shows the detail on the bonding of the pads performed on the device.

- For the second method, bonding is performed by hand. To start, after the sample is glued to the chip carrier, silver epoxy is mixed and deposited on top of the gold pads in the sample. Then, using a small scalpel, pieces of gold wire are cut with enough length to join together the gold pads in the sample and the pads on the chip carrier. The gold wires are then joined to the epoxy, and then the system is left unperturbed until the joint is firm, which pretty much depends on the curing properties of the epoxy used. Then, the process is repeated for the pads on the chip carrier: a bit of silver epoxy is deposited on top, and the free ends of the Au wires are attached to those. The maximum separation of contact pads when hand-bonding is limited to around 100-300µm depending upon the skill of the bonder. An example of a bonded device is shown in *figure 4.22*.

4.8 Example: InSe heterostructure for thermal studies

In this section, the fabrication of a complex heterostructure based on 2D materials is described with the spirit of serving as an example of how all the techniques described during the chapter can be applied. The heterostructure chosen was an encapsulated InSe Hall bar with graphene contacts. Besides the fabrication presented here, plans for future work involving this heterostructure will be described in *chapter 7* and *chapter 8*.

To start, the heterostructure must be fabricated. For this, the PMMA carrying layer method (*section 4.6.3*) was applied. The hBN required for the bottom layer was exfoliated first onto 300 nm SiO₂/Si, that was just cleaned with the solvent method described in *section 4.3.1*. From all

the flakes exfoliated, only suitable ones were considered. Good candidates for the bottom layer were the ones with bigger size, high homogeneity and lack of defects. These properties were checked by using both bright and dark field microscopy. An example of suitable bottom hBN layer is shown in *figure 4.23(a)*. To create electrical contacts, graphene was selected instead of InSe in order to minimise the contact resistance as explained in *section 4.7*.

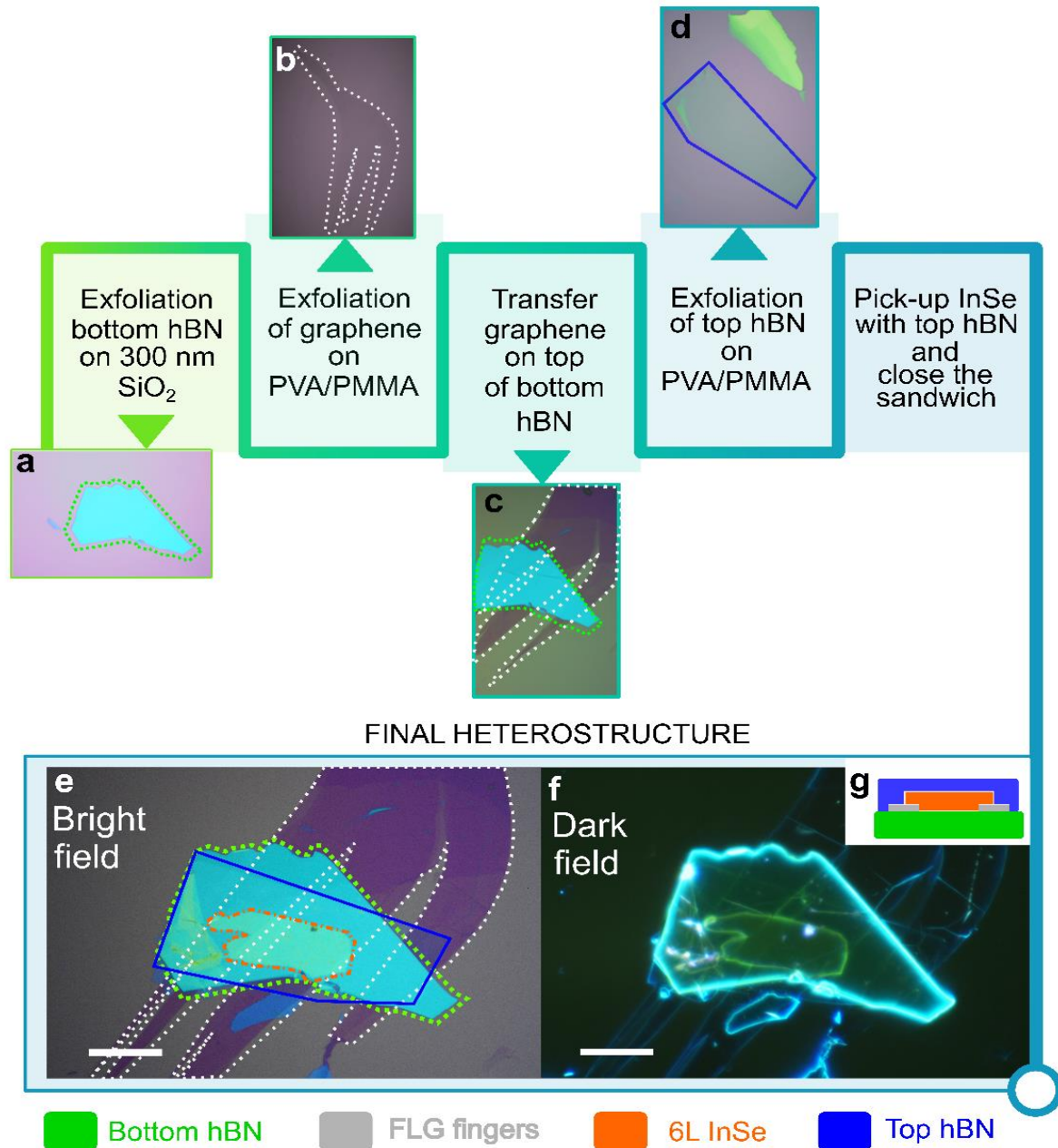


Figure 4.23. Flowchart of the fabrication steps followed to produce an encapsulated InSe heterostructure with graphene finger contacts, employing the PMMA stamp transfer method. (a) Bottom hBN exfoliated on 300 nm SiO₂/Si. (b) Graphene finger contacts exfoliated onto PVA/PMMA, and surrounded by a white dotted line. (c) Transferred graphene fingers onto the bottom hBN layer using the PMMA carrying layer method. (d) Top hBN layer exfoliated onto PMMA/PVA and surrounded by a dark blue line. Final result of the heterostructure shown in (e) bright field, and (f) dark field. The scale bar in both images is 20 μm. (g) A schematic lateral view of the layers conforming the heterostructure following the colour legend at the bottom for the different materials.

To facilitate its posterior transfer, graphene was exfoliated onto PMMA/PVA wafers. In order to create graphene contacts there are two possible routes to follow, which will affect the types of flakes that are searched for after the exfoliation: (1) Either two different graphene flakes with similar thickness can be exfoliated and then transferred to serve as contacts, or (2) a flake that is already divided forming a finger-like structure can be selected. It is important to highlight that in order to be used as contacts, the graphene doesn't need to be necessarily monolayer, but it has to have a specific shape, ideally thin and large. In the case of the heterostructure presented here, the latter option was chosen as shown in *figure 4.23(b)*. The main reasons to select option (2) above (1), are that by using only one flake the chances of having homogeneous thickness all throughout the flake area are increased, plus the number of transfer steps are automatically reduced from 2 to 1, which reduces the risk of damaging the structure. After a suitable flake was selected, a membrane was created following the procedures depicted in *figure 4.16*, and then transferred on top of the selected bottom hBN, as shown in *figure 4.23(c)*. Next, hBN was exfoliated onto PMMA/PVA substrates to serve as a top closing layer for the heterostructure. In this case, a suitable flake needed to be at least big enough to cover the InSe flake and part if not all, the graphene fingers to be used as contacts. Also, in this case, as the intentions for these devices is to study them with complex microscopic and spectroscopic techniques, the top hBN layer needed to be as thin as possible to avoid masking the thermal or optical effects of the InSe flake, which is in reality the main interest. Once a suitable top hBN layer was found as shown in *figure 4.23(d)*, a membrane was cut with the flake in its centre, then mounted onto a plectrum, and finally introduced into the glovebox.

Inside the glovebox, the InSe was exfoliated to avoid direct contact with oxygen, and therefore, any possible degradation, as discussed in *section 4.6.3*. After finding a suitable InSe flake, which in the case of this structure were the ones with a thickness of $\sim 6L$, it was picked-up directly with the top hBN flake previously prepared, leaving a stack of InSe/hBN attached to the PMMA membrane. This step is one of the most delicate during the procedure as the membrane can break and remain attached to the substrate, which would mean that the whole process has to be re-started. Finally, the heterostructure was finished by dropping down the InSe/hBN system on top the bottom graphene/hBN. The alignment of both heterostructures is extremely important in this stage. The InSe had to fall necessarily on top of the graphene fingers, leaving at least a bit of the InSe just covered by hBN to become the main channel of the devices. An example of the finished heterostructure is shown in bright and dark field microscopy in *figure 4.23(e)* and *figure 4.23(f)*, respectively. The different layers are highlighted according to the colour scale at the bottom of the figure.

To follow, after the heterostructure was finished, the device fabrication could be initiated. The first step in this case, was to clean the heterostructure as much as possible both from surface residual polymeric contamination from the transfer process, as well as from hydrocarbons trapped between the layers. To do this, the AFM brooming technique resulted effective: a soft AFM tip (i.e. Budget sensors, multi-75G probes with $k = 3 \text{ N/m}$ [282]) was scanned in contact over the layers with a very low set-point (i.e. very low normal force), medium speed and low feedback parameters. Over time, the set-point was gradually increased to eliminate more of the residues and create a channel area as clean as possible as shown in *figure 4.24(b)*[181]. The process is monitored using the friction signal as it provides clearer information on the effect of the brooming. It can take from minutes to hours depending on the device, but it is important to keep the set-point as low as possible, to avoid tearing the layers. Another important point to consider, is to never use new probes, as they can tear the heterostructures. Slightly blunt or used probes are better for this task. Once this step was completed, the heterostructure chip was placed in the centre of the field of view of a microscope, and a set of optical images with different magnifications was taken. Then, these images were all mounted together in a software of choice, Layout Editor in the case of this thesis, to serve as a canvas for the design of the device and contacts as shown in *figure 4.24(d)*. Note that the final designs for EBL had to be converted to an appropriate format (.gds). Following this, as presented in *figure 4.24(c)* a first step of resist, EBL and metallisation was performed to place alignment marks around the heterostructure. As explained in the previous section, these marks are extremely important in order to properly align the EBL, and therefore to produce accurate designs on the device. Once the design was selected, several rounds of resist (PMMA in the case of this thesis) deposition, EBL, etching and metallisation were needed to finalise the devices.

1. First, the big contact pads were drawn and deposited without modifying the heterostructure as shown in *figure 4.24(e)* and *(f)*.

2. The next step consisted on the creation of electrical contact to the InSe via the graphene. For this, PMMA was spin coated again and 1D contacts to graphene were developed via EBL and the developer, based on the .gds design. Then, RIE etching was used to eliminate the hBN/Gr/hBN materials to form a tilted plane. Finally, metal was evaporated in the form of an adhesion layer and the contact metal in the proportions: 1 – 5 nm Cr/20 – 50 nm Au. In this run the heater and thermometers were also created.

3. Finally, the Hall bar was shaped. For this, another layer of PMMA was spin coated, and lithography was applied following the etch mask design. To cut through the InSe, ion milling was employed, defining the Hall bar shape of the final device as shown in *figure 4.24(g)*. This way, also, the remaining graphene was eliminated, preventing the graphene from short circuiting the device.

4. Once the devices were ready, they were wire bonded by hand, as shown in *figure 4.22*. Further measurements will be discussed in the section of future work in *chapter 8*.

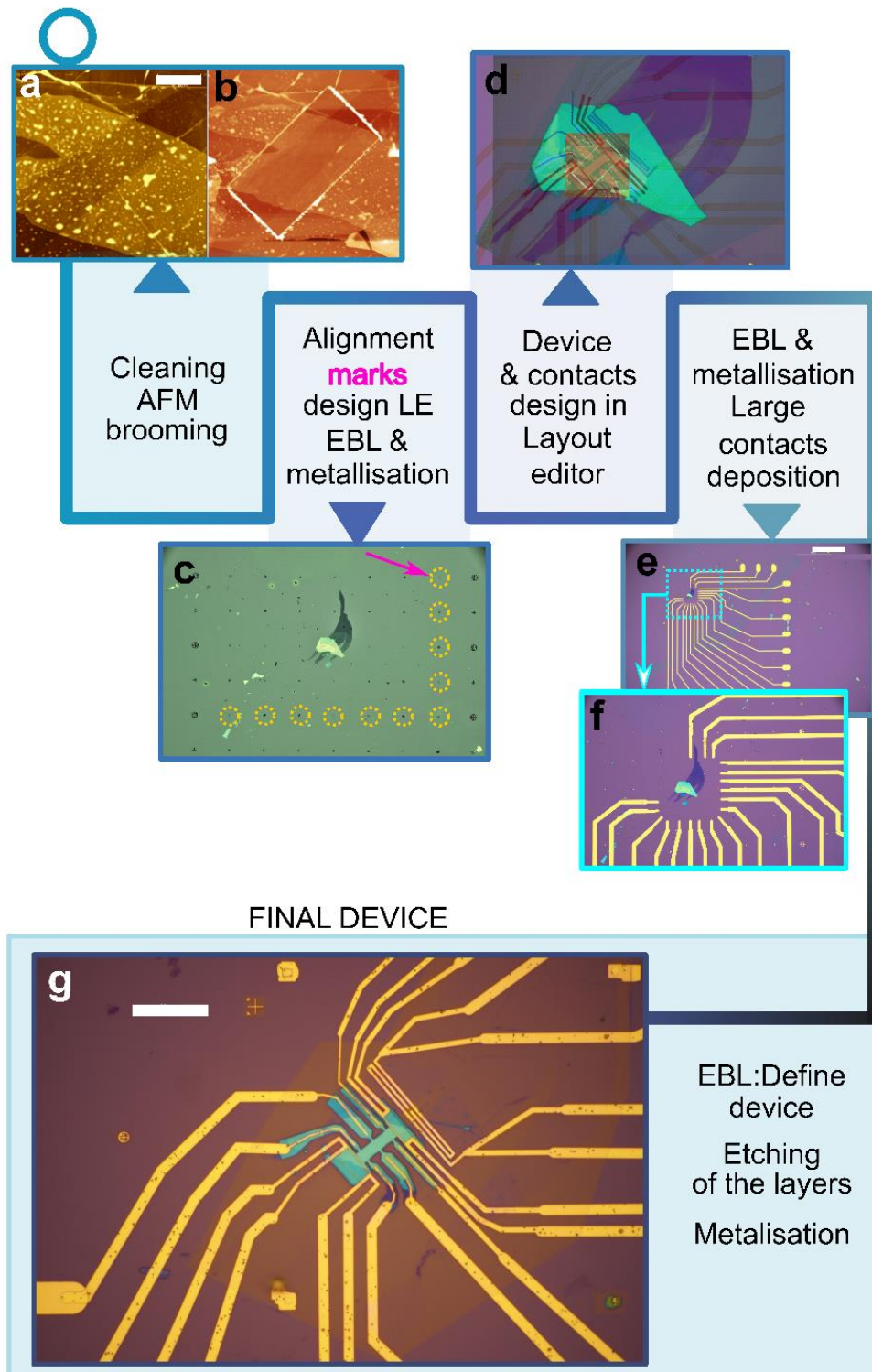


Figure 4.24. Flowchart of the steps followed to transform the heterostructure presented in the previous figure into a finalised device. (a) AFM scan over the device area showing wrinkles and bubbles. Scale bar: 5 μm (b) AFM image after brooming. The area scanned appears clean with the dirtiness accumulated at the sides. (c) Alignment marks (surrounded by yellow circles) created around the heterostructure. (d) Layout editor design of the device, later exported to .gds format compatible with EBL. (e) EBL and metallisation of the big contact pads. (f) Detail showing the untouched heterostructure and the Cr/Au contacts deposited around it. (g) Final device produced after few cycles of resist, EBL, etching and

metallisation. The final device consisted of a Hall bar of 6 arms, with two thermometers and a gold heater. Scale bar: 20 μm

As it can be seen from the example presented above, the process of fabricating devices out of 2D materials is not a simple one. Many steps are involved in the production of a final device, and each of them poses a risk to the integrity of the end result. Besides this, the lack of automation present in the field so far, means that each step must be undertaken by a trained user, making the process still expensive and specially, extremely time-consuming.

4.9 Conclusions

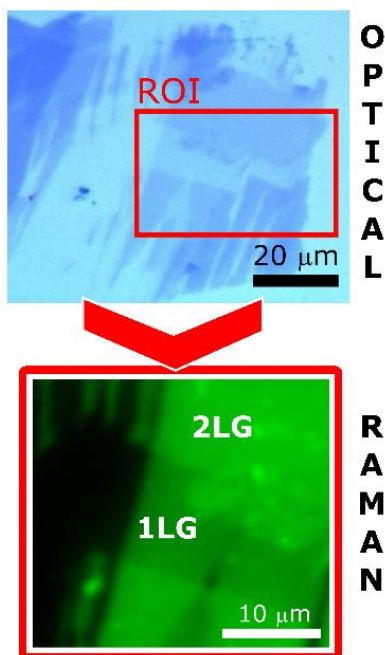
In this chapter, the fundamental techniques for fabrication of 2D materials and related heterostructures used during this thesis were described in detail: from the selection of materials, to different exfoliation techniques, covering also two different stacking methods for heterostructure production and, finally, also discussing the steps needed for device fabrication. At the end of the chapter, an example showing the steps for fabrication of a complex device, consisting of an encapsulated InSe Hall bar with graphene contacts was presented.

One of the main advantages of the methods discussed here is that their combination allows the fabrication of several kinds of complex heterostructure and/or devices, and besides EBL, generally the techniques employed in this chapter are rather inexpensive and can be implemented at a very minimal cost [283].

Another conclusion that can be extracted from this chapter is that even after all the years that have passed since the first discovery of graphene, still the process of production of 2D materials heterostructures relies heavily on the experience of the researcher and his/her skill undertaken it, in a way, similar to a craftsmanship. Part of this is due to the random nature of the exfoliation process. Although there are some methods that statistically lead to a higher yield of flakes, the lack of repeatability in terms of thickness and sizes, makes the process of flake finding extremely time-consuming. On the other hand, the process of heterostructure stacking is a very delicate one, and every little misstep can ruin the whole fabrication, forcing the researcher to re-start from the beginning. For these reasons, the current 'handmade-nature' of device fabrication can be seen as a bottleneck for the production of devices, and therefore, the exploration of different physical properties. It makes the process time-consuming, expensive and extremely lengthy. To sort out this issue, one of the next steps to undertake is the automation of all these processes: from exfoliation, to flake identification, to finally heterostructure production. The group of Masubuchi et al. [262, 263] has already published papers in this direction, and it is clear that in the incoming years the automation processes will be a great deal in the papers related to fabrication of 2D materials, exploring different Neural Network implementations for the identification of 2D

materials in different substrates, to the use of robots inside gloveboxes to produce heterostructures.

Understanding the effect of water adsorption on graphene doping via Raman spectroscopy in environments of controlled humidity



The purpose of this chapter is to explore the interactions between adsorbed water and graphene in environments of controlled humidity levels. For this, Raman spectroscopy is employed to characterize how graphene behaves under varying levels of relative humidity. Samples prepared by different methods: exfoliated, CVD and epitaxial, are considered, as well as samples with different thicknesses: monolayer graphene (1LG) and bilayer graphene (2LG). The changes in the main Raman graphene peaks, the G and 2D peaks, are systematically extracted and compared for the different conditions and samples. Finally, the carrier concentrations of the exfoliated and CVD monolayer samples are calculated and compared with previous data.

Acknowledgments: *This chapter is a modified version of the article ‘Contactless probing of graphene charge density variation in a controlled humidity environment’ [284] me and my co-authors published in Carbon in 2020, and has been reproduced here with the permission of the copyright holder. The results discussed here are a joint work performed between Karl Brown, Christos Melios and Florina S. Rus (Raman measurements), Tom Vincent (Data interpretation, carrier concentration extraction with the Raman data using an algorithm adapted from refs [285,*

286]), *Olga Kazakova (leadership, discussions), Cristina E. Giusca (leadership, supervision, discussions and writing) and myself (supervision, fabrication of exfoliated graphene samples, Raman measurements, data interpretation, writing). The CVD samples were prepared by Graphenea, while the epitaxial graphene samples were fabricated by Dr Kurt D. Gaskill's group at the Naval Research laboratory in Washington.*

5.1 Introduction

Due to its outstanding electronic properties graphene has shown great promise for many applications such as gas sensing [287–289], transparent conducting electrodes [290, 291], or energy storage [292], among others. To face the demands of such a wide variety of fields, great efforts have been dedicated to improve the synthesis techniques of graphene from mechanical exfoliation, which is often employed for research purposes; to epitaxial growth or chemical vapour deposition (CVD), which actually hold the promise of achieving mass-production of graphene devices [293]. However, regardless of the fabrication route, the electronic properties of graphene are known to be eminently sensitive to changes in the environment. This is a positive feature for certain applications such as graphene sensing, but it can become a challenge when the doping is unwanted and unavoidable.

In this sense, the presence of water can be problematic. It exists in the atmosphere mostly in gaseous form, and it is continuously cycling, always present in varying concentrations (i.e. levels of relative humidity (R.H.)) very dependent on the geographical location. Relative humidity has proven to dope graphene, and although it is not the strongest environmental dopant, its contribution is still non-negligible [137, 288]. Some studies have highlighted the potential of graphene as a humidity sensor [146], while others have demonstrated how relative humidity can obscure the performance of non-encapsulated graphene based devices [294, 295]. Early experimental research demonstrated that water molecules act as loosely bound p-dopants when physisorbed by graphene [25, 296]. These results are supported by DFT calculations, which suggest that although free-standing graphene should be inert to water, the experimentally observed induced doping is related to interactions with the substrate, at least for samples lying on SiO₂, and the possible formation of dipoles of the water molecules [297, 298]. For this reason, different responses to the humidity exposure can be expected for types of graphene prepared by different methods, as well as for varying number of layers. However, although some research has been performed on the effect of humidity on specific configurations, there are no previous studies comparing the response of different types of graphene, considering the effects of the underlying substrate and the number of layers.

In order to tackle this gap in the research, here a systematic study comparing the doping effects of varying levels of relative humidity on different types of graphene (i.e. exfoliated, CVD and epitaxial), with varying thickness (i.e. 1LG and 2LG), is performed via in-situ Raman spectroscopy. This technique has been selected as it has proven to be fast, non-invasive and capable of providing realistic estimations of the doping levels of graphene.

5.2 Experimental methods

5.2.1 Sample description and characterisation

The effect of varying levels of humidity has been investigated for three different graphene samples: CVD, epitaxial and exfoliated graphene. These have been prepared following different synthesis procedures as summarised below:

- CVD samples were synthesised at high temperatures ($\sim 1,000$ °C) using Cu foil as catalyst as described by Li et al. [78]. The graphene was removed from Cu by spin coating a layer of polymethyl-methacrylate (PMMA) and then wet etched of the Cu substrate. The film was cleaned with distilled water several times and transferred onto 300 nm SiO₂/Si substrate annealed at 450 °C for 2h in N₂ to remove PMMA.
- Epitaxial graphene was fabricated on (0001)6H-SiC substrates via Si sublimation from SiC, as explained in *chapter 2, section 2.2.2*. The substrates were etched in H₂ at 200 mbar using a ramp from room temperature to 1580°C. At the end of the ramp, the H₂ was evacuated and Ar added to a pressure of 100 mbar and the graphene was synthesised at 1580°C in the Ar. More details can be found here [299].
- The exfoliated graphene was fabricated in-situ on top of 300 nm SiO₂/Si substrates following the *superposition method* explained in *chapter 4, section 4.3*.

5.2.2 Environmental chamber and Raman system set-up

Raman measurements were performed in-situ using a Renishaw inVia Raman microscope system equipped with a THMS600 Linkam temperature and environmental chamber [300], where the samples were placed. To precisely control the environment and achieve different humidity and temperature conditions the chamber was connected to a Linkam RH95 humidity controller [301]. Raman maps were acquired using an excitation wavelength of $\lambda = 532$ nm and a diffraction grating of 1800 lines/mm. The light beam was focused with a 50x long-working distance objective in order to have enough space to place the environmental stage containing the sample. A schematic picture of the set-up is presented in *figure 5.1*. Prior to the measurements the system

was calibrated using the main peak of an internal silicon sample ($\sim 520 \text{ cm}^{-1}$) that serves as a reference.

Initially, Raman spectra were acquired in ambient conditions at a temperature of $T = 21 \text{ }^\circ\text{C}$ and a R.H. of 40%. Following this, the samples were annealed at $150 \text{ }^\circ\text{C}$ for 1 h under a continuous flow of N_2 gas (BOC research grade: 99.9995% purity [302]) at atmospheric pressure. This annealing step was performed between measurements in order to recover the initial state of the graphene's surface by producing the desorption of the water molecules [287, 303]. After the annealing, the samples were cooled down back to room temperature and exposed to different concentrations of water vapour balanced with N_2 . For the exposure, the R.H. was increased in a stepwise manner from 0% to 60%, and the Raman maps were recorded immediately after reaching the target humidity level. The step size was 10% R.H. for exfoliated and CVD graphene, and 20% R.H. for epitaxial graphene. The Raman maps were started immediately after the exposure of graphene to each humidity concentration.

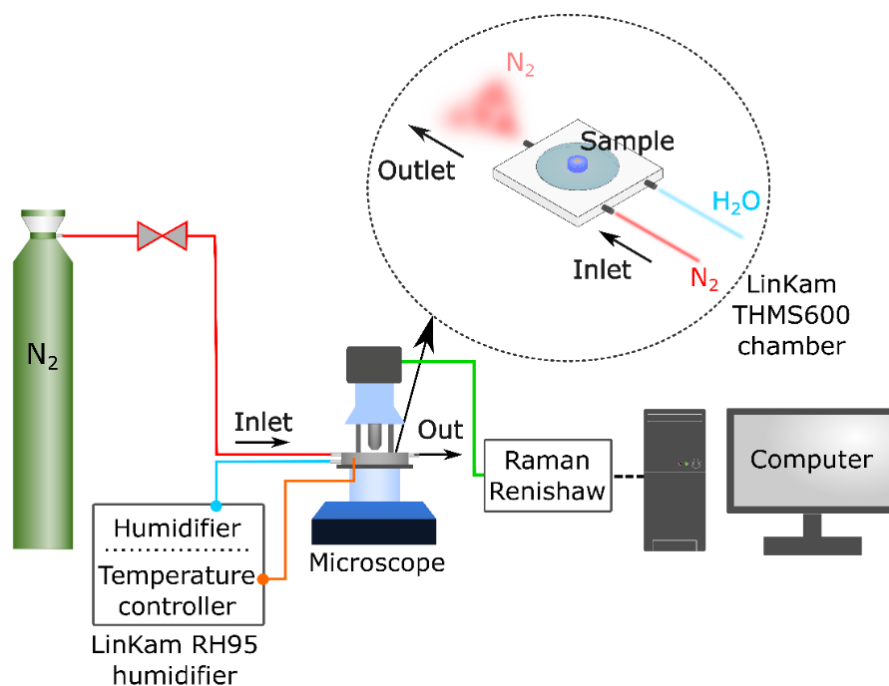


Figure 5.1. Scheme of the Raman humidity measurements experimental set-up. The Raman scan parameters are controlled directly from the computer. The different values of humidity within the LinKam THMS600 environmental stage are achieved via a constant flow of water drops (blue) produced by a LinKam RH95 humidifier with nitrogen used as carrier gas (red). As shown in the inset, both gases are connected to the inlet of the chamber, where the sample is placed. The resulting gas is expelled from the outlet. The flow of gases and the temperature are controlled via the LinKam RH95 system.

As a consequence of this type of set-up, the measurement parameters had to be carefully adjusted in order to avoid the presence of artefacts in the final Raman maps that could lead to inaccurate results. To minimise lateral sample drift in the humidity chamber during mapping, short

acquisition times of 0.3 s/pixel were employed. Additionally, a laser power of 0.5 mW was used to keep thermal effects to a minimum and to achieve a suitable signal-to-noise ratio. This value was selected for the power as a compromise: Lower laser powers would require longer acquisition times, which would lead to excessive lateral drift in the sample due to the nature of the measurement set-up. On the other hand, using higher laser power could induce small offset within the measured doping values. In this respect, it is important to highlight that in the case that any offset was present in the measurements of the samples, it would be constant across all maps, and therefore, all humidity-induced trends observed would still be valid.

5.2.3 KPFM set-up

Kelvin probe force microscopy (KPFM) measurements were acquired with a Bruker Dimension Icon AFM under ambient conditions. Maps of the topography and the contact potential difference were acquired simultaneously in single-pass frequency-modulated Kelvin probe force microscopy (FM-KPFM). For this purpose, highly doped Si probes (PFQNE-Al) were employed, having $f_0 = 300$ kHz and $k \approx 0.8$ N · m⁻¹ [304].

5.3 Humidity effects on different graphenes

5.3.1 Morphology studies of various types of graphene

Prior to the Raman measurements, all the samples were characterised by different methods: optical microscopy, AFM or KPFM, in order to assess their morphology and the number of layers of the different graphene samples. Representative results are summarised in *figure 5.3*.

In the case of the exfoliated sample, the optical image (*figure 5.2(a)*) shows two different flakes with a wide distribution of areas of different thicknesses, t . These domains are identified with respect to the bright blue substrate based on the contrast: light blue regions correspond to thinner flakes, whereas darker blue regions are the result of a higher number of flakes stacked together. An area that seemed to contain the desired thicknesses (1LG and 2LG) was identified and surrounded by a red square (denominated as region of interest, ROI). In order to clearly identify the thickness of the flakes contained in the ROI, an AFM scan was acquired over the area as a complementary technique. The resulting topographical map (*figure 5.2(b)*) shows variations of the thickness of the flake as expected. The quantitative values have been confirmed by taken profiles on *figure 5.2(b)* following the yellow dotted line for 1LG with respect to the substrate, and the blue dashed line for 1LG with respect to 2LG. The profile showing the thickness of 1LG with respect to the substrate is shown in *figure 5.2(c)* giving $t_{1LG} \sim 0.34$ nm, while the profile for 1LG with respect to 2LG is shown in *figure 5.2(d)* giving $t_{2LG-1LG} \sim 0.37$ nm, which is a total of

$t_{2LG} \sim 0.71$ nm of 2LG with respect to the substrate. These quantitative results confirm the initial assessments of the thickness of the flakes performed using the optical image.

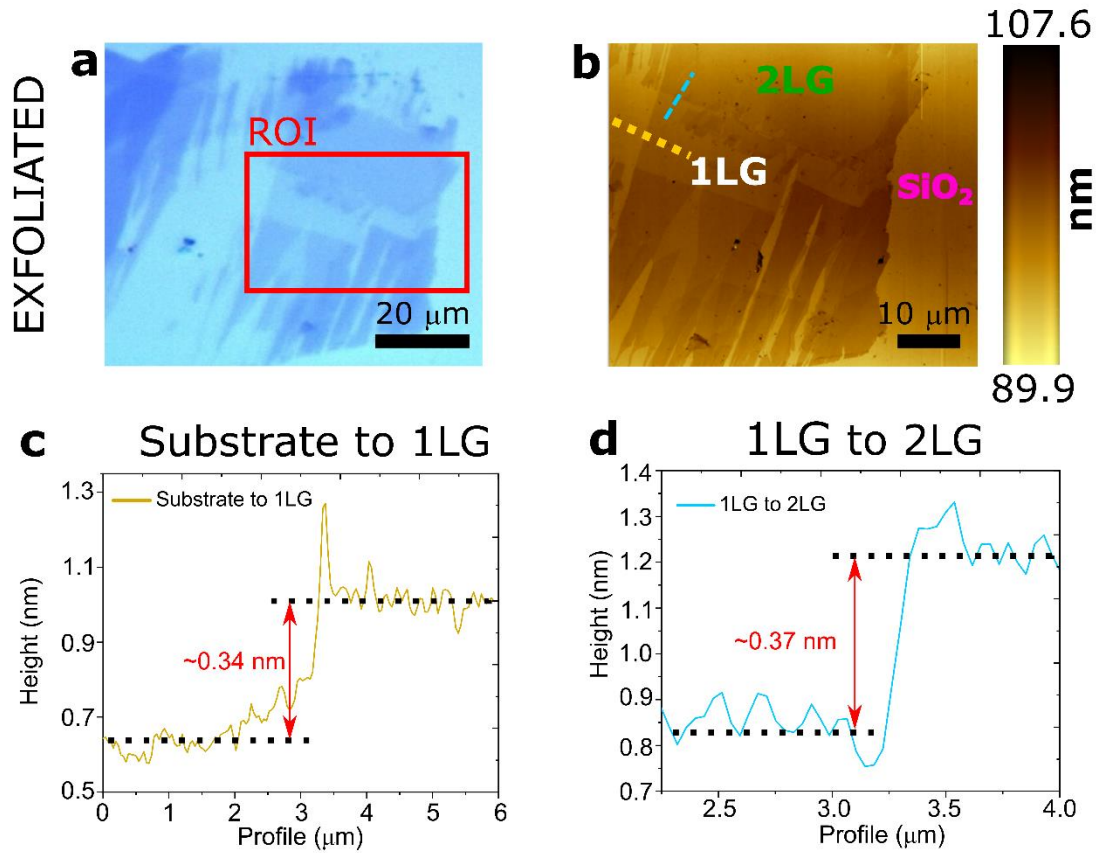


Figure 5.2. (a) Optical image of the exfoliated flake on 300 nm SiO₂/Si. The region of interest (ROI) surrounded by a red square presents mainly two distinct regions with a very light contrast with respect to the bright blue substrate, corresponding to monolayer (1LG) and bilayer (2LG) areas. (b) The thickness of the flakes in the ROI is confirmed by AFM topography using profiles from the substrate to 1LG (yellow dotted line), and from the 1LG to 2LG (blue dashed line). (c) Profile following the yellow dotted line from (b) giving a total thickness of 1LG with respect to the substrate of $t \sim 0.34$ nm. (d) Profile following the blue dashed line from (b) giving a total thickness of 2LG with respect to 1LG of $t \sim 0.37$ nm, and thus a total thickness with respect to the substrate of $t \sim 0.71$ nm.

For the CVD and epitaxially grown samples, optical contrast is typically not well-suited to provide information about the layer thickness, and therefore it is more convenient to use other techniques such as KPFM [288, 305, 306]. For the CVD sample, the topography (figure 5.3(a)) shows relatively homogenous graphene domains (dark contrast) separated by ridges. It is quite relevant to note that although in the topography there are no signs of different thickness distributions across the graphene, the contact potential difference map (figure 5.3(b)) reveals the presence of higher surface potential areas (high contrast based on our scale) corresponding to 2LG and 3LG patches, indicated by green and blue arrows, respectively.

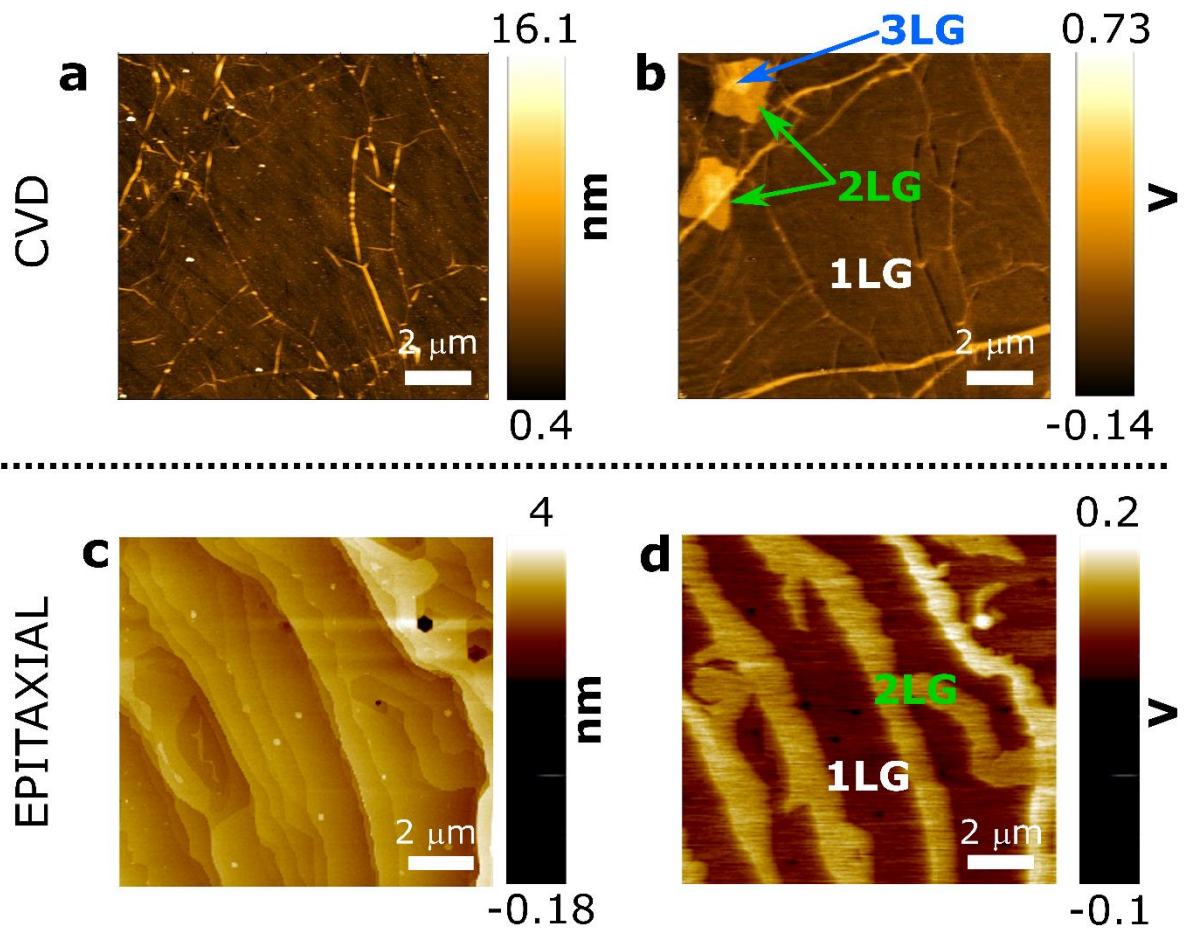


Figure 5.3. **(a)** Topography and **(b)** surface potential images of the CVD sample. The KPFM map shows a homogeneous area mostly 1LG (dark contrast), with higher contrast areas corresponding to 2LG (green) and 3LG (blue). **(c)** Topography of the epitaxial graphene sample displaying the typical terraced surface, and **(d)** contact potential difference map showing 1LG (dark contrast), and stripes of higher contrast areas corresponding to 2LG, typically located at the edges of the terraces

For the epitaxial graphene, the topography (*figure 5.3(c)*) shows the typical terraced surface with mostly parallel edges, consistent with the morphology of the underlying SiC substrate, as explained in *chapter 2, section 2.2.2*. As with the CVD sample, the contact potential difference map (*figure 5.3(d)*) revealed the presence of two different types of regions, not obvious in the topography. In the same manner, the areas with higher surface potential are associated with 2LG, which in this kind of sample typically grows at the edges of the terraces. The regions of lower surface potential (dark contrast) correspond to 1LG which typically grows on the centre of the terraces [137, 288].

5.3.2 Raman results in environments of varying humidity

Raman spectroscopy is an optical technique typically employed to determine the number of layers of a given graphene sample, as explained in *chapter 3, section 3.2.3*. Furthermore, it has also proven to be an excellent tool for studying the effect of external perturbations such as doping on the

electron-phonon interactions in graphene. Early research showed that the characteristics G and 2D graphene peaks were strongly influenced by changes in the doping, achieved either by electrostatic gating or charged impurities, or even both [307–309]. However, no systematic studies were found assessing the doping of graphene due to environmental factors via Raman spectroscopy.

Here, representative Raman maps of the three different samples acquired in ambient conditions are presented in *figure 5.4*. These are generated by measuring the individual Raman spectrum at specific pixels separated by $0.2 \mu\text{m}$, and then using the integrated signal of the G-peak intensity to represent each point. As the intensity of this peak is directly proportional to the number of layers, the areas containing higher green intensity values correspond to 2LG [210].

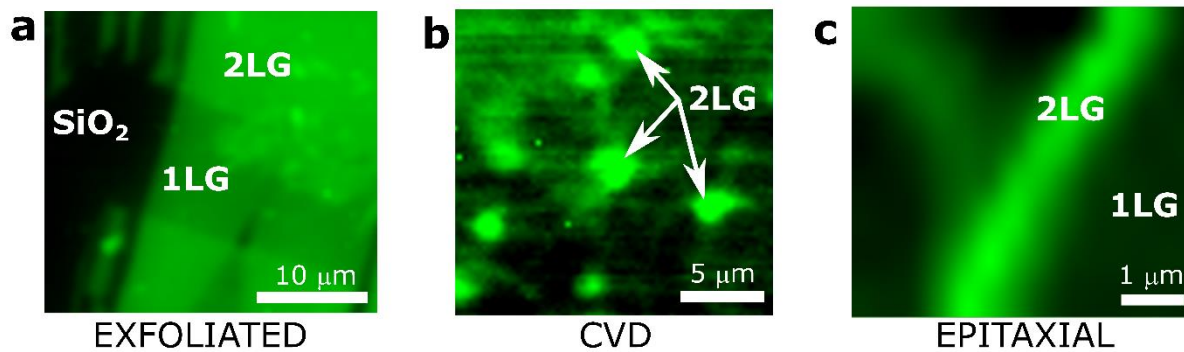


Figure 5.4. Raman maps representing the G-peak integrated intensity for (a) exfoliated, (b) CVD-grown and (c) epitaxial graphene using 532 nm excitation wavelength. The regions corresponding to 1LG and 2LG are indicated in each image. The measurements were carried out in ambient.

In order to understand the rest of the contrast in the images it is convenient to divide the samples in two groups:

- The CVD and epitaxial graphene samples, can be considered thin films, with the areas examined being comparatively small with respect to the whole wafer size. This means that no parts of the bare substrate are imaged in the maps, and therefore, the regions presenting lower intensity (less saturated green or black) correspond to 1LG.
- On the other hand, for the exfoliated sample, the 300 nm SiO_2/Si substrate is also mapped, appearing in black in *figure 5.4(a)*, and thus creating a sharper contrast with respect to the 1LG.

Using this layer information from the acquired maps, individual Raman spectra were extracted on the different 1LG and 2LG regions for each of the samples. The main parameters of the G and 2D characteristic graphene peaks (i.e. the position and the full-width half maximum (FWHM)) were then obtained by applying Lorentzian fittings.

Table 5.1 summarises the averaged results acquired over 1LG and 2LG in ambient conditions. The general values observed for all the samples coincide with previous experimental data: the FWHM of the 2D-peak increases quite noticeably in all cases for 2LG with respect to 1LG, and it is possible

to fit it with 4 Lorentzian components as expected from a double-resonance process (see *chapter 3, section 3.2.3* for more details) [310]. Additionally, for the G-peak the FWHM widens and becomes more intense for 2LG compared to 1LG, as expected with the evolution of the electronic bands on the transition from one to two graphene layers.

	Graphene type	Exfoliated		CVD-grown		Epitaxial	
	Thickness	1LG	2LG	1LG	2LG	1LG	2LG
PEAK POSITION	G peak (cm^{-1}) $\pm 2\text{cm}^{-1}$	1585	1582	1602	1594	1595	1608
	2D peak (cm^{-1}) $\pm 2\text{cm}^{-1}$	2674	2691	2693	2699	2690	2714
FWHM	G peak (cm^{-1}) $\pm 2\text{cm}^{-1}$	13	15	13	24	25	36
	2D peak (cm^{-1}) $\pm 2\text{cm}^{-1}$	31	57	44	52	35	54

Table 5.1. Characteristic averaged values for the position and FWHM of the G and 2D peaks recorded in ambient ($T = 21^\circ\text{C}$, $RH = 40\%$). The spectral resolution of the Raman spectrometer is specified in the table as $\pm 2\text{ cm}^{-1}$

Another detail of interest is that for the exfoliated and CVD types, the G peak experiences a slight red-shift, when passing from 1LG to 2LG, which has been already addressed in literature by Gupta et al. [311]. Regarding the position of the peaks, it is also noticeable that CVD and epitaxial graphene show a clear blue-shift of the G and 2D-peak positions with respect to the exfoliated type. This is justified as the phonon frequencies of graphene can be influenced by different factors such as doping, both from the environment and the substrate, and by mechanical strain. Local variations of the strain are practically unavoidable as these are induced in the graphene lattice upon deposition on a substrate [312–314], thermal annealing [315, 316] and stacking with other 2D materials [317, 318]. The deconvolution of both quantities will be further discussed in the next section. Besides this, it is also important to highlight that as shown by Casiraghi et al. [309], although the general trends observed for certain graphene types in certain specific conditions are reliable, there is always an unavoidable variability between nominally identical samples (i.e. fabricated following the same procedure) in terms of doping induced by the substrate that must be taken into account when comparing Raman results.

In order to visualise how the humidity affects the different graphene samples, representative spectra recorded at humidity levels ranging from 0 to 60% R.H. are displayed in *figure 5.5(a-c)* both for 1LG (top) and 2LG (bottom):

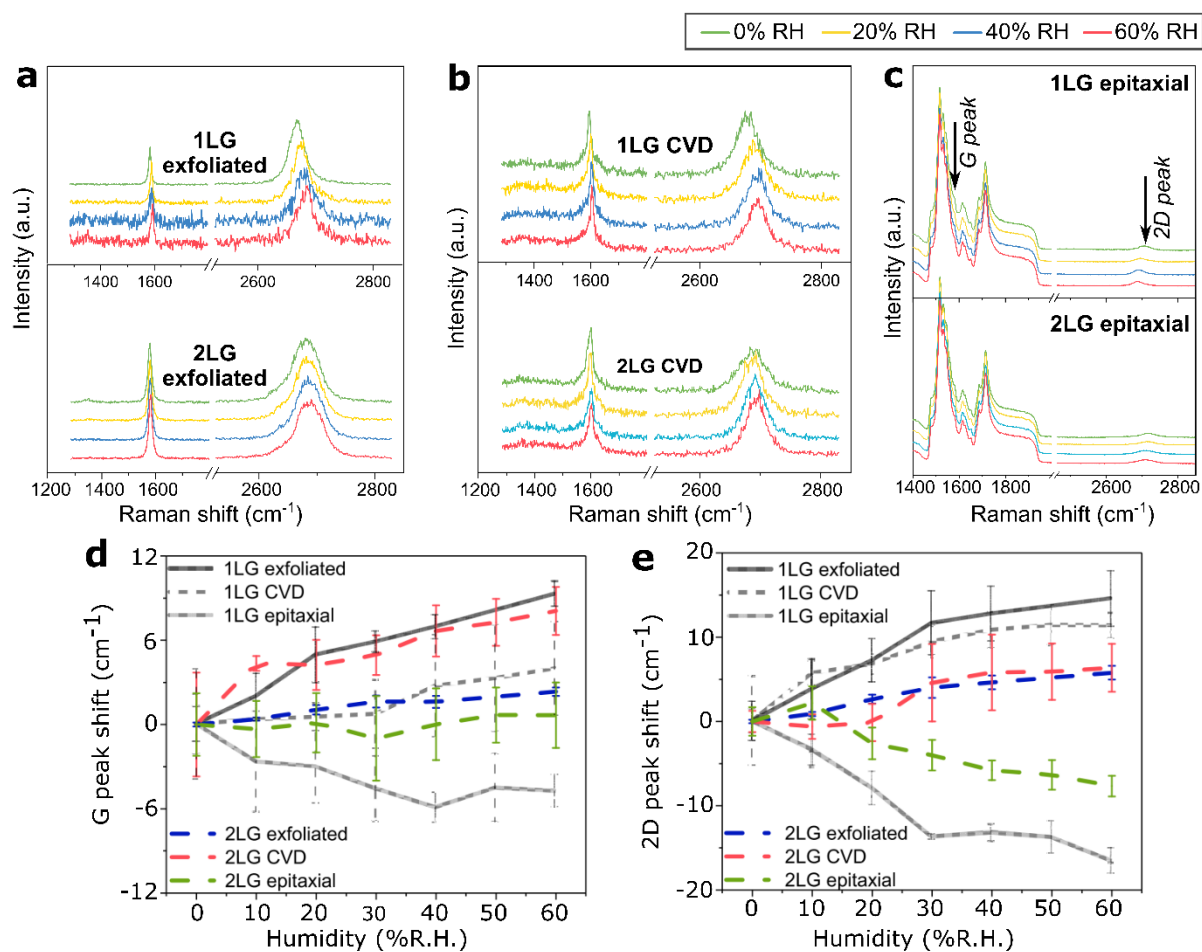


Figure 5.5. Representative Raman spectra for (a) exfoliated, (b) CVD-grown, and (c) epitaxial graphene at varying humidity levels from 0% to 60% RH. In all cases, results corresponding to 1LG are represented at the top, and results for 2LG at the bottom. Spectra are shifted vertically for clarity. In (d) and (e) a summary of the peak position variation with humidity is shown for the of the G and 2D peaks, respectively.

There is a clear observed shift in the position of the Raman peaks. For exfoliated (figure 5.5(a)) and CVD (figure 5.5(b)) graphene the 2D peak presents a blueshift with increasing humidity levels, more pronounced in both cases for 1LG. In contrast, the G-peak varies much less noticeably, with a very slight blueshift for all the curves, remaining almost constant for the 2LG exfoliated sample. For the epitaxial (figure 5.5(c)) graphene sample, the G peak position for 1LG redshifts with increasing humidity and remains unaffected for 2LG, whereas the 2D peak displays a pronounced red shift with increasing humidity both for 1LG and 2LG. Another important feature to highlight for the exfoliated and CVD samples is the absence of the disorder-related D peak near 1350 cm⁻¹ which is the most salient feature of defect-free graphene [310].

In order to bring some clarity to these observations, the position of the G and 2D peaks are calculated using Lorentzian fittings and plotted as a function of humidity in figure 5.5(d) and figure 5.5(e), respectively. Positive and negative values of the y-axis (peak-shift) correspond to blue-shift and red-shift, respectively. Based on these curves it is more evident that the exfoliated and epitaxial 1LG are the samples showing the highest variations in the position of both peaks, presenting a

monotonic trend, upward (blue-shift) and downward (red-shift) respectively, in which the shift increases for higher humidity levels. Additionally, for both of them as well the shift is bigger for the 2D peak being $\sim 15 \text{ cm}^{-1}$, while the G-peak displacement was $\sim 10 \text{ cm}^{-1}$ for the exfoliated sample and $\sim -6 \text{ cm}^{-1}$ for the epitaxial. These results also highlight that the doping produced by the humidity shown by exfoliated and epitaxial graphene is thickness dependent, as the 2LG does not change as drastically as the 1LG. Interestingly, for the CVD sample, 2LG shows a similar blueshift of both, the G and 2D peaks of $\sim 6 \text{ cm}^{-1}$, while 1LG presents a very pronounced shift only for the 2D peak of $\sim 12 \text{ cm}^{-1}$.

With water acting as a p-dopant of graphene [25, 298], our observations of the Raman shifts agree with previous experimental data: Pisana et al. [319] and Das et al. [307] employed electrostatic gating to dope exfoliated graphene samples sitting on SiO_2 , and reported a blue-shift both for the G and 2D peaks when p-doping the graphene. Same trends were observed for CVD graphene by Kominkova et al. [320] using an electrochemical approach. In the case of the epitaxial graphene, the effect of the water doping results in quite a noticeable red-shift of both the G and the 2D peaks, also demonstrated by Yang et al. [321] employing substrate induced doping. The different in shifting direction of the phonons observed for exfoliated and CVD (i.e. blue shift), and for epitaxial (i.e. red shift), might be attributed to the different substrate induced doping in the samples, which lead to p-doping induced from SiO_2 for exfoliated and CVD, and to n-doping induced from the interfacial layer in epitaxial graphene.

In general, the cumulative doping of a sample accounts for different components such as the substrate induced doping, environmental doping (in the case the sample is not encapsulated between hBN) or electrostatic gating. This is important because as the electron-phonon coupling is strong in graphene, these components will also contribute to the observed Raman shifts. However, the variations of the G and 2D peaks are not only related to doping, but also, they can be a result of strain induced in the lattice. This correlation is explored in the following section.

5.3.3 Correlation of strain and doping

Changes in the lattice constants lead to variations in the phonon frequencies, therefore, the shifts experienced by the 2D and G peaks in graphene are a result not only of the doping mechanisms, but also of the strain present in the sample. Strain in the lattice can be induced uncontrollably through different processes such as the polymeric transfer or thermal treatments [322, 323].

In principle, due to the natural convolution of the strain and doping, obtaining quantitative values of one of the two properties, would require the prior knowledge of the other. However a method first proposed by Lee et al. [285], and further developed by Froehlicher and Berciaud [324], allows separating the contributions of strain and doping for Raman measurements, by correlating

the G and 2D peak positions with respect to an empirical trusted reference showing no strain and no doping (i.e. 1LG on SiO₂ measured by Bruna et al. [325]), via a vector decomposition method, illustrated in *figure 5.6*.

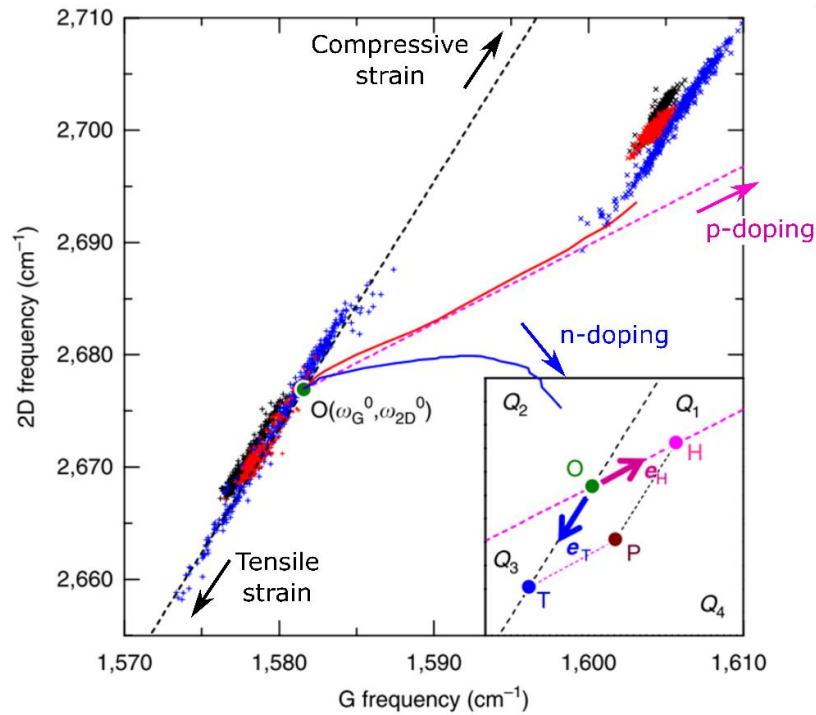


Figure 5.6. Example of the application of the vector decomposition method. Figure representing the relation between the 2D frequency versus the G frequency, in which the data is obtained from fitting the graphene Raman peaks using Lorentzian curves. The position of the green dot corresponds to free-standing graphene, not affected by strain or doping. Displacement up or down on the black dotted line results in undoped graphene with an increase of compressive or tensile strain, respectively. Increases in doping are slightly more complex: movement along the pink dotted line towards higher frequencies results in strain-free graphene with higher p-doping, as denoted by the pink arrow; while the n-doping is determined by the curved trajectory in solid blue, also highlighted with a blue arrow. Inset: decomposition of the effects of hole doping and strain using a vector model. Any point in the map can be represented as a vector, \overline{OP} , which can be further decomposed into two directions: along the \overline{OH} 'strain-free' with hole doping, and along the \overline{OT} 'charge-neutral' for tensile strain. These two lines divide the space into four quadrants (Q1-Q4). (Note that the data reported here is just an example, and it is not related to the discussion of the Raman) Adapted with permission from [322]

The position of the measured points with respect to the experimentally chosen reference, that is, their position within the quadrants formed by the strain-free (pink dotted line in *figure 5.6*) and doped-free (black dotted line in *figure 5.6*) provides information of the level of doping and strain present in the sample. One of the main disadvantages of this procedure is that it is not applicable to thicker graphite or other materials, as it is based on experimental values taken from monolayer graphene. Additionally, as a result of the non-linearity in the 2D and G peaks position for n-doped samples such as epitaxial graphene, the method is restricted to p-doped samples, in which the trend remains linear [306]. The technical details of this approach are out of the scope of this thesis, but more information can be found in references [44,45,48].

For our study presented here, the data extracted from this method was employed to produce quantitative maps of the doping of the samples with respect to the relative humidity for the

monolayer regions on the p-doped graphene samples (i.e. exfoliated and CVD), as shown in the *figure 5.7* below:

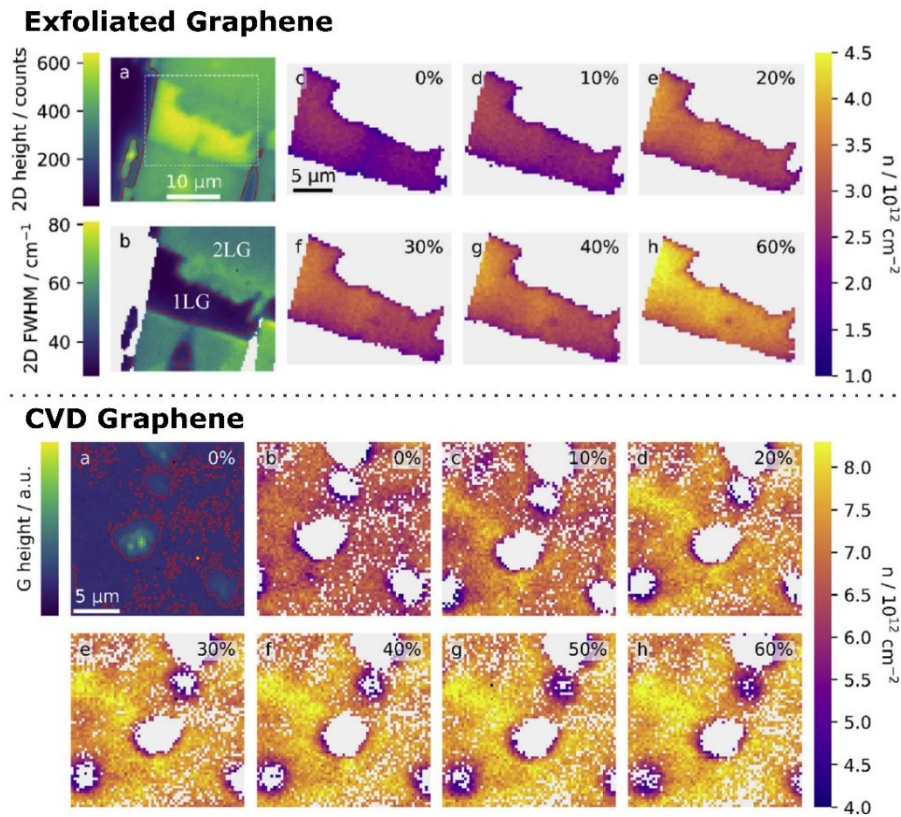


Figure 5.7. Top panel - Exfoliated graphene sample. (a) Raman intensity map of the 2D peak at 0% R.H. This map was employed to distinguish the areas of mono- and bi-layer graphene, as well as the substrate regions. The red lines show the threshold value of 300 counts used to discriminate between the graphene region, and the substrate. The white dashed rectangle indicates the area of interest containing 1LG, and focused on in detail in the maps (c-h). (b) Raman map of the FWHM of the 2D peak at 0% R.H. This map was used to distinguish between areas of 2LG and 1LG. The red lines show the threshold value of 40 cm^{-1} , above which the graphene was judged to be 2LG. The size of the map in (a-b) is shown by the scale bar in (a). (c-h) Sequence of spatially resolved doping maps collected from the exfoliated 1LG area, while the humidity was changing from 0% RH to 60% RH, as indicated in each image. The scale bar in (c) is shared for all (c-h) maps. Light grey areas in (c-h) maps have been masked out of the analysis. Bottom panel - CVD graphene sample. (a) Map of the G peak intensity at 0% R.H., used to exclude bilayer regions from the analysis. The red lines show the threshold value, of $1.05 \times$ the median height of the map, above which the graphene was judged to be 2LG. (b-h) Sequence of spatially resolved doping maps collected from the same region of the CVD grown graphene, while the humidity was changing from 0% R.H. to 60% R.H., as indicated in each image. The scale bar in (a) is common for all images. Light grey areas in the maps have been masked out of the analysis using the threshold value as shown in (a). These figures have been reproduced with permission from [284].

In order to produce these maps, the positions of the 2D and G peaks were found for each individual spectrum comprising a confocal Raman map by applying single Lorentzian fits and then, the aforementioned vector transformation plots were constructed. For both samples, it is evident from the maps that the hole carrier concentration (n) is higher in environments with higher concentration of relative humidity, thus presenting an increasing trend. In order to quantify this change, the doping level for each humidity concentration was calculated by averaging over the maps. These values have been represented versus the R.H in *figure 5.8*.

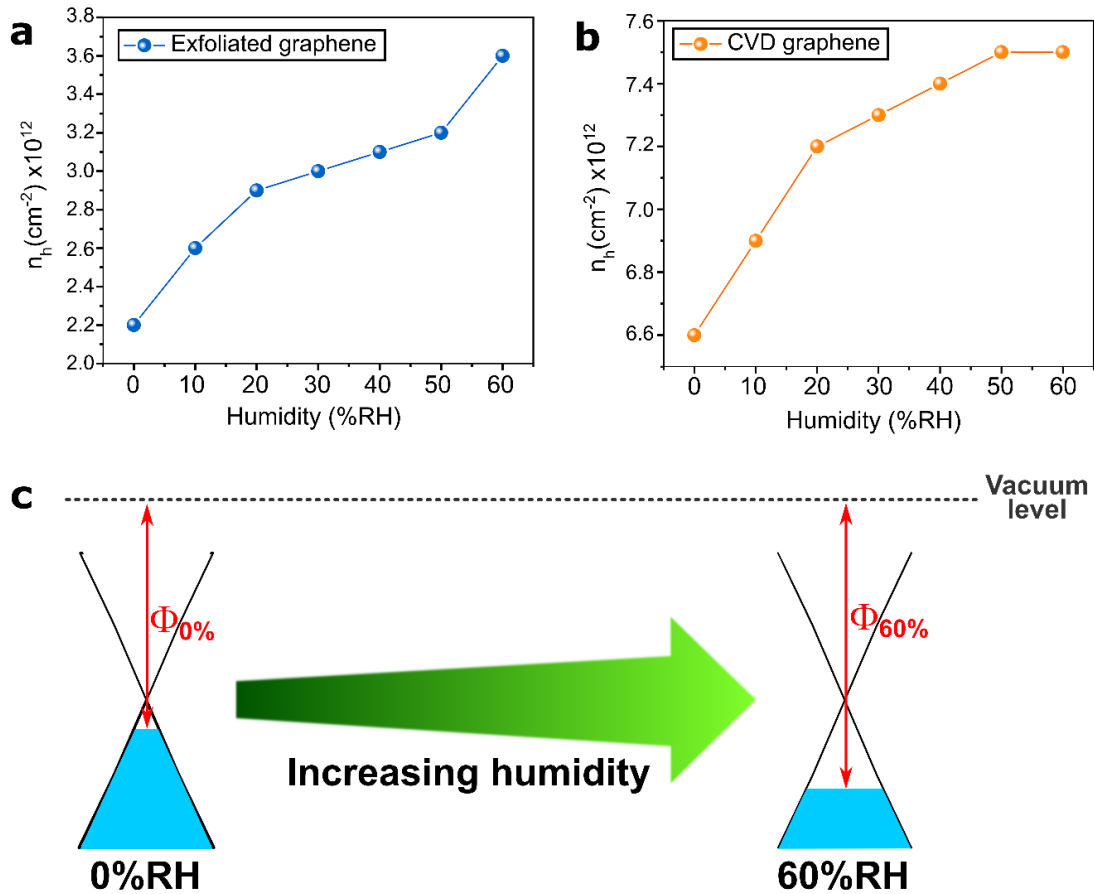


Figure 5.8. Variation of the holes carrier concentration with respect to varying humidity levels from 0%RH up to 60%RH for (a) exfoliated and (b) CVD graphene. (c) Schematic diagram of how the relative humidity affects the work-function of graphene resulting in p-doping.

For the exfoliated graphene, the average value of doping increases from $\sim 2.2 \cdot 10^{12} \text{ cm}^{-2}$ at 0% R.H. to $\sim 3.6 \cdot 10^{12} \text{ cm}^{-2}$ at 60% R.H., while for the CVD sample the values change from $\sim 6.6 \cdot 10^{12} \text{ cm}^{-2}$ at 0% R.H. to $\sim 7.5 \cdot 10^{12} \text{ cm}^{-2}$ at 60% R.H. As it is clear, the CVD graphene displays the highest overall doping, however the change in doping with increased humidity is greater for the exfoliated sample, as expected from the shift of the Raman peaks presented in the previous section. Similar orders of magnitude for the carrier density values reported here are found in previous van der Pauw studies of CVD graphene where the carrier density determined $\sim 9.9 \cdot 10^{12} \text{ cm}^{-2}$ for 20% R.H. [305]. This agreement between techniques suggests that the Raman method provides a good estimate of the order of magnitude of the level of doping in a graphene sample.

5.4 Conclusions

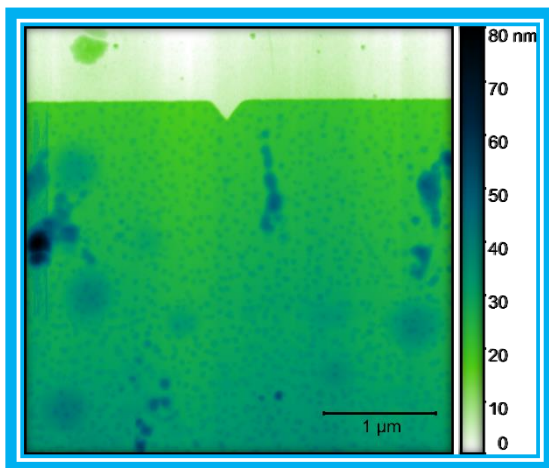
In this work, an in-situ Raman spectroscopy study was performed evaluating the effect of varying humidity levels on graphene samples of different types (i.e. exfoliated, CVD-grown and epitaxial) and thicknesses (i.e. 1LG and 2LG). For this evaluation, the G and 2D characteristic graphene

peaks were systematically analysed and compared for all the different environmental conditions. Additionally, a vector decomposition analysis method was applied to the p-doped 1LG samples (i.e. exfoliated and CVD) to extract the doping values, which were then compared with those obtained from previous studies.

From the measured Raman data, a clear shift of the G and 2D peaks for all the samples was observed under varying levels of humidity, confirming previous observations of the sensitivity of the electronic properties of graphene towards humidity. In our case, 1LG exfoliated and epitaxial samples showed the highest shifts both for the G and 2D peaks. However, generally, the dependence of the position of the peaks in all cases was increasing monotonic, showing blue-shift of the frequency for the exfoliated and CVD samples, and red-shift for the epitaxial sample. Additionally, layer dependency was observed, with the position of the peaks for 2LG of exfoliated and epitaxial graphene showing smaller change than 1LG. The same behaviour is observed for the 2D peak position for 2L CVD graphene.

These results demonstrate the potential of Raman spectroscopy as a non-invasive, fast and reliable characterisation method for the environmental doping effects in graphene. Additionally, as presented here, there is a clear route to quantify the effect of humidity in terms of carrier density change for monolayer exfoliated and CVD graphene via the vector decomposition method. The values obtained here were in agreement with previous experimental results performed by an alternative method, highlighting the robustness of our Raman based procedure.

KPFM studies: calibration method and its application for the characterisation of GFET devices



This chapter is dedicated to the study and characterisation of the local electronic properties of graphene via Kelvin probe force microscopy (KPFM). The first part of the chapter describes a calibration protocol for KPFM covering different aspects: from the fabrication of the reference samples and their UPS characterisation, to the adjustment of the KPFM parameters, which are important to minimise the feedback effects

ubiquitous in close-loop (CL) operation. Then, the tip calibration protocol is demonstrated for a set of probes with Pt coatings of different thickness, and the results are employed to find out the optimal Pt coating thickness. Finally, this part of the chapter is concluded by studying real samples of exfoliated graphene flakes of varying thickness, and obtaining the quantitative values of their work-function using the calibration protocol described. After this, in the second part of the chapter, the effect of the edge disorder in the charge transport of narrow channel gated graphene field effect transistors (GFET) is studied with KPFM. To start, the fabrication of the devices is discussed. Then, the KPFM response is analysed. Finally, the potential of KPFM as a non-invasive visualisation and characterisation technique for buried layers is discussed. The calibration protocol developed in the first section is used to extract maps of the work-function of the GFET devices.

Acknowledgments: *The first part of this chapter (section 6.3) is a slightly modified version of the article 'Calibrated Kelvin-probe force microscopy of 2D materials using Pt-coated probes' [327] published in Journal of Physics Communications in 2020, and has been reproduced here with the*

permission of the copyright holder. The results presented are a joint work performed between Dr Alexander Fernández Scarioni and Dr Hans W. Schumacher (fabrication of the calibration samples at PTB), Dr Steve Spencer (UPS measurements at NPL), Dr Richard Perry and Dr James A. Vicary (fabrication of tailored probes at NuNano), Dr Charles A. Clifford, Dr Hector Corte-Leon and myself (KPFM measurements at NPL). The second part of the chapter (section **Error! Reference source not found.**) includes results from a collaboration with DTU (Technical University of Denmark) researchers in which encapsulated narrow GFET channels were produced by Dr Xiaojing Zhao and Dr Jose Caridad, while KPFM measurements were performed at NPL by Dr Christos Melios, Dr Hector Corte-Leon and myself.

6.1 Introduction

With devices evolving continuously towards smaller sizes, and especially after the advent of 2D materials, the ability to reliably characterise the surface electronic properties of materials at the nanoscale became extremely important. In this sense, Kelvin-probe force microscopy (KPFM) is an ideal technique able to provide maps of contact potential difference V_{CPD} with high resolution. Through the V_{CPD} information of different electronic characteristics of the sample can be extracted, including local spatial distribution of the dopant species [328, 329], information about defects, dislocations and grain boundaries [330, 331], or about interfacial charge transport in heterojunctions [332–334], to name a few. Furthermore, KPFM allows to obtain quantitative values of the work-function of the sample when characterising the work-function of the tip using a calibration method, as stated by:

$$V_{CPD} = \frac{(\Phi_{tip} - \Phi_{sample})}{e} \quad (16)$$

where e is the fundamental charge of the electron, and Φ_{sample} and Φ_{tip} , are the work-functions of the sample and the tip, respectively. The work-function (Φ), defined as the energy difference between the highest occupied electronic energy level (i.e. the Fermi level) and the vacuum level, is an extremely important property, strongly dependent on the condition of the surface under investigation, and the environmental conditions. The presence of minute amounts of contamination, or the occurrence of surface reactions can change the work function substantially. This makes the experimental determination of the work-function (Φ) extremely challenging, however, it is an exceedingly important property to be characterised as it can provide important information about the surface of a material, can help to predict and understand the energy distribution channels over a surface, and also when the KPFM has been calibrated (i.e. the work-function of the tip is known), it is a quantity that can be easily comparable among different laboratories [187, 335, 336].

For the reasons stated above, KPFM has become extremely important in different fields such as the semiconductor industry [337, 338], energy applications [339, 340] or optoelectronic devices [341], among others. In recent years, KPFM became important in the growing field of 2D materials, providing information about the number of layers [342], the band alignment in 2D material heterostructures [343–346], and even about the doping levels in different environmental conditions [137, 287].

However, there are still some challenges lying ahead regarding the acquisition of accurate work-function values. Specially for 2D materials, there are several areas in which the opportunities of KPFM characterisation have not been explored yet. In this chapter, both these issues are tackled, and some insights are provided to advance the field in these two directions:

First, despite all the collective effort from the community, proper calibration of the technique to obtain reliable and consistent work-function values is still challenging. This is a consequence of the effect of certain factors such as the great dependence of the V_{CPD} of the sample on external and chemical factors [334], the status of the probe while scanning or parasitic influences such as capacitive coupling, among others. For this reason, the first half of this chapter is dedicated to the discussion of how to optimise the measurement conditions to minimise the effect of undesired parasitic contributions in frequency-modulated Kelvin probe force microscopy (FM-KPFM). Then, improvements will be developed over a currently existing method [347] with the goal of reducing the uncertainty of the obtained work-function. Finally, the robustness of this approach will be tested against real samples, exfoliated graphite/graphene flakes on top of gold contacts.

In the second half of the chapter, KPFM is employed to visualise the effect of edge disorder in the surface potential and charge transport of gated narrow channel encapsulated GFET devices. Also, the capabilities of KPFM as a non-invasive characterisation tool for buried layers is explored, using the calibration procedure developed in the first part of the chapter to obtain quantitative values of the work-function of the GFET devices.

6.2 Experimental methods

In this section, the experimental KPFM set-up, which is common for both parts of the chapter, is described, together with a short description of the samples studied.

6.2.1 KPFM set-up

The experiments were carried out on a NT-MDT Aura SPM system using FM-KPFM with the topography and surface potential images acquired simultaneously in single-pass mode [348]. This method takes advantage of the Coulombic force gradient between the tip and the sample to

compensate the contact potential difference, V_{CPD} , as explained in *chapter 3*. The measurements were performed in vacuum at $\sim 10^{-6}$ mbar and room temperature, with no prior surface conditioning of the samples, unless stated otherwise. In total, three different probes were employed as listed in the *table 6.1* below.

MODEL	SUPPLIER	MATERIAL	f_0 (kHz)	k ($N \cdot m^{-1}$)	Tip height	Tip cone angle	Curvature radius	REF
NSG03	TipsNano	Pt-coated	~ 70	1.74	14 – 16 μm	10 – 30°	~ 35 nm	[349]
PFQNE-Al	Bruker	Highly doped Si	~ 300	0.8	2.5 – 8 μm	15 – 25°	~ 5 -12 nm	[350]
SPARK 350	NuNano	Pt-coated	~ 350	42	5 – 8 μm	15 – 40°	~ 18 nm	[351]

Table 6.1. List of the probes employed during the development of a KPFM calibration procedure

In order to perform KPFM measurements reliably, the samples must be grounded. In the case of the experiments discussed in this chapter, the samples were grounded by establishing electrical connection with the NT-MDT Aura SPM system (which is directly connected to ground). This was done via a custom-made sample holder as the one shown in *figure 6.1(a)*, that was connected to the system. The samples were mounted and bonded into custom-made ceramic TO-8 headers, as the one shown in *figure 6.1(b)*, which were then fit into the sample holder.

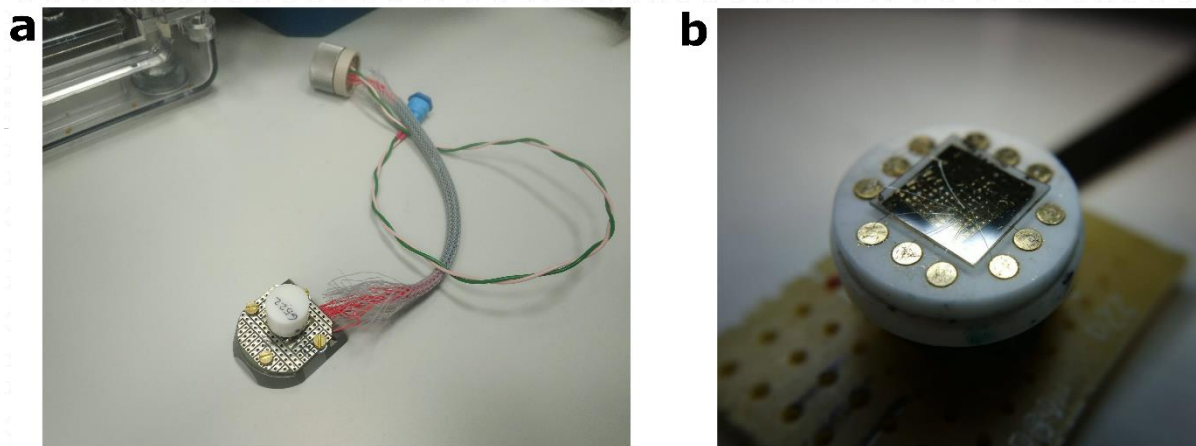


Figure 6.1.(a) Custom made sample holder for electrical measurements in the NT-MDT AURA system, allowing measurements in different environmental conditions. (b) Custom made TO-8 ceramic header. As shown in the image, the samples were fit in the centre of the holder and then connected via 12 Au pads.

Different samples were investigated in this chapter:

- For the first part (*section 6.3*), two custom calibration samples for KPFM were designed by NPL and fabricated at Physikalisch-Technische Bundesanstalt (PTB) in Germany, in order to develop a calibration protocol for KPFM. Additionally, in order to test the calibration protocol, exfoliated graphene samples were fabricated following the ‘Superposition method’ described in *chapter 4, section 4.4*, and deposited on top of pre-

patterned substrates with metallic contacts. The metallic pads in the sample were wire bonded onto the chip carrier for grounding purposes, as explained above.

- For the second part (*section **Error! Reference source not found.***), encapsulated narrow channel GFET devices with patterned constrictions were fabricated following the ‘PPC/PDMS transfer method’, explained in *chapter 4, section 4.6.2* on top of 300 nm SiO₂/Si substrates at DTU.

6.3 KPFM calibration methodology

As mentioned in the introduction of the chapter, one of the main purposes of KPFM is to provide reliable quantitative work-function values of the samples under investigation. Essentially, this depends on the correct determination of two parameters: (1) the contact potential difference (V_{CPD}) and (2) the work function of the tip used (Φ_{tip}).

Regarding the first point, it is relatively challenging to obtain accurate results of the V_{CPD} . This is so, because the value of the V_{CPD} depends on several parameters: from the status of the surface, to the measurement environment [352, 353], including the tip geometry [354], instrumentation and feedback effects [355], or even signal crosstalk [356, 357], common in close-loop (CL) KPFM operation. These deviations in the recorded V_{CPD} values difficult the comparison between measurements from different groups, or with theory. Correct selection of scanning parameters, that could minimise all these aforementioned artefacts, crosstalk and parasitic effects, are more often than not overlooked in published papers. For this reason, they will be analysed in detail in following sections.

Regarding the second point, the determination of the work-function of the tip, also known as *tip calibration*, can be done using a reference sample and rearranging the fundamental relation (*eq. 6.1*) as:

$$\Phi_{\text{tip}} = \Phi_{\text{Ref_Sample}} - eV_{\text{CPD}} \quad (17)$$

The two points described above highlight the need of having a robust calibration sample with a stable surface that does not oxidised over time or that is easy to clean. This will reduce the variability of the surface properties during the measurements, which in turn, would lead to reduced uncertainty in the resulting V_{CPD} or $\Phi_{\text{Ref_Sample}}$ measured. In previous studies, the calibration of the tip is normally performed only against one material, typically Au or HOPG. On one hand, Au is employed as it is a noble metal presenting high resistance to oxidation, while HOPG presents the advantage of being easy to peel-off, exposing a clean surface each time [331, 358]. Also, in many cases, the work-function of the reference material is not measured with an

alternative technique such as ultraviolet photon spectroscopy (UPS), but just taken from tabulated values. Based on the high variability of the contact potential difference with the status of the surface, these procedures are likely to introduce high values of uncertainty, and provide inaccurate results of work function of the sample. To overcome this, a calibration method is developed here as a robust and reliable solution: For this, the work-function of the tip is measured against several metallic surfaces, which are previously characterised by UPS. In total, two different calibration samples, including four metallic surfaces, were designed and fabricated:

- A first sample containing thin film squared pads of Au/Ti (20 nm/5nm), and Pt/Ta (20nm/5nm) deposited on a Si substrate
- Another sample of thin film squared pads of Ta (30 nm) and Ti (30 nm) on 2 μm SiO₂/Si.

These metals were selected based on the varied range of work-function values that they cover (see *table 6.2*), as well as for having high resistance to oxidation (corrosion), or because they develop a passivation oxide layers that stabilizes their surface [359–361]. Additionally, the metallic thin films were electrically connected, allowing the application of a certain bias to the pads. By doing this, the carrier density of the metals was affected, varying their work-function, and providing more than one measurement point per sample. This way, the final metal work-function was obtained by applying a linear fitting through several points, rather than a single measurement, and thus reducing the error associated with the measurement.

In the following sections, we will cover all the details related to the calibration method: UPS characterisation of the calibration samples, correct determination of scanning parameters, calibration of different probes using the fabricated samples and the result of characterising a sample of exfoliated graphene following the procedure described.

6.3.1 Ultraviolet photon spectroscopy (UPS)

Prior to the KPFM measurements, the work-function of the calibration samples (i.e. different metallic thin films) was characterised by ultraviolet photon spectroscopy (UPS). This technique takes advantage of the photoelectric effect to extract electronic information of the samples. The surfaces under study are irradiated with an ultraviolet photon beam generated by a gas discharge lamp filled with Helium, which produces photons with energies ~ 21.2 eV (He I). The impact of the photons on the surface results in the emission of photoelectrons which are then captured by an energy analyser providing information of the valence-band electronic structure of the sample and its work-function, as shown in the representative UPS spectra in *figure 6.2*.

The work-function is determined from the higher part of the binding energy spectrum (i.e. low kinetic energy), which is dominated by inelastically scattered electrons forming a high intensity

tail with a sharp cut-off. This former feature corresponds to the electrons that have just enough energy to leave the sample.

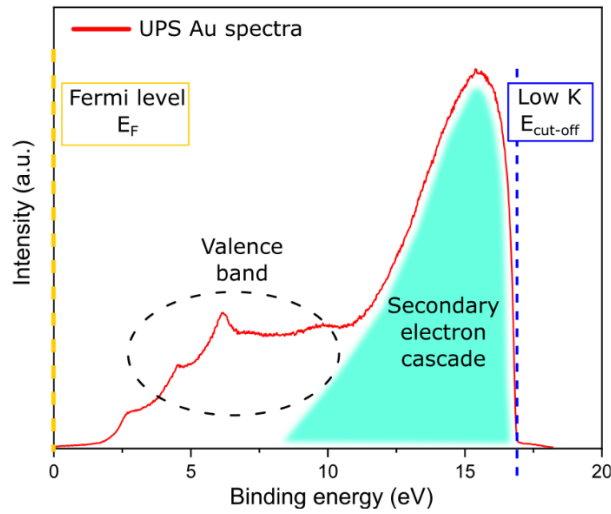


Figure 6.2. Ultraviolet photon spectroscopy diagram of the intensity versus the binding energy extracted and modified from experimental data taken from our Au reference sample. The valence band electrons area is surrounded by a dashed black circle. The area corresponding to secondary electron cascade emission is highlighted by a green background. The cut-off energy is extracted by fitting the sharp region on the curve with a straight line, represented here as a dashed dark blue line. The Fermi level is represented by a dashed yellow line.

Fitting this part of the curve (i.e. blue dashed line in figure 6.2) and extracting the intersection with the x-axis provides the cut-off energy, $E_{\text{cut-off}}$, needed to calculate the work-function as follows:

$$\Phi_{\text{sample}}^{\text{UPS}} = E_{\text{incident photon}} - E_{\text{cut-off}} = 21.2 \text{ eV} - E_{\text{cut-off}} \quad (18)$$

Optical images and UPS representative spectra of the Au and Pt reference samples are presented in the figure 6.3 below.

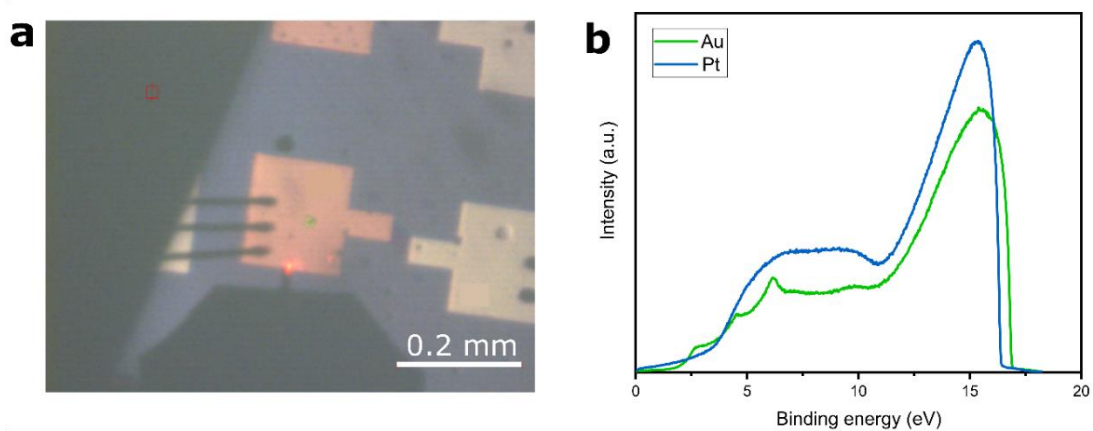


Figure 6.3. (a) Optical image of one of the calibration samples acquired with the camera of the Aura NT-MDT SPM system prior to a measurement. The wire bonds performed to the pads for grounding are visible in the image, as well as the AFM probe with the back reflected laser. (b) UPS spectra for Au (green) and Pt (blue), representing the intensity versus the binding energy.

The values of the work-functions obtained by UPS for all the different thin films reference samples are summarised in the table below:

Metal	$\Phi_{Ref_Sample}^{UPS} \pm 0.01(\text{eV})$	$\Phi^{Tab_Reference} (\text{eV})[339]$
Pt	4.84	5.40
Ti	4.43	4.10
Au	4.35	5.32
Ta	4.00	4.22

Table 6.2. Work-function values for the different selected metals obtained via UPS and from a tabulated reference[339].

According to eq.6.2, the work-function of the tips used for the KPFM measurements can now be determined just by considering the work-function values of the reference thin film samples calculated by UPS, as well as by measuring their respective V_{CPD} . For this, the samples are brought into vacuum (10^{-6} mbar) inside the NT-MDT AURA system and scanned with the selected KPFM probes. Before continuing to the next section, it is important to highlight the fact that the work-function values obtained from the UPS measurements are not close to the theoretical tabulated values obtained from the reference [339]. This could be related to different reasons, as for example, having some contamination on the surface, the presence of defects, having a different crystallographic plane with respect to the tabulated values, or even having polycrystalline films. Further experiments would be required in order to confirm these hypotheses. However, the deviation observed here, just highlights the importance of being able to use a second technique to obtain the work-function of the reference sample, rather than just rely on theoretical, tabulated or previously obtained values.

6.3.2 KPFM parameters optimisation

In this section, using the as-fabricated calibration samples, the main sources of error, parasitic signals and parameter optimisations methods for KPFM are analysed, as part of the first step of the calibration method.

Since FM-KPFM is an AFM based technique, operated in tapping mode and single-pass (at least, in this case), its operational methods involving a LIA and bias feedback could introduce some parasitic effects, related to the feedback gains and the stray capacitances. The net effect of these factors is that the input signal arriving to the feedback loop might contain contributions which are not associated with the electrostatic tip-sample forces. Therefore, not accounting for them may essentially result in unpredictable systematic errors up to hundreds of millivolts, heavily affecting the sensitivity and reliability of the measurements.

Feedback gains

As mentioned previously, the simultaneous acquisition of the topography together with the surface potential means that both signals must be optimised at the same time (*figure 6.4*), as poor calibration of one of the signals could potentially induce undesired crosstalk effects between them. Although it is rarely discussed in experimental methods section of papers, incorrect scanning gains can easily result in deviations of surface potentials corresponding to 100s of mV, therefore the selection of an optimal parameter configuration is of uppermost importance for true measurements using KPFM [357].

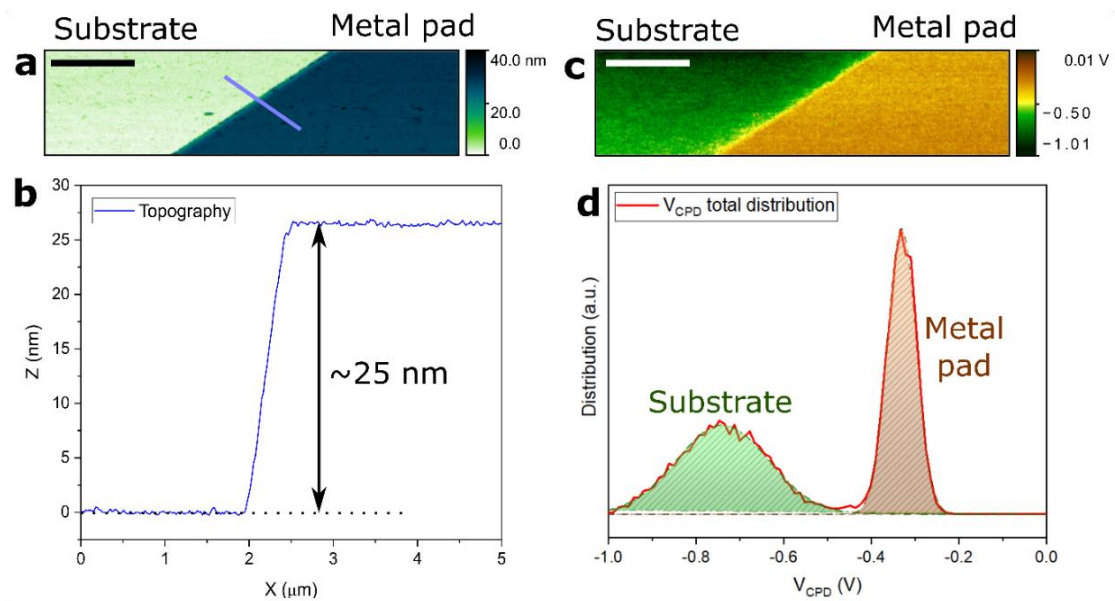


Figure 6.4. Calibration sample maps acquired using single pass FM-KPFM providing simultaneous imaging of the (a) topography and the (c) surface potential (V_{CPD}). (b) Profiles extracted from the blue line in the topography showing a step of ~ 25 nm height, and (d) V_{CPD} distribution map over the sample area showing two differentiated regions corresponding to the substrate (green) and the metal pad (brown). Scale bar: 1 μ m

Therefore, the first parameters to consider are the individual gains both for the mechanical and electrostatic loops. Due to the huge variations between systems, the effect of the PID specific values will not be discussed here¹². Alternatively, a more general and straight forward procedure based on basic AFM principles can be applied instead, which is valid for all kinds of systems.

¹² For more information, consultation of the specific manuals of the AFM system used in each case is recommended.

Most commercial AFM systems scan twice for each profile including the trace scan and the retrace scan, also known as forward and backwards scans, respectively. As demonstrated by previous studies, the correct selection of feedback parameters and line scanning rate leads to coinciding trace and retrace signals [362, 363]. The reason is that the feed between the trace and the retrace is very small, excluding the inherent mechanical hysteresis of the scanner, which results in the scanned topography by both scans almost in the same position. If the difference between the trace and retrace scans is big, it means that the tip does not trace the sample surface very well and the measurement results are poor. Thus, monitoring the trace and retrace, and using how much they match as a measure of how optimized is the system, is a good way of adjusting the gains. In the case of KPFM, it relies on long-range electrostatic forces, which means that normally the signal acquired is a weighted average of a certain region under the tip. This region is typically larger than the region covered by the topography, as the latter relies on the gradient of the van der Waals forces which is of shorter range

than the electrostatic forces, however, the same criteria as for the topography is valid, and thus monitoring trace and retrace and looking for their match when adjusting gains is also a good way of optimizing the parameters. In this regard, one of the main advantages of the prepared calibration samples is that they present two clearly differentiated topographical and potential areas, namely the thin film and the substrate, separated by a sharp edge. This clear feature (i.e. a step change) has been used as a typical potential profile in different simulations as it helps providing information of any possible cross-talk, or inconsistencies [348, 364].

Therefore, to ensure the proper functioning of the system, both topography and surface potential signals are continuously acquired while scanning across the sharp boundary, as shown in *figure 6.5*. The gains and scanning rate/speed are then adjusted until the signal to noise ratio is reduced to its minimum and both trace and retrace signals match.

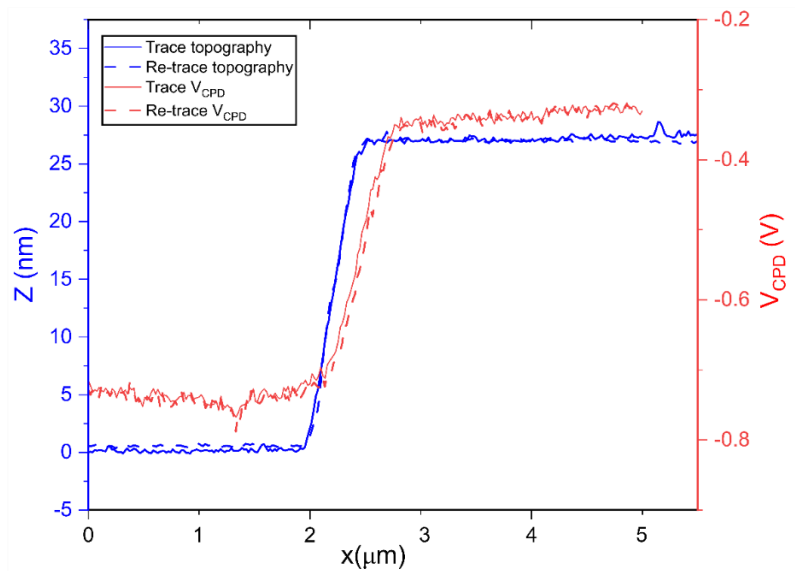


Figure 6.5. Trace and retrace profiles for the topography (blue) and the surface potential (red) acquired over the step between the metal pad and the substrate on the calibration sample.

Type of probe and the scanning speed

As it has already been discussed in previous literature, the geometry of the tip and the design of the whole cantilever is the most critical factor defining the resolution and accuracy of the acquired surface potential maps [334, 354]. Here, following the research by Jacobs et al. [357], the settling time, together with its influence on the scanning speed, is tested for two types of probes: NSG-03 probes with a Pt coating, and PFQNE-Al which are highly doped silicon probes. The settling time can be defined as the time delay between the tip potential measurement and the application of the compensating external potential. This parameter depends on the tip-sample capacitance, the gain in the feedback and the contact resistance of the tip-sample system. Furthermore, the variation of the settling time directly affects the scanning speed, a scanning parameter which is often overlooked. It is highly important to optimise this parameter as incorrect scan speeds (i.e. too fast scans) could lead to poor image quality, damage of the tip or the sample, or even artifacts, and therefore misleading or incorrect results of the V_{CPD} .

In order to find the fastest scan speed possible, stationary measurements were performed between the metal pad and the substrate alternatively, displacing the tip in non-contact between the measurement spots, as depicted in *figure 6.6(a)*. All the measurements were performed after optimizing the topography and KPFM signals using the step method described earlier. The results of the settling times obtained for the PFQNE-Al are presented in *figure 6.6(b-c)*, while for the NSG-03, these can be seen in *figure 6.6(d-e)*. In the figures, the changes in the X and Y piezo positions of the tips are shown in red full and red dashed lines, respectively, with the measured V_{CPD} signal depicted in black. The time spent measuring on top of the metal pad is highlighted in brown and the time on top of the substrate in green. Analysing the data, specially the zoomed-in details presented in *figure 6.6(c)* and *(e)*, it is obvious that the PFQNE-Al probe presents a higher settling time, needing up to ~ 140 ms for the V_{CPD} to settle to a constant value, whereas the response of the NSG-03 probes seems to be much shorter, with settling times down to ~ 30 ms. This noticeable difference in settling times, assuming that the gains were optimized to the best values in both cases, is attributed mainly to two factors: (1) the material of the probe, and (2) the radius of curvature, both of which affect the probe-sample capacitance. Regarding the first point, the PFQNE-Al probes are formed of highly n-doped silicon and have a high concentration of electrons. However, the charges in a semiconductor are not localised at the surface, instead they are distributed inside the whole semiconductor, and they react to the applied V_{AC} modulation. This means that although for certain measurement conditions the system could be approximated as a capacitor (i.e. metal-insulator-metal), in the case of the measurements performed here, it is possible that the system is behaving in a more complicated manner (i.e. metal-insulator-semiconductor). Considering the latter, the observed delayed response could be a consequence

of having the charges in the probe subjected to the effect of the varying tip-sample distance and the varying excitation voltage V_{AC} applied [185, 365]. Also, the presence of an oxide passivation layer over the highly doped silicon surface, and the presence of trapped charges in the semiconductor material could potentially have an effect on this response delay [366]. In this sense, the metal coating of the NSG-03 probes is probably an important factor to its shorter settling time, as it ensures the formation of a true capacitor between the sample and the tip (i.e. metal-insulator-metal). With respect to the radius of curvature(see *table 6.1*), previous studies have demonstrated that higher values like the one presented by the NSG-03 probes produce steeper and faster responses in agreement with our findings [354]. In the following sections only probes with metallic coatings are employed.

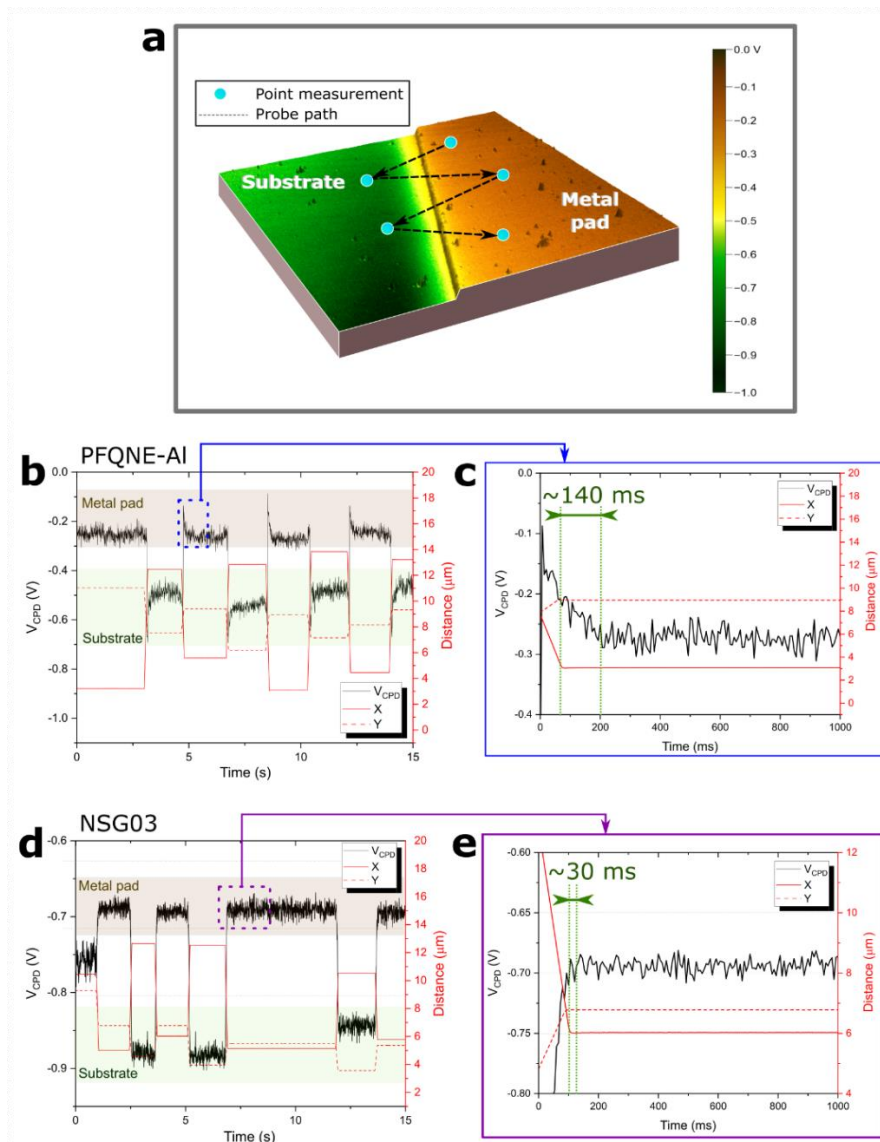


Figure 6.6. (a) 3D representation of the measured contact potential difference superimposed on the topography of the calibration sample. The substrate is shown in green, the bond pad in brown and the edge is shown in yellow. The black dashed arrows represent the trajectory followed by the probe during the measurement. Point-measurements are performed at the locations highlighted by blue dots. Temporal response of the (b) PFQNE-AI and (d) NSG03-Pt probes represented by a black line, with the profiles followed by the X and Y scan directions represented by full and dotted red

lines, respectively. Detail of the response during the first seconds of measurement for the (c)PFQNE-AI and the (e)NSG03-Pt probes.

KPFM parameters

The other two parameters that require attention, which are specifically KPFM related, are the amplitude, V_{AC} , and the frequency, f_{AC} , of the modulation voltage applied to the probe. These two parameters affect more the quantitative values measured than the settling speed. As explained in *chapter 3-section 3.1.2*, the electrostatic force between the tip and the sample is separated from the Van der Waals forces by applying a V_{AC} modulation bias together with the compensation V_{DC} . The total electrostatic force experienced by the system can be written as[185, 187, 367]:

$$F_{el} = \frac{1}{2} \frac{\partial C}{\partial z} [V_{tip} - V_{sample}]^2 = \frac{1}{2} \frac{\partial C}{\partial z} [(V_{DC} - V_{CPD}) + V_{AC} \sin(\omega t)]^2 \quad (19)$$

Where C is the capacitance of the system, and the $\partial C/\partial z$ term corresponds to the capacitive gradient between the cantilever and the sample. By expanding the square in *eq.6.4*, the final expression of the electrostatic force gives:

$$F_{el} = \frac{\partial C}{\partial z} \left[\frac{(V_{DC} - V_{CPD})^2}{2} + \frac{V_{AC}^2}{4} \right] + \frac{\partial C}{\partial z} (V_{DC} - V_{CPD}) V_{AC} \sin(\omega t) - \frac{\partial C}{\partial z} \frac{V_{AC}^2}{4} \cos(2\omega t) \quad (20)$$

The resulting *eq.6.5* can be also divided in three spectral components as:

$$F_{el} = F_{DC} + F_{\omega} + F_{2\omega} \quad (21)$$

where F_{DC} corresponds to the static term, and F_{ω} and $F_{2\omega}$ correspond to the modulated forces on the first and second harmonic, respectively. These three different terms are shown individually below:

$$F_{DC} = \frac{\partial C}{\partial z} \left[\frac{(V_{DC} - V_{CPD})^2}{2} + \frac{V_{AC}^2}{4} \right] \quad (22)$$

$$F_{\omega} = \frac{\partial C}{\partial z} (V_{DC} - V_{CPD}) V_{AC} \sin(\omega t) \quad (23)$$

$$F_{2\omega} = -\frac{\partial C}{\partial z} \frac{V_{AC}^2}{4} \cos(2\omega t) \quad (24)$$

Here, *eq.6.7* refers to the additional static force contributing to the topography output signal, F_{DC} . *Eq.6.8* is the first-harmonic of the force at the AC frequency that it is used to adjust the V_{CPD} in KPFM. Finally, *eq.6.9* is the second harmonic of the force at the AC frequency, which contains information of the gradient capacitance between the tip and the sample.

In an ideal situation, the PID controller dedicated to the KPFM looks at the deflection of the probe at frequency ω , which is proportional to F_ω , and adjusts V_{DC} until the deflection becomes zero, thus nullifying the term F_ω . Since the F_ω , according to *eq.6.8*, only nullifies when $V_{DC}=V_{CPD}$, the KPFM assumes that the value of the V_{DC} is equal to the contact potential. Under this assumption, the measured contact potential difference can then be determined independently from parameters such as the V_{AC} bias amplitude or frequency, f_{AC} .

However, this is a consequence of assuming that the capacitive coupling between the probe and the sample doesn't change due to the probe's oscillations. If the capacity does change periodically due to the oscillating probe, then the condition to minimize the force between the probe and the sample stated in *eq.6.8* becomes more complicated:

$$V_{DC} = \frac{V_{CPD}^{loc} \frac{dC_{loc}}{dz} + V_{CPD}^{Avg} \frac{dC_{cant}}{dz}}{\frac{dC_{loc}}{dz} + \frac{dC_{cant}}{dz}} + \frac{\delta}{V_{AC} \left(\frac{dC_{loc}}{dz} + \frac{dC_{cant}}{dz} \right)} \quad (25)$$

Where δ is some finite term accounting for the feedback effect and electronic offsets; V_{CPD}^{loc} and C_{loc} are the local contributions from the surface potential and the cantilever capacitance; and V_{CPD}^{Avg} and C_{cant} are the average contributions from the surface potential and the cantilever capacitance. In this way, a dependence with V_{AC} appears in the formula for the minimisation of the V_{CPD} when first order errors in capacitive compensation are considered. This also means that the role of the voltage is, in principle, more predominant than that of the excitation frequency.

Kalinin et al. [368] already studied the dependence of the feedback effect and the AC amplitude for different distances in dual-pass schemes. Here, the case of single-pass KPFM is analysed. For this, the dependence of the V_{CPD} with the modulation amplitude is studied against the Au and the Pt electrodes of the reference sample, with the results being represented in *figure 6.7(a)*. It can be seen that the V_{CPD} measured for Au and for Pt tends to constant values for AC voltage amplitudes between 3 V and 6 V. It is safe to consider that within this interval the feedback effects will be minimised, leading to measurements that are just purely a result of the electrostatic interaction. It is important to note that the point located at $V_{AC} = 2$ V does not fit within the constant value, following instead a different trend, therefore this amplitude of the AC voltages was avoided in our measurements.

Additionally, as a secondary test, the difference in V_{CPD} measured for the two metals only matches the results obtained using UPS for amplitude values above $V_{AC} = 3$ V, indicating that the voltage should be kept at least higher than this value to minimize the error introduced by uncompensated electrostatic interaction. Finally, as discussed by Glatzel et al. [185], although it is important to

keep the V_{AC} as low as possible to reduce any effect on the sample, as for example band-bending in semiconductors [184], higher voltages ($V_{AC} \geq 3$ V) are advisable in order to improve the signal to noise ratio.

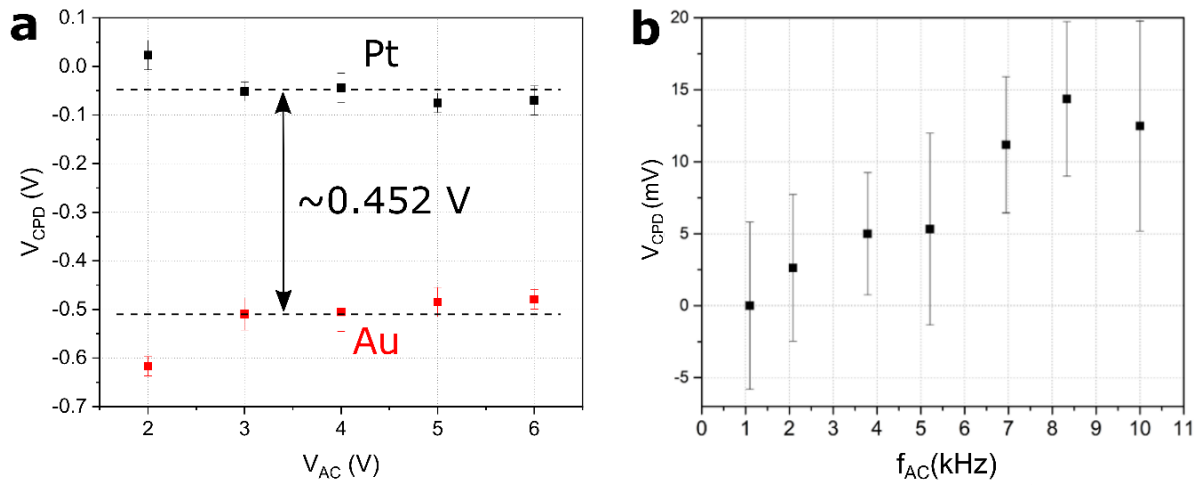


Figure 6.7. Effect of varying the (a) amplitude and (b) the frequency of the AC modulation applied to the probe on the V_{CPD} . As seen in (a), the variation of the V_{CPD} with respect to the V_{AC} has been tested for both contacts Pt and Au, showing a difference on the contact potential difference of around 450 mV, similar to the separation between the work-functions obtained with UPS measurements (~ 490 mV). In (b), The variations of the frequency have been only measured for the Au contact, however the contact potential difference changes only ~ 15 mV for the total range of frequencies tested (1 – 10 kHz).

As for the effect of the excitation frequency, f_{AC} , on the measured sample, results are presented in figure 6.7(b). This data are acquired by measuring a single electrode while keeping the V_{AC} amplitude constant and changing the excitation frequency f_{AC} , between 1 kHz and 10 kHz. Typically, for single-pass FM-KPFM, the lower limit of the frequency is dictated by an increasing cross talk between the V_{CPD} and the topography signal. The higher the frequency the lower the coupling between the topography and the surface potential, however, the bandwidth of the modulator determines the upper limit of the frequency range. In this case, the V_{CPD} presents a total deviation of ~ 25 mV, with a slight upward monotonic variation. It is important to highlight that the variation is much smaller than that produced by changes in the amplitude of V_{AC} , and therefore its contribution is minimal as expected from eq.6.10 [369].

6.3.3 Probe calibration and performance test

After analysing and optimising the scanning parameters, the calibration protocol was tested using SPARK 350 NuNano probes, made of Si with a coating of 40 nm Pt. As shown in figure 6.8(a), the values of the V_{CPD} were determined for all the reference metals with different bias voltages: For the tantalum (black) and titanium (red) samples the V_{CPD} has been measured with an applied bias between -1.5 and 1.5 V in 6 steps of 500 mV, while for the gold (pink) and platinum (blue) samples, the bias has been applied between -1 and 1 V in 8 steps of 250 mV. Each material follows a linear

trend where the intercept is given by $Intercept = V_{CPD} = \left(\frac{\phi_{probe} - \phi_{Ref_sample}}{e} \right)$, in accordance with eq.6.2.

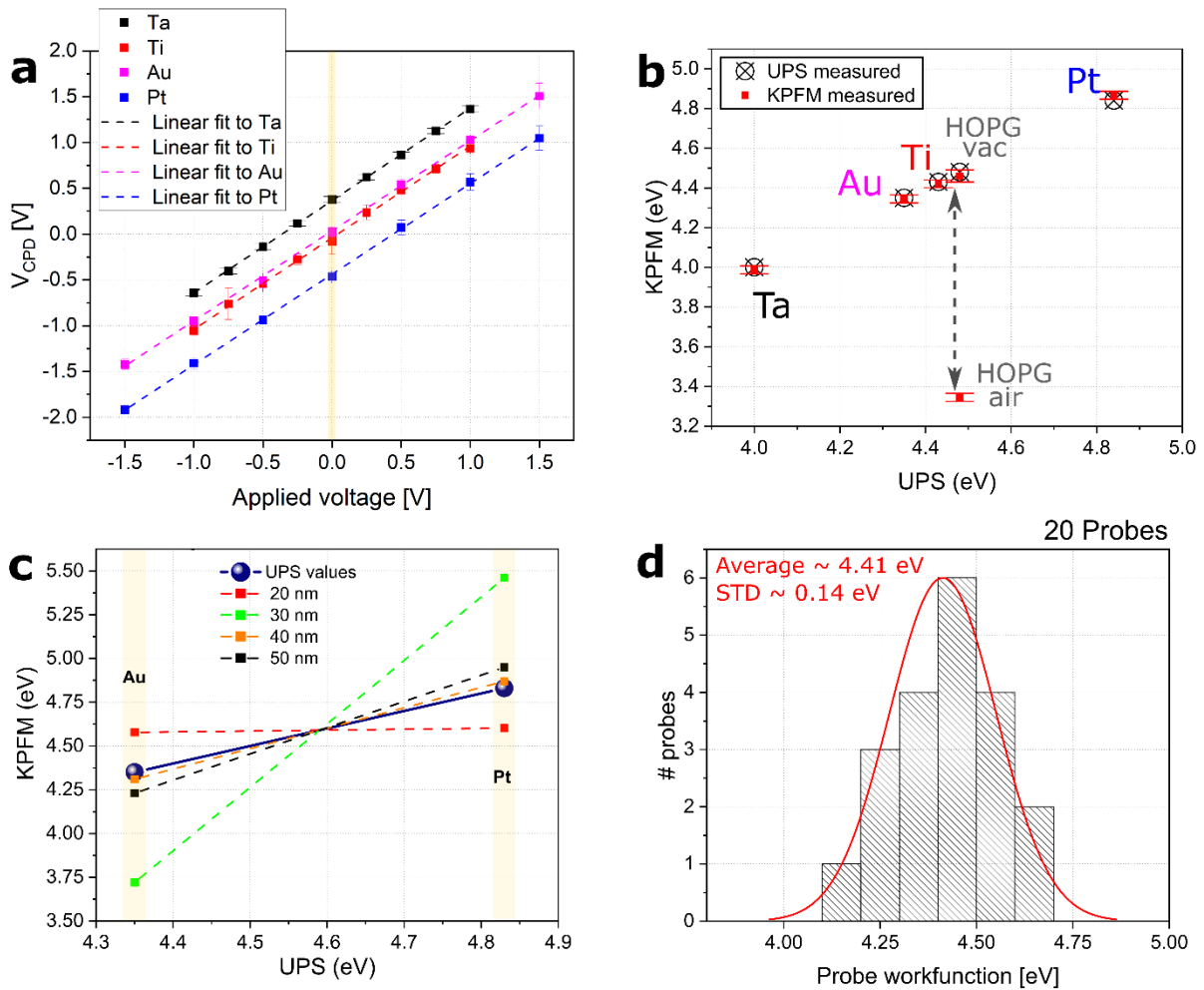


Figure 6.8.(a) Contact potential difference (V_{CPD}) measured using Pt-coated probes for all the reference samples: Pt (black), Ti (pink), Au (red) and Ta (blue) as a function of the bias voltage applied to the metal pads. The value of the V_{CPD} at $V_{BG} = 0$ is highlighted in yellow (b) Comparison of the KPFM work-function results against the UPS measured values for the different metallic reference thin films (same as in (a)) including HOPG, measured in air and in vacuum (c) Measurement of Pt and Au work-function using SPARK-350 NuNano probes with different Pt coating thickness (d) Distribution of work function values for a batch of 20 nominally identical probes (SPARK-350 NuNano, 40 nm coating).

Therefore, in order to know the intercept, the results were fit using a linear regression, and the summary of the data is presented in the table 6.3 below:

Material	Intercept (V)	Intercept standard error (V)	$\Phi_{Ref_Sample}^{UPS} \pm 0.01$ (eV)	ϕ_{probe} (eV)
Pt	-0.4341	0.007	4.84	4.41
Ti	-0.0385	0.008	4.43	4.39
Au	0.0329	0.009	4.35	4.38
Ta	0.3665	0.003	4.00	4.37

Table 6.3. Data extracted from figure 6.8(a): the intercept from the linear fitting, its error, the work function measured using UPS, and the calculated probe work-function based on the KPFM measurements using eq.6.2.

Since $\phi_{\text{Ref_sample}}$ was known via UPS, the work function of the probe was calculated from the data in the table giving an average value of ~ 4.39 eV, with a standard deviation of 14 meV. This result already improves the ones presented by other methods in which the errors typically shown are on the order of 20-100 mV, and are obtained using only based on one reference material, typically highly oriented pyrolytic graphite (HOPG) or Au [71, 184]. At this point, it is important to note that HOPG has been used as the preferred reference sample by many authors due to its low cost, easiness of manipulation, flatness and excellent electrical properties. However, it was not used for us as a calibration sample in this study as its work-function values measured in different previous studies present a large dispersion, both in air and vacuum, with values ranging from 4.5 eV up to 5 eV [184, 353, 370]. These discrepancies might be due to surface contamination, inhomogeneities, or rapid reactivity with the environment, regardless they make this reference sample unreliable.

Another advantage presented by the method here is that the results are cross-correlated with respect to another technique (i.e. UPS). To test the similarity or disparity between both methods, the KPFM work-function values for all the reference thin films (Ta, Ti, Pt, Au) tested were then compared back with the values obtained for the UPS measurements, using the newly found probe's work function, and as summarised in *figure 6.8(b)*. Besides the reference samples already tested, the calibration protocol proposed here was used to calculate the work-function of HOPG, in order to check if the values in air and vacuum present such a high variability as found in the literature. For this, two different sample preparation protocols were followed:

- The HOPG sample was cleaved in air, left it exposed to air for a short period of time (~ 10 min) and then placed it into the vacuum system ($\sim 10^{-6}$ mBar) to measure. This measurement is denominated as *HOPG Air* in *figure 6.8(b)*.
- The sample was cleaved and directly introduced in vacuum ready for the measurements. It is referred as *HOPG vac* in *figure 6.8(b)*.

It is possible to see that for all the thin films tested except Pt, the work function measured with KPFM provides generally slightly lower values than the WF calculated by UPS, however all of them are in the expected range, showing very good agreement between both techniques. However, for the HOPG there is a difference of ~ 1 eV between the air cleaved sample and the vacuum cleaved, as it has been pointed out previously [184, 371].

As in the previous section, the Pt coated probes demonstrated faster settling times with respect to the highly doped silicon ones, further studies were performed to characterise the response of Pt-coated probes (SPARK 350, NuNano) with different coating thicknesses (20 nm, 30 nm, 40 nm and 50 nm). For this, the probes were calibrated against the Au and Pt pads. The results are shown

in *figure 6.8(c)*. It can be seen that the difference between the measured work-function of the two metals vary significantly (as expected from *eq.6.10* when there is capacitive coupling). The probe with 30 nm Pt coating shows the maximum deviation from the ideal values, measuring a work function difference between Au and Pt of ~ 1.5 eV. Additionally, the probe covered with 20 nm thick Pt presents a difference between the measured Au and Pt values of around 0.004 eV, which is a deviation of $\sim 5\%$ with respect to the expected difference. Meanwhile, the values measured for the probes with 40 and 50 nm thick-coverage present a maximum deviation of only 2% with respect to the UPS-measured values. Typically, for KPFM, metal-coated tips are very popular as they are commercially available and easy to produce. Unfortunately, this type of probes could exhibit poor stability, and it is not uncommon for the metallic coating to get damaged ~~or even~~ to fall off during measurements or even capture contamination, as shown in *figure 6.9*.

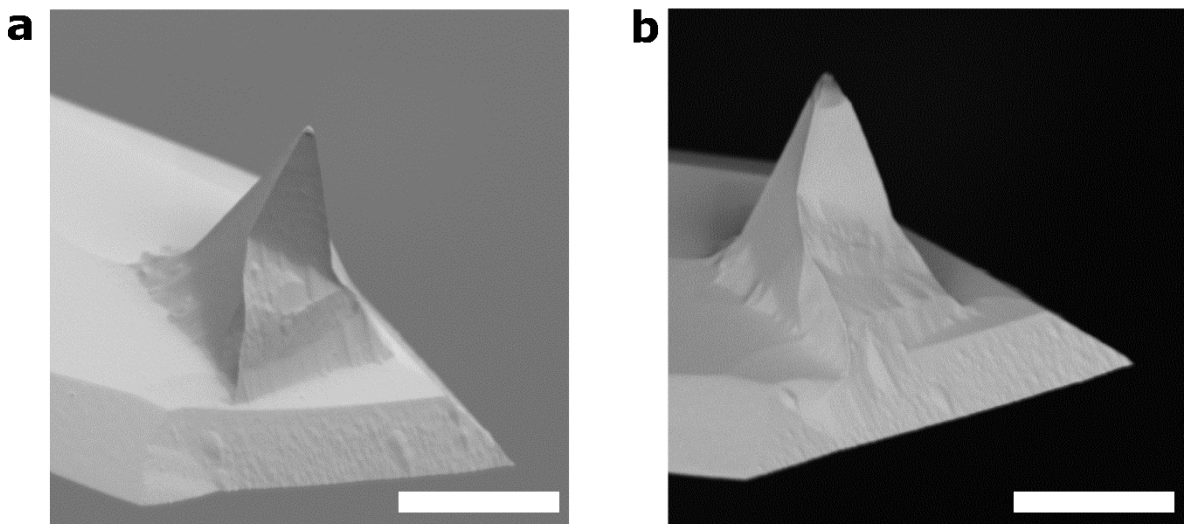


Figure 6.9. SEM images of the NSG-03 probes acquired (a) before and (b) after performing KPFM measurements. From the image in (b), it is obvious that some damage has been induced to the coating of the probe, most probably affecting the surface potential values obtained. It is not possible either to rule out the presence of contamination. Scale bar: 10 μm .

This degradation directly affects the surface potential measured, producing variations up to 350 mV, as highlighted by Jacobs et al. [357]. From the results presented in *figure 6.8(c)* seem to point out to better stability and less degradation happening for the probes with thicker coating.

However, it is also common to find variability between probes coming from the same batch. This is explored here by using the calibration protocol developed here to compare the work-function of 20 nominally identical probes with 40 nm Pt coating SPARK 350 probes. The results, presented in *figure 6.8(d)*, show that the average work function of the 20 probes is ~ 4.41 eV with a standard deviation of 0.15 eV. This value of the work function presents a 3% deviation with respect to the first probe tested. Although the deviation is relatively low within the same batch, showing very small variability due to fabrication, this deviation must be taken into account as it also adds to the uncertainty of the KPFM final results.

6.3.4 Characterisation of the KPFM spatial resolution

The resolution of the probes, both in terms of topography and contact potential difference, is characterised using the so-called *graphene fingers* sample. This sample consists of epitaxial graphene grown from a SiC substrate by stopping the development before a continuous graphene monolayer was developed through the whole substrate. The name of graphene fingers is used due to the characteristic shape of the monolayer, which forms long thin stripes similar to fingers (See [372] for further details). The sample was chosen for this task due to the small topographic features it presents, which minimize the effect of topography in the KPFM signal [364], and the relative big difference in work function from the graphene to the substrate needed for a good quantification of the KPFM spatial resolution [373].

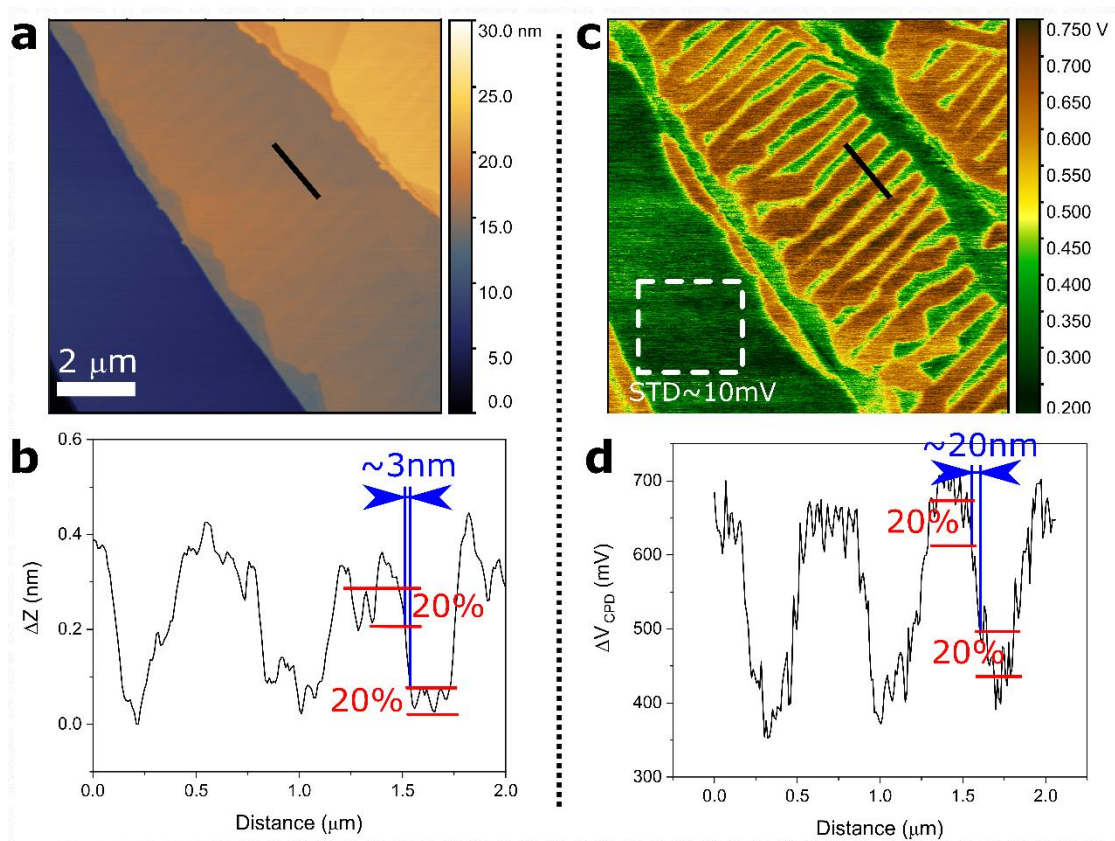


Figure 6.10. Maps of the (a) topography and (c) surface potential of an area with graphene fingers. Scale bar is $2\ \mu\text{m}$, and both images present the same aspect-ratio. Profiles extracted from the black line are represented for the (b) topography and the (d) surface potential.

Figure 6.10(a) shows the topography of an area with graphene fingers, with a cross-section profile of the height acquired over several fingers shown as a black line. By using the 20-80 rule of Edge Spread Function defined in Standards on Lateral Resolution [374], the spatial resolution of the probes was estimated to be $\sim 3\ \text{nm}$. FIGURE 6.10(c) shows the V_{CPD} measurements of the same area as in figure 6.10(a). A profile of the surface potential acquired across the black line in figure 6.10(c) over several fingers shows that the spatial resolution of the KPFM is $\sim 20\ \text{nm}$ for these

probes. By measuring the standard deviation of an homogeneous area (dashed square in *figure 6.10(c)*), the noise of the KPFM measurements was measured at ~ 10 mV.

6.3.5 Example: work-function vs thickness dependence

In this last section, the reliability of the proposed calibration protocol was tested against a real 2D material's-based sample using different probes. The assumption is that by following the calibration protocol, different probes should be able to reproduce certain measurements, and be consistent and accurate in the V_{CPD} values measured. To test this, the work-function of a set of exfoliated graphite flakes of different thicknesses were studied using different probes, SPARK 350 NuNano, calibrated following the procedure described in the previous section.

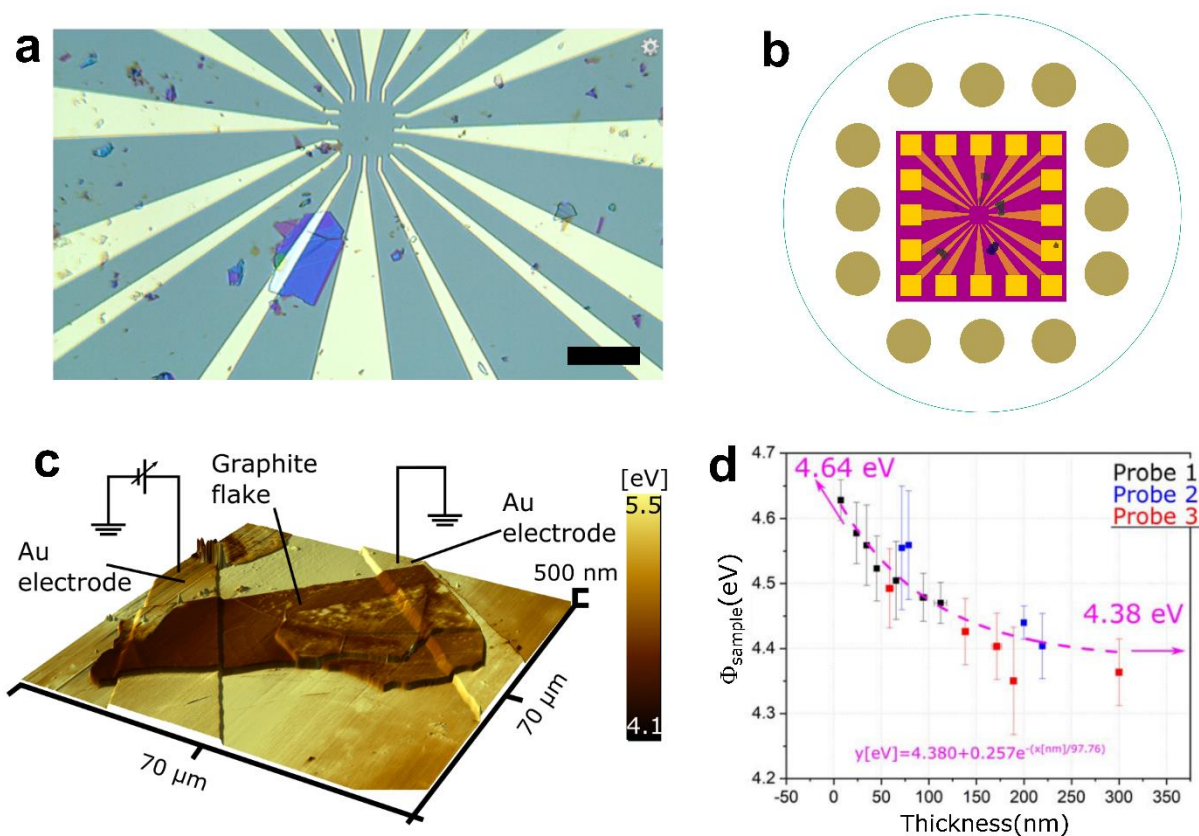


Figure 6.11. (a) Optical image of exfoliated flakes deposited on SiO_2 substrates with pre-patterned gold contacts. Scale bar: 10 μm . (b) Schematic depiction of the hand-made TO-8 headers, with the exfoliated sample placed in the centre, ready to perform bonding to the Au contact pads, depicted in gold colour. (c) 3D topographic view of a graphite flake sitting on top of two Au electrodes, with the work-function map superimposed. (d) Evolution of the work-function with respect to the graphite thickness. The results were obtained for 3 different probes, calibrated following the proposed method. The arrows indicate that graphene work-function tends to ~ 4.64 eV for monolayer, and to ~ 4.38 eV for bulk.

For the fabrication of the samples, graphite flakes were exfoliated onto pre-patterned metal electrodes on a Si/SiO₂ substrate following the ‘Superposition method’ explained in *chapter 4, section 4.4*, which led to a random distribution of flakes over the surface, as shown in *figure 6.11(a)*. Then, optical inspection was performed to see if any suitable flake was deposited onto

one or two electrical Au contacts. If so, the sample was mounted on the previously described TO-8 headers, as depicted in the schematics shown in *figure 6.11(b)*, and then contacted electrically through wire-bonding. This procedure was repeated several times in order to obtain a collection of contacted graphene/graphite flakes of varying thicknesses. The samples were then measured using KPFM in vacuum (10^{-6} mbar) as shown in *figure 6.11(c)*, using the three different probes already calibrated. As shown in *figure 6.11(d)*, it is possible to see there that there is a correlation between the number of layers (i.e. thickness), and the work function of graphene. Also it can be seen that the results obtained using three different probes match each other allowing to reconstruct the thickness dependence. The experimental results were fitted with an exponential curve (no theoretical justification, just one of the curves that best fits the results), with arrows showing that for thin flakes the values approached to ~ 4.64 eV, while for bulk the workfunction tended to ~ 4.38 eV. These values are slightly different from what was measured in previous studies which presented work-functions of 4.55 eV [71] and 4.48 eV for monolayer and bulk graphite, respectively. This difference can be attributed mainly to variations of the work-function of graphene due to the type of substrate and the fabrication method employed, which has proven to be able to introduce variations up to ~ 0.25 – 1.02 eV [375–378], mainly as a result of the different doping mechanism. However, what is clear from these measurements is the value of a good calibration procedure, as it allows comparing results taken at different moments in time, and even with different probes.

6.4 KPFM studies of gate electrostatic on GFET devices

In this section, graphene field effect transistors (GFET) were studied as part of a collaboration with Denmark Technical University (DTU). The main idea behind the experiment was to investigate the effect of the edge disorder in the charge transport profiles of narrow graphene devices for different back-gate voltages (V_{BG}).

In general, the relation of V_{BG} and the local distribution of the induced carrier density in graphene devices is complicated, and still nowadays remains largely unexplored. The relationship between the two quantities arises from classical electrostatic interactions together with quantum mechanical effects related to modifications in the graphene band structure under gating. But not only that, $V_{BG}(n)$ is also sensitive to other factors such as the device geometry, edge morphology and external conditions. Previous theoretical studies have predicted the macroscopic charge accumulation along the boundaries of graphene stripes of mechanically exfoliated graphene films as a consequence of the hard wall potential boundaries, leading to an inhomogeneous charge distribution of classical origin [379]. More recent magnetoconductance experiments have demonstrated that edge disorder has an extremely important effect on the level of charge

accumulation on the devices. For devices with large edge disorder (> 5 nm roughness) nearly homogeneous capacitance profile across the device channel has been observed, very close to the ideal parallel plate capacitor model. However, in contrast, devices with lower edge disorder (> 1 nm roughness) have shown a larger effective capacitance profile, strongly influenced by the fringing electrostatic field present at the graphene boundaries, meaning that the charge distribution on a graphene narrow channel would be highly dependent on the type of edge present in the device [380, 381].

As there are no experimental visualisations of the effects described above to the best of our knowledge, the experiment presented in this section was designed to provide further details of the charge transport profiles of gated systems with abrupt potentials and with the presence of a V_{BG} . For this, GFET devices were fabricated with a very specific architecture. All the theoretical and experimental observations described above were performed with narrow graphene stripes, therefore, the devices studied here consisted on graphene stripes with typical lengths of $\sim 3.5 - 5$ μm and widths ~ 1.5 μm , with a constriction section of ~ 1 μm width as shown in the schematic design of *figure 6.12*. To avoid having any kind of external disruption in the electrostatic potential, whether coming from substrate-induced random potentials or environmentally adsorbed species, the graphene devices were all fully encapsulated with hBN. To apply the gate, the devices were deposited on top of 300 nm SiO_2/Si . To be able to study both, edges with low disorder (LD), called natural edges from now on, and edges with high disorder (HD), denominated as etched edges in the following, special considerations and techniques were applied during fabrication, as it will be discussed in the next section.

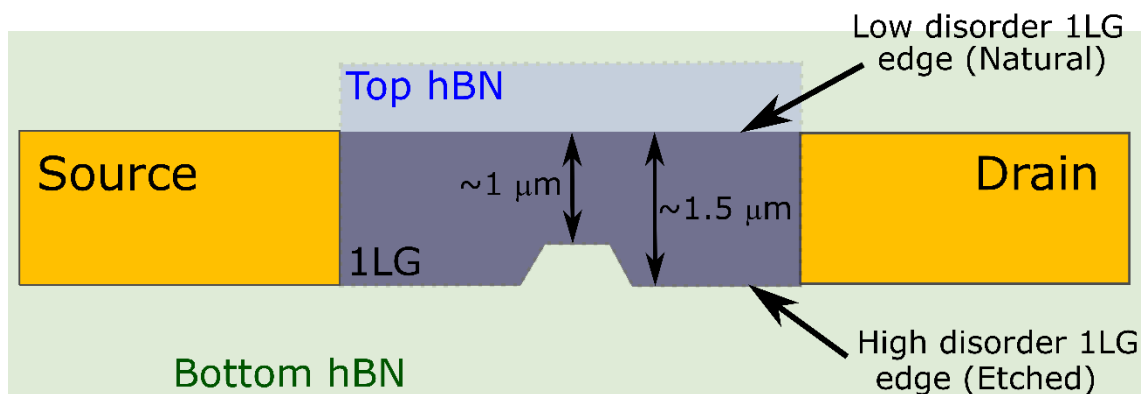


Figure 6.12. Schematic design for the narrow channel GFET encapsulated devices. The bottom hBN is signalled as light green background, the top hBN with a blue square and the graphene is shown as a grey stripe.

As a visualisation technique, FM-KPFM was used to obtain maps of the surface potential, V_{CPD} , across the channels for different values of the back-gate. This allowed the study of the profiles of the surface potential and therefore of the induced modulation of the carrier concentration and the charge accumulation with varying V_{BG} . The system was calibrated following the procedure

described in the previous section to obtain quantitative information of the surface potential fluctuations and local work-function distribution of our devices. FM-KPFM was selected as the imaging tool due to its high resolution ($< 20 - 25$ nm) and its non-invasiveness nature compared with other techniques [187, 358].

6.4.1 GFET device fabrication

The encapsulated graphene devices (hBN/1LG/hBN) were fabricated following the exfoliation methods and the PPC/PDMS transfer procedure previously explained in *chapter 4, section 4.6*. It is important to highlight that, in order to create the natural edge (i.e. low disorder edge), graphene flakes showing one straight edge directly after fabrication were selected to create the heterostructures, while the rough edge was produced by etching the other side. The process of patterning the shape of the GFET devices used here is quite unique, as it allowed patterning several devices for each heterostructure created. The details of the process are explained below:

1. **Resist deposition:** A layer of 4wt% PMMA 996K, purchased from Sigma-Aldrich, was spun-coated on top of the chip containing the heterostructure at a speed of 2000 revolutions per minute (rpm) for 1 minute with an acceleration of 500 rpm.
2. **Shape patterning:** Then, the resist was cured using e-beam lithography (JEOL JBX-9500FS) following the desired geometry for the devices with a current of 6 nA and a dose of $800-1000 \mu\text{C}/\text{cm}^2$. The PMMA was used as a high-resolution positive resist, therefore the areas exposed to the electron beam experienced a change in their molecular weight and were subsequently removed during the developing process.

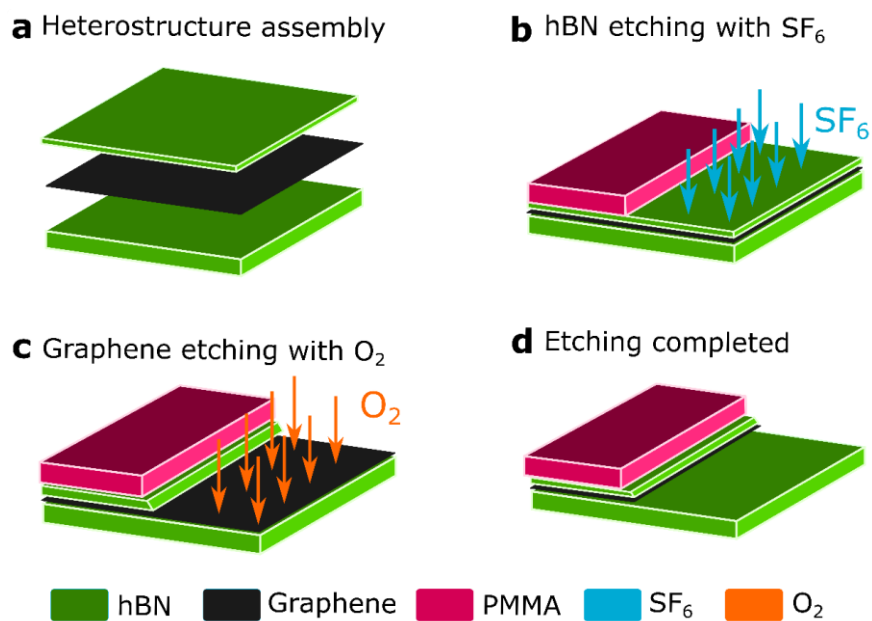


Figure 6.13. Selective etching process of the encapsulated graphene heterostructure shown in (a). (b) hBN etching with SF₆ (c) Graphene etching with O₂ and (d) Final device after etching

3. **Developing:** A weak developer formed by IPA:H₂O in a proportion 3:1 was used in this case. The chip was immersed and swung in the developer for ~1 minute, which resulted in the removal of all the PMMA cured by the electron beam. Following this, the chip was rinsed with IPA and blow with dry with N₂ to eliminate any further contamination from the surface.
4. **Etching:** To finalise the pattern shaping, the top hBN and the graphene layers were etched. For this, highly selective etching techniques were applied, attacking the layers individually in a two-step process performed in an SPTS ICP etcher. The hBN was initially etched using sulfur hexafluoride (SF₆) at a flow rate of 40 sccm, with pressure of 80 mTorr and a coil/platen power of 0/75 W during 5 seconds, as shown in *figure 6.13(b)*. Then, the graphene layer was etched using a mixture of O₂/Ar at flow rates of 5/15 sccm with 80 mTorr and a coil/platen power of 0/20 W during 10 seconds, as depicted in *figure 6.13(c)*. Monolayer graphene is not etched by the SF₆, working as a mask for the bottom hBN. However, as a result of this process the graphene becomes fluorinated. The bottom hBN layer was not etched in order to minimise the effect of the substrate during KPFM measurements.
5. **PMMA mask removal:** After the etching, the rest of the PMMA mask was removed by rinsing the chip in acetone, IPA and DI water, and finally dried with N₂.
6. **Annealing:** To follow, the structure was annealed at 180 °C for a duration of 5-10 min.
7. **Resist deposition:** a new layer of resist, in this case consisting of 6wt% PMMA, was spun coated on top at a speed of 2000 rpm, during 1 minute, with an acceleration of 500 rpm. The structure was baked at 180 °C for 2 minutes.

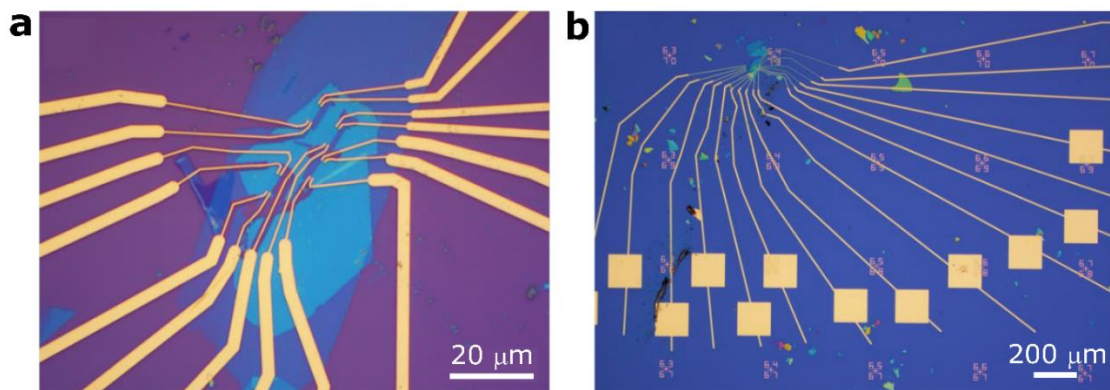


Figure 6.14. Optical images of the devices after the fabrication process with magnification (a) x20 and (b) x5.

8. **Shaping the contacts:** EBL was then used again in order to create a mask with the suitable shape of the contacts with the same current and dose as for the previous process.
9. **PMMA evaporation and metallisation:** After developing the resist, the contacts were deposited, by evaporating first an adhesion 10 nm layer of chromium at a rate of 1 Å s⁻¹,

and second a 100 nm layer of gold to be used as the contacts at a rate of 3 \AA s^{-1} . Here, 1D contacts as the ones explained in *chapter 4, section 4.7* were employed.

10. **Resist removal:** the sides of the carrier chip were carefully scratched using a pair of tweezers in order to favour the successful removal of the resist during the lift-off process. Then, the chip was immersed in acetone until the surface of the top metallic layer that was deposited became corrugated. Finally, a pipette was used to gently spray the acetone at the wrinkled metal to speed up the process.

After all this process, the graphene heterostructures were patterned as shown in the optical images in *figure 6.14*. As it can be seen, one of the advantages of this fabrication technique is that it allowed patterning several devices on the same heterostructure, maximising the output and efficiency of the fabrication method, and highly minimising the fabrication time. Additionally, another important point to highlight from the fabrication procedure is the use of oxygen plasma ashing to edge the graphene rather than other alternatives, such as RIE argon. This choice was done so based on previous studies which have demonstrated that plasma ashing led to rougher graphene edges than other methods (i.e. high disordered edges), enhancing this way the difference between the natural (i.e. low-disorder) and the etched (high-disorder) edges [381–383].

In the case of this experiment, several sets of samples were measured. For the initial set of samples wire bonding was employed to establish electrical connection between the sample and the chip carrier. However, as explained in *chapter 4, section 4.7*, the leakage current observed in some cases was high, meaning that the samples were shorted as the wire bonding pierced through the oxide layer. In order to avoid this issue, for following sets of samples, the metallic pads of the samples were connected to the chip carrier pads using silver epoxy instead. The results presented in this chapter correspond to this last set of measurements.

6.4.2 KPFM measurements

The study of the local surface potential and charge distribution of the GFET devices was performed using FM-KPFM. Quantitative work-function values were extracted as the work-function of the tip was obtained following the calibration procedure developed in the previous part of the chapter (*section 6.3*). The schematics of the experimental set-up are depicted in *figure 6.15(a)*, with the compensation voltage, V_{DC} , applied to the tip in this case, and with the work-function of the sample calculated following *eq.6.1*. As highlighted in orange in the optical micrograph in *figure 6.15 (b)*, four devices were fabricated on the same heterostructure.

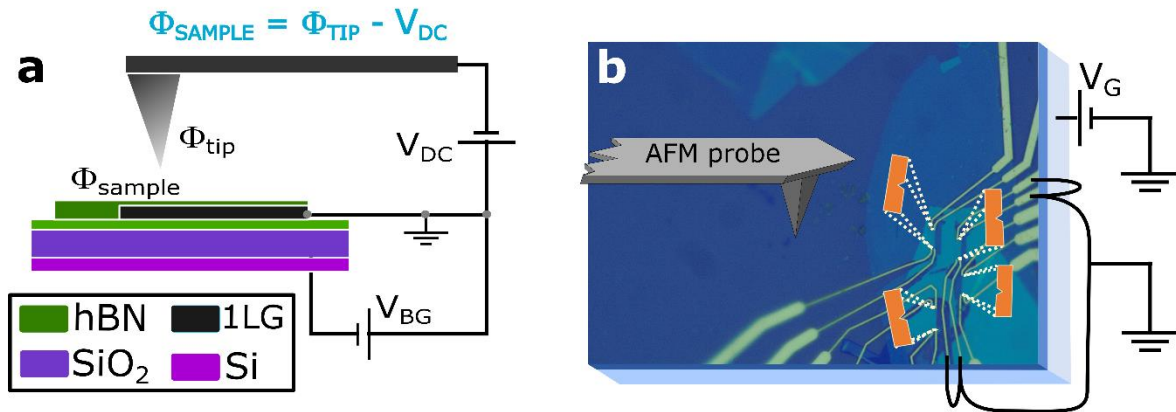


Figure 6.15. **(a)** Electrical schematics of the KPFM experiment with a back-gate voltage applied. The compensation voltage, V_{DC} , was applied to the tip. The work-function of the sample can be locally calculated by using the already known work-function of the tip and the measured V_{DC} . **(b)** Optical micrograph of the device. Four different devices fabricated in the same heterostructure are highlighted by orange rectangular shapes. The approaching direction of the probe with respect to the devices is shown. The electrical connections are represented by black lines.

Also, and very importantly, the probe was approached from the left side of the devices in order to avoid scanning on top of the contacts, which could induce additional parasitic capacitance effects in the KPFM measurements. Details of the topography of the heterostructures are presented in *figure 6.16(a)*, with the bottom hBN layer showing a light green contrast, and also, signalled by black letters. The encapsulated graphene is surrounded by a yellow dashed line, while the top hBN is highlighted by a dark blue dotted line. The Cr/Au contacts are located in pairs at the sides of the graphene channel, showing a thickness of ~ 110 nm, and therefore presenting darker green contrast. The surface potential acquired over the same area is shown in *figure 6.16(b)* for two different values of the backgate voltage, having on the top, $V_{BG} = 0$ V, and on the bottom, $V_{BG} = 5$ V.

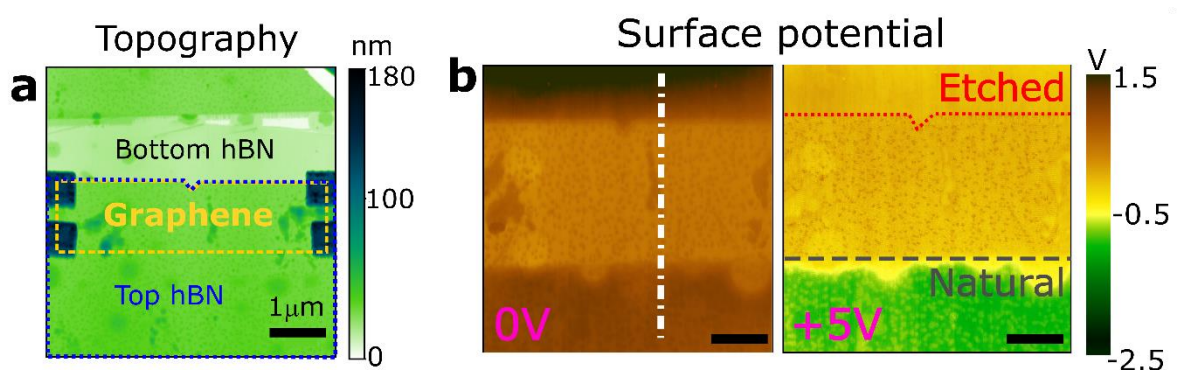


Figure 6.16. **(a)** Topography of the device showing the different layers: the bottom hBN(black sign), the graphene buried layer(yellow outline) and the top hBN(Blue dotted outline). The contacts are located in pairs on the sides, showing a dark green contrast. **(b)** Surface potential maps of the narrow graphene channel from (c). Two different SP maps are presented for two different applied backgate voltages, 0 V (top) and +5 V (bottom). The voltage colour scale has been normalised for both measurements. Scale bar: $1 \mu\text{m}$.

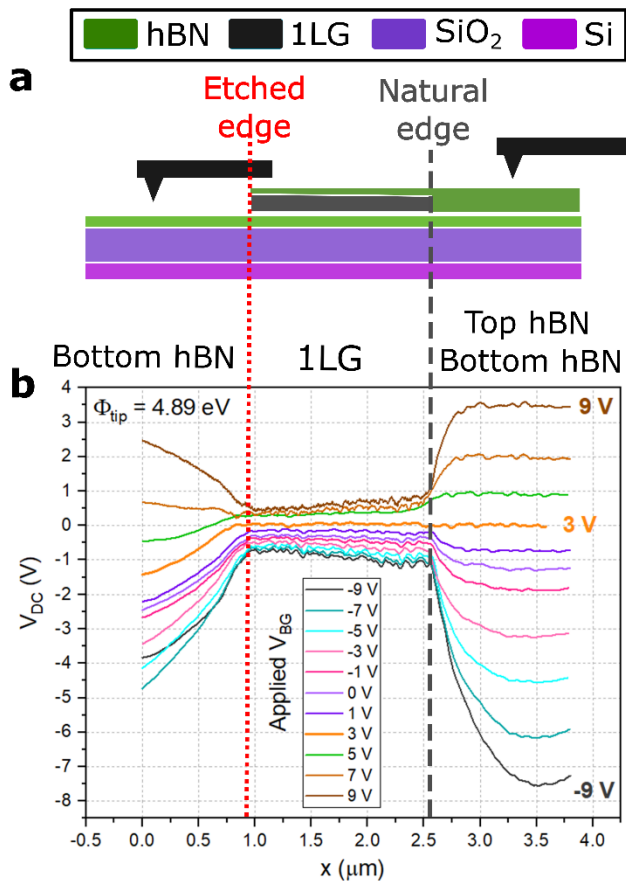
Changing the values of V_{BG} applied to the degenerately doped Si substrate can be translated into a modification of the charge carrier density in the graphene layer, and hence in the surface potential of the sample following:

$$U(x) = -\hbar v_F \sqrt{\pi n_{el}(x)} \quad (26)$$

where $U(x)$ is the electrostatic potential associated with the applied electric field, \hbar and v_F are the reduced Planck constant and Fermi velocity, respectively; $n_{el}(x)$ is the effectively injected charges which are position-dependent, and x is the planar position across the graphene channel. The changes on the surface potential for different values of the V_{BG} are obvious when comparing the top and bottom images of the V_{CPD} shown in *figure 6.16(b)*.

Another very noticeable feature that can be observed directly when comparing *figure 6.16(a)* and *(b)* together is that, although the sandwiched graphene layer is not distinguishable in the topography map due to the top hBN covering it, it becomes clearly visible in the surface potential map, especially for $V_{BG} = 0V$, with the graphene layer showing higher surface voltage than the dielectric background. Taking advantage of the clearer contrast observed for the buried graphene layer on the surface potential images, the outlines corresponding to the etched (high disorder) and natural (low disorder) edges are highlighted in red and grey, respectively, in the bottom *figure 6.17(a)*.

In order to study the surface potential distribution, and quantify if there is charge accumulation at the two different edges present in the device, etched vs natural, line profiles of the V_{CPD} were acquired following the white dashed line in *figure 6.16(b)*, and represented in *figure 6.17(b)*. As



mentioned in the introduction of this section, recent theoretical and experimental studies have pointed out that due to the small DOS in graphene, the in-plane charge density for narrow graphene channels should follow a non-monotonic trend, varying as a function of the position, x , across the device. Especially at the edges, the accumulation of charges is expected to be higher than in the centre of the device. Furthermore, it is expected that low-disorder edges, natural in our case, would have higher concentration of carriers than high-disorder edges (etched edges).

Figure 6.17. (a) Schematic lateral view of the device, showing the substrate formed of Si (light purple) and 300 nm of SiO₂ (dark purple), with a graphene layer (black) encapsulated between hBN layers (green) on top. (b) V_{CPD} line profiles represented for different V_{BG} and acquired following the white dashed line in figure 6.16(b).

Based on this, the potential profile that is expected for a graphene stripe like the one studied here is similar to the one presented in figure 6.18. It is formed by a U shape section, typically present for metals shaped in this geometry and subjected to an external electric field, and with downturned brims appearing at the edges due to the charge accumulation. This latter element is considered “graphene-specific” and it is exactly what we are trying to visualise with this experiment.

As can be observed in figure 6.17(b), the potential lines across the graphene channel, denoted as 1LG, in the figure present a very clear ambipolar behaviour when shifting V_{BG} . However, no relevant features were observed near the edges, but just smooth transitions of the V_{CPD} . Several GFET devices with the same architecture were investigated following the same procedure, but no clear change of the surface potential was observed in any of them.

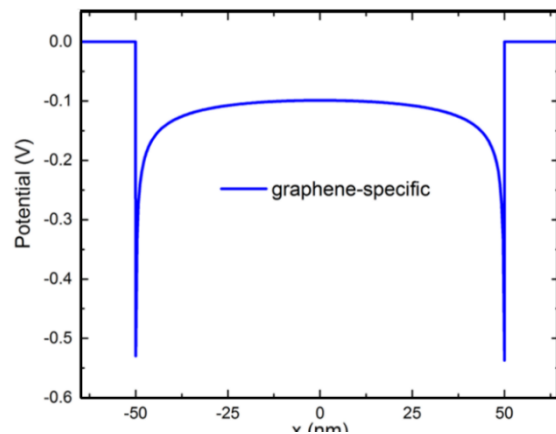


Figure 6.18. Graphene specific potential profile across a 100 nm wide graphene strip for a $V_{BG} = +10V$. The downturned brims at the edges originate from quantum capacitance effects characteristic for graphene. Image adapted with permission from [439]

The resolution of KPFM, down to $\leq 20 \text{ nm}$ should be enough to allow the visualisation of the effect. Therefore, the absence of accumulation of charge around the boundaries is attributed, in this case, to the dirtiness trapped between the layers of the heterostructure, probably polymeric residues result of the transfer process (which can be seen as dark grains in the graphene area in *figure 6.16(b)*). For this type of effect to be observed it is extremely important to have a pristine graphene surface as the transport needs to be ballistic. Any trapped contamination or p-dopants such as oxygen or water, would act as scattering centres and affect the charge distribution of graphene[384, 385]. Unfortunately, this contamination was common to all the devices investigated for this experiment. Generally, the PPC/PDMS method is relatively clean, however, it can happen that contamination is trapped between the layers. This is normally a consequence of rushing up the transfer process, using fast speeds that don't leave time to the PPC front (as shown in *chapter 4*) to push the dirtiness away, or even, a consequence of using the wrong temperatures during transfer. It can also be just part of statistically defective stacks. In order to try to still visualise the effect of the charge accumulation at the edges, there are two possible routes to undertake:

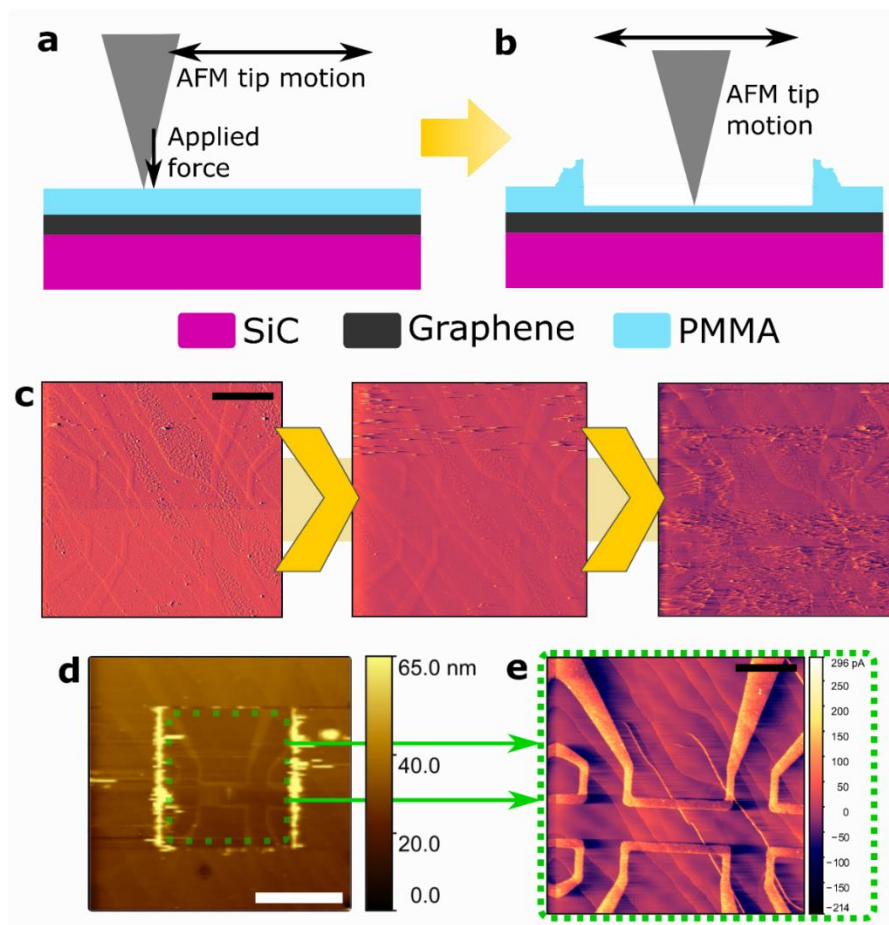


Figure 6.19. Schematic drawing showing: (a) the concept of AFM brooming, and (b) the effect of removing the PMMA layers with the consequent accumulation of debris on the sides of the scan. At the end of the process the PMMA in the central area is fully removed and accumulated at the sides. (c) Deflection signal showing the effect of the removal of the PMMA layer

from the surface through time. Scale bar: 2 μm **(d)** Larger topography map including the area that has been broomed, showing the accumulation of the polymer at the edges of the square. Scale bar: 5 μm **(e)** Deflection detail taken around the dashed green square after the cleaning has been finished. Scale bar: 2 μm .

- Use the brooming process with contact AFM to try to remove the dirtiness accumulated in between the layers, as shown in the example in *figure 6.19*, in which contact mode was used to remove the protective PMMA layer of epitaxial graphene devices.
- Build new stacks and design new devices, making sure prior to the KPFM measurements that the devices are completely clean with no accumulated contamination between the layers.

Coming back to the contact potential difference profiles presented in *figure 6.17(b)*, the profiles observed from the insulating regions are also of interest. As a result of the unscreened electric field from the back-gate, the value of V_{CPD} tends to increase to values comparable to V_{BG} . However, there is a clear asymmetry between the two insulating regions considered in our device. The area with a dielectric layer formed by air/bottom hBN/SiO₂/(see lateral view of *figure 6.15(a)*), presents a lower increase on the V_{CPD} with respect to the area formed by air/top hBN/bottom hBN/SiO₂. This notable variation is attributed to the position of the tip during the measurement. While measuring latter, the probe is only placed over a dielectric, therefore experiencing long-range unscreened electrostatic forces directly from the Si back-gate. The former was measured with the probe positioned on top of graphene, which partially screened the electrostatic forces from the back-gate, reducing its effect on the V_{CPD} measured in that area. A simple solution to test if this interpretation is correct would be to rotate the devices 180°. However, for these devices, this test could not be applied, as rotating the devices would imply scanning on top of all the metallic contacts, which would result in strong capacitive coupling effects between the probe and the contacts. Another solution would be to produce a design for the heterostructures with contacts placed at the top and the bottom, leaving the possibility of rotating the devices 180°.

At this point, although the main results expected from the experiment were not observed, there was another aspect of the measurements that seemed outstanding and worth further exploration: the capability of imaging buried layers provided by KPFM. As discussed in previous chapters, hBN encapsulation has become a paramount procedure in order to preserve and protect the properties of 2D materials. However, while encapsulation offers unparalleled performance advantage, it obscures the sample characterization. Accessing the buried layers to characterise their position within the stacks, the levels of contamination, the number of layers, or their flatness, is of vital importance. Currently, Raman spectroscopy can be employed for this, and can provide information of the number of layers, doping, defects and strain, as discussed in the previous chapter. On the other hand, dark field microscopy can also be employed to image buried layers, but only for thin top layers. However, the main disadvantage of these optical techniques is that

their resolution is hugely limited by diffraction down to $\sim 500\text{nm} - 1\mu\text{m}$. As an alternative AFM, which has resolution in the nanoscale range, can only provide information of the thickness of the layers, but only in the best-case scenario [386, 387].

In this sense, KPFM seems to be the perfect tool to overcome all these challenges. It has proven to be a fast, effective and non-invasive technique to find the position of the buried layers, identify the presence of interlayer contaminants and map the local surface potential variations with high resolution, competing in versatility with the already established techniques, such as Raman and AFM. This can be observed in the collection of maps acquired for the different back-gate voltages (labelled in blue) presented in *figure 6.20*. Also, note that these are work-function maps, rather than V_{CPD} . As mentioned in the beginning of the section, the tip was calibrated using the procedure developed in the first part of the chapter, allowing the calculation of quantitative values of the work-function of these devices following $\Phi_{sample} = \Phi_{tip} - eV_{CPD}$.

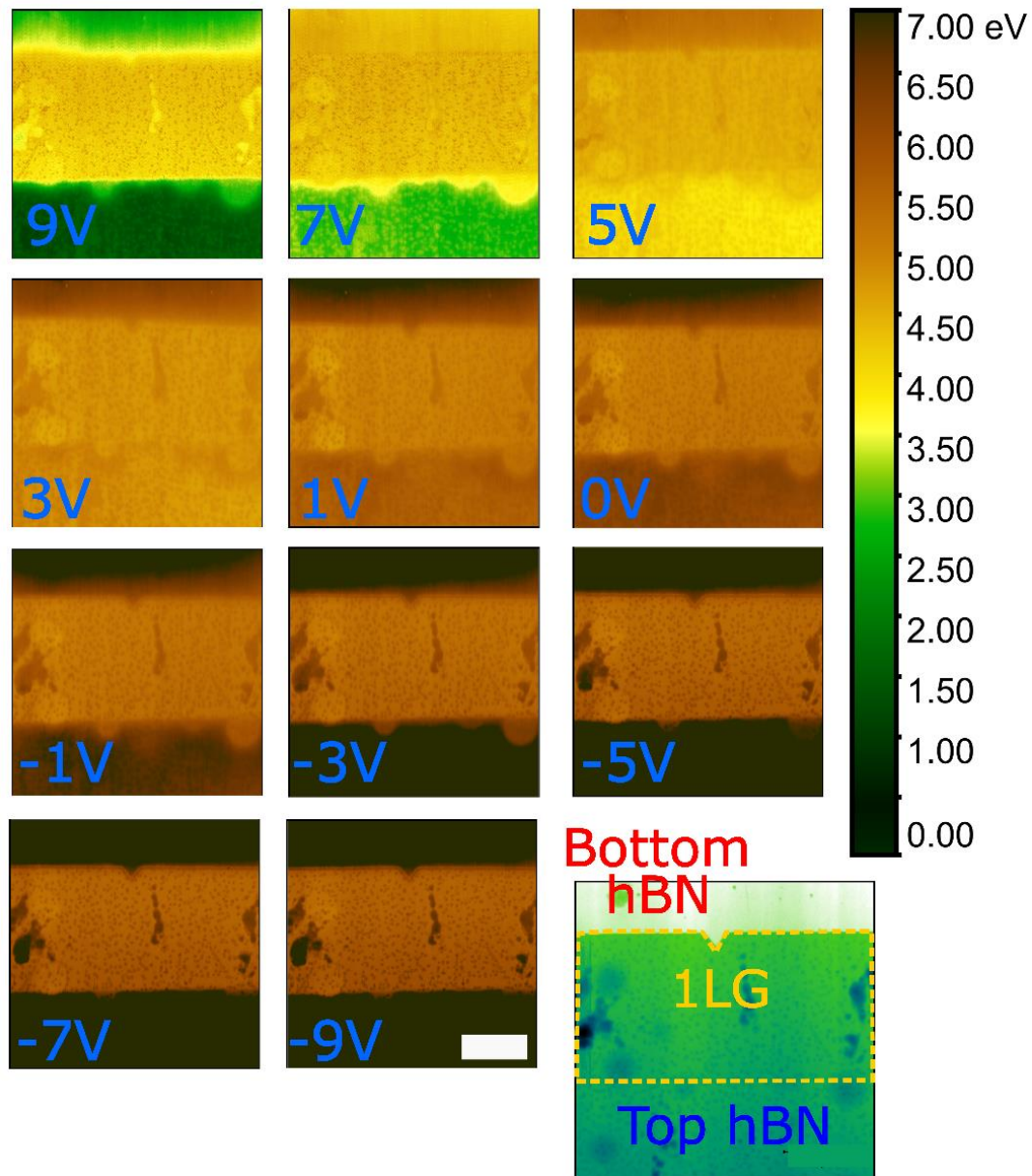


Figure 6.20. KPFM work-function maps of the sample for different back gate voltages. The work-function of the sample was calculated by using $\Phi_{\text{sample}} = \Phi_{\text{tip}} - eV_{\text{DC}}$. The value of the backgate voltage applied in each case is specified by the blue labels placed inside the images. The scale has been normalised and it is common to all work-function maps. On the bottom left corner, an image of the topography is shown in green with the different layers highlighted: bottom hBN in red, graphene in yellow, and top hBN in dark blue. Scale bar: 1 μm

From direct observation of the contrast of the Φ_{sample} for different V_{BG} , we corroborate what was observed for the line profiles. The work-function of graphene shows a slight variation while the area of the hBN follows the voltage of the back-gate. The contamination is more clearly visible for $V_{\text{BG}} = -9\text{V}$, showing patches and dots with darker contrast, which means higher work-function, and therefore, more p-doping, which could be expected from hydrocarbon contamination [388, 389].

In order to quantify the variations in the work-function of graphene, statistical distribution curves were taken for each of the maps acquired for each individual V_{BG} . The peaks were fitted with

Gaussian distribution profiles to obtain the values of the work-function of graphene, together with its standard deviation, for each back-gate voltage applied. The quantitative values of the work function, or Fermi level modulation, achieved by varying the V_{BG} for each of the devices are shown in *figure 6.21*.

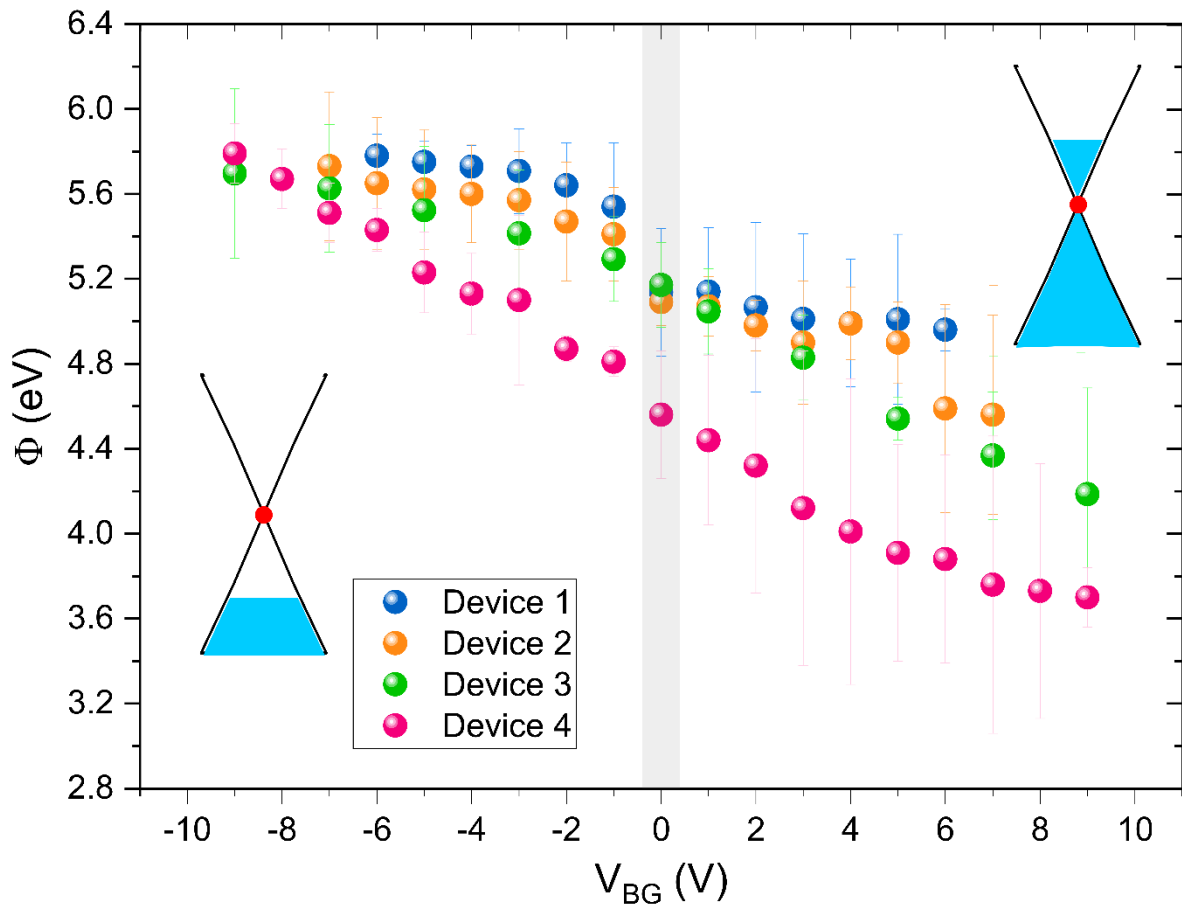


Figure 6.21 (a) Measured work function of SLG encapsulated samples as a function of V_{BG} . The point of $V_{BG} = 0V$ is highlighted in light grey.

The work-function values were lying within the range between 4.2 eV and 5.7 eV, and all four devices present the expected trend for the measured work-function. For $V_{BG} > 0V$ typically electrons are injected within the device, resulting in n-doping, rising the Fermi level, and reducing the work-function. On the contrary, when $V_{BG} < 0V$ the electrons flow from the graphene layer to the Si backgate, p-doping it, and resulting in higher values of the WF. This is all in agreement with the curves presented here: Interestingly, devices 1-3 show almost the same response and shape of the curve, whereas device 4 seem to follow a more linear trend, also presenting lower work-function values (i.e. comparatively more n-doped behaviour than the other devices). Quantitative values of the WF were extracted for $V_{BG} = 0V$ and summarised in the *table 6.4*. work-function measured values for the encapsulated graphene devices for $V_{BG} = 0$

Device	$\Phi (V_{BG} = 0V)$ (eV)
1	5.1
2	5.1
3	5.2
4	4.6

Table 6.4. Work-function measured values for the encapsulated graphene devices for $V_{BG} = 0$

The value obtained for the work-function for the device 4 is in good agreement with the WF values from previous studies, typically reported to be between 4.5 eV and 4.8 eV for single layer graphene [71, 137, 331]. However, for the other three devices, the value of the work-function was significantly larger showing values of 5.1 eV and 5.2 eV, which indicates the presence of p-doping in the graphene layer. As mentioned before, this is attributed to the presence of different levels of inter-layer contamination in the encapsulated devices [342]. However, further experiments would be performed in the future employing the brooming technique to verify this hypothesis, as detailed in *chapter 8*.

In summary, KPFM has proven to be an excellent tool, fast and non-invasive, to visualise and characterise encapsulated or buried layers, which are very difficult to image otherwise. Also, by employing the calibration protocol for the tip, the work-functions of the encapsulated graphene were obtained with high accuracy, providing information about the doping levels. On the other hand, KPFM results were inconclusive for the charge inhomogeneous distribution around the edges of graphene. This challenge still remains open and different strategies can be applied to ensure better conditions for the visualisation.

6.5 Conclusions

In this chapter, several directions were explored regarding both the improvement of the KPFM measurement methodology and the characterisation of the electronic properties of 2D materials at the nanoscale.

To start, a further improvement over a currently existing method [347] for KPFM calibration has been developed providing higher accuracy on determining the probe's work-function, and thus, helping to overcome the constant challenge of obtaining reliable values of the sample's work-function. For this, custom-made reference samples were created using four metals with high resistance to corrosion and/or high stability: Au, Pt, Ti and Ta. The thin film pads, which were deposited on Si and SiO₂ substrates, were also electrically connected, which allowed us to obtain several points of the V_{CPD} per sample, just by applying some gating. Therefore, the work-function was calculated from several points for each sample, reducing the standard deviation of the final

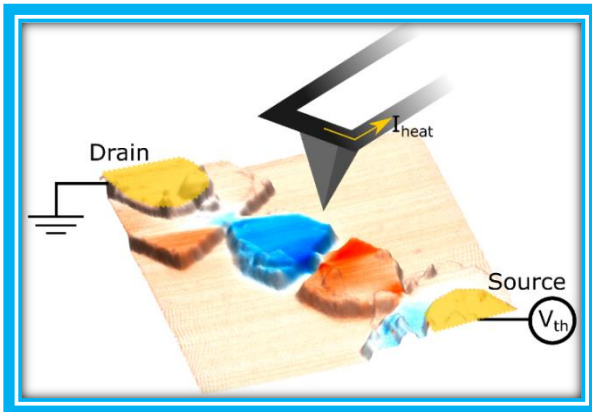
result, and therefore the uncertainty. Furthermore, a complementary technique, ultraviolet photon spectroscopy (UPS), was employed to obtain the values of the work-function of the reference samples. To be highlighted as well is the section dedicated to the optimisation of parameters for KPFM, which are often overlooked in literature, however, the proper selection of the feedback parameters, and the type of probe employed for the measurements is extremely important. In this last regard, although highly doped silicon probes provide better spatial resolution, as a result of their smaller radius, here we demonstrated that Pt coated probes have lower settling time, and therefore higher responsivity and faster scanning times. However, as metallic coatings have proven to be unstable under certain scanning conditions, wearing and presenting variations of the V_{CPD} up to hundreds of mV, here we also studied the robustness in the response of probes with coatings of different thicknesses (20 nm, 30nm, 40nm, and 50 nm). Thicker coatings (40 nm) resulted to be more accurate in the results provided, probably due to a thicker protection and resistance of the coating to fall off. Then, to estimate the homogeneity of the probes coming from the same batch, a set of 20 probes with 40 nm Pt-coating were studied following the calibration protocol, resulting in a total deviation up to 3% of the V_{CPD} provided. Finally, in this section, the robustness of the calibration protocol was tested against a real sample produced by exfoliation of graphene flakes on top of pre-patterned substrates. Three different probes were calibrated and employed to measure independent set of flakes of different thicknesses to obtain the work-function dependence of the graphene with the thickness. The results show how robust is this calibration method, allowing to use completely different probes and still providing results following the same trend. For the graphene flakes, consistent values of the work-function were obtained, with thin flakes approaching ~ 4.64 eV, while for bulk, the workfunction tended to ~ 4.38 eV. The slight discrepancy with values measured from other authors is attributed to the existing statistical variation between similar samples produced by the different doping mechanisms between the substrate and the flake.

In the second part of the chapter, KPFM was employed to explore the relationships between the gate dependent charge carrier concentration in GFET devices, as well as the charge distribution inside the 1LG channel, and the dissimilar accumulation of charges at low-disordered versus the high-disordered edges. This complex topic has been studied theoretically in the literature, and although charge modulation through back-gating is commonly used in laboratories around the world, the inhomogeneity of the charge distribution inside the devices is an area that remains largely unexplored. Visualisation of the distribution of the electrostatically-induced charges is of paramount importance to compare the spatial charge distribution with theoretical models, and ultimately understand electronic transport in gated graphene devices. To tackle this, a novel technique was employed to fabricate the devices, allowing the presence of four devices within the

same heterostructure, and the presence as well of a natural (low-disorder) and etched (high-disorder) edges. The surface potential of these devices was then studied with KPFM in vacuum for different gate voltages V_{BG} . Line profiles were then extracted across the devices to study the presence or not of bumps at the edges of the surface potential maps. Although several devices were studied with this technique, the effect was not observed. This was attributed to the high amount of contaminants trapped between the layers, which obscured any kind of transport, acting as dopants and scattering centres. Normally, when using the PPC/PDMS method described in *chapter 4 section 4.6.2*, clean interfaces between the layers are likely to be obtained, but only when employing certain speeds and temperatures in the fabrication. These last two factors could have affected the level of dirtiness present in the heterostructures.

Additionally, one strong capability of KPFM for the exploration of 2D materials was identified while performing this experiment. Normally, the obtention of data from the buried layers in heterostructures is performed via Raman spectroscopy or other optical techniques, which have a diffraction limited resolution. Here to demonstrate the capabilities of KPFM, maps of the work-function were produced for different backgate voltages. The quantitative values of the graphene work-function were between 4.6 eV and ~ 5.2 eV for all the devices, indicating a p-doped graphene layer, probably due to the contamination between the layers.

Thermal nanoscale characterisation of 2D materials with advanced SPM



In this chapter, the nanoscale thermal properties of 2D materials are studied using advanced SPM methods. In the first section, the thermal conductance of exfoliated InSe on different substrates and environments is studied using scanning thermal microscopy (SThM). To follow, encapsulated graphene heterostructures patterned with constrictions

are employed to study the local variations of the thermovoltage and thus, the Seebeck coefficient, with scanning thermal gate microscopy (STGM).

Acknowledgments: *The majority of the experiments presented in this chapter were conducted by myself with the exception of the SThM measurements in ambient presented in section 7.3.2. For these, I performed the exfoliation of the crystals, while the measurements were conducted by David J. Buckley at NPL. The figures presented here regarding these measurements have been adapted from 'Anomalous low thermal conductivity of atomically thin InSe probed by scanning thermal microscopy' [106], and reproduced with permission of the copyright holder.*

The fabrication of the exfoliated γ -InSe was performed in-situ prior to the measurements. The encapsulated graphene heterostructures were fabricated at the NGI. I would like to acknowledge Dr Roman Gorbachev, Dr Daniel J. Terry and Dr Matthew J. Hammer from the NGI for all their guidance and help during the fabrication process. The thermal and electrical measurements were performed at Lancaster University. I would like to express my gratitude to Sergio Gonzalez, Dr Agarwal

Kushboo, Andy Niblett, Dr Leonid Ponomarenko, and Dr Sergey Kafanov, for the useful discussions and guidance.

7.1 Introduction

During the 20th century, thermoelectric (TE) devices were confined to very niche applications, such as thermocouples, small scale Peltier coolers or thermoelectric generators for space exploration. However, since the 1990s, there has been a renewed interest in TE materials, due to the increasing social needs for renewable energy, and the new prospects in increased efficiency in thermal control coming from the advances in nanoscale science [390, 391].

As briefly discussed in *chapter 2, section 2.5*, the thermoelectric performance of a material is characterised by the figure of merit, $ZT = \frac{S^2\sigma}{\kappa}T$, where S , σ , κ and T are the Seebeck coefficient, the electrical conductivity, the thermal conductivity and the temperature, respectively. Increasing ZT is essential as higher values of the ZT correspond to higher energy conversion from heat to electricity, and *vice versa*. In this sense, from the expression of the ZT , it is clear that large S and σ are needed, along with a small value of κ . The first TE generators reached values of $ZT \sim 0.7$, and still, most of the commercially available TE devices nowadays present values of $ZT \sim 1$, significantly less than the corresponding ideal Carnot engine. This small increase in the efficiency of standard TE materials such as Bi_2Te_3 , PbTe or SiGe is related to the inter-dependence that exists between the thermal and the electrical conductivities for classical semiconductors. However, after the 1990s this value was enhanced by the use of nanostructures up to $ZT \sim 1.5 - 2.5$. Essentially, this quantitative jump could be achieved via two effects: (1) the quantum confinement which enhanced the so-called power factor, $S^2\sigma$; and (2) the reduction of the thermal conductivity by promoting phonon scattering while preserving the electron conductivity. This second strategy is normally achieved by introducing controlled scattering centres or by nanopatterning [392–394].

Based on these reasons, 2D materials are promising candidates for TE applications. However, even with all these prospects, the realm of thermal properties of 2D materials remains still widely unexplored. In order to achieve real-life working TE devices based on them, a detailed understanding of the behaviour of the thermal conductivity and Seebeck coefficient in these systems is needed. Here, different thermal properties of graphene and InSe , which are materials that have presented extremely good prospects as components for TE applications, are studied via advanced SPM methods:

- **Indium selenide (InSe)** presents itself as an extremely good candidate for thermoelectric applications. Among all the members of the chalcogenides family, it has

shown the highest carrier mobility, reaching values of $\sim 10^3 \text{ cm}^2 \text{ V}^{-1} \text{ s}^{-1}$ for few layer InSe ($\sim 6L$) at room temperature [119, 120]. With respect to the thermal properties of this material, earlier experiments performed in bulk crystals have already showed that InSe exhibits low thermal conductivity reaching values of $\kappa < 1.2 \text{ Wm}^{-1} \text{ K}^{-1}$ and large Seebeck coefficients up to $-400 \text{ } \mu\text{V/K}$ [121, 395]. However, although theoretical studies of the TE properties of 2D InSe have been already performed showing promising results [122, 396], there is a lack of experimental research on the dependence of the thermal conductivity with the thickness of the material, or the values of the Seebeck coefficient. Here we present results studying the dependence of the thermal conductance of exfoliated InSe with respect to the thickness of the flakes. The measurements are performed via SThM in ambient [106] and in vacuum environments (*section 7.3*). Further characterisation of the Seebeck coefficient of more complex InSe heterostructures patterned into Hall bar devices will be discussed as part of future work in *chapter 8*.

- **Local variations of the Seebeck coefficient in graphene devices** with nanopatterned bow-tie constrictions and mono-bilayer junctions have been studied in recent experiments [397, 398]. Due to its importance, we further study this topic here, exploring this new phenomenon for the first time on encapsulated graphene with nanopatterned constrictions of different geometries. Adding to the previous studies already mentioned, we are going to investigate the effect on the local Seebeck response on graphene produced by the device geometry, the back-gate voltage (i.e. the sign of charge carriers), and the local gating effect produced by the probe. In order to do this, we employ a novel technique called scanning thermal gate microscopy (STGM) [397, 398] in vacuum at room temperature and at low temperature $T_S \sim 170 \text{ K}$ (*section 7.4*).

7.2 Experimental methods

The procedures explained in this section are common for all the experiments described in the chapter unless stated otherwise.

7.2.1 Custom microscope set-up

The experimental set-up employed for all the measurements presented in this chapter is depicted in *figure 7.3*. It consists of an NT-MDT Smena microscope in-house adapted for studying thermal properties at the nanoscale. A general view of the system can be seen in *figure 7.1(a)*, with details presented in *figure 7.1(b)* and *figure 7.1(c)*.

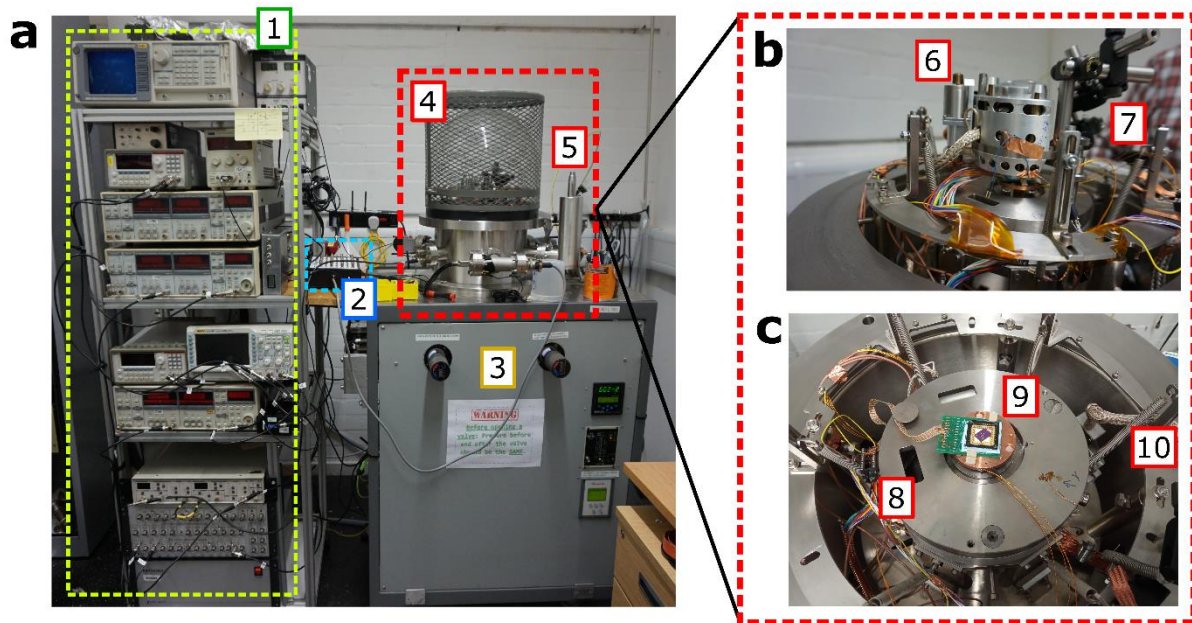


Figure 7.1. **(a)** System set-up. 1-The electronics rack used to perform the measurements. 2-Connection box. 3-Vacuum pumps, a rotary, a turbo and an ion pump used to achieve different vacuum environments. Surrounded by a red squared: the main head of the microscope. 4- Glass bell to hold the vacuum in the system. 5-Thermal reservoir. **(b)** Detail of the microscope in which we can see the 6- NT-MDT head of the microscope and 7-the camera. **(c)** Detail of the microscope head in which we can see 8-the sample holder and 9-the suspended base using springs.

In *figure 7.1(a)-[1]*, the rack of electronic equipment surrounded by a green dotted square comprises different pieces that help functioning the system. The different elements and their uses will be discussed in the following sections. The custom breakout box, presented in *figure 7.1(a)-[2]* and surrounded by a blue dotted square, serves to establish electrical communication with the devices placed inside the chamber via a special connector and a sample holder shown in *figure 7.1(c)-[8]*. This piece of equipment is especially important as it allows access to the electronic properties of the devices under study even when the sample is in vacuum. Behind the grey panel presented in *figure 7.1(a)-[3]*, a set of 3 different vacuum pumps is kept: a rotary and a turbo pumps accessed through the valve on the right-hand side, and an ion pump accessed through the valve on the left side. Finally, the microscope head with the vacuum bell-jar is presented in *figure 7.1(a)* surrounded by a red dotted square. Details of the inside of the microscope are shown in *figure 7.1(b)*, with the [6] NT-MDT microscope head and the [7] optical camera, and in *figure 7.1(c)* in which the [9] sample holder is shown. It is important to highlight that in order to help heat propagation the sample holder is made out of copper and it is directly connected via copper braids to the liquid nitrogen (LN_2) thermal reservoir shown in *figure 7.1(a)-[5]*. The sample holder is attached to the X-Y microscope stage via low thermal conductivity glass spacers to reduce the heat transport from the locally controlled sample stage. The whole mechanical frame structure of the microscope is suspended, held by springs as shown in *figure 7.1(c)-[10]*, with magnetic eddy current pacifiers to minimise the effects of the external vibrations.

The measurements presented in this chapter were performed in different conditions of (a) pressure: ambient and high vacuum (10^{-7} mbar), and (b) temperature: room temperature (RT, $T \sim 293$ K) and low temperatures (LT, $T \sim 170$ K). The experimental conditions used each time will be specified when discussing the results. Finally, it is important to clarify that using this same set-up, different techniques were employed. The details are covered in the sections below, with the schematics shown in *figure 7.3*.

7.2.2 Scanning thermal microscopy (SThM) set-up

Two different SThM probes were employed for the experiments presented in this chapter, with their details described in *table 7.1*. The AN-200 cantilevers have a similar geometry to a standard micromachined AFM probe, with two highly doped Si legs connected at their end to a low doped resistive region, as shown in *figure 7.2(b)*. The tip has a conical shape and a radius of curvature of < 30 nm, thus providing very high spatial resolution. However, as a consequence of its sharpness, these tips present a high thermal resistance, whereas when used in ambient conditions, the effective volume probed is made of a much bigger volume than the one just below the apex due to heat conductance from the cantilever to the sample. For this reason, these probes cannot provide reliable measurements in ambient, and vacuum environment is essential. These probes are employed for all the SThM measurements performed in vacuum in this chapter.

MODEL	SUPPLIER	MATERIAL	k ($N \cdot m^{-1}$)	Tip height	Max. T ($^{\circ}C$)	Curvature radius	R_{th}^{vac} (KW^{-1}) ¹³	REF
AN2-200	Anasys Instruments	Doped Si	0.1-0.6	3 – 6 μm	400	<30 nm	$5.18 \cdot 10^4$ [399]	[400]
KNT-SThM-2an	Kelvin NanoTechnology	SiN-Pd thermal sensor	~ 0.4	10 μm	200	<100 nm	$7.2 \cdot 10^4$ [399]	[401]

Table 7.1. Thermal probes employed in the experiments described in this chapter

On the other hand, the KNT-SThM-AN200 probes are formed by a silicon nitride cantilever, with Au contact pads leading to two Pd thermosensitive films that are joint at the end of the tip, as depicted in *figure 7.2(a)*. This, combined with its triangular geometry, helps better coupling the temperature of the sample at the tip apex and the thermally sensitive heater, while reducing the heat transfer through parasitic channels, and thus, making it better suited for operation in ambient conditions. These probes are employed for all the SThM measurements performed in ambient environment in this chapter.

¹³ R_{th}^{vac} is to the thermal resistance of the probes. The values shown here correspond to the ones obtained experimentally in vacuum conditions in [399]

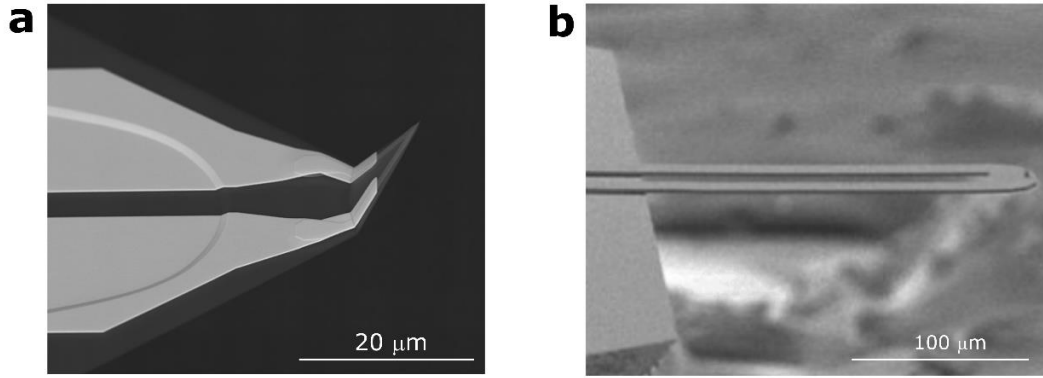


Figure 7.2. (a) SEM image of a KNT Pd coated probe. Figure reproduced with permission of [401]. (b) SEM image of a doped-Si probe from Anasys AN2-200. Figure reproduced with permission of [400].

For reference, the SThM details discussed here are represented by orange lines in the schematics of figure 7.3. The excitation of the probe (i.e. heating) was produced by a *Keithley 3390 Arbitrary Waveform Generator* [402] which sent a harmonic signal directly to the Wheatstone bridge, while the reference signal was fed to the lock-in amplifier (LIA) 3. All the measurements were performed with $f = 91$ kHz, $V_{AC}^{PP} = 3V$ and $V_{DC}^{Offset} = 2V$, unless stated otherwise. The output voltage signal from the Wheatstone bridge, ΔV , which represents the imbalance of the bridge due to change of the probe resistance as a result of heating, was pre-amplified by an instrumental amplifier, and then further amplified and filtered using a bandpass *SR650 filter* [403], with the high pass filter set to $f > 86.8$ kHz and 10 dB input gain, and the low-pass set to detect $f < 94.7$ kHz without any gain. The output from the filter was then measured with the A input of the LIA 3. The output of the LIA 3 was connected to the external input port of the microscope controller, Ext3, which permitted us to scan continuously the SThM signal. All the lock-in amplifiers used here and in following sections are *LIA SR830 DSP* (Stanford Research Systems, USA) [404].

As already discussed in *chapter 3, section 3.1.3*, SThM measurements in vacuum were important to avoid the formation of the water meniscus and eliminate the contribution of parasitic heat transfer mechanisms such as conduction through convection, or liquid. In our measurements, the spatial resolution was limited by the size of the tip-sample contact, which is on the order of tens of nanometers. Across

7.2.3 Scanning thermal gate microscopy (STGM) set-up

For the STGM measurements, the AN2-200 probe was heated up and used as a source of local heating while the resulting potential on the device was measured. This “thermal gate” applied by the probe, generated a voltage drop within the device denominated as thermovoltage. The generated signal was then extracted by connecting the device to the A and B inputs of a *SR650*

low-noise pre-amplifier filter [403], operating as the DC amplifier with a gain of 40 dB and LP cut-off frequency of 1 kHz. The output of the filter was then connected to the external 1 port, Ext1, of the microscope controller, and mapped along with the scans. Note that the generated thermovoltage was also constantly monitored using the LIA 1 in *figure 7.3*, where the STGM connections are represented by light blue outlines. The SThM response (orange outline in *figure 7.3*) can be monitored simultaneously with the STGM signal.

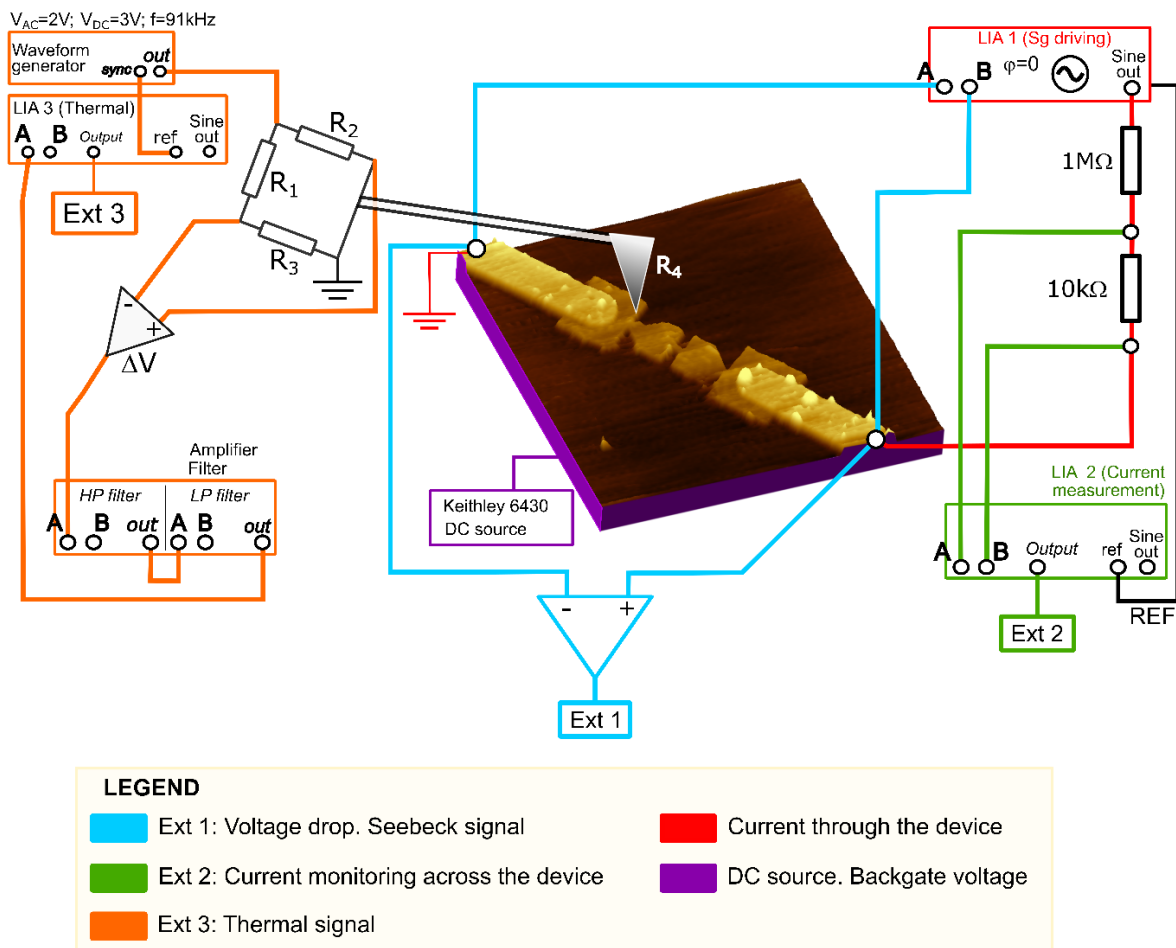


Figure 7.3. Schematic set-up employed for all the measurements in the chapter: SThM, STGM and electrical measurements.

7.2.4 Electrical characterisation set-up

In particular for the encapsulated graphene devices, the position of the Dirac point was determined by using the 2-point probe method, following the red, green and purple paths in *figure 7.3*. The LIA 1 was employed to provide the driving current through the device with parameters set as follows: $V_{out}^{LIA1} = 0.1V$, $f^{LIA1} = 2.7kHz$, $\tau = 100 ms$, Harmonic = 1, and sensitivity = 100mV. Two resistances in series were connected between the LIA1 and the device: the first one, a 1 M Ω resistor was used to limit the total constant current through the device up to $I = 1 \mu A$; while the second resistance of 10 k Ω was employed to monitor the current passing through the

device. This was done by connecting the two ends of the resistor to the A and B terminals of a second lock-in, LIA 2.

Back-gating was performed by connecting the silicon substrate to a *Keithley 6430 SubFemtoAmp Sourcemeter* [405] which provided DC current, as highlighted by the purple outlines in *figure 7.3*.

7.3 Study of the thermal properties of exfoliated InSe via SThM

Early research has pointed out the high potential of InSe as a TE material [396, 406]. However, as mentioned in the introduction, the accurate characterisation of the thermal conductivity dependence with the thickness for InSe is of uttermost importance for the realisation of TE applications. Theoretical studies by Nissimagoudar et al. [122] and Shafique et al. [407] have calculated for InSe monolayers at room temperature thermal conductivities of $27.60 \text{ Wm}^{-1}\text{K}^{-1}$, and $44.4 \text{ Wm}^{-1}\text{K}^{-1}$, respectively. Also, these two studies have highlighted the size dependent thermal conductivity as a consequence of decreased phonon mean free path (MFP), and the increased phonon-boundary scattering. However, dependence of the thermal conductivity on the thicknesses of InSe was not addressed in these papers. At the time this research was performed, no experimental results were available studying the aforementioned dependence. Here, in order to provide some clarity in this topic, the thermal properties of exfoliated InSe were explored using SThM in ambient environment and in vacuum environment ($\sim 10^{-7} \text{ mbar}$). For the latter, the thermal response was compared for InSe exfoliated in two different substrates: i.e. SiO_2 and Si.

7.3.1 InSe exfoliation

Following the ‘*Steps method*’ explained in *chapter 4, section 2.2*, InSe flakes of various thicknesses were prepared from the as-grown crystal.

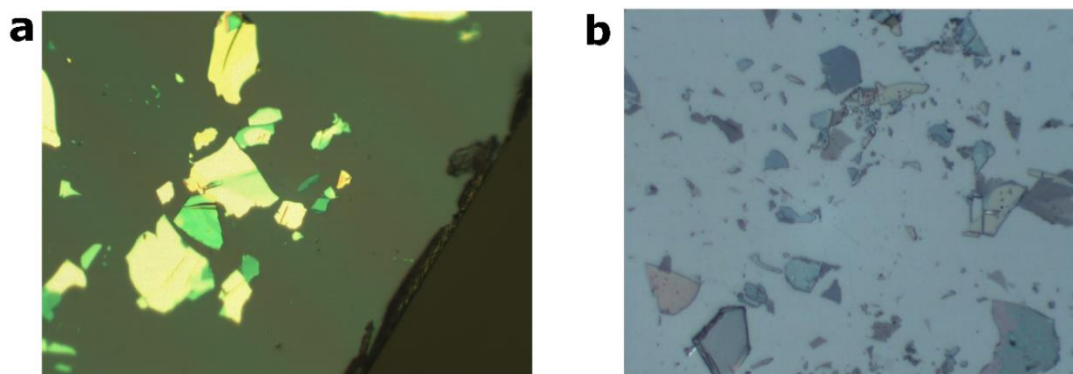


Figure 7.4. InSe exfoliated on (a) 300 nm SiO_2/Si and (b) Si

The high quality γ -InSe crystals were grown in Ukraine employing the Bridgman method from a polycrystalline source of $\text{In}_{1.03}\text{Se}_{0.97}$ [408]. The InSe was exfoliated using a Nitto ELP-BT-150P-

LC tape, after removing the top layer from the crystal, to avoid using air-exposed material that could be degraded. Then, the InSe on the tape was brought into contact with the surface of the substrate. In this case, two substrates were employed: 300 nm SiO₂/Si and Si. In both cases, the tape was left on top of the substrate for 5 minutes to increase the adhesion of the InSe flakes. However, for the Si, a final step was added, and the substrate with the tape in contact was heated up to 40°C for 1 minute, in order to further increase the adhesion between the flakes and the substrate. Finally, the tape was peeled off from the substrate, and after optical inspection, as shown in *figure 7.4*, the chips with the highest variety of flake thicknesses were separated for their posterior study in the SThM system.

7.3.2 SThM measurements in ambient environment

To start, the SThM results in ambient environment of exfoliated InSe on top of SiO₂ are presented. These measurements were performed at NPL with a nanoIR2 system from Anasys, and KNT probes (see *section 7.2.2*) [106].

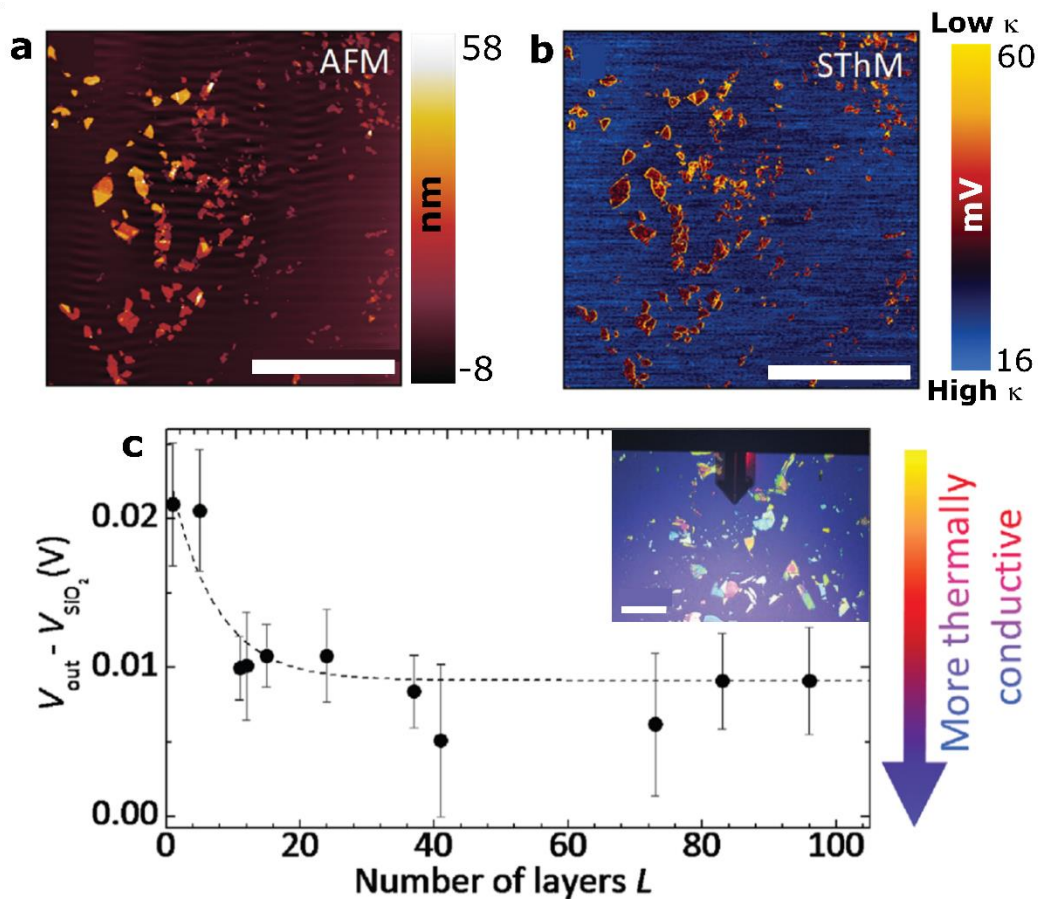


Figure 7.5. (a) Topography and (b) SThM response maps of an area on the sample showing a large collection of InSe flakes of varying thicknesses on top of a SiO₂ substrate. Scale bar: 20 μm . (c) SThM voltage response, where V_{out} is the voltage on the inner area of the flake, and V_{SiO_2} the voltage of the probe measured on the substrate, as a function of the number of layers. Note that the study only considers flakes with area $> 4 \mu\text{m}^2$. Inset: Optical image showing another area of the sample with a collection of InSe flakes of different thicknesses exfoliated on top of SiO₂. Scale bar: 100 μm . The maps and

optical images were acquired with the microscope of the nanoIR2 system. The KNT probe can be seen in the image with the laser spot placed almost at its base. Reproduced with permission from [106].

Areas with different coverage of flakes were scanned in order to obtain information about the thermal conductance dependence on the thickness of the material. A topography AFM map showing a collection of flakes of varying thicknesses sitting on top of the SiO₂ is shown in *figure 7.5(a)*. The SThM voltage response map of the same area is presented in *figure 7.5(b)*. InSe flakes presented higher thermal voltage signal values (red contrast) than the silicon oxide substrate (blue contrast).

In order to interpret this voltage changes in terms of thermal conductance, we must understand how the heat propagates in the system. Normally, a resistor equivalent model is employed to describe the heat propagation channels between an SThM probe and the sample under study. Two different scenarios can be considered depending if the probe is out-of-contact or in-contact with the surface as follows:

Out of contact	In-contact
$\Delta T_{nc} = \alpha V_{nc} = Q \cdot R_p$ (7.1)	$\Delta T_c = \alpha V_c = Q \cdot R_{eq} = Q \cdot \left(\frac{1}{R_p} + \frac{1}{R_x} \right) = Q \cdot \frac{R_p R_x}{R_p + R_x}$ (7.2)

Table 7.2. Equations showing the resistor model for heat propagation when the probe is out-of-contact or in-contact with the sample

where

- T_{nc} temperature of the probe out of contact
- T_c temperature of the probe in-contact with the surface
- V_{nc} voltage of the probe out of contact
- V_c voltage of the probe in-contact with the surface
- α a certain calibration factor
- Q is the heat transferred
- R_p is the thermal resistance of the cantilever
- R_x is the resistance of the contact.

When applying a power load to the probe, its temperature increases due to Joule heating. The latter is reflected by the output thermal signal voltage measured by the LIA3 (see *figure 7.3*), as expressed from the equations presented in *table 7.2*. However, the relationship between the heat generated and the variation of temperature, and thus the variation of voltage, is governed by the thermal resistance of the system considered. When the probe is far away from the surface (i.e. out-of-contact), only the effective thermal resistance of the probe (cantilever) matters, R_p , as it is the only channel for heat dissipation in this case, and includes thermal conductance through the air for the ambient environment measurements. However, when the probe is in-contact with the

substrate, there is an additional heat transfer channel, R_x , which appears as a consequence of the contact itself, and that is included in the equations as a parallel resistor. In *figure 7.6(a)* and *figure 7.6(b)*, a schematic diagram of the thermal resistance network is depicted for both scenarios.

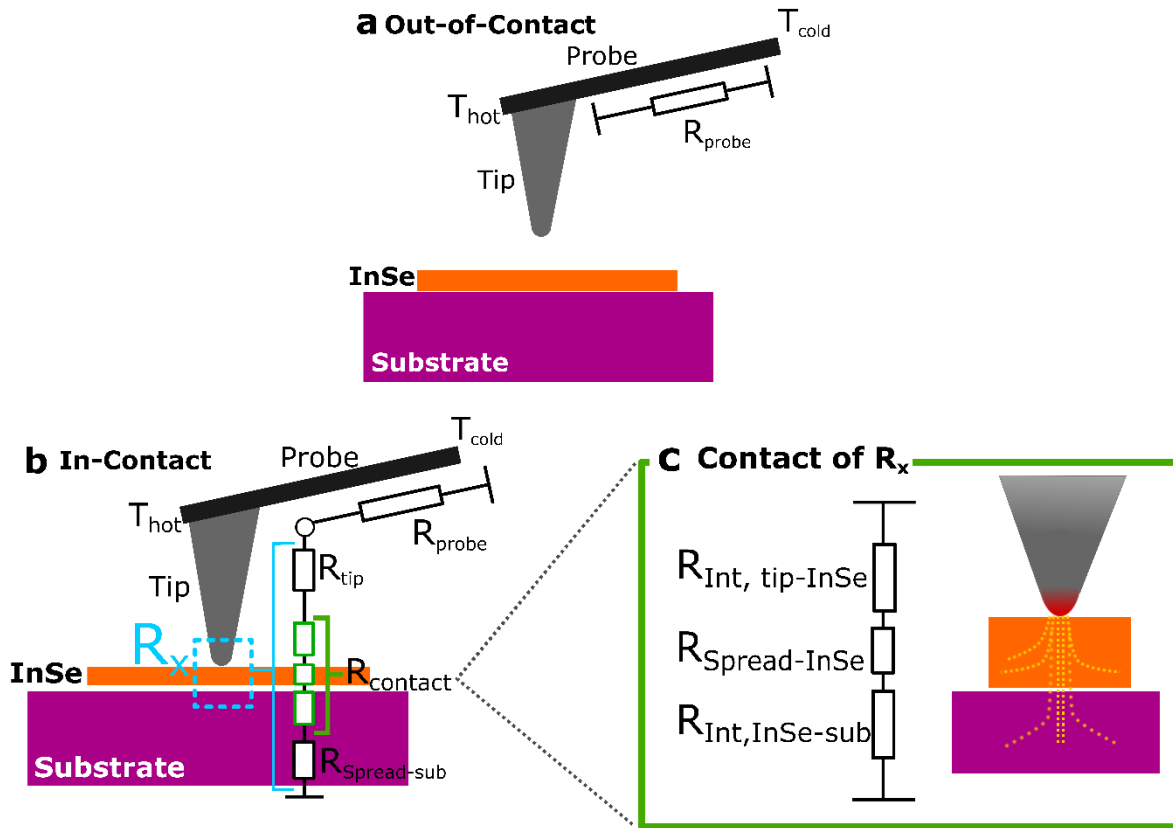


Figure 7.6. Schematic diagram of the thermal resistances present in the system: (a) When the probe is out-of-contact, only the thermal resistance of the probe has an effect on the heat propagation. (b) However, when the probe is in-contact with the surface, a set of resistances appear, including: R_{tip} , $R_{contact}$ and $R_{spread-sub}$, corresponding to the thermal resistance of the tip itself, the detail of the contact and the heat spreading ability of the substrate, respectively. All these resistances are summed together in series under one term, R_x , which is then added in parallel to the original R_p . (c) Zoom-in detail to the resistances that conform $R_{contact}$, including $R_{Int,tip-InSe}$, the thermal interfacial resistance of the tip and the material; $R_{Spread-InSe}$ the thermal resistance of the heat spread inside the InSe flakes, and $R_{Int,InSe-sub}$, the thermal interfacial resistance between the InSe and the substrate. Note that for (a-b), the heating of the probe is represented as temperature gradient established between the colder base of the cantilever (T_{cold}), and the hotter part at the tip region (T_{hot}).

In order to interpret our results, we are interested in the changes of the voltage in-contact and thus in the effect of the contact resistance R_x in the response (see *eq. 7.2*). This resistance contains different contributions that can be expressed as a set of three different resistances in series:

$$R_x = R_{tip} + R_{contact} + R_{Spread-Sub} \quad (7.3)$$

where R_{tip} is the thermal resistance of the tip, and $R_{Spread-Sub}$ is related to how the heat propagates inside the substrate material, while $R_{contact}$ can be also decomposed in different resistances as shown in *figure 7.6(c)*, and including:

$$R_{contact} = R_{Int, tip-InSe} + R_{Spread-InSe} + R_{Int, InSe-Sub} \quad (7.4)$$

being $R_{Int,tip-InSe}$ and $R_{Int,InSe-Sub}$ the interfacial resistance or thermal contact resistance between the tip-InSe and the InSe-Substrate, respectively. The term $R_{Spread-InSe}$ is the thermal resistance related to the heat propagation inside the InSe flake, and ultimately, the quantity of interest. In the case of InSe, being a highly anisotropic material with different out-of-plane and in-plane thermal conductivities, the $R_{Spread-InSe}$ value will account for both contributions.

The thermal resistance of the tip is normally a fixed value characteristic of the probe employed, and the environmental conditions in which the measurements are performed (see *table 7.1*). The interfacial resistance or contact thermal resistance is generally difficult to quantify, as it depends on both geometrical parameters such as the contact area and also the type of materials brought into contact. Since we are probing the same material and only the number of layers varies, we can assume it remains constant. Finally, the spreading thermal resistance is how the heat propagates inside the material. It strongly depends on its thermal conductivity, and thus, on its isotropic or anisotropic nature, as explained above. We can assume that the spreading thermal resistance is inversely proportional to the thermal conductance of the material, $G_{material}$, as $R_{spreading} \sim 1/G_{material}$. Therefore, the changes of the LIA thermal signal voltage in contact can be assumed to be monotonously dependent on the changes in conductance of the material:

$$V_c \sim \frac{1}{G_{material}} \quad (7.5)$$

Generally, it is not straightforward to decouple all these resistances from our SThM signal variation, but we can compare the values of the different materials present in our maps to at least extract the trends of the thermal conductance of the InSe flakes.

Coming back to the measurements presented in *figure 7.5(c)*, the higher the voltage value, the lower the thermal conductance. Based on this, the signal presented by the InSe flakes, showing high values of the voltage (i.e. red contrast), would indicate lower thermal conductance than the SiO_2 substrate, which presents lower voltage values (i.e. blue contrast). Assuming that the interfacial thermal resistances between the tip- SiO_2 and the tip-InSe systems are similar, then it is safe to discuss these in terms of thermal conductivities and not conductances, and establish that as observed here, at room temperature, the thermal conductivity of InSe appears to be lower than that of SiO_2 , $\kappa_{InSe} < \kappa_{SiO_2} = 1.4 \text{ W} \cdot \text{m}^{-1} \cdot \text{K}^{-1}$. However, it is important to highlight that in order to understand the contribution of the geometrical effects of the tip to the signal, and thus obtain the real contribution of the interfacial thermal resistance and thermal conductivity, further modelling would be required [409, 410].

Following this, the possible dependence between the InSe thickness and its thermal conductance is studied. However, unlike in the topography maps in which the flakes of different thicknesses were easily identified by their different contrast (*figure 7.5(b)*), in the SThM map the thermal contrast obtained for the InSe flakes of different thickness seemed similar and often indistinguishable from each other. Therefore, a more rigorous analysis was required to study the presence of variations in the voltage values. For this, an Otsu thresholding algorithm was applied to all the SThM maps in order to extract the voltage response of the individual flakes. Then, as the substrate presented a constant value of the voltage for all the images acquired, it was established as the reference point. Finally, the difference between the voltage of the flakes and the substrate, $V_{out} - V_{SiO_2}$, was represented with respect to the thickness of the flakes, as shown in *figure 7.5(d)*. Note that larger values of $V_{out} - V_{SiO_2}$ correspond to lower values of $G_{material}$. Therefore, the trend indicates that the thermal conductance of the flakes increases with the thickness up to $\sim 20L$ ($\sim 16\text{nm}$), where it stabilises, remaining constant for all increasing thicknesses. Referring back to *eq. 7.4* this means that $R_{spread-InSe}$ has reduced to the point where the other two terms dominate, and since they are independent of the number of layers, and thus constant, the voltage measured also remains constant. It is important to highlight that for these results only flakes with an $area > 4\mu\text{m}^2$ were analysed in order to avoid any size dependent variations of the thermal conductance. Furthermore, only the data from the centre of the flakes was employed, generally eliminating the contribution of the edges, while some effect of these may still be present. This was done to avoid any artefacts affecting the result, i.e. lower thermal conductance at the edges, as normally the contact area of the probe with the flakes at the edges changes, as it can be appreciated in the yellow contrast shown by the flakes in *figure 7.5(c)*, more predominant in thicker flakes.

7.3.3 SThM measurements in vacuum and the effect of the substrate

A very important consideration is that the measurements presented in the previous section were acquired in ambient environment, in which several parasitic contributions affect the final value of the thermal signal measured, as discussed in *chapter 3, section 3.1.3*. Namely, the air conduction channels, as well as the water meniscus formed around the contact point at the very end of tip can affect the different resistance channels considered in our model, as for example, they can lead to a height dependent behaviour of the probe's resistance $R_p(z)$, which was assumed to be constant so far. Also, they can have an effect in the value of R_x , described above, specially in the interfacial thermal resistance of the tip-sample contact, $R_{Int, tip-sample}$. In order to eliminate all these contributions, a new set of measurements was performed in vacuum (10^{-7}mbar), using doped silicon probes instead of the KNT probes, and freshly exfoliated InSe samples.

Another important consideration is the choice of the substrate. The thermal response of a system depends on the interfacial thermal resistance existing between its individual parts and the spreading thermal resistance of the substrate. Therefore, it is safe to assume that it will also be reflected on the SThM response via the interfacial resistance term between the flakes and the substrate, $R_{Int, InSe-Sub}$. Previous studies, have demonstrated the strong influence of the substrate on the thermal response on other 2D materials [203], however there are none performed on InSe in vacuum. In order to study the influence of the interfacial thermal resistance, two substrates are employed here: Silicon oxide presenting low bulk thermal conductivity ($\kappa_{SiO_2} = 1.4 W \cdot m^{-1} \cdot K^{-1}$), and Si with high bulk thermal conductivity ($\kappa_{Si} = 148 W \cdot m^{-1} \cdot K^{-1}$) with both can be generally treated as isotropic thermal conductors.

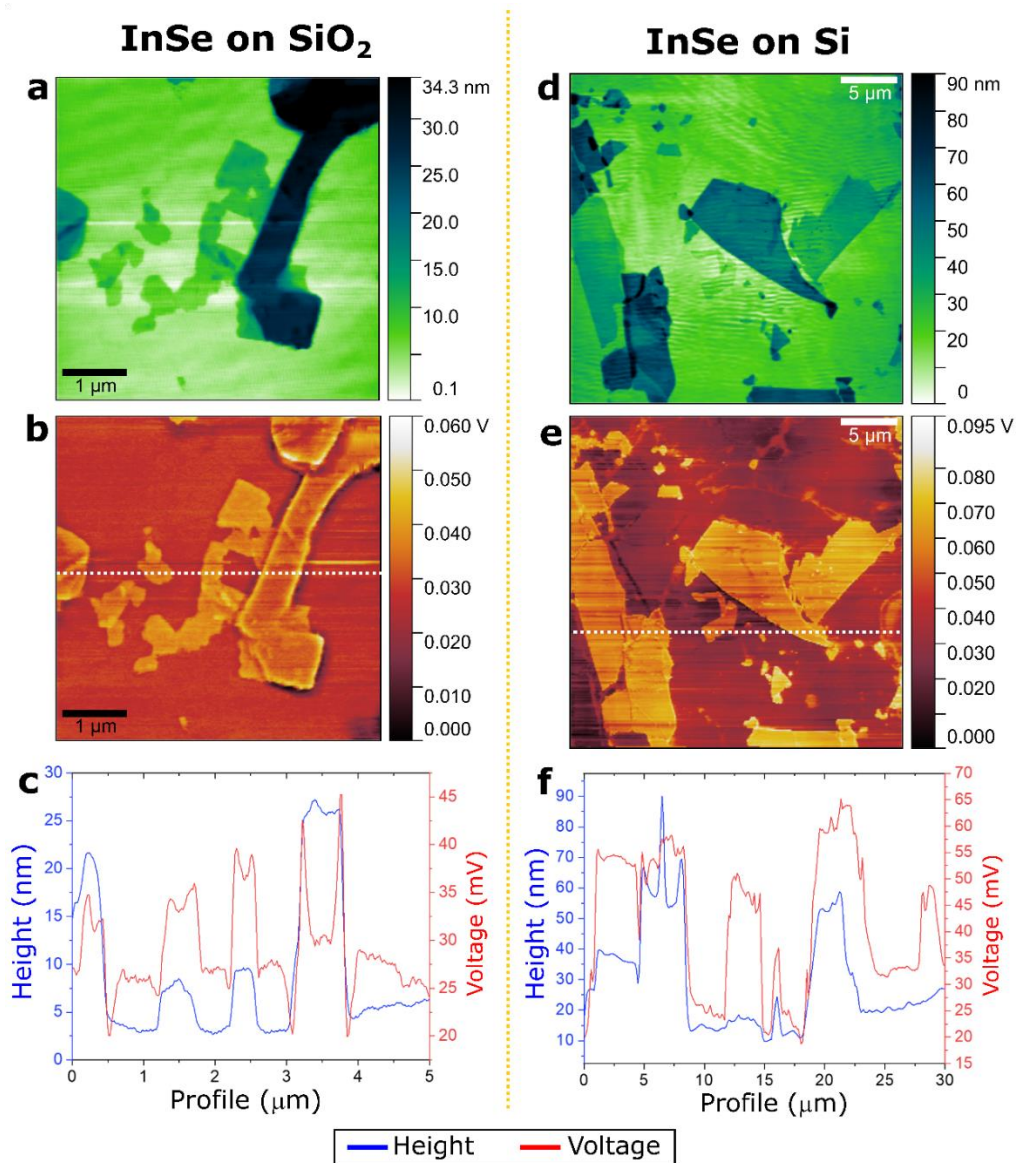


Figure 7.7. Representative example of the measurements acquired for exfoliated InSe in vacuum ($\sim 10^{-7}$ mbar). In the left column, measurements of the InSe exfoliated on SiO_2 showing in (a) the topography, (b) the SThM response and in (c) the profiles of the topography and the SThM response depicted together and acquired over the dotted white line in (b). On the

right column, measurements of the InSe exfoliated on Si showing in (d) the topography, (e) the SThM response and in (f) the profiles of the topography and the SThM response depicted together and acquired over the dotted white line in (e).

Several samples were exfoliated and measured for this study. Representative examples of the measurements are shown in figure 7.7. Both topography images of InSe exfoliated on SiO₂ (figure 7.7(a)) and Si (figure 7.7(d)), present a varied collection of flakes with different areas and thicknesses. The thermal response obtained for the InSe on SiO₂, (figure 7.7(b)), reveals higher values of the voltage for the InSe (i.e. orange-yellow contrast) than the ones obtained for the substrate, which presents a darker contrast. This means that the InSe presents lower thermal conductivity than the SiO₂, in agreement with the results obtained for the measurements in ambient shown in the previous section[1], even with the presence of parasitic signals in the latter case. In order to assess the dependence of the thermal response with the thickness, profiles of the topography and the SThM response were acquired following the white-dotted line from figure 7.7(b), and are shown in figure 7.7(c). There is good correlation between the data from the topography and the SThM signal, with the thermal response presenting peaks according to the position of the flakes, and also variations in height depending on the thickness of the flakes. With respect to the thermal response of the InSe flakes exfoliated on Si (figure 7.7(e)), similar contrast is observed, with the InSe having higher thermal signal voltage, and therefore lower thermal conductance than the silicon substrate. Profiles were also obtained as in the previous case for the topography and the SThM response following the white dotted line from figure 7.7(e). The results presented in figure 7.7(f), also show an evident thickness dependence of the thermal response. In order to better represent the dependence of the thermal response with the thickness, the same method used in the previous section of masking the flakes with Otsu thresholding is employed here.

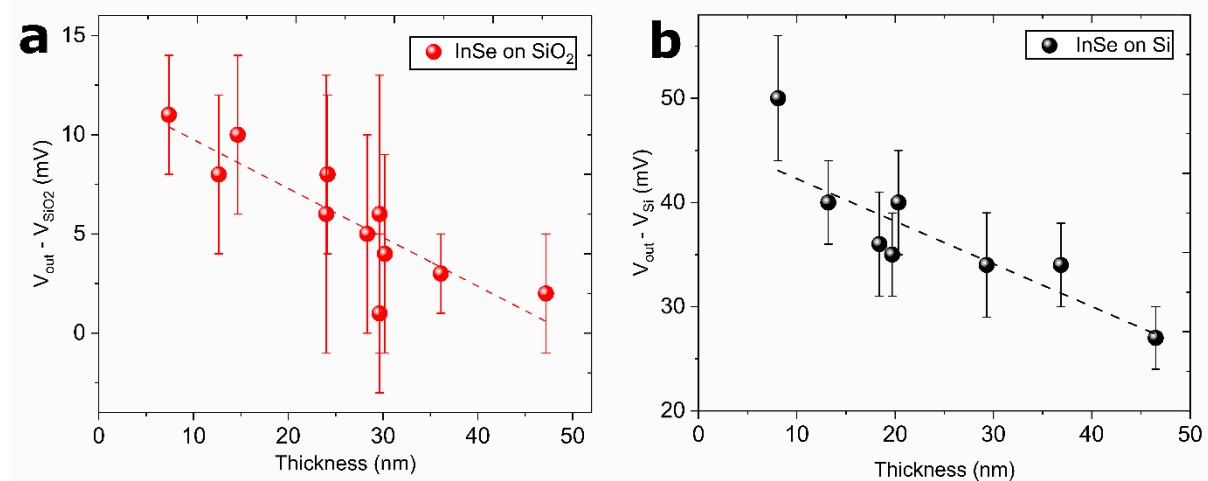


Figure 7.8. SThM response measured in vacuum ($\sim 10^{-6}$ mbar) as a function of the number of layers for InSe exfoliated on (a) SiO₂ and (b) Si substrates.

The results, summarised in *figure 7.8*, show a decreasing value of the signal of the flakes with respect to the substrate for increasing thickness. Following the resistance model discussed above, the decreasing thermal signal can be interpreted as an increased thermal conductivity with respect to the thickness. This agrees with the data obtained for the ambient environment measurements presented in the previous section, eliminating the possible topographic effect on the thermal conductance measurements. However, in this case, the trend is more linear and it does not stabilise to a constant value for thicker flakes (*thickness* > 20 nm). This reduction of the thermal conductance with thickness is in agreement with previous findings for other materials, as for example Al and Cu [411]. As discussed before, the thickness dependence indicates which terms dominate in *e.q 7.4*, and having eliminated the air, most likely reduces the contribution from $R_{Int,tip-InSe}$ leaving $R_{spread-InSe}$ dominating the resistance for many more layers than when imaging in air, and thus explaining the linear behaviour seen in this case. With respect to the different substrates studied here, variations of κ could be expected based on previous experimental results [106, 412].

In this case, although the trend observed is linear in both cases, the change of the signal with respect to the substrate for InSe deposited on Si is higher than the variation of the thermal response for InSe on SiO₂. Based on this, the thermal conductivity of InSe on Si appears to be lower than the thermal conductivity of InSe deposited on SiO₂, at least for the range of thicknesses studied here.

Another extremely important point to highlight is that the InSe presents a very high anisotropy in its thermal response. A very recent experimental study, found when finalising this section, has measured values of the InSe thermal conductivity in-plane and out-of-plane to be $\kappa_{\parallel} = 8.5 \text{ Wm}^{-1}\text{K}^{-1}$ and $\kappa_{\perp} = 0.76 \text{ Wm}^{-1}\text{K}^{-1}$, respectively [413]. In this sense, one of the problems of SThM is that the quantitative separation of both in-plane and out-of-plane contributions of the measured thermal conductance is non-trivial, requiring specific sample geometries and modelling to be able to separate them. Thus, it can be assumed that the SThM signals measured here in both cases, ambient and vacuum environments, are a convolution of the two contributions up to a certain point. Having clarified this, our measurements suggest that out-of-plane thermal conductance dominates the SThM response obtained here, at least for thin flakes, as the values of the thermal conductivity are even lower than the thermal conductivity of SiO₂. Also, the observed increase of the thermal conductivity for thicker flakes could be attributed to an increasing contribution also from the in-plane component in the SThM signal. In the “future work” section presented in *chapter 8* at the end of the thesis, we are suggesting approaches that may help to investigate this anisotropic thermal transport in 2D materials.

Finally, it is clear from the experiments performed here that SThM presents an advantage in terms of resolution when compared with other methods for the determination of the thermal properties at the nanoscale, such as photocurrent microscopy or time-domain thermo-reflectance (TDTR) [413, 414]. In order to further exploit the unique capabilities of SThM, next steps could involve the calibration of the SThM probes together with the development of specific modelling for the system presented here, in order to unravel the value of the interfacial thermal resistance of the tip-sample junction and to produce quantitative values of the thermal conductivities of InSe with nanoscale resolution [409].

7.4 Local Seebeck coefficient variations in GFET devices with patterned constrictions

The thermoelectric properties of graphene have generated great interest due to its extraordinary electronic and thermal properties, its gate-controlled ambipolar behaviour, and competitive Seebeck coefficient, S , with respect to bulk TE materials [173, 415, 416]. Furthermore, in recent studies, the effects of nanostructuring on the enhancement of the TE properties of graphene have been studied, showing local variations of the Seebeck coefficient [397, 398]. This effect has been observed previously in thin films stripes and gold nanowires [417, 418], however, achieving control of the Seebeck coefficient in 2D materials could lead to the development of thermal management systems with nanoscale thickness. For graphene, the enhancement and control of the TE properties could lead to the development of single metal thermocouples for temperature sensing or coolers for thermal load distribution and hot-spot removal with nanoscale dimensions.

The variations of the local Seebeck coefficient in graphene have been attributed to the energy dependent reduction of the electronic mean-free path (EMFP). Therefore, a common strategy proposed in order to engineer the value of S relies on increasing the scattering by creating rough edges, additional interfaces or patterned boundaries. In the previous studies performed by Harzheim et al., these strategies were exploited by studying a CVD graphene sample with a nanopatterned bow-tie constriction [397], and a mono-bilayer graphene junction [398]. However, in both these studies, the thermovoltage measurements were performed on graphene samples deposited on SiO_2 substrates, which have surface charge states and impurities that introduce large potential fluctuations in graphene, p-doping it and inducing electron-hole puddles in the vicinity of the charge-neutrality point. This results in reduced value of the Seebeck coefficient, and thus, of the thermovoltage, as shown by previous studies [416]. Additionally, the lack of a passivation layer covering these devices (e.g. hBN encapsulation), could lead to electrical doping and charge transfer directly from the tip which is always in direct contact with the sample. Finally, as only one geometry was studied in each of the two cases presented above, the effect of the

symmetry on the geometrical and the electrostatic gating on the TE phenomena was not fully characterised.

Here, we tackled these issues by studying the spatial distribution of the thermoelectric voltage in encapsulated graphene devices using electrostatic back-gate to control the charge doping. Different constrictions with asymmetric geometries and varying widths were patterned, as shown in *figure 7.9(a-d)*, allowing to study the effect of symmetry in the EMFP and thus, in the thermovoltage signal. To determine the thermovoltage changes, scanning thermal gate microscopy (STGM) was employed. This is a novel SPM mode in which a tip is employed as the local heating source and scanned over the sample in open circuit configuration (*figure 7.9(e)*), creating thermovoltage maps with nanoscale resolution as described above.

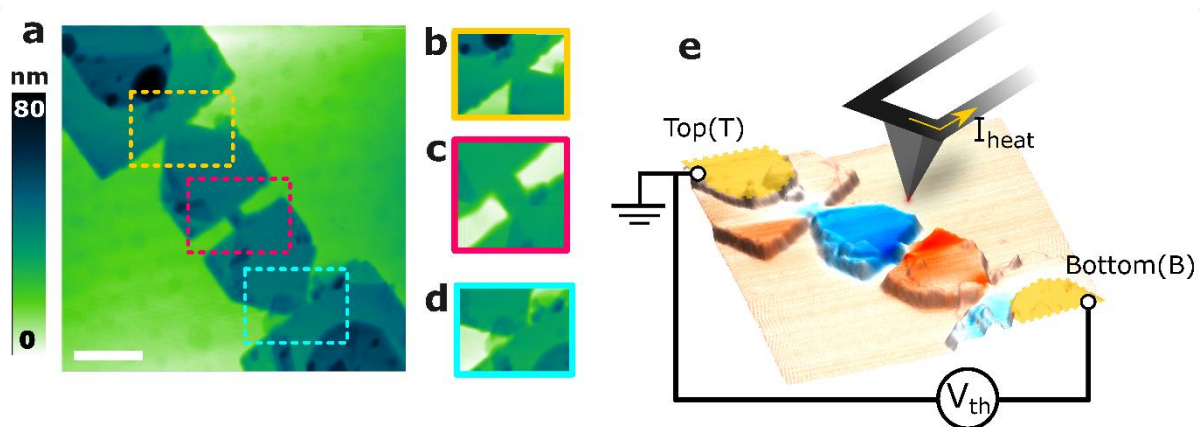


Figure 7.9. (a) Topography of the graphene encapsulated device (Scale bar: $1\mu\text{m}$) with different patterned constrictions: (b) half bow-tie-flat junction top, (c) rectangular flat-narrow-flat central and (d) half bow-tie-flat junction bottom constriction. (e) Schematic of the experimental set-up for STGM. The probe acts as a local heater, while the thermovoltage generated on the graphene layer is measured through the Au contacts, highlighted in yellow in the figure.

7.4.1 Graphene device fabrication

The encapsulated graphene was fabricated following the *PMMA carrying layer method*, explained in *chapter 4, Section 4.6.3*. The exfoliation of the bottom hBN was performed on a 90 nm $\text{Si}_2\text{O}/\text{Si}$ chip, and the flake finally selected for the heterostructure was relatively big in size, clean and homogeneous (i.e. with no obvious folds or cracks), as the one shown in *figure 7.10*. Then, the top hBN and the graphite were exfoliated separately in different chips of PMMA/PVA/Si. For the top hBN layer, a homogeneous and thin layer (i.e. $\sim 10\text{L}$) was selected, cut into a membrane and separated. Once a suitable 1LG film was selected, the top hBN flake was used to pick up the graphene leaving both flakes hBN/1LG stuck to the membrane. The only requirement for this is that the top hBN has to be larger than the 1LG flake. Finally, the system of Top-hBN/1LG is aligned with the bottom hBN and transferred, creating an encapsulated graphene heterostructure as

shown in *figure 7.10(a)*. The different layers, together with any specific contamination or defects are more clearly visible in dark field mode shown in *figure 7.10(b)*.

A device formed of three constrictions, two external half bow-ties-flat junction and an internal rectangular flat-narrow-flat constriction, was designed using *Layout Editor* to fit into the area covered by graphene, as shown in *figure 7.10(c)*, and then fabricated following the procedures explained in *chapter 4, section 4.7*. One-dimensional(1D) electrical contacts to the device were created by a chromium adhesion layer (between 1 – 5 nm) followed by a thicker film of gold (~50 nm). Then, the chip in which the device was fabricated was cut in a smaller sized piece for easy handling. In order to do the measurements, the device was placed on a gold chip carrier suitable for the NT-MDT microscope used in the following sections. As shown in *figure 7.10(e)*, a mica spacer was placed between the bottom Si surface of the substrate and the Au coated surface of the chip carrier to avoid shorting. Bonding to the contact pads was performed by hand following the method described in *chapter 4, section 4.7*. For this, a two-part epoxy (EPO-TEK® H21D [419]) was used. First, the epoxy was mixed in a 10:1 ratio, and then, after mixing the two parts, small blobs were dropped on the gold pads of the device. While the epoxy was still wet, Au wires were cut with appropriate length and stuck onto the epoxy. In order to harden the mixture, the device was annealed at 80 °C for 90 minutes. Then, a bit of silver paint was used over the hardened epoxy contacts to ensure proper electrical connection. The final shape of the contacts can be seen in *figure 7.10(e)*. The process is repeated for the contacts on the chip carrier, connecting there the opposite ends of the wires.

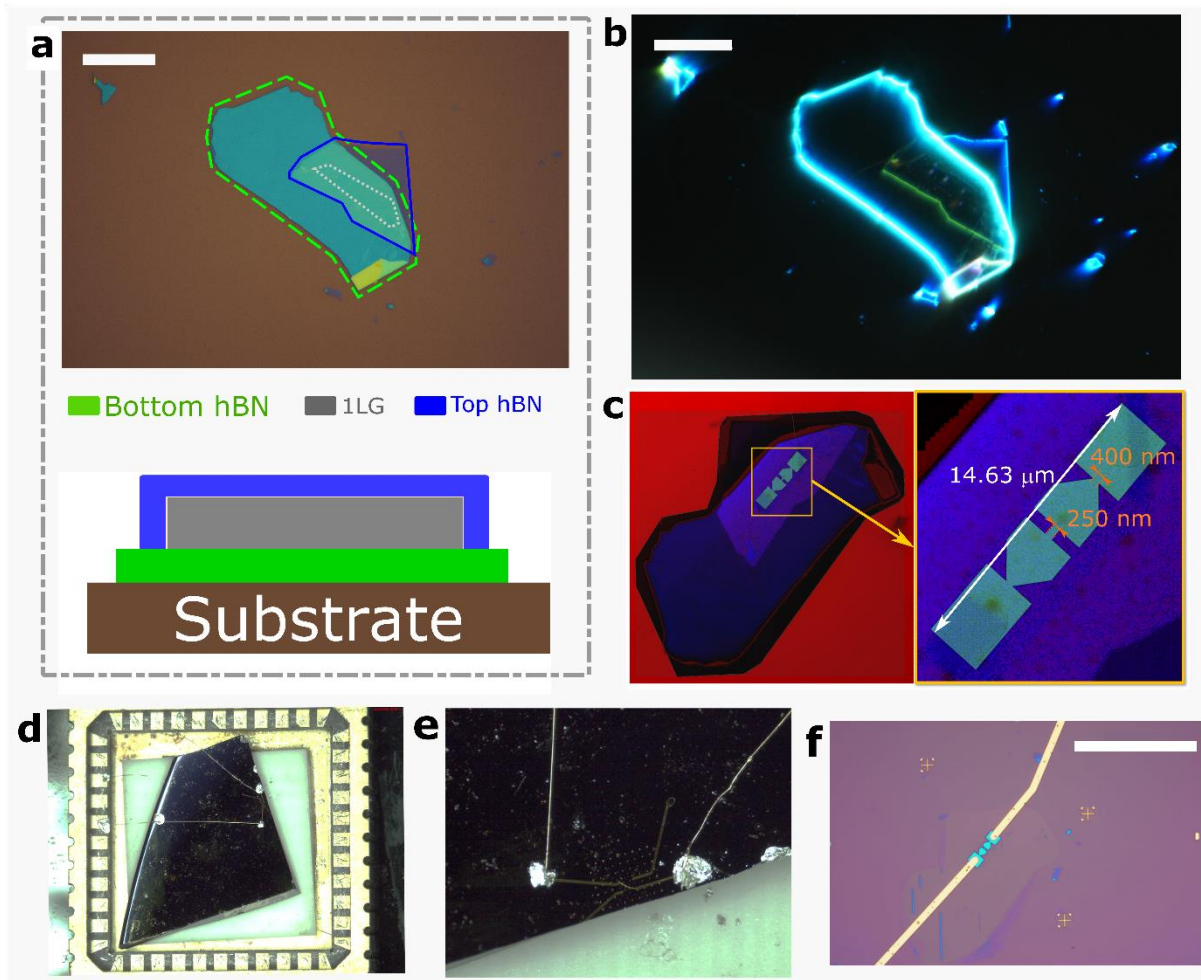


Figure 7.10. Fabrication process of the encapsulated graphene device. In (a), the top panel shows a bright field image with the bottom hBN, 1LG and top hBN surrounded by light green, grey and dark blue lines, respectively. In the bottom panel, a schematic lateral view of the layers is displayed following the same colour convention, with a legend for guidance. In (b), the dark field microscopy image shows more clearly the contours of the different layers. The scale bar both in (a) and (b) images is 20 μm . In (c) the design of the device is performed in Layout Editor. In the left panel, an overview of the whole heterostructure with the design placed on top is presented, while the right panel shows a more detailed view of the constrictions. (d) Sample containing the device mounted on a gold chip carrier and wire bonded by hand. (e) Detail of the bonding on the contact pads of the device. (f) Close zoom-in of the device on the chip with three alignment marks. The area in which the rest of the heterostructure was placed is clearly visible as it presents a different contrast than the rest of the surface of the 300 nm SiO_2 chip. Scale bar: 50 μm .

7.4.2 Graphene device characterisation

Prior to the STGM measurements, the graphene device was characterised using different techniques. As shown in figure 7.11(a), AFM maps were initially performed to study the topography of the device. Profiles of the Au contacts (figure 7.11(b)) and of the encapsulated graphene (figure 7.11(c)) revealed thicknesses of $\sim 45 \text{ nm}$ and $\sim 25 \text{ nm}$, respectively. The contacts are separated a distance of $\sim 4.2 \mu\text{m}$, which corresponds to the length of the device. The width of the graphene was $\sim 1.5 \mu\text{m}$, narrowing to $\sim 400 \text{ nm}$ for the two outer half bow-tie constrictions and $\sim 250 \text{ nm}$ for the central rectangular constriction.

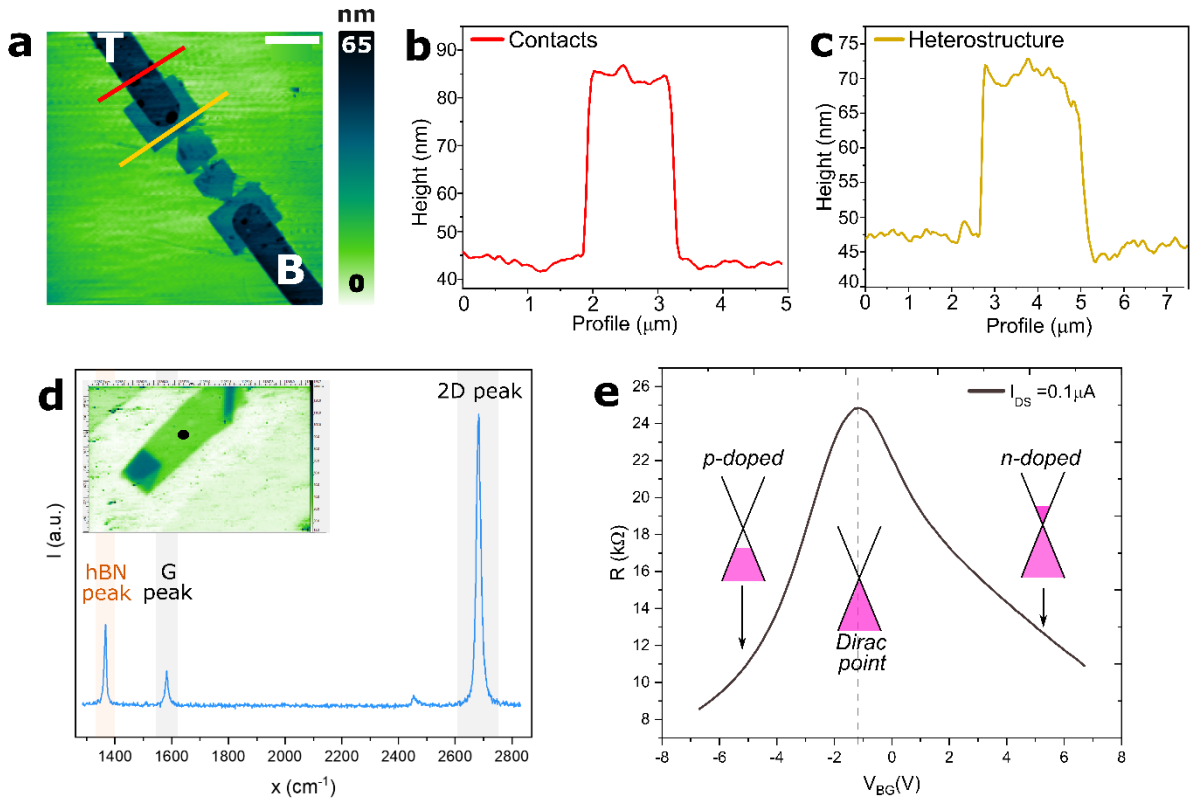


Figure 7.11. (a) AFM topography of the encapsulated device. Scale bar: 2 μm . The contact pads have been named as top(T) and bottom(B), establishing a reference notation for the following sections. Profiles of the contact and the device are acquired following the red and yellow lines, and are shown in (b) and (c), respectively. (d) Raman spectrum showing the characteristic hBN peak (highlighted in orange) and the G and 2D graphene peaks (highlighted in grey). Inset: Intensity map obtained using the G-peak of graphene. The spectrum was acquired at the black dot position in the inset (e) Channel resistance versus backgate voltage measured at room temperature and $P = 10^{-7}$ mbar. The measurements were performed using a 2 point-probe set-up ($V_{\text{DS}}^{\text{L/A}} = 0.1\text{V}$, which resulted in $I_{\text{DS}} \sim 0.1\mu\text{A}$).

Raman maps were acquired over the area of the heterostructure before patterning the device with a Renishaw InVia using $\lambda = 532$ nm. This technique was employed as the only way to evaluate the thickness and quality of the graphene prior to the final steps of the fabrication. An example map showing the graphene G-peak intensity of the area is displayed in the inset of figure 7.11(d). A representative spectrum is displayed in figure 7.11(d), with the characteristic G and 2D peak of graphene highlighted in light grey, together with a symmetric peak at $\sim 1360\text{cm}^{-1}$ corresponding to the presence of hBN, highlighted in orange. The ratio of intensities between the 2D and G peaks, $I(2D)/I(G) > 1$, is attributed to the presence of monolayer graphene.

Using the set-up described in section 7.2.4, the resistance of the graphene contacts was measured using a 2-point probe configuration giving a total value of ~ 22.0 k Ω , which is acceptable for this type of devices, especially considering that this value includes the contact resistance as well as the device resistance. Additionally, the variation of the resistance of the graphene channel with respect to the applied back gate voltage was measured at room temperature and $P = 10^{-7}$ mbar. As shown in figure 7.11(e), the Dirac point was found to be at $V_{\text{Dirac}} \sim -1.16\text{V}$, revealing slightly intrinsic n-doping on the device.

The device was also studied using SThM in vacuum conditions (10^{-7} mbar) with AN2-200 doped silicon probes (as in Section 7.3.3). A representative SThM map is displayed in figure 7.12(a). The surface of the device shows the lowest contrast of the map, i.e. darker colour, thus indicating higher thermal conductivity than the neighbouring regions (i.e. the SiO₂ substrate and the Au contacts, as indicated in the figure). This agrees with previous measurements which estimated a thermal conductivity for graphene encapsulated heterostructures supported on SiO₂ as high as $\sim 850 \text{ Wm}^{-1}\text{K}^{-1}$ [420], in contrast with the values reported for SiO₂ and Au, being $\sim 1.2 \text{ Wm}^{-1}\text{K}^{-1}$ and $\sim 314 \text{ Wm}^{-1}\text{K}^{-1}$, respectively [421, 422].

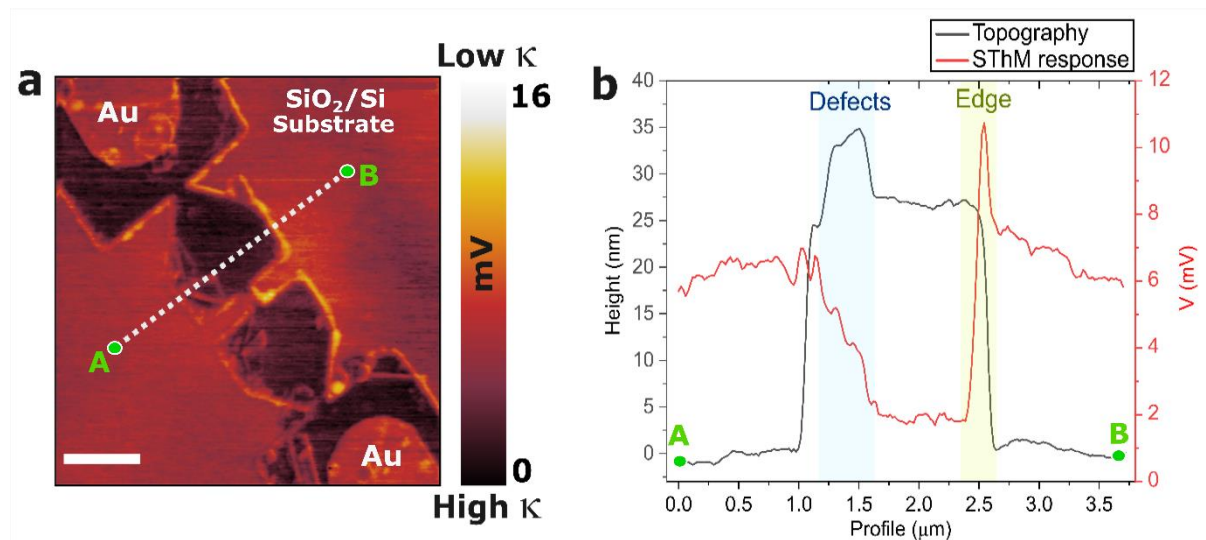


Figure 7.12. (a) SThM map of hBN encapsulated graphene test device. Darker contrast corresponds to higher thermal conductivity as expected from the hBN and graphene stack. Scale bar: $1 \mu\text{m}$. (b) Comparison of the profiles acquired for the topography (black) and the SThM response (red) signals

Another interesting feature observed in the SThM maps is that the different boundaries in the device present higher SThM voltage which correspond to lower thermal conductivity values. Two types of boundaries can be distinguished in this case: the natural borders of the device formed by etching, and the defective areas in which the hBN has been peeled off with the AFM tip. The lower thermal conductivity values of these areas can be related to the higher scattering occurring at the edges, as well as to tip artefacts. Just for the purpose of visualising these effects, profiles of the topography and the SThM response were acquired following the white dotted line from the point A to the point B in figure 7.12(a) and represented in figure 7.12(b). The areas corresponding to defects (i.e. peeled off hBN) and device edges, effectively present higher voltages (i.e. lower thermal conductivity) than the graphene device area as highlighted in figure 7.12(b) by blue and green backgrounds, respectively. This is especially noticeable for the later, i.e. the clean edge, which presents a tall sharp peak. However, as mentioned above, the deconvolution of this signal into the contribution corresponding to either the edge or the probe, requires modelling as the interaction of the tip with the edge of a material is more complex than the normal contact

occurring on the surface. Further analysis on this topic is out of the scope of this research, but it is an interesting route to explore edge effects, and scattering mechanisms that could affect 2D material's based devices performance.

7.4.3 Probing TE response of encapsulated graphene nanostructures via STGM

The thermoelectric voltage (V_{th}) difference created between the contact leads of the patterned device is given by the convolution of the distribution of the thermal gradient and the spatial distribution of the Seebeck coefficient along the direction of the potential difference:

$$V_{th} = - \int_{x_B}^{x_T} S(x, T) \cdot \nabla T(x) dx \quad (7.6)$$

where x_B and x_T represent the position of the bottom and top contacts, S is the position and temperature dependent Seebeck coefficient, and ∇T the local gradient in the temperature created by the hot tip. In the configuration studied here, the device is heated at particular point on the device surface with the contact leads kept at identical temperatures. Assuming that $\nabla T(x)$ is a symmetric function (given that heat diffusion through the substrate likely dominates any asymmetries the graphene could have), eq.7.6 shows that V_{th} reflects the local variations (asymmetry) of S around the position of measurement, x_0 , within a length scale given by the thermal resistances of the sample. Therefore, in the areas where the Seebeck coefficient is constant, the overall thermovoltage signal measured would be zero, whereas in the areas where the Seebeck coefficient is asymmetric, hence with a spatial gradient (e.g. above the junction of two dissimilar materials with different Seebeck coefficient) the resulting thermovoltage would be non-zero.

As mentioned previously, at the nanoscale, the value of S can be locally modified by changes in the EMFP. For encapsulated graphene the EMFP is on the order of hundreds of nanometres, even reaching micrometre values [36, 423]. However, the value of the EMFP is not only influenced by the carrier density or the temperature, but it is also heavily affected by various scattering mechanisms as for example, surface trapped charges, defects in the lattice or defect potentials stemming from rough edges, or trapped charges, among others [424, 425]. Here, the presence of patterned constrictions enhances the scattering produced by the rough edges. This scattering mechanism becomes more dominant as the size of the constriction reduces, thus leading to a position dependent mean free path as expressed by:

$$l(x) = l_0 \left[1 + c_n \left(\frac{l_0}{\Delta y(x)} \right)^n \right]^{-1} \quad (27)$$

Where l_0 is the bulk mean free path, c_n and n are numerical coefficients specifying the transport regime and the influence of scattering in the EMFP ($c_n, n \in \mathbb{R}$), and $\Delta y(x)$ is the position dependent width of the device. The variation of the Seebeck coefficient with the device width, and thus with the EMFP, can be obtained by applying the Mott formula for metals. In Harzheim et al. [397] a full derivation of thermopower dependence on $\Delta y(x)$ can be found for bare graphene with a patterned bow-tie constriction, predicting the decrease of the Seebeck coefficient with the width of the channel, leading to regions with different effective Seebeck coefficient.

With the devices studied here, the encapsulation should lead to an enhanced thermovoltage signal, however, we expect to observe similar responses in the areas close to the constrictions. In order to test this, STGM measurements were acquired in vacuum with the sample at room temperature, $T_{sample} \sim 297K$, and an excess temperature on the tip apex of $\Delta T_{tip} \approx 50K$, to locally heat the surface. The excess temperature of the tip has been calculated using a calibration performed on similar probes allowing the transformation of the applied signal to the probe (i.e. a combination of AC and DC signals) to a certain temperature. Also, the charge carrier distribution was controlled by a global back-gate, and thermovoltage maps were acquired at two different positions of the backgate: for p-doped, and n-doped graphene channel.

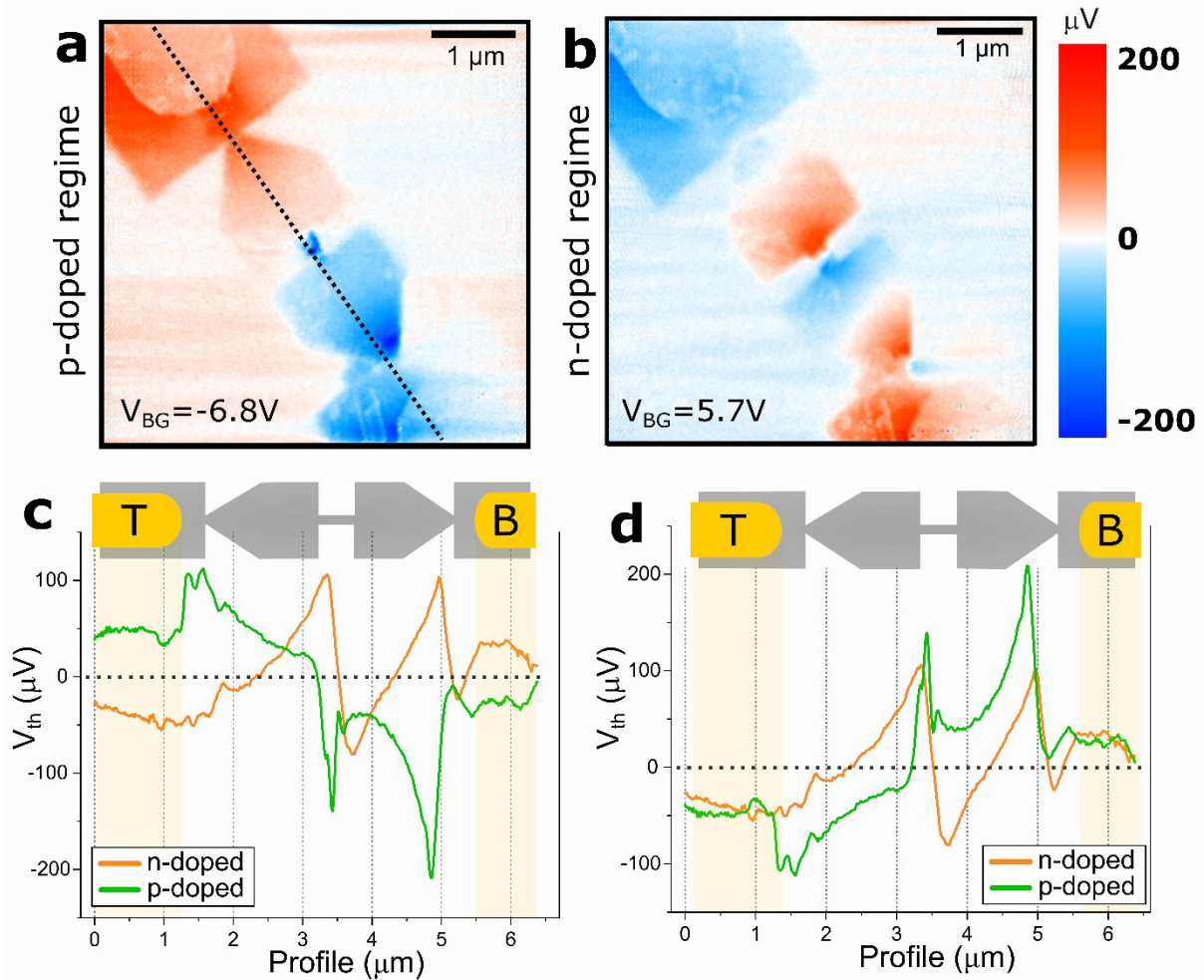


Figure 7.13 Thermovoltage measurements performed in vacuum ($\sim 10^{-7}$ mbar), with the sample at room temperature ($T_s \sim 293$ K), and an excess temperature on the tip of ~ 50 K. Measurements were performed for different backgate voltages: (a) $V_{BG} = -6.8$ V, therefore showing p-doped behaviour, and at (b) $V_{BG} = 5.7$ V, with an n-doped behaviour. In (c) profiles acquired across grey dotted line in (a) are compared for both p (orange) and n (green) type doping behaviours. In (d), the p-doped image was inverted, and the n-type (orange) and inverted p-type (green) profiles were compared in order to assess the symmetry of the response for opposite charge doping in the device.

In figure 7.13(a) and (b), thermovoltage maps (V_{th}) are presented for p-doped ($V_{BG} = -6.8$ V) and n-doped ($V_{BG} = 5.7$ V) graphene, respectively. In both maps, local variations of the measured V_{th} polarity are observed around the rectangular central constriction, which could be related to the local variation of the Seebeck coefficient in that area. It is particularly interesting that for the n-doped case, the V_{th} is inverted again before the half bow-tie constrictions, leading to opposite polarity of V_{th} than for the p-doped case on the Au contacts-graphene area. In order to study these responses in more detail, profiles were acquired for both p- and n-doping cases following the dotted line in figure 7.13(a), and represented in figure 7.13(c). The highest relative thermovoltage signal happens at the rectangular constriction, and at the bottom half bow-tie constriction, for both cases: p-doped (green line) and n-doped (orange line) graphene, although showing opposite polarity. These observations would agree with the initial assumption that the Seebeck coefficient depends on the variations of the electron mean free path, and thus in the disorder of the area and

the geometry. This is especially notable when comparing the two half-bow-tie constrictions: even having the same width ($\sim 400 \text{ nm}$), the bottom half bow-tie constriction presents higher V_{th} than the top half bow-tie constriction. This is attributed to the higher levels of disorder present in the bottom half-bow-tie constriction, as shown in *figure 7.9(d)*, compared to the top half-bow-tie constriction shown in *figure 7.9(b)* which remains almost pristine. The disorder is caused by the fact that the hBN in the bottom half-bow-tie was unintentionally peeled by the tip while scanning, creating folds which act as scattering centres. The same happened in the area close to the central constriction, as shown in *figure 7.9*. Finally, the similarity of the V_{th} signals was tested by comparing the n-doped profile response with the p-doped profile obtained for an inverted image, as shown in *figure 7.13(d)*. The observed similarity between both signals, highlights the symmetry in the device response obtained for almost opposite charge doping profiles. In both cases, the Au-graphene contacts present a constant value of V_{th} , with opposite polarity for top (T) and bottom (B) contacts, and regions of opposite polarity appear through the device with maxima of V_{th} at the constriction location.

In order to enhance the Seebeck response, S , and verify these initial observations, another set of measurements were performed in vacuum ($\sim 10^{-7} \text{ mbar}$) with a higher applied temperature gradient, ∇T . For this, liquid nitrogen was poured into the thermal reservoir of the system (*figure 7.1-5*), which is connected to the sample, leading to the reduction of the sample temperature down to $T_S \sim 170 \text{ K}$. Keeping the temperature of the probe the same, $T_P \sim 340 \text{ K}$, the temperature difference between both systems changed from $\Delta T_{tip}^{RT} \sim 50 \text{ K}$ at room-temperature, up to $\Delta T_{tip}^{LT} \sim 170 \text{ K}$ at low-temperature. Thermovoltage maps performed for p-doped and n-doped graphene are presented in *figure 7.14(a)* and *(b)*, respectively. The thermovoltage response signal in this case is much higher reaching values up to 1 mV , while for the measurements with the smaller ∇T presented in *figure 7.13*, we obtained values of the V_{th} signal around $200 \mu\text{V}$.

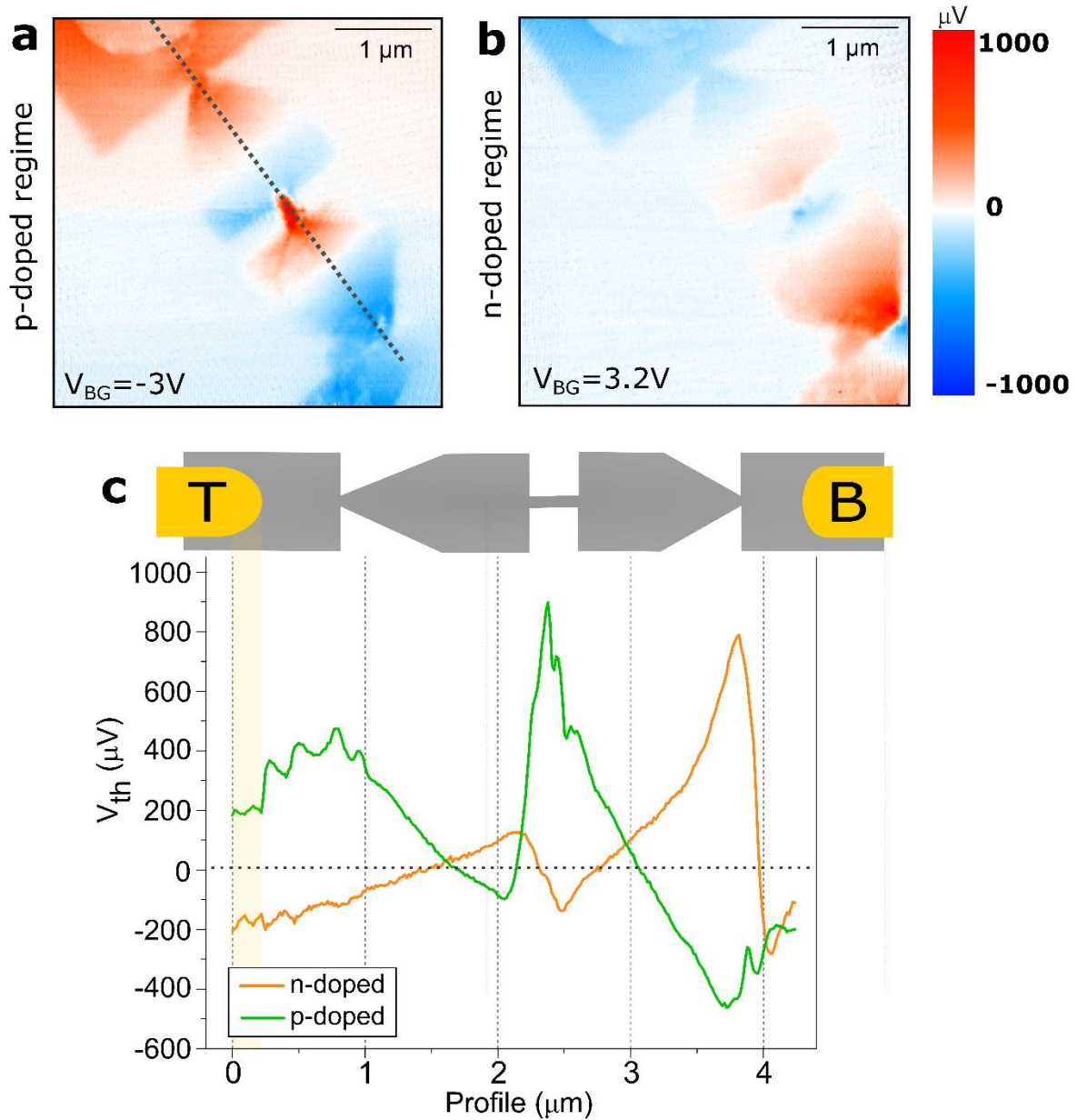


Figure 7.14. Thermovoltage measurements performed in vacuum ($\sim 10^{-7}$ mbar) and low sample temperatures ($T_s \sim 170$ K). Almost opposite Seebeck domains can be observed for (a) p-doped graphene ($V_{BG} = -3$ V) and (b) n-doped graphene ($V_{BG} = 3$ V). (c) Profiles of the p-doped (green) and the n-doped (orange) maps are compared. The profiles were acquired along the dotted grey line in (a). The contacts have been labelled as S (source) and D (drain) corresponding to the top and bottom contacts, respectively.

Besides the aforementioned difference in V_{th} signal strength, the observed polarity of the V_{th} ‘domains’ for both p-doped and n-doped cases, remains the same at low sample temperatures (figure 7.14) than at room sample temperatures (figure 7.13). Finally, when comparing the profiles for the p-doped and n-doped cases with a low sample temperature, as shown in figure 7.14(c), the highest V_{th} response is again observed for the central rectangular constriction and the bottom half-bow-tie constriction as in figure 7.13(c).

The results observed here, specifically for the central rectangular constriction which had a width of 200 nm, 7.5 narrower than the full width of the device of 1.5 μm , seem to point out that nanosized constrictions effectively work in reducing the EMFP, and thus affecting the Seebeck coefficient. In this sense, it could be understood as having two different materials with different Seebeck coefficients, S_{Gr} and $S_{constriction}$, for example, leading to the formation of a nanosized thermocouple.

7.4.3.1 Additional contributions to the measured V_{th}

The voltage signal measured can contain different contributions besides the thermovoltage signal coming from the device, such as additional effects from the probe or Seebeck response of the Au top contact area. In this section, these contributions are shortly addressed:

Heating the tip is achieved by applying a combination of AC and DC current to the probe. As the STGM measurements are performed in contact, this applied ‘heating’ can potentially influence the device response if the tip contacts the sample. It was observed that at the edges, in areas in which the hBN was peeled off, and on top of the metallic Au contacts occasional spikes appeared while measuring, indicating electrical connection, “shorting” between the tip and a device. Despite these observations, this was not an issue during the measurements due to the presence of the hBN cover acting as a passivation layer and protecting the graphene.

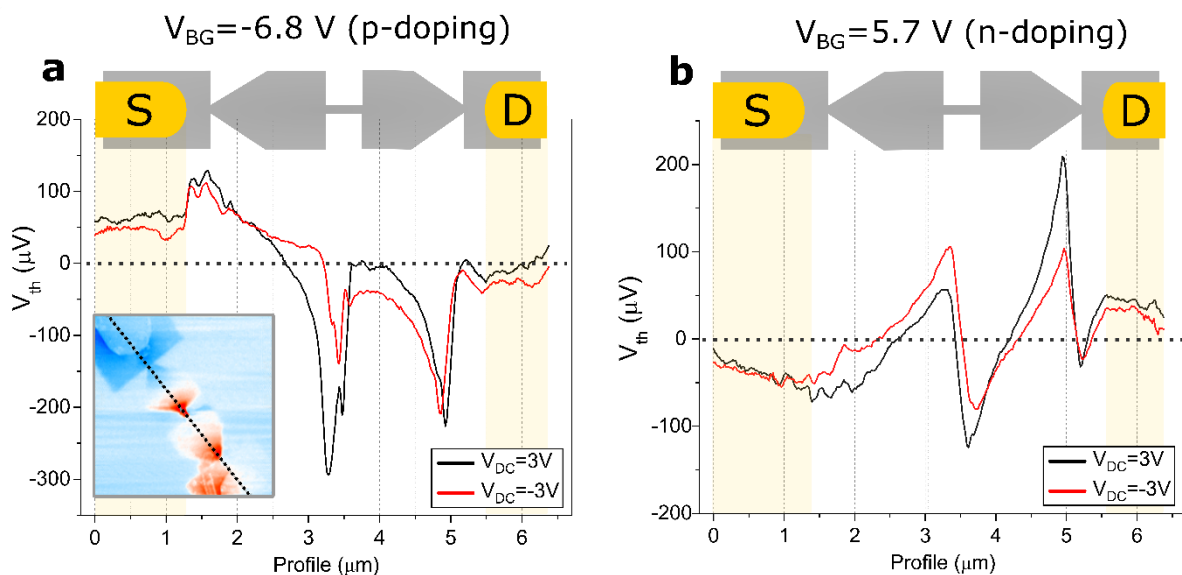


Figure 7.15. Tip gating effect studied by comparing the signal profiles obtained along the line shown in the inset. Two heating voltages are depicted, namely $V_{DC} = 3\text{ V}$ (black) and $V_{DC} = -3\text{ V}$ (red) for (a) p-doped graphene ($V_{BG} = -6.8\text{ V}$), and (b) n-doped graphene ($V_{BG} = -5.7\text{ V}$)

Besides shorting the device, the tip can act like one plate of a parallel plate capacitor, being the conductive graphene the other one, leading to charge accumulation while scanning. In order to study the effect of the probe on the measured V_{th} response, scans were acquired for different

graphene doping levels while the DC voltage applied to the probe was modified from negative to positive. In *figure 7.15*, representative profiles are compared for $V_{DC} = 3V$ (black line) and $V_{DC} = -3V$ (red line), for p-doped graphene with an applied $V_{BG} = -6.8V$ (*figure 7.15(a)*), and for n-doped graphene with $V_{BG} = 5.7V$ (*figure 7.15(b)*). The results show very similar responses in both cases, with small deviations that are statistically acceptable. From this, it can be concluded that the tip gating has very little influence in the measured thermovoltage signal for encapsulated graphene devices.

Another element that could also contribute to the measured V_{th} signal are the Au contacts. In previous studies, the graphene underneath the contacts was demonstrated to be shielded from the global backgate, leading to strong V_{th} on the contact region which could lead to charge doping from the contacts to the graphene, thus adding an extra contribution to the measured thermovoltage and Seebeck coefficient [398]. However, in the measurements presented here the scenario is not exactly the same as 1D contact is established between the Cr/Au layer with graphene, and there is no other direct contact between the two materials, as the graphene is encapsulated with hBN. Here, a slightly high thermovoltage signal can be observed around the metallic contacts, as for example shown in *figure 7.13*, although not as strong as the one observed by Harzheim et al. [398]. The origin of this thermovoltage build is not fully understood, and modelling or further experiments would be needed to clarify the origin of the observed charge build-up.

7.5 Conclusions

This chapter includes different studies of nanoscale thermal properties of 2D materials. In the first section, SThM measurements were performed on exfoliated InSe both in ambient and vacuum conditions for the first time, providing important insights on the local thermal conductivities and interfacial thermal resistance of the InSe nanoscale layers.

One of the first things that became apparent from this study is the importance of the thermal anisotropy present in this material. Previous studies on bulk γ – InSe have demonstrated an in-plane thermal conductivity six times larger than the corresponding out of plane, being $k_{in-plane} = 10.42 Wm^{-1}K^{-1}$ and $k_{out-of-plane} = 1.74 Wm^{-1}K^{-1}$. Comparing these values with the results presented here, it seems that the SThM responses obtained are mainly linked to the cross-plane thermal conductivity, especially for thin flakes, with an increasing contribution of the in-plane thermal conductivity for thicker flakes. In principle, SThM cannot distinguish between both components, thus the results obtained here are a convolution of the two contributions and in order to separate them further modelling would be required. Another important observation

is that the interfacial thermal resistance between InSe and the substrate dominates the thermal transport and heat dissipation in these nanostructures. To quantify this contribution, a detailed study of InSe with different thicknesses on different substrates would be needed. One effective solution for this would be the combination of beam assist cross-sectional polishing (BEXP) with SThM measurements, as it will be discussed in more detail in *chapter 8*.

In the second section of the chapter, the thermoelectric voltage (V_{th}) in encapsulated graphene devices with patterned constrictions was studied via STGM for the first time. This experiment was developed as the following step to previous research which explored the effects of nanostructuring on the local variations of the Seebeck coefficient on bare graphene devices [397, 398]. Here, two novel approaches were adopted and studied: (1) the enhancement of the thermovoltage, and thus the Seebeck coefficient via graphene encapsulation, gate carrier control, and temperature gradient control; and (2) the creation of local S domains by patterning constrictions of varying geometry, symmetry and width. The conclusions presented in the following comprise the application of these two strategies combined: To start, the thermovoltage sign inversion was observed in the devices confirming the previous measurements in bare graphene, and thus, the effect of nanopatterning as an effective strategy to modify the thermoelectric properties of this material. Also, the magnitude, sign and size of the V_{th} regions consistently showed strong spatial dependence, often linked to the presence of the patterned constrictions, which was especially clear for the central rectangular one. Additionally, the high magnitude of the measured thermovoltage is attributed to the encapsulation of the graphene channel. In the previous studies, CVD graphene was directly deposited on top of SiO_2 . This substrate has demonstrated to present surface charges and impurities causing Coulomb scattering on the graphene devices, thus limiting the charge carrier mobility, introducing large potential fluctuations, and leading to the reduction of the total magnitude of the V_{th} . Therefore, here, by using encapsulation the intrinsic electronic properties of graphene were better preserved, isolating it from external contributions from the substrate, and therefore, leading to an enhanced TE intrinsic signal, and increased intrinsic EMFP. This is a qualitative observation that would be interesting to test in further experiments. Another suitable strategy studied here to manipulate the thermovoltage signal is the variation of the temperature gradient applied in the system. Based on our results, in which a 5-fold increased in the V_{th} signal magnitude was observed when the sample was cooled to low temperatures ($T_S \sim 170\text{K}$), by applying higher values of ΔT the intensity of the V_{th} signal can be highly increased. With respect to sign switching of the V_{th} signal, its origin is attributed to the presence of constrictions and inhomogeneities, as shown by the profiles acquired. However, as demonstrated here, this effect can be also controlled by changing the carrier concentration of the graphene sheet using global back-gate.

These results, including the observed geometry dependence of the TE graphene properties, together with their control via different strategies such as encapsulation, or electronic and thermal gating, are fundamental as they could represent a new paradigm for the control of TE properties at the nanoscale, enabling the development of single metal thermocouples[426] for temperature sensing and coolers for thermal load distribution and hot-spot removal with nanoscale dimensions. In order to fully understand the influence of the microstructure on the absolute Seebeck coefficient, and also the contributions of thermodiffusion and phonon drag in the measured signal, performing modelling on the system would be an interesting future route.

Finally, an important conclusion extracted from this study was the suitability of STGM as a non-invasive tool to study the thermovoltage, and in general, the TE properties of 2D materials at the nanoscale. Besides offering higher resolution than currently employed optical methods, such as the photo-thermoelectric measurements [175, 427], it requires a simple set-up and provides fast and reliable measurements, thus competing with other SPM options based on SNOM[428].

Conclusions and perspectives

In the very beginning of this thesis I quoted A. Castellanos-Gomez who raised the question ‘*Why all the fuss about 2D semiconductors (and graphene)?*’ [16]. Prior research revealed a plethora of exciting properties held by graphene and its other 2D cousins, presenting an enormous potential for the development of new applications in different fields, and appearing as ideal candidates to push the scaling limits already reached by current technologies [429]. The number of possibilities increases when considering the van der Waals forces that hold the layers of 2D materials together, which facilitates their separation and re-stacking, and thus, the fabrication of novel heterostructures, in turn displaying new physical and chemical properties. However, as the landscape of opportunities and possible combinations are so vast, many promising research topics remained widely unexplored. The aim of this work was to address some of these questions, contributing to the progress and understanding in several interlinked areas. For this, we have investigated the fabrication methods for 2D materials, heterostructures and devices, and explored the nanoscale electronic and thermophysical properties of these using spectroscopic and advanced scanning probe methods. Below, is the brief summary of the key results achieved in this thesis and the future perspectives arising from the work performed are discussed.

8.1 Conclusions and key results

Chapter 4 - Fabrication of 2D materials: In this chapter, the fabrication techniques for 2D materials and heterostructures, focusing on mechanical exfoliation and polymeric transfer methods were explored in depth. Also, the processes required to produce devices based on 2D materials were investigated. As a reference, an example of fabrication of a complex heterostructure developed during this thesis was presented in the last section of the chapter (*section 4.7*), including a detailed explanation of all the steps undertaken to convert material

crystals into complex devices. The main achievements of this line of research are highlighted below:

- **Fabrication of tailored 2D material exfoliated samples, complex heterostructures and devices:** A variety of exfoliated 2D materials, heterostructures and devices based on graphene and other less explored materials like InSe, were successfully fabricated during this PhD project using the procedures explained in the chapter. These were used in a variety of different experiments, some of which are discussed in the other chapters of the thesis. It is important to highlight that some of the results obtained for the fabricated samples have led to journal publications [106, 277, 284]. Also, the successful collaboration with other research centres (i.e. Denmark Technical University and the National Graphene Institute) produced some 2D materials nanostructures that were successfully used in the studies beyond the scope of this thesis.
- **Development of a novel edge detection algorithm for flake identification:** In order to overcome the poor contrast offered by some exfoliated 2D materials when observed through a white light microscope, together with the necessity to automate the finding of flakes with the right geometry for the complex heterostructures, an edge detection algorithm for 2D materials detection was developed in Python. The program consists of a graphical user interface (GUI) that allows the scientist to upload an image, apply and tune a certain filter from a list (i.e. Sobel, Scharr and Laplacian), and then save the result. This provided the foundation for the subsequent correlation of the output of the filters with the number of layers of the flakes under study, and implementing follow up tools to improve the image quality.
- **Design and fabrication of a 2D materials transfer station for heterostructure production:** I initiated a 2D materials fabrication facility at NPL. For this purpose, I prepared a space in the cleanroom exclusively dedicated for mechanical exfoliation of 2D materials, and I developed and built a custom-made transfer station. All these resources were essential for the successful production of exfoliated flakes and 2D heterostructures.

Chapter 5 – Doping effects in graphene: here, a systematic study was performed comparing the Raman response of samples grown by different methods and with different thicknesses: exfoliated, CVD and epitaxial, monolayer and bilayer graphene, under different levels the relative humidity. The key outcome from this research is summarised in the following:

- **Undertaking a novel approach for the study of environmental doping effects in graphene using Raman spectroscopy:** Raman spectroscopy was employed previously

to characterise the electrostatic and substrate induced doping response of graphene exfoliated samples [307, 309]. However, here we expand its application and employ the technique to study the doping effect of an environmental molecule (i.e. H₂O) in the comparison of different types of graphene and with different thicknesses. The sensitivity of graphene to varying levels of relative humidity was observed in terms of Raman shifts, finding unique characteristic responses for each of the different types of graphene analysed. Furthermore, the charge concentration for the exfoliated and CVD graphene samples was calculated using a vector decomposition method applied to the acquired Raman maps. Good agreement was found when comparing these results with previously obtained data via van der Pauw methods on similar samples, thus demonstrating the robustness of this approach. This method therefore serves as a demonstration of an alternative way to study the environmental doping variation in graphene in a fast, non-invasive and robust manner via Raman spectroscopy.

Chapter 6 - KPFM electronic characterisation of graphene: In this chapter, the electronic properties of graphene were studied via KPFM. In the first section, an improvement over currently existing calibration methods for the tip was developed, achieving lower uncertainty in the determination of the work-function of the tip. The calibration method was successfully tested on exfoliated graphene flakes. In the second section of the chapter, the calibration protocol developed was employed to study the local variations of the charge distribution in encapsulated GFET devices, and its dependence with the edge disorder. Finally, the capabilities of KPFM for visualisation of buried layers in encapsulated heterostructures were exploited. The main points extracted from this research are outlined below:

- **Improvement on currently existing calibration methods for the tip work-function determination in KPFM:** The reliable determination of the work-function of materials using KPFM remains challenging. In this thesis, an improvement on a currently existing method was implemented, achieving values of the work-function of the tip (Φ_{tip}) with lower uncertainty. In order to obtain this, and in contrast with current methods which employ only one reference sample (normally, Au or HOPG), here we produce the calibrated work-function of the tip against 4 samples: thin films of Au, Pt, Ta and Ti. Additionally, another difference with current methodologies is that instead of measuring only one point, we connected electrically the metallic pads formed by the thin films via wire-bonding, and we measured the contact potential difference (V_{CPD}) for different applied voltage bias. This procedure results in a collection of points, following a linear trend, from which Φ_{tip} can be extracted just by simple linear interpolation. Then the final Φ_{tip} is calculated by averaging the results obtained for all the metallic reference samples.

As a consequence of having a collection of points and different surfaces against which to measure Φ_{tip} , the obtained results are statistically robust and the final uncertainty of the measurement is reduced.

Additionally, as demonstrated previously, as the V_{CPD} of a sample is highly dependent on its surface status, then rather than using tabulated values, we independently characterised the work-function of all our reference samples using ultraviolet photon spectroscopy (UPS) prior to the KPFM measurements, thus ensuring even higher reliability in the final calibrated Φ_{tip} .

- **Demonstration of the KPFM capability as a versatile visualisation tool for buried layers in encapsulated heterostructures.** The use of a passivation layer to cover a flake or even its full encapsulation, are commonly applied strategies in order to preserve the intrinsic electronic properties of the 2D materials under study. However, as a drawback, these architectures difficulty the access and characterisation of the buried layers. In order to overcome this, the application of KPFM was explored using encapsulated GFET. The buried graphene layers were visualised using KPFM for different values of the back-gate voltage (V_{BG}), allowing the location of the graphene flake and also the visualisation of the contamination trapped in between the layers. Besides being a fast and non-invasive tool, its high nanoscale resolution allowed to overcome the capability of Raman spectroscopy for example, a technique typically employed for imaging buried layers, but with the lateral resolution limited by optical diffraction. Furthermore, by employing the calibration protocol for the tip explained in the previous paragraph, the back-gate voltage-dependent work-function of the encapsulated graphene was obtained with high accuracy, providing information about the doping levels.

Chapter 7 - Characterisation of the thermophysical properties of 2D materials nanostructures: This chapter was dedicated to the study of the thermal properties of 2D materials at the nanoscale using scanning thermal probe microscopy (SThM) and scanning thermal gate microscopy (STGM). First, the dependence of the thermal conductance of exfoliated γ – InSe with respect to its thickness was characterised using SThM. Following this, the local variations of the Seebeck coefficient present in encapsulated graphene samples with patterned constrictions were characterised using STGM. Finally, the thermoelectric properties of encapsulated InSe heterostructures patterned as Hall bars were studied.

- **Characterisation of the thickness dependent thermal properties of exfoliated γ – InSe:** The thermal conductance dependence with respect to the flake thickness for exfoliated γ – InSe is measured here for the first time using SThM. The measurements

were performed in ambient and vacuum environments, with thicker flakes indicating higher thermal conductance. Although the thermal conductance anisotropy of InSe cannot be completely resolved with SThM, the observed behaviour is attributed to an increased contribution of the in-plane thermal transport component for thicker flakes. Also, we demonstrated that the interfacial thermal resistance between InSe and the substrate as well as between the SThM probe and the InSe dominates the thermal transport and heat dissipation in these nanostructures and during SThM measurements.

- **Investigation of the geometrically defined thermoelectric properties of encapsulated graphene heterostructures:** The effect of nanopatterning on the manipulation of the electron mean free path (EMFP) of graphene, which directly affects its thermoelectric (TE) properties is investigated here for the first time in encapsulated graphene devices with different patterned constrictions. The measured thermovoltage signal has shown opposite polarity around the constrictions, confirming the model of geometrically defined thermoelectricity phenomena established in previous studies with bare graphene on SiO₂/Si substrate devices. The reduction in width, leads to the formation of areas with different Seebeck coefficient, which could be potentially useful for the production of nanoscale single material thermocouples. Also, here, the enhancement and control of the thermovoltage signal using different strategies such as encapsulation, electrostatic doping and manipulation of the thermal gradients, has been demonstrated.

Overall, the fabrication techniques explored in this work have demonstrated to be extremely versatile, allowing us to produce different types of materials and heterostructures. Also, the results presented here demonstrate the potential of Raman spectroscopy and advanced SPM methods to characterise 2D materials and related heterostructures for nanoscale characterisation of different physical properties.

8.2 Future work

After the work performed in this thesis, I believe that there are several routes to expand the lines of research initiated here and that these could be of high interest for the 2D material's community. The main ideas are summarised below:

- An interesting line of work could be the upgrade of the transfer station developed within this PhD project in order to automatize part of the process, allow remote working, and incorporate algorithms to improve flake selection. Twistronics, or the manipulation of the

physical properties of 2D materials by stacking them with specific angles, has emerged as a very interesting line of research, hence a first improvement would be the incorporation of an electronic system for precise rotation [430, 431]. Following this, the next step would be to develop a computer-controlled system for in-plane and out-of-plane displacement and temperature control, which will allow higher precision achieved during the transfer process, together with easier tailoring of recipes to specific materials to improve adhesion/release of flakes. The optical system could be also upgraded with the addition of filters and the edge detection software developed in this thesis. All these upgrades combined together would improve the yield of the system, increase the fabrication speed, enable remote working (e.g. once loaded with the exfoliated flakes, the process of fishing for flakes and pick-up, which could take a couple of hours, could be done remotely), and more importantly, will enable the fabrication of new heterostructures not accessible with the current design.

- Another interesting future route to undertake is the exploration of the automation possibilities offered by artificial intelligence (AI) and machine learning. As discussed in *chapter 4*, the group of Masubuchi et al. [262, 432] has already published papers in this direction, and it is clear that in the incoming years the automation processes will be a great deal in the papers related to fabrication of 2D materials. This, combined with the development of Neural Network (NN) algorithms for the identification of 2D materials in different substrates, will lead to an improved fabrication capability, offering considerably lower heterostructure production time, and higher success rates. The edge detection algorithm produced in this thesis could be implemented as part of the aforementioned NN as one of the steps of the processing.
- Regarding KPFM, the development of systematic tip degradation studies could be of great interest, both for the scientific community and for the probe production companies. Currently, AFM, and KPFM in particular, are regularly employed in quality control when performing nanofabrication, and an important part of the cost is the preventive replacement of probes to avoid downtime of the AFM system [433, 434]. By performing degradation studies, it will be possible to estimate more precisely when tip failure is about to happen, and thus running costs will be lowered. The comparison could be done combining scanning electron microscopy (SEM), for the morphology characterisation of the probes, and KPFM, for the electrical performance. The idea consists in comparing the response of the probes, via their Φ_{tip} , when subjected to measurements in different conditions of pressure, temperature and humidity, in order to ensure the robustness of

the results obtained and quantify the level of damage suffered by the probes (i.e. measure their lifespan). To study the variability between similar probes, the same measurements can be performed for batches of probes all corresponding to the same type.

- Another route that could be of interest is the further exploitation of KPFM as a powerful characterisation tool for encapsulated graphene, or other metallic/semiconducting 2D materials. Its high resolution, and capability of imaging buried layers and providing quantitative values of the work-function, could be extremely useful in order to further understand the effects of interlayer contamination, and also the effects of commonly applied cleaning techniques for heterostructures, such as AFM brooming or annealing. For example, performing calibrated KPFM before and after the brooming process could provide information of the level of cleanliness achieved and the amount of doping introduced by the contamination.
- Regarding thermal measurements at the nanoscale, the accurate characterisation of the dependence between the thermal properties and the thickness of the materials is one of the current biggest challenges for 2D materials. A direct follow up from the experiments with exfoliated InSe presented in *chapter 7*, would be the combination of SThM with beam exit cross-sectional polishing (BEXP). BEXP is a technique that uses an Argon ion beam to produce cuts at very shallow angles with high precision [435, 436]. It could be applied, for example, to exfoliated thick flakes of different materials to create a controlled gradient of thicknesses, from monolayer to hundreds of nanometers, easily accessible for SPM studies. This way, the variations of the thermal resistance of the material as its thickness varies from the substrate to the surface could be studied in only one measurement.

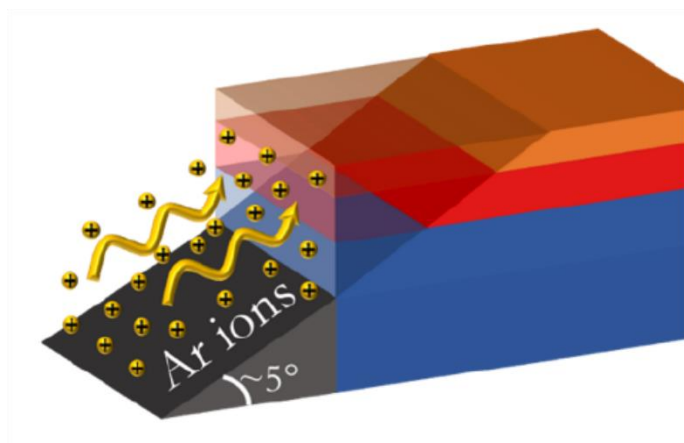


Figure 8.1. Schematic of beam-exist cross-section polishing (BEXP), in which the Ar ions are attacking the surface at an angle of 5° , etching the top material and creating a gradient surface suitable for SPM studies. Image reproduce with permission from [436]

- Another area of interest related with thermal characterization is the study of twisted heterostructures. The most famous example of novel properties arising from stacked twisted structures is the superconductivity of twisted bilayer graphene [437]. Additionally, very recent theoretical papers have predicted a strong dependence of the thermal conductivity of materials in heterostructures with the misfit angle [438]. A systematic study of the thermal properties of different materials stacked at different angles, could be performed using SThM or STGM. This type of experiment could bring to light unexpected thermal properties, e.g. increased thermoelectrical response, or unusual high/low thermal conductivity.
- Finally, as per the thermoelectric applications based on 2D materials heterostructures, there is still plenty of room for novel research in this area as it is widely unexplored. As explained in *chapter 7*, InSe is an excellent candidate for thermoelectric applications. This material presents high values of electrical conductivity up to $\sim 10^3 \text{ cm}^2 \text{ V}^{-1} \text{ s}^{-1}$ for few layer InSe ($\sim 6L$) at room temperature [119, 120], and low values of the thermal conductivity both in-plane and out-of-plane with $\kappa_{\parallel} = 8.5 \text{ Wm}^{-1} \text{ K}^{-1}$ and $\kappa_{\perp} = 0.76 \text{ Wm}^{-1} \text{ K}^{-1}$, respectively [413]. In principle, these are already good prospects in order to achieve high values of the ZT. In order to explore this, an experiment was designed here to investigate the gate-tunable and temperature dependent thermoelectric transport in $\gamma - \text{InSe}$, and to provide quantitative values of the Seebeck coefficient, S, and ZT.

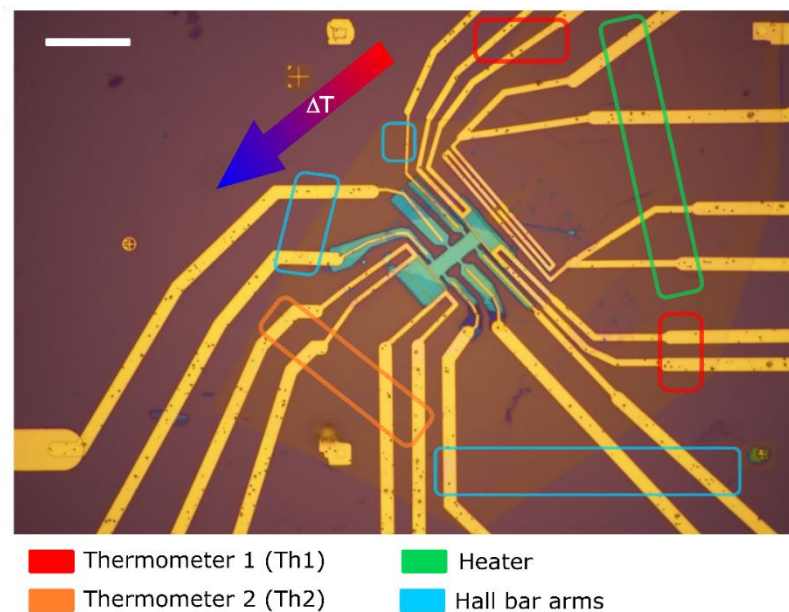


Figure 8.2. Encapsulated InSe Hall bar devices. The contacts connecting the heater are highlighted by a green square. Two micro-thermometers were patterned onto the InSe structure and their contacts are surrounded

by red and orange, for the one closest to the heater and for the furthest one, respectively. Finally, the contacts connecting the Hall bar are surrounding the InSe are shown in light blue.

For this, encapsulated InSe heterostructures were produced with a $t_{InSe} \sim 4.8 \text{ nm}$, corresponding to 6L, which based on previous studies performed by Bandurin et al. [119], presented the highest electrical conductivity. Then, the heterostructures were patterned into a Hall bar shape, and contacted to Au pads via graphene. The full fabrication process of these complex devices was explained in detail in *chapter 4, section 4.8*. To quantitatively measure S , a heater and two micro-thermometers were integrated into the device set-up as shown in *figure 8.2*. The heater was fabricated as large as possible trying to cover at least the full width of the Hall bar in order to produce a uniform heat distribution along the device.

The idea of the experiment is then to quantitatively measure the Seebeck coefficient using two methods:

- First, by applying a temperature gradient along the InSe channel (following the arrow direction) by passing an electric current through the heater. This, would produce a thermovoltage across the device that can be characterised by measuring the voltage drop, ΔV_{th} , across the terminals of the Hall bar. Using the micro-thermometers to measure the total temperature drop, ΔT , the global Seebeck coefficient could be obtained by calculating $S_{global} = \Delta V_{th} / \Delta T$.
- Second, by using STGM and the tip as the active heating element. This would allow to produce local variations of the temperature. By measuring the ΔV_{th} across the Hall bar terminals, the local variation of the Seebeck coefficient, S_{local} , could be characterised with nanoscale resolution.

Comparing these two results would provide information of the global and local variations of the Seebeck coefficient on the devices of under study. Additional measurements of the electrical transport and the nanoscale thermal properties via SThM could be performed in order to obtain quantitative values of the ZT. However, due to the complexity of the heterostructure, having layers of hBN, InSe and graphene in contact, modelling would be required to deconvolute the contribution of each material to the total measured signal.

It is important to highlight that this experiment was conceived by the end of this PhD funding, and thus it was not possible to fit it within the assigned time-frame. However, due to the potential relevance of these results, this experiment will be continued after the conclusion of the studies presented here.

Edge detection algorithms for 2D materials identification

Acknowledgements: The first version of this program was developed by Catarina Areias in Python 2.0 during the summer of 2019, in which she did a placement at NPL under my supervision. Later on, I continued with the project, uploading the code from Python 2.0 to Python 3.0, further developing the GUI and investigating new tools for the visualisation of 2D materials.

A.1. Edge detection GUI for 2D materials

The code for the implementation of edge detection algorithms for 2D materials has been developed in Python 3.0, and programmed with VisualStudio.

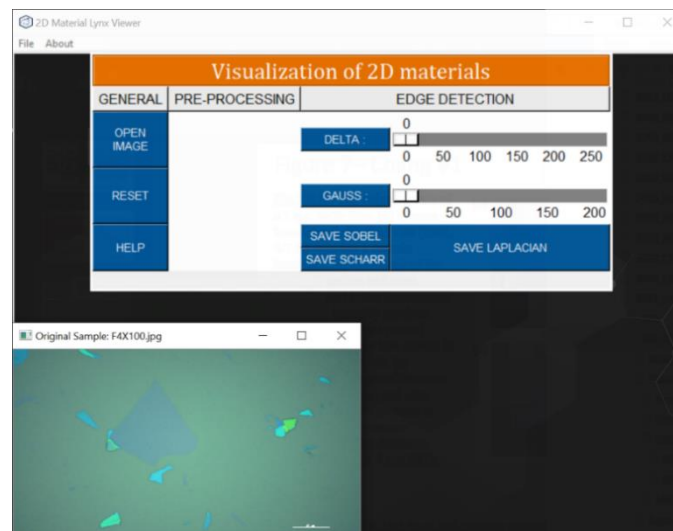


Figure A.1. Graphical user interface (GUI) developed for the application of edge detection algorithms to 2D materials. Using the controls in the left section, an image can be opened from folder. Images will open on the bottom-left corner. On the right side of the menu, options to modify the values of the filters are available.

When the code is executed, it produces the GUI presented in *figure a.1*. A file explorer window can be accessed from the GUI, using the 'OPEN IMAGE' button in order to find and load the image of interest (e.g. hBN exfoliated on 300 nm SiO₂ is shown in the left bottom corner of the figure below). Once located and loaded, the image appears in a separate window along with other three

images showing the effects of the different edge detection algorithms. The sliders on the right allow varying the parameters of the edge detection algorithms, as discussed in *chapter 4, section 4.5.1*. The remaining buttons allow saving each of the processed images separately, resetting the configuration, or accessing the help.

In the centre of the GUI, a column called 'PRE-PROCESSING' remains empty. Future developments of the code will include the implementation of tools fitting that category such as de-noising filters and background subtraction algorithms, essentially with the intention to reduce the noise and improve the quality of the images.

A.2. Python 3.0 code: LynxViewer v3.0

```
# Catarina Areias & Eli Castanon (2019-2021)
# Description: GUI for image processing of 2D materials.
# - Show a window
# - Import logos from NPL
# - Load images
# Colors: https://davidmathlogic.com/colorblind/#%23E66100-%235D3A9B
# Conversion to png with PIL: https://www.youtube.com/watch?v=6Qs3w0belWwc
# C:\Users\castanon\Documents\Python\Master in Python\21-
Tkinter\NPL - Image processing

#=====
# IMPORTING LIBRARIES
#=====
import cv2
from PIL import ImageTk, Image
import numpy as np
import tkinter as tk
from tkinter.font import Font
from tkinter import filedialog # To get the dialog box to open when required
from tkinter import colorchooser
from tkinter import messagebox as MessageBox
from tkinter.filedialog import askopenfilename
import os, sys, subprocess
import ntpath
import matplotlib.pyplot as plt
from matplotlib.backends.backend_tkagg import FigureCanvasTk, NavigationToolbar2Tk # Importing canvas and tools to manipulate the plot in canvas
# Implement the default Matplotlib key bindings.
from matplotlib.backend_bases import key_press_handler
from matplotlib.figure import Figure

#=====
```

```

#                                PROGRAM STYLES
#=====
#imgtk = 0

## Defining colours for the GUI display:
NPL2 = '#00689f'
NPL1 = '#015697'
orange_enh = '#e67000'
black_back = '#ececec'

## Defining fonts:
LARGE_FONT = ("Helvetica", 12)
NORM_FONT = ("Helvetica", 10)
SMALL_FONT = ("Helvetica", 8)
TITLE_FONT = ('Cambria', 20)

## Area of computer screen
A_screen = 1910 * 1030

## Path folder
path = ('C:/Users/castanon/Documents/PhD documents-NPL-
LU/PhD measurements/PhD - Experimental/2019_Image_Processing_Python/GUI_2DMats
')

#=====
#                                POP-UP MESSAGE
#=====

def popupmsg(msg):
    popup = tk.Toplevel()
    popup.wm_title("Credits & Acknowledgements")
    popup.configure(bg='gray16')
    popup.wm_attributes('-alpha', 0.97)

    label_thanks = tk.Label(popup, text=msg, font=LARGE_FONT, bg='gray16', foreground=
'khaki1')
    label_thanks.grid(column = 0, row = 0, columnspan = 3, sticky='n', padx =
3, pady = 3)

    label_separation1 = tk.Label(popup, text= '', font=LARGE_FONT)
    label_separation1.grid(column = 0, row = 1, columnspan = 3, sticky='n')

    npl = ImageTk.PhotoImage(Image.open(f"{path}/logos/NPL2.png").resize((200,
80),Image.ANTIALIAS))
    label_NPL = tk.Label(popup, image = npl)
    label_NPL.grid(column = 0, row = 2, sticky='sw')

```

```

    LU = ImageTk.PhotoImage(Image.open(f"{path}/logos/LU.jpg").resize((200, 80),Image.ANTIALIAS))
    label_NPL = tk.Label(popup, image = LU)
    label_NPL.grid(column = 1, row = 2, sticky='s')

    Sepnet = ImageTk.PhotoImage(Image.open(f"{path}/logos/SEPNET.jpg").resize(
(200, 80),Image.ANTIALIAS))
    label_NPL = tk.Label(popup, image = Sepnet)
    label_NPL.grid(column = 2, row = 2, sticky='se')

    label_separation1 = tk.Label(popup, text= '', font=LARGE_FONT)
    label_separation1.grid(column = 0, row = 3, columnspan = 3, sticky='n')

    popup.mainloop()

#=====
#           EDGE DETECTION FUNCTIONS
#=====
## defining the Laplacian edge detection function:
def Laplacian(path, name, k): ## function depends on image file path, name of
image, and k-vale (size of gaussian blur matrix)
    window = 'Laplacian method for {}'.format(name) ## creating a window where
the image will be displayed
    cv2.namedWindow(window, cv2.WINDOW_NORMAL) ## making the window resizable
    cv2.moveWindow(window,810,0) ## moving the window on the screen 810 pixels
in the x direction and 0 pixels in the y direction

    src = cv2.imread('{}'.format(path)) ## reading image file from folder
    src_blur = cv2.GaussianBlur(src,(k,k),0) ## applying a Gaussian blur of ma
trix size k*k to the image, 0=standard deviation of kernel
    src_gray = cv2.cvtColor(src_blur, cv2.COLOR_BGR2GRAY) ## making image gray
scale
    laplacian = cv2.Laplacian(src_gray,cv2.CV_64F) ## applying the Laplacian e
dge detection algorithm: cv2.CV_64F is the datatype of image outputted, has to
be 64F in order to be visible

    ## if the original image size is bigger than the screen size then the wind
ow will be resized to fit screen:
    w = int(src.shape[1] * 50 / 100) ## reading the width of the image (src.sh
ape[1]) and scaling it down by 25% to be used as the new image size if image f
ile is too big to fit on screen
    h = int(src.shape[0] * 50 / 100) ## reading the height of the image (src.s
hape[0]) and scaling it down by 25% to be used as the new image size if image
file is too big to fit on screen
    A = src.shape[1] * src.shape[0] ## image area
    if (A >= A_screen): ## if the area of the image is greater than or equal t
han the computer screen then resize image window --
> you can adjust window size in line 21

```

```

        cv2.resizeWindow(window, w, h)
    else: ## if not then do nothing
        pass

    cv2.imshow(window, laplacian) ## showing Laplacian on the window we create
d

def Sobel(path, name, delta):
    ddepth = cv2.CV_16S ## have to define image datatype, again have to use th
is type for edge visibility

    ## creating window:
    window = 'Sobel method for {}'.format(name)
    cv2.namedWindow(window, cv2.WINDOW_NORMAL)
    cv2.moveWindow(window, 810, 0)

    src = cv2.imread('{}'.format(path)) ## reading image file
    src_gray = cv2.cvtColor(src, cv2.COLOR_BGR2GRAY) ## converting to grayscale
e

    src_blur = cv2.GaussianBlur(src_gray, (5,5), 0) ## applying Gaussian Blur
with 5*5 matrix(kernel), 0=standard deviation of kernel

    grad_x_sobel = cv2.Sobel(src_blur, ddepth, 1, 0, 3, 1, delta) ## applying
Sobel in x direction where you're taking the first order derivative in x and z
ero order derivative in y (1,0), with a kernel size of 3, scale factor of 1,
delta is user-defined and it increases intensity value of the edges
    abs_grad_x_sobel = cv2.convertScaleAbs(grad_x_sobel) ## taking the absolut
e value of the Sobel in x direction so that an image can be outputted (program
doesn't like negative derivatives)
    grad_y_sobel = cv2.Sobel(src_blur, ddepth, 0, 1, 3, 1, delta) ## same thin
g as Sobel in x but now in y (0, 1)
    abs_grad_y_sobel = cv2.convertScaleAbs(grad_y_sobel) ## have to take absol
ute value of the Sobel in y
    grad_sobel = cv2.addWeighted(abs_grad_x_sobel, 0.5, abs_grad_y_sobel, 0.5,
0) ## creating an image combining Sobel in x and Sobel in y, both weighing 50
% (0.5), 0=scalar added to result

    ## resizing image if too big:
    w = int(src.shape[1] * 25 / 100) ## image width agjustment (see def Laplac
ian)
    h = int(src.shape[0] * 25 / 100) ## image height adjustment
    A = src.shape[1] * src.shape[0] ## image area
    ## same if-else statement as line 38:
    if (A >= A_screen):
        cv2.resizeWindow(window, w, h)
    else:
        pass

```



```

cv2.imshow(window, grad_sobel) ## show total Sobel

def Scharr(path, name, delta):
    ddepth = cv2.CV_16S ## setting datatype

    ## creating window:
    window = 'Scharr method for {}'.format(name)
    cv2.namedWindow(window, cv2.WINDOW_NORMAL)
    cv2.moveWindow(window, 810, 300)

    src = cv2.imread('{}'.format(path)) ## reading image
    src_gray = cv2.cvtColor(src, cv2.COLOR_BGR2GRAY) ## converting to grayscale

    src_blur = cv2.GaussianBlur(src_gray, (5,5), 0) ## applying Gaussian blur

    ## same procedure as Sobel (see line 57):
    grad_x_scharr = cv2.Scharr(src_blur, ddepth, 1, 0, 3, 1, delta)
    abs_grad_x_scharr = cv2.convertScaleAbs(grad_x_scharr)
    grad_y_scharr = cv2.Scharr(src_blur, ddepth, 0, 1, 3, 1, delta)
    abs_grad_y_scharr = cv2.convertScaleAbs(grad_y_scharr)
    grad_scharr = cv2.addWeighted(abs_grad_x_scharr, 0.5, abs_grad_y_scharr, 0
.5, 0)

    w = int(src.shape[1] * 25 / 100) ## width
    h = int(src.shape[0] * 25 / 100) ## height
    A = src.shape[1] * src.shape[0]
    ## same if-else statement as line 38
    if (A >= A_screen):
        cv2.resizeWindow(window, w, h)
    else:
        pass

    cv2.imshow(window, grad_scharr)

#=====
#           CLASS THAT CREATES THE GUI
#=====

class App(tk.Frame):

    def __init__(self, master, directory): ## creates GUI main window
        tk.Frame.__init__(self, master)

        ## Creating a menu-bar application
        container = tk.Frame(master)
        container.config(bg = black_back)
        container.grid(sticky="nw")

```

```

menubar = tk.Menu(container)
menubar.config(bg = black_back, fg = 'white')

filemenu = tk.Menu(menubar, tearoff=0)
filemenu.add_command(label="Open file", command = self.open_image, font = NORM_FONT)
filemenu.add_command(label="Save settings", command = lambda: popupmsg("Not supported just yet!"), font = NORM_FONT)
filemenu.add_separator()
filemenu.add_command(label="Exit", command=quit, font = NORM_FONT)

menubar.add_cascade(label="File", menu=filemenu, background = black_back, font = NORM_FONT)
menubar.add_command(label = 'About', font = NORM_FONT, command = lambda: popupmsg("Open source by: E_Castanon (2020)\nEspecial thanks to Catarina Aréias, Tom Vincent and Andrew Tolmie\n2020"))

App.config(master, menu=menubar)

## Putting white frame in master window w/ white background and has an empty filling of 5 pixels in the x direction and 2 in the y direction
frame = tk.Frame(master, bg = 'white')
frame.grid(column=0, columnspan=4, row=0, sticky='nsew')

## Background image main screen
bg_img1 = Image.open(f"{path}/Background/Bc_prov6.png")
w, h = bg_img1.size #Obtaining width and height of the image
print('Width Frame:', w, 'Height Frame:', h)

bg_image = ImageTk.PhotoImage(bg_img1)
bg_label = tk.Label(frame, image = bg_image)
bg_label.image = bg_image # Safekeeping
bg_label.grid()

# Stablish the geometry of the master screen and placing it on the top-left corner
master.geometry('%dx%d+0+0' % (w,h))

# Store directory path for logos
self.directory = directory

## Create input controls
self.makeInputs(frame)
self.Pintaycolorea(frame)

## Frame for widget positioning
def makeInputs(self, frame):

```

```

    InputFrame = tk.Frame(frame, bg='white', width = 950, height = 600, bd
= 3) ## Creating a frame for inputs
    InputFrame.grid(column = 0, row = 0, sticky='n') ## Placing frame

    ## Labels:
        ## Title label for the GUI
        self.Title_label = tk.Label(InputFrame, text='Visualization of 2D mate
rials', bg = orange_enh, bd=2, activebackground=NPL1,
relief = 'groove', activeforeground='white', fg='white', font = TITLE_
FONT)
        self.Title_label.grid(column = 0, row = 0, colspan = 4, sticky='nse
w')
        #self.Title_label.grid_propagate(flag = True)

        ## General sub-label for the GUI
        self.Title_label = tk.Label(InputFrame, text=' GENERAL ', bg = black_b
ack, bd=2, activebackground=NPL1, pady = 4,
relief = 'raised', activeforeground='white', fg='black', font = LARGE_
FONT)
        self.Title_label.grid(column = 0, row = 1, sticky='nsew')

        ## Pre-processing sub-label for the GUI
        self.Title_label = tk.Label(InputFrame, text=' PRE-
PROCESSING ', bg = black_back, bd=2, activebackground=NPL1, pady = 4,
relief = 'raised', activeforeground='white', fg='black', font = LARGE_
FONT)
        self.Title_label.grid(column = 1, row = 1, sticky='nsew')

        ## Edge detection sub-label for the GUI
        self.Title_label = tk.Label(InputFrame, text=' EDGE DETECTION ', bg =
black_back, bd=2, activebackground=NPL1, pady = 4,
relief = 'raised', activeforeground='white', fg='black', font = LARGE_
FONT)
        self.Title_label.grid(column = 2, row = 1, colspan = 2, sticky='nse
w')

    ## Sliders:
        ## Slider for delta variable, part of Scharr and Sobel methods, sp
ans from 0 to 255 with increments of 1, triggers function that calculates the
Sobel and Scharr edges
        self.ent_delta = tk.Scale(InputFrame, orient=tk.HORIZONTAL, from_=0, t
o=255, resolution=1, bg='white', length=255,
repeatdelay=0, tickinterval=50, troughcolor='grey', highlightbackground
d='white',
activebackground=NPL2, command=self.calcSobelScharr, font=LARGE_FONT)
        self.ent_delta.grid(column = 3, row = 2, sticky='nsew')

```

```

        ## Slider for gaussian variable, part of Laplacian method, spans f
rom 0 to 200 with increments of 2 (only even numbers), triggers fuction that
calculates Laplacian edges
        self.ent_gauss = tk.Scale(InputFrame, orient=tk.HORIZONTAL, from_=0, t
o=200, resolution=2, repeatdelay=0, tickinterval=50, bg='white',
        length=255, troughcolor='grey', highlightbackground='white', activebac
kground=NPL2, command=self.calcLap,
        font=LARGE_FONT)
        self.ent_gauss.grid(column = 3, row = 3, sticky='nsew')

        ## Buttons:
        ## Button that when pressed triggers a popup explaining delta
        self.but_delta = tk.Button(InputFrame, text = 'DELTA :', command=self.d
elta_def, bg=NPL1, bd=2, activebackground=NPL2,
        activeforeground='white', fg='white', font=NORM_FONT)
        self.but_delta.grid(column = 2, row = 2, sticky='ew')
        ## Button that when pressed triggers a popup explaining gaussian v
ariable
        self.but_gauss = tk.Button(InputFrame, text = 'GAUSS :', command=self.g
auss_def, bg=NPL1, bd=2, activebackground=NPL2,
        activeforeground='white', fg='white', font = NORM_FONT)
        self.but_gauss.grid(column = 2, row = 3, sticky='ew')
        ## Button to save Sobel image
        self.butSaveSobel = tk.Button(InputFrame, text = 'SAVE SOBEL', command
= self.saveSobel, bg=NPL1, bd=2, activebackground=NPL1,
        activeforeground='white', fg='white', font = NORM_FONT)
        self.butSaveSobel.grid(column = 2, row = 4, sticky='nsew')
        ## Button to save Scharr image
        self.butSaveScharr = tk.Button(InputFrame, text = 'SAVE SCHARR', comman
d = self.saveScharr, bg=NPL1, bd=2,
        activebackground=NPL1, activeforeground='white', fg='white', font= NOR
M_FONT)
        self.butSaveScharr.grid(column = 2, row = 5, sticky='nsew')
        ## Button to save Laplacian image
        self.butSaveLap = tk.Button(InputFrame, text = 'SAVE LAPLACIAN', comman
d = self.saveLap, bg=NPL1, bd=2,
        activebackground=NPL1, activeforeground='white', fg='white', font = NO
RM_FONT)
        self.butSaveLap.grid(column = 3, row = 4, rowspan=2, sticky='nsew')
        ## Button to open image
        self.butClear = tk.Button(InputFrame, text = 'OPEN\nIMAGE', command = s
elf.open_image, bg=NPL1, bd=2, activebackground=NPL1,
        activeforeground='white', fg='white', font = NORM_FONT)
        self.butClear.grid(column = 0, row = 2, sticky='nsew')
        ## Button to reset values
        self.butClear = tk.Button(InputFrame, text = 'RESET', command = self.re
set, bg=NPL1, bd=2, activebackground=NPL1,
        activeforeground='white', fg='white', font = NORM_FONT)

```

```

self.butClear.grid(column = 0, row = 3, sticky='nsew')
    ## Button to open Help regarding the functions
self.PDFButton = tk.Button(InputFrame, text="HELP", command=self.open_
file, bg=NPL1, bd=2, activebackground=NPL1,
activeforeground='white', fg='white', font = NORM_FONT)
self.PDFButton.grid(column = 0, row = 4, rowspan = 2, sticky='nsew')

self.label_Sep2 = tk.Label(InputFrame, text=' ')
self.label_Sep2.grid(column = 0, row = 6, columnspan = 4, sticky='nsew
')

def Pintaycolorea(self, frame):
    PintaFrame = tk.Frame(frame, bg='white', width = 300, height = 300, bd
= 3) ## Creating a frame for inputs
    PintaFrame.grid(column = 0, row = 0, sticky='sw') ## Placing frame

    self.filepath = askopenfilename(parent=self.master, title='Choose Samp
le', filetypes=[('Image files', '*.png ' '*.gif ' '*.jpg')]) ## popup of file
directory

    head, tail = ntpath.split(self.filepath) ## splitting image file path
so that I can access name of file
    self.name_tail = tail
    self.name_head = ntpath.basename(head)
    self.sample = self.name_tail or self.name_head # image name

    # Put it in the display window
    #window = 'Original Sample: {}'.format(self.sample) ## creating window
to display image
    src = cv2.imread('{}'.format(self.filepath))

    b, g, r = cv2.split(src)
    img2 = cv2.merge((r,g,b))
    im33 = Image.fromarray(img2)
    imgtk = ImageTk.PhotoImage(image = im33)
    self.Canvacillo = tk.Canvas(PintaFrame)
    self.Canvacillo.create_image(0, 0, anchor = 'nw', image = imgtk)
    self.Canvacillo.grid(sticky = 'nsew')

#=====
#           Pop - up for delta function
#=====
def delta_def(self): ## creating popup for delta button
    self.popup_delta = tk.Toplevel(bg='white') ## popup window
    self.popup_delta.title('Delta')

```

```

        self.label_delta1 = tk.Label(self.popup_delta, text='- Intensity value
added to each pixel during convolution', bg='white', font=Font(family="Helvel
tica", size=10))
        self.label_delta1.grid(column=1, row=1, sticky='nsw', padx=16, pady=10
)
        self.label_delta2 = tk.Label(self.popup_delta, text='- Makes edges vis
ible (bigger delta means brighter edges)', bg='white', font=Font(family="Helve
ltica", size=10))
        self.label_delta2.grid(column=1, row=2, sticky='nsw', padx=16)
        self.popbut_delta = tk.Button(self.popup_delta, text='OKAY', command =
self.popup_delta.destroy, bg=NPL2, activebackground=NPL1, fg='white', bd=2, f
ont=Font(family="Helvetica", size=10)) ## pressing OKAY button will collapse
the window
        self.popbut_delta.grid(column=1, row=4, pady=10)

def gauss_def(self): ## see delta_def (line 178)
    self.popup_gauss = tk.Toplevel(bg='white')
    self.popup_gauss.title('Gaussian')
    self.label_gauss1 = tk.Label(self.popup_gauss, text='- Changes size of
Gaussian-
Blur matrix applied to image', bg='white', font=Font(family="Helvetica", size
=10))
    self.label_gauss1.grid(column=1, row=1, sticky='nsw', padx=16, pady=10
)
    self.label_gauss2 = tk.Label(self.popup_gauss, text='- Adjusts noise (
bigger Gaussian means bigger noise filtered out)', bg='white', font=Font(famil
y="Helvetica", size=10))
    self.label_gauss2.grid(column=1, row=2, sticky='nsw', padx=16)
    self.popbut_gauss = tk.Button(self.popup_gauss, text='OKAY', command =
self.popup_gauss.destroy, bg=NPL2, activebackground=NPL1, fg='white', bd=2, f
ont=Font(family="Helvetica", size=10))
    self.popbut_gauss.grid(column=1, row=4, pady=10)

#=====
#                               Open files
#=====
def open_file(self): ## open poster file from directory for 'Open Poster'
button
    if sys.platform == "win32":
        os.startfile('Poster')
    else:
        opener = "open" if sys.platform == "darwin" else "xdg-open"
        subprocess.call([opener, 'Poster.pdf'])

def open_image(self): ## open file image chosen from directory, following
'open sample' button

```

```

        self.filepath = askopenfilename(parent=self.master, title='Choose Sample', filetypes=[('Image files', '*.png ' '*.gif ' '*.jpg')]) ## popup of file directory

        head, tail = ntpath.split(self.filepath) ## splitting image file path so that I can access name of file
        self.name_tail = tail
        self.name_head = ntpath.basename(head)
        self.sample = self.name_tail or self.name_head # image name

        #self.img1 = cv2.imread(image_name)
        #Rearrang the color channel
        #b,g,r = cv2.split(self.img1)
        #self.img2 = cv2.merge((r,g,b))
        # Convert the Image object into a TkPhoto object
        #self.im = Image.fromarray(self.img2)
        #self.imgtk = ImageTk.PhotoImage(self, image=self.im)
        #imgtk_display = Label(InputFrame, image=imgtk)
        #imgtk_display.grid (column = 0, row = 6, columnspan = 2, sticky='nsew')

        # Put it in the display window
        window = 'Original Sample: {}'.format(self.sample) ## creating window to display image
        src = cv2.imread('{}'.format(self.filepath))

        cv2.namedWindow(window, cv2.WINDOW_NORMAL)
        cv2.moveWindow(window,0,550)

        cv2.imshow(window, src) ## show image

        #=====
        #                Saving files
        #=====
        def saveLap(self):
            ## have to refind edges in order to create save function
            src = cv2.imread('{}'.format(self.filepath))
            src_blur = cv2.GaussianBlur(src,(self.k, self.k),0)
            src_gray = cv2.cvtColor(src_blur, cv2.COLOR_BGR2GRAY)
            laplacian = cv2.Laplacian(src_gray,cv2.CV_8U)

            (thresh, binary) = cv2.threshold(laplacian, 128, 255, cv2.THRESH_BINARY | cv2.THRESH_OTSU) ## using cv2.imwrite with the Laplacian method was producing a black screen so have to binarize Laplacian and use matplotlib package to save image

            ## using matplotlib package to plot and save Laplacian:
            plt.figure('Laplacian', figsize=(10,7))

```

```

plt.xticks([],plt.yticks([])
plt.tight_layout(pad=0, w_pad=0, h_pad=0)
plt.imsave('{} /processed data/{} - Laplacian at G={}.png'.format(direc
tory, self.sample, self.k), binary, cmap='gray') ## save function

    ##popup: creating a popup when Laplacian save button is pressed, shows
save file directory, gets value of variable used in corresponding function
    self.popup_saved = tk.Toplevel(bg='white')
    self.popup_saved.title('Save file success')
    self.label_saved1 = tk.Label(self.popup_saved, text='{} Laplacian at G
={}.png'.format(self.sample, self.k), bg='white', font=Font(family="Helveltica
", size=10))
    self.label_saved1.grid(column=1, row=1, sticky='nsew')
    self.label_saved2 = tk.Label(self.popup_saved, text='was saved to:', b
g='white', font=Font(family="Helveltica", size=10))
    self.label_saved2.grid(column=1, row=2, sticky='nsew')
    self.label_saved3 = tk.Label(self.popup_saved, text='{} \processed data
'.format(directory), bg='white', font=Font(family="Helveltica", size=10))
    self.label_saved3.grid(column=1, row=3, sticky='nsew')
    self.popbut_saved = tk.Button(self.popup_saved, text='OKAY', command =
self.popup_saved.destroy, bg=NPL2, activebackground=NPL1, fg='white', bd=2, f
ont=Font(family="Helveltica", size=10))
    self.popbut_saved.grid(column=1, row=4)

def saveSobel(self): ## same idea as saveLap (see line 221):
ddepth = cv2.CV_16S ## need to change datatype so that image is saved
## recalculating edges:
src = cv2.imread('{}'.format(self.filepath))
src_gray = cv2.cvtColor(src, cv2.COLOR_BGR2GRAY)
img = cv2.GaussianBlur(src_gray, (5,5), 0)
grad_x_sobel = cv2.Sobel(img, ddepth, 1, 0, 3, 1, self.delta)
abs_grad_x_sobel = cv2.convertScaleAbs(grad_x_sobel)
grad_y_sobel = cv2.Sobel(img, ddepth, 0, 1, 3, 1, self.delta)
abs_grad_y_sobel = cv2.convertScaleAbs(grad_y_sobel)
grad_sobel = cv2.addWeighted(abs_grad_x_sobel, 0.5, abs_grad_y_sobel,
0.5, 0)

    cv2.imwrite('{} /processed data/{} - Sobel at D={}.png'.format(director
y, self.sample, int(self.delta)), grad_sobel) ## save function

    ##pop-up: popup triggered by pressing Sobel save button, see line 237
    self.popup_saved = tk.Toplevel(bg='white')
    self.popup_saved.title('Save file success')
    self.label_saved1 = tk.Label(self.popup_saved, text='{} Sobel at D={}.
png'.format(self.sample, int(self.delta)), bg='white', font=Font(family="Helve
ltica", size=10))
    self.label_saved1.grid(column=1, row=1, sticky='nsew')

```



```

        self.label_saved2 = tk.Label(self.popup_saved, text='was saved to:', bg='white', font=Font(family="Helvetica", size=10))
        self.label_saved2.grid(column=1, row=2, sticky='nsew')
        self.label_saved3 = tk.Label(self.popup_saved, text='{}\processed data'.format(directory), bg='white', font=Font(family="Helvetica", size=10))
        self.label_saved3.grid(column=1, row=3, sticky='nsew')
        self.popbut_saved = tk.Button(self.popup_saved, text='OKAY', command = self.popup_saved.destroy, bg=NPL2, activebackground=NPL1, fg='white', bd=2, font=Font(family="Helvetica", size=10))
        self.popbut_saved.grid(column=1, row=4)

    def saveScharr(self): ## see saveSobel (line 248)
        ddepth = cv2.CV_16S
        src = cv2.imread('{}'.format(self.filepath))
        src_gray = cv2.cvtColor(src, cv2.COLOR_BGR2GRAY)
        img = cv2.GaussianBlur(src_gray, (5,5), 0)

        grad_x_scharr = cv2.Scharr(img, ddepth, 1, 0, 3, 1, self.delta)
        abs_grad_x_scharr = cv2.convertScaleAbs(grad_x_scharr)
        grad_y_scharr = cv2.Sobel(img, ddepth, 0, 1, 3, 1, self.delta)
        abs_grad_y_scharr = cv2.convertScaleAbs(grad_y_scharr)
        grad_scharr = cv2.addWeighted(abs_grad_x_scharr, 0.5, abs_grad_y_scharr, 0.5, 0)
        cv2.imwrite('{}\processed data/{} - Scharr at D={}.png'.format(directory, self.sample, int(self.delta)), grad_scharr)

        ##pop-up:
        self.popup_saved = tk.Toplevel(bg='white')
        self.popup_saved.title('Save file success')
        self.label_saved1 = tk.Label(self.popup_saved, text='{} Scharr at D={}.png'.format(self.sample, int(self.delta)), bg='white', font=Font(family="Helvetica", size=10))
        self.label_saved1.grid(column=1, row=1, sticky='nsew')
        self.label_saved2 = tk.Label(self.popup_saved, text='was saved to:', bg='white', font=Font(family="Helvetica", size=10))
        self.label_saved2.grid(column=1, row=2, sticky='nsew')
        self.label_saved3 = tk.Label(self.popup_saved, text='{}\processed data'.format(directory), bg='white', font=Font(family="Helvetica", size=10))
        self.label_saved3.grid(column=1, row=3, sticky='nsew')
        self.popbut_saved = tk.Button(self.popup_saved, text='OKAY', command = self.popup_saved.destroy, bg=NPL2, activebackground=NPL1, fg='white', bd=2, font=Font(family="Helvetica", size=10))
        self.popbut_saved.grid(column=1, row=4)

    def reset(self): ## resets GUI by closing open windows and resetting variable sliders
        cv2.destroyAllWindows()
        self.ent_delta.set(0)

```

```

self.ent_gauss.set(0)
cv2.destroyAllWindows()

def calcSobelScharr(self, event): ## function triggered by delta slider, calls in functions defined in line 45(Sobel) and 75 (Scharr)
    self.delta = float(self.ent_delta.get()) ## gets value from delta slider
    self.Sobel = Sobel(self.filepath, self.sample, self.delta) ## calculating Sobel by fetching image sample filepath, image sample name, and delta defined by user
    self.Scharr = Scharr(self.filepath, self.sample, self.delta) ## same as above but for Scharr

def calcLap(self, event): ## function triggered by gauss slider, calls in Laplacian function defined in line 24
    self.k = int(self.ent_gauss.get()) + 1 ## gaussian variable defines size of Gaussian blur matrix, which needs to be odd. Because of a bug in Tkinter package, I can only set the slider to show even values and not odd, therefore, when calling in value from slider, need to add 1 to make k-size odd
    self.Lap = Laplacian(self.filepath, self.sample, self.k) ## calculating Laplacian (see calcSobelScharr above)

# Calling the GUI
def main():

    # Getting the directory to the code where logos are stored
    script_path = __file__
    script_dir = os.path.dirname(script_path)
    print(f'directory: {script_dir}')

    # Initialise tkinter window
    root = tk.Tk()
    root.resizable(1,1) # In (0,0) the window will not change size. Change to (1,1) to allow resizing
    root.wm_attributes('-alpha', 0.99)
    root.title('2D Material Lynx Viewer')
    root.iconbitmap(r'C:\Users\castanon\Documents\PhD documents-NPL-LU\PhD measurements\PhD - Experimental\2019_Image_Processing_Python\GUI_2DMats\g4837.ico')
    app = App(root, script_dir)
    root.mainloop()
    cv2.destroyAllWindows() ## closing all windows when master window is closed

    ## creating loop to run GUI (DON'T TOUCH OR YOU'LL BREAK IT)

if __name__ == '__main__':
    main()

```

References

- [1] Drexler K E 1986 *Engines of creation* ed Anchor Books (New York: Random House Inc)
- [2] Feynman R 1960 There's plenty of room at the bottom *Eng. Sci.* **23** 22–36
- [3] Taniguchi N 1974 On the Basic Concept of Nanotechnology *Proc. Int. Conf. Prod. Eng.* 18–23
- [4] Binnig G and Rohrer H 1983 Scanning tunnelling microscopy *Surf. Sci.* **126** 236–44
- [5] Binnig G, Quate C F and Gerber C 1986 Atomic Force Microscope *Phys. Rev. Lett.* **56** 930–4
- [6] Kroto H W, Heath J R, O'Brien S C, Curl R F and Smalley R E 1985 C₆₀: Buckminsterfullerene *Nature* **318** 162–3
- [7] Iijima S 1991 Helical microtubules of graphitic carbon *Nature* **354** 56–8
- [8] Novoselov K S, Geim A K, Morozov S V., Jiang D, Zhang Y, Dubonos S V., Grigorieva I V. and Firsov A A 2004 Electric Field in atomically thin carbon films *Science (80-.)*. **306** 666–9
- [9] Topwal D 2015 Quantum confinement effects in low-dimensional systems *Pramana - J. Phys.* **84** 1023–32
- [10] Hung N T, Hasdeo E H, Nugraha A R T, Dresselhaus M S and Saito R 2016 Quantum Effects in the Thermoelectric Power Factor of Low-Dimensional Semiconductors *Phys. Rev. Lett.* **117** 1–5
- [11] Gobre V V. and Tkatchenko A 2013 Scaling laws for van der Waals interactions in nanostructured materials *Nat. Commun.* **4** 1–6
- [12] Rogers B, Adams J and Pennathur S *Understanding small systems* (CRC Press)
- [13] Franklin A D 2015 Nanomaterials in transistors: From high-performance to thin-film applications *Science (80-.)*. **349**
- [14] Keyes R W 2001 Fundamental limits of silicon *Proc. IEEE* **89** 227–39
- [15] Yoffe A D 2002 Low-dimensional systems: Quantum size effects and electronic properties of semiconductor microcrystallites (zero-dimensional systems) and some quasi-two-dimensional systems *Adv. Phys.* **51** 799–890
- [16] Castellanos-Gomez A 2016 Why all the fuss about 2D semiconductors? *Nat. Photonics* **10** 202–4
- [17] Landau L D and Lifshitz E M 1980 Statistical physics *Volume 5* (Elsevier) pp 436–9
- [18] Mermin N D 1968 Crystalline order in two dimensions *Phys. Rev. B* **176** 369–72
- [19] Novoselov K S, Jiang D, Schedin F, Booth T J, Khotkevich V V, Morozov S V and Geim A K 2005 Two-dimensional atomic crystals *Proc. Natl. Acad. Sci. U. S. A.* **102** 10451–3
- [20] Novoselov K S, Mishchenko A, Carvalho A and Castro Neto A H 2016 2D materials and van der Waals heterostructures *Science (80-.)*. **353**
- [21] Das T, Sharma B K, Katiyar A K and Ahn J H 2018 Graphene-based flexible and wearable electronics

- [22] Bae S et al 2010 Roll-to-roll production of 30-inch graphene films for transparent electrodes *Nat. Nanotechnol.* **5** 574–8
- [23] Xia F, Wang H, Xiao D, Dubey M and Ramasubramaniam A 2014 Two-dimensional material nanophotonics *Nat. Photonics* **8** 899–907
- [24] Bonaccorso F, Sun Z, Hasan T and Ferrari A C 2010 Graphene photonics and optoelectronics *Nat. Photonics* **4** 611–22
- [25] Schedin F, Geim A K, Morozov S V., Hill E W, Blake P, Katsnelson M I and Novoselov K S 2007 Detection of individual gas molecules adsorbed on graphene *Nat. Mater.* **6** 652–5
- [26] Melios C, Panchal V, Edmonds K, Lartsev A and Yakimova R 2018 Detection of Ultralow Concentration NO₂ in Complex Environment Using Epitaxial Graphene Sensors *ACS Sensors* **3** 1666–74
- [27] Huang X, Qi X, Boey F and Zhang H 2012 Graphene-based composites *Chem. Soc. Rev.* **41** 666–86
- [28] Dikin D A, Stankovich S, Zimney E J, Piner R D, Dommett G H B, Evmenenko G, Nguyen S T and Ruoff R S 2007 Preparation and characterization of graphene oxide paper *Nature* **448** 457–60
- [29] Gui G, Li J and Zhong J 2008 Band structure engineering of graphene by strain: First-principles calculations *Phys. Rev. B - Condens. Matter Mater. Phys.* **78** 1–6
- [30] Han M Y, Özyilmaz B, Zhang Y and Kim P 2007 Energy band-gap engineering of graphene nanoribbons *Phys. Rev. Lett.* **98** 1–4
- [31] Dean C R et al 2010 Boron nitride substrates for high-quality graphene electronics *Nat. Nanotechnol.* **5** 722–6
- [32] Wang Q H, Kalantar-Zadeh K, Kis A, Coleman J N and Strano M S 2012 Electronics and optoelectronics of two-dimensional transition metal dichalcogenides *Nat. Nanotechnol.* **7** 699–712
- [33] Appalakondaiah S, Vaitheeswaran G, Lebègue S, Christensen N E and Svane A 2012 Effect of van der Waals interactions on the structural and elastic properties of black phosphorus *Phys. Rev. B - Condens. Matter Mater. Phys.* **86** 1–9
- [34] Magorrian S J, Zólyomi V and Fal'Ko V I 2016 Electronic and optical properties of two-dimensional InSe from a DFT-parametrized tight-binding model *Phys. Rev. B* **94** 1–20
- [35] Novoselov K S, Fal'Ko V I, Colombo L, Gellert P R, Schwab M G and Kim K 2012 A roadmap for graphene *Nature* **490** 192–200
- [36] Wang L et al 2013 One-Dimensional Electrical Contact to a Two-Dimensional Material *Science (80-.).* **342** 614–7
- [37] Khan K, Tareen A K, Aslam M, Wang R, Zhang Y, Mahmood A, Ouyang Z, Zhang H and Guo Z 2020 *Recent developments in emerging two-dimensional materials and their applications* vol 8 (Royal Society of Chemistry)
- [38] Lavoisier A L 1789 *Traité élémentaire de chimie*
- [39] Jorio A, Saito R, Dresselhaus G and Dresselhaus M S 2011 *Raman Spectroscopy in graphene related systems* (Wiley-VCH)
- [40] Sivek J 2019 Carbon allotropes *Wikimedia Commons*
- [41] Alves J 2013 Graphene, *Wikimedia commons* (CC0)
- [42] Lee C, Wei X, Kysar J W and Hone J 2008 Measurement of the Elastic Properties and Intrinsic Strength of Monolayer Graphene *Science (80-.).* **321** 385–8
- [43] Ranjbartoreh A R, Wang B, Shen X and Wang G 2011 Advanced mechanical properties of graphene paper *J. Appl. Phys.* **109**

- [44] Castro Neto A H, Guinea F, Peres N M R, Novoselov K S and Geim A K 2009 The electronic properties of graphene *Rev. Mod. Phys.* **81** 109–62
- [45] Wallace P R 1947 The band theory of graphite *Phys. Rev.* 622–34
- [46] Slonczewski J C and Weiss P R 1958 Band structure of graphite *Phys. Rev.* **109** 33–41
- [47] Novoselov K S, Geim A K, Morozov S V., Jiang D, Katsnelson M I, Grigorieva I V., Dubonos S V. and Firsov A A 2005 Two-dimensional gas of massless Dirac fermions in graphene *Nature* **438** 197–200
- [48] Zhang Y, Tan Y and Stormer H 2005 Experimental observation of the quantum Hall effect and Berry's phase in graphene *Nature* **438** 201–4
- [49] Wu X, Hu Y, Ruan M, Madiomanana N K, Hankinson J, Sprinkle M, Berger C and De Heer W A 2009 Half integer quantum Hall effect in high mobility single layer epitaxial graphene *Appl. Phys. Lett.* **95** 4–7
- [50] Katsnelson M, Novoselov K S and Geim A K 2006 Chiral tunneling and the Klein paradox in graphene *Nat. Phys.* **2** 620–5
- [51] Li Z, Zhang W and Xing F 2019 Graphene Optical Biosensors *Int. J. Mol. Sci.* **20** 24–8
- [52] Morozov S V., Novoselov K S, Katsnelson M I, Schedin F, Elias D C, Jaszczak J A and Geim A K 2008 Giant intrinsic carrier mobilities in graphene and its bilayer *Phys. Rev. Lett.* **100** 11–4
- [53] Chen J H, Jang C, Xiao S, Ishigami M and Fuhrer M S 2008 Intrinsic and extrinsic performance limits of graphene devices on SiO₂ *Nat. Nanotechnol.* **3** 206–9
- [54] Nair R R, Blake P, Grigorenko A N, Novoselov K S, Booth T J, Stauber T, Peres N M and Geim A K 2007 Fine Structure constant defines visual transparency of Graphene *Indian J. Med. Res.* **44** 453–62
- [55] Balandin A A 2011 Thermal properties of graphene and nanostructured carbon materials *Nat. Mater.* **10** 569–81
- [56] Mahmoudi T, Wang Y and Hahn Y B 2018 Graphene and its derivatives for solar cells application *Nano Energy* **47** 51–65
- [57] Ishikawa R, Watanabe S, Yamazaki S, Oya T and Tsuboi N 2019 Perovskite/graphene solar cells without a hole-transport layer *ACS Appl. Energy Mater.* **2** 171–5
- [58] Chen X et al 2020 Graphene Hybrid Structures for Integrated and Flexible Optoelectronics *Adv. Mater.* **32** 1–24
- [59] Manchester University 2021 Graphene-based composite materials
- [60] Buckley D J, Black N C G, Castanon E G, Melios C, Hardman M and Kazakova O 2020 Frontiers of graphene and 2D material-based gas sensors for environmental monitoring *2D Mater.* **7**
- [61] Nizami M Z I, Takashiba S and Nishina Y 2020 Graphene oxide: A new direction in dentistry *Appl. Mater. Today* **19** 100576
- [62] Zheng Q, Lee J, Shen X, Chen X and Kim J-K 2020 Graphene-based wearable piezoresistive physical sensors *Mater. Today* **36** 158–79
- [63] 3M Scotch® Magic™ Tape Dispensed Rolls
- [64] Berger C et al 2004 Ultrathin epitaxial graphite: 2D electron gas properties and a route toward graphene-based nanoelectronics *J. Phys. Chem. B* **108** 19912–6
- [65] Tromp R M and Hannon J B 2009 Thermodynamics and kinetics of graphene growth on SiC(0001) *Phys. Rev. Lett.* **102** 1–4
- [66] Johansson L I and Virojanadara C 2014 Properties of epitaxial graphene grown on C-face SiC compared to Si-face *J. Mater. Res.* **29** 426–38

- [67] Norimatsu W and Kusunoki M 2014 Structural features of epitaxial graphene on SiC {0 0 0 1} surfaces *J. Phys. D. Appl. Phys.* **47**
- [68] Emtsev K V., Speck F, Seyller T, Ley L and Riley J D 2008 Interaction, growth, and ordering of epitaxial graphene on SiC{0001} surfaces: A comparative photoelectron spectroscopy study *Phys. Rev. B - Condens. Matter Mater. Phys.* **77** 1–10
- [69] Forti S, Emtsev K V., Coletti C, Zakharov A A, Riedl C and Starke U 2011 Large-area homogeneous quasifree standing epitaxial graphene on SiC(0001): Electronic and structural characterization *Phys. Rev. B - Condens. Matter Mater. Phys.* **84** 1–10
- [70] Burnett T, Yakimova R and Kazakova O 2011 Mapping of local electrical properties in epitaxial graphene using electrostatic force microscopy *Nano Lett.* **11** 2324–8
- [71] Panchal V, Pearce R, Yakimova R, Tzalenchuk A and Kazakova O 2013 Standardization of surface potential measurements of graphene domains *Sci. Rep.* **3** 1–8
- [72] Robinson J A, Trumbull K A, Labella M, Cavalero R, Hollander M J, Zhu M, Wetherington M T, Fanton M and Snyder D W 2011 Effects of substrate orientation on the structural and electronic properties of epitaxial graphene on SiC(0001) *Appl. Phys. Lett.* **98** 10–3
- [73] Yazdi G R, Vasiliauskas R, Iakimov T, Zakharov A, Syväjärvi M and Yakimova R 2013 Growth of large area monolayer graphene on 3C-SiC and a comparison with other SiC polytypes *Carbon N. Y.* **57** 477–84
- [74] Lartsev A, Lara-Avila S, Danilov A, Kubatkin S, Tzalenchuk A and Yakimova R 2015 A prototype of RK /200 quantum Hall array resistance standard on epitaxial graphene *J. Appl. Phys.* **118**
- [75] Virojanadara C, Syväjärvi M, Yakimova R, Johansson L I, Zakharov A A and Balasubramanian T 2008 Homogeneous large-area graphene layer growth on 6H-SiC(0001) *Phys. Rev. B - Condens. Matter Mater. Phys.* **78** 1–6
- [76] Yu Q, Lian J, Siriponglert S, Li H, Chen Y P and Pei S S 2008 Graphene segregated on Ni surfaces and transferred to insulators *Appl. Phys. Lett.* **93**
- [77] Li X, Cai W, Colombo L and Ruoff R S 2009 Evolution of graphene growth on Ni and Cu by carbon isotope labeling *Nano Lett.* **9** 4268–72
- [78] Li X et al 2009 Large-Area Synthesis of High-Quality and Uniform Graphene Films on Copper Foils *Science (80-.).* **324** 1312–4
- [79] Sun Z, Yan Z, Yao J, Beitler E, Zhu Y and Tour J M 2010 Growth of graphene from solid carbon sources *Nature* **468** 549–52
- [80] Kondrashov I I, Rybin M G, Obratsova E A and Obratsova E D 2019 Controlled Graphene Synthesis from Solid Carbon Sources *Phys. Status Solidi Basic Res.* **256** 1–6
- [81] Mattevi C, Kim H and Chhowalla M 2011 A review of chemical vapour deposition of graphene on copper *J. Mater. Chem.* **21** 3324–34
- [82] Saubestre E B 1959 Copper Etching in Ferric Chloride *Ind. Eng. Chem.* **51** 288–90
- [83] Suk J W, Kitt A, Magnuson C W, Hao Y, Ahmed S, An J, Swan A K, Goldberg B B and Ruoff R S 2011 Transfer of CVD-grown monolayer graphene onto arbitrary substrates *ACS Nano* **5** 6916–24
- [84] Deokar G, Avila J, Razado-Colambo I, Codron J L, Boyaval C, Galopin E, Asensio M C and Vignaud D 2015 Towards high quality CVD graphene growth and transfer *Carbon N. Y.* **89** 82–92
- [85] Wei W, Deokar G, Belhaj M, Mele D, Pallecchi E, Pichonat E, Vignaud D and Happy H 2014 Fabrication and characterization of CVD-grown graphene based Field-Effect Transistor *Eur. Microw. Week 2014 Connect. Futur. EuMW 2014 - Conf. Proceedings; EuMC 2014 44th Eur. Microw. Conf.* 367–70
- [86] Jung D H, Kang C, Kim M, Cheong H, Lee H and Lee J S 2014 Effects of Hydrogen Partial Pressure in the Annealing Process on Graphene Growth *J. Phys. Chem. C* **118** 3574–80

- [87] Kozlova J, Niilisk A, Alles H and Sammelseg V 2015 Discontinuity and misorientation of graphene grown on nickel foil: Effect of the substrate crystallographic orientation *Carbon N. Y.* **94** 160–73
- [88] Regmi M, Chisholm M F and Eres G 2012 The effect of growth parameters on the intrinsic properties of large-area single layer graphene grown by chemical vapor deposition on Cu *Carbon N. Y.* **50** 134–41
- [89] Banszerus L et al 2015 Ultrahigh-mobility graphene devices from chemical vapor deposition on reusable copper 1–7
- [90] Gong Y et al 2015 Two-Step Growth of Two-Dimensional WSe₂/MoSe₂ Heterostructures *Nano Lett.* **15** 6135–41
- [91] Zhao M, Ye Y, Han Y, Xia Y, Zhu H, Wang S, Wang Y, Muller D A and Zhang X 2016 Large-scale chemical assembly of atomically thin transistors and circuits *Nat. Nanotechnol.* **11** 954–9
- [92] Kretinin A V et al 2014 *Electronic Properties of Graphene Encapsulated with Different Two-Dimensional Atomic Crystals*
- [93] Cassabois G, Valvin P and Gil B 2016 Hexagonal boron nitride is an indirect bandgap semiconductor *Nat. Photonics* **10** 262–6
- [94] Greim J and Schwetz K A 2006 Boron Carbide, Boron Nitride, and Metal Borides *Ullmann's Encyclopedia of Industrial Chemistry* (Weinheim, Germany: Wiley-VCH Verlag GmbH & Co. KGaA)
- [95] Gorbachev R V et al 2010 Hunting for monolayer Boron Nitride: Optical and Raman signatures *Harvard Bus. Sch. Cases* 1
- [96] Banszerus L, Janssen H, Otto M, Epping A, Taniguchi T, Watanabe K, Beschoten B, Neumaier D and Stampfer C 2017 Identifying suitable substrates for high-quality graphene-based heterostructures *2D Mater.* **4**
- [97] Laturia A, Van de Put M L and Vandenberghe W G 2018 Dielectric properties of hexagonal boron nitride and transition metal dichalcogenides: from monolayer to bulk *npj 2D Mater. Appl.* **2** 1–7
- [98] Hunt B, Taniguchi T, Moon P, Koshino M and Ashoori R C 2013 Massive Dirac Fermions and *Science (80-.)*. **340** 1427–31
- [99] Georgiou T et al 2013 Vertical field-effect transistor based on graphene-WS₂ heterostructures for flexible and transparent electronics *Nat. Nanotechnol.* **8** 100–3
- [100] Britnell L, Morozov S V., Peres N M, Leist J, Geim A K, Novoselov K S and Ponomarenko L A 2012 Field effect tunneling transistor based on vertical graphene heterostructures *Science (80-.)*.
- [101] Jiang H X and Lin J Y 2014 Hexagonal boron nitride for deep ultraviolet photonic devices *Semicond. Sci. Technol.* **29**
- [102] Aharonovich I, Englund D and Toth M 2016 Solid-state single-photon emitters *Nat. Photonics* **10** 631–41
- [103] Tran T T, Bray K, Ford M J, Toth M and Aharonovich I 2016 Quantum emission from hexagonal boron nitride monolayers *Nat. Nanotechnol.* **11** 37–41
- [104] Yankowitz M, Ma Q, Jarrillo-Herrero P and Leroy B J 2019 Van der Waals heterostructures combining graphene and hexagonal boron nitride *Nat. Rev. Phys.* **1** 112–25
- [105] Politano A, Chiarello G, Samnakay R, Liu G, Gürbulak B, Duman S, Balandin A A and Boukhvalov D W 2016 The influence of chemical reactivity of surface defects on ambient-stable InSe-based nanodevices *Nanoscale* **8** 8474–9
- [106] Buckley D et al 2021 Anomalous Low Thermal Conductivity of Atomically Thin InSe Probed by Scanning Thermal Microscopy *Adv. Funct. Mater.* **2008967** 1–10
- [107] Ukraine N A of S of Institute for Problems of Materials Sciences
- [108] Balakrishnan N and Balakrishnan N 2018 Epitaxial growth of γ -InSe and α , β , and γ -In₂Se₃ on ϵ -

GaSe

- [109] Camara M O ., Mauger A and Devos I 2002 Electronic structure of the layer compounds GaSe and InSe in a tight-binding approach *Phys. Rev. B* **65**
- [110] Gomes da Costa P, Dandrea R G, Wallis R F and Bakanski M 1993 First-principles study of the electronic structure of g-InSe and b-InSe *Phys. Rev. B* **48**
- [111] Sun Y, Luo S, Zhao X G, Biswas K, Li S L and Zhang L 2018 InSe: A two-dimensional material with strong interlayer coupling *Nanoscale* **10** 7991–8
- [112] Lei S et al 2015 An atomically layered InSe avalanche photodetector *Nano Lett.* **15** 3048–55
- [113] Mudd G W, Molas M R, Chen X, Zólyomi V, Nogajewski K and Kudrynskiy Z R 2016 The direct-to-indirect band gap crossover in two-dimensional van der Waals Indium Selenide crystals *Nat. Publ. Gr.* 1–10
- [114] Lei S et al 2015 Optoelectronic memory using two-dimensional materials *Nano Lett.* **15** 259–65
- [115] Mudd G W et al 2015 High Broad-Band Photoresponsivity of Mechanically Formed InSe-Graphene van der Waals Heterostructures *Adv. Mater.* **27** 3760–6
- [116] Tamalampudi S R, Lu Y Y, Kumar U. R, Sankar R, Liao C Da, Moorthy B. K, Cheng C H, Chou F C and Chen Y T 2014 High performance and bendable few-layered InSe photodetectors with broad spectral response *Nano Lett.* **14** 2800–6
- [117] Li Y et al 2019 Elastic properties and intrinsic strength of two-dimensional InSe flakes *Nanotechnology* **30**
- [118] Zhao Q, Frisenda R, Wang T and Castellanos-Gomez A 2019 InSe: A two-dimensional semiconductor with superior flexibility *Nanoscale* **11** 9845–50
- [119] Bandurin D A et al 2017 High electron mobility, quantum Hall effect and anomalous optical response in atomically thin InSe *Nat. Nanotechnol.* **12** 223–7
- [120] Feng W, Zheng W, Cao W and Hu P 2014 Back Gated Multilayer InSe Transistors with Enhanced Carrier Mobilities via the Suppression of Carrier Scattering from a Dielectric Interface *Adv. Mater.* **26** 6587–93
- [121] Rhyee J-S, Lee K H, Lee S M, Cho E, Kim S Il, Lee E, Kwon Y S, Shim J H and Kotliar G 2009 Peierls distortion as a route to high thermoelectric performance in $\text{In}_4\text{Se}_3-\delta$ crystals *Nature* **459** 965–8
- [122] Nissimagoudar A S, Ma J, Chen Y and Li W 2017 Thermal transport in monolayer InSe *J. Phys. Condens. Matter* **29**
- [123] Shi L, Zhou Q, Zhao Y, Ouyang Y, Ling C, Li Q and Wang J 2017 Oxidation Mechanism and Protection Strategy of Ultrathin Indium Selenide: Insight from Theory *J. Phys. Chem. Lett.* **8** 4368–73
- [124] Kistanov A A, Cai Y, Zhou K, Dmitriev S V. and Zhang Y W 2018 Atomic-scale mechanisms of defect- and light-induced oxidation and degradation of InSe *J. Mater. Chem. C* **6** 518–25
- [125] Bunch J S, Verbridge S S, Alden J S, Van Der Zande A M, Parpia J M, Craighead H G and McEuen P L 2008 Impermeable atomic membranes from graphene sheets *Nano Lett.* **8** 2458–62
- [126] Hu S et al 2014 Proton transport through one-atom-thick crystals *Nature* **516** 227–30
- [127] Mayorov A S, Elias D C, Mukhin I S, Morozov S V., Ponomarenko L A, Novoselov K S, Geim A K and Gorbachev R V. 2012 How close can one approach the dirac point in graphene experimentally? *Nano Lett.* **12** 4629–34
- [128] Martin J, Akerman N, Ulbricht G, Lohmann T, Smet J H, Von Klitzing K and Yacoby A 2008 Observation of electron-hole puddles in graphene using a scanning single-electron transistor *Nat. Phys.* **4** 144–8
- [129] Geim A K and Novoselov K S 2007 The rise of graphene *Nat. Mater.* **6** 183–91

- [130] Ahn C H et al 2006 Electrostatic modification of novel materials *Rev. Mod. Phys.* **78** 1185–212
- [131] Agnoli S and Favaro M 2016 Doping graphene with boron: A review of synthesis methods, physicochemical characterization, and emerging applications *J. Mater. Chem. A* **4** 5002–25
- [132] Wang H, Maiyalagan T and Wang X 2012 Review on recent progress in nitrogen-doped graphene: Synthesis, characterization, and its potential applications *ACS Catal.* **2** 781–94
- [133] Wehling T O, Novoselov K S, Morozov S V., Vdovin E E, Katsnelson M I, Geim A K and Lichtenstein A I 2008 Molecular doping of graphene *Nano Lett.* **8** 173–7
- [134] Leenaerts O, Partoens B and Peeters F M 2008 Paramagnetic adsorbates on graphene: A charge transfer analysis *Appl. Phys. Lett.* **92**
- [135] Leenaerts O, Partoens B and Peeters F M 2008 Adsorption of H₂ O, N H₃, CO, N O₂, and NO on graphene: A first-principles study *Phys. Rev. B - Condens. Matter Mater. Phys.* **77** 1–6
- [136] Das A et al 2008 Monitoring dopants by Raman scattering in an electrochemically top-gated graphene transistor *Nat. Nanotechnol.* **3** 210–5
- [137] Giusca C E, Panchal V, Munz M, Wheeler V D, Nyakiti L O, Myers-Ward R L, Gaskill D K and Kazakova O 2015 Water Affinity to Epitaxial Graphene: The Impact of Layer Thickness *Adv. Mater. Interfaces* **2** 1–10
- [138] Liu X, Cheng S, Liu H, Hu S, Zhang D and Ning H 2012 A survey on gas sensing technology *Sensors (Switzerland)* **12** 9635–65
- [139] Wang H, Ma J, Zhang J and Feng Y 2021 Gas sensing materials roadmap
- [140] Zhang J, Qin Z, Zeng D and Xie C 2017 Metal-oxide-semiconductor based gas sensors: Screening, preparation, and integration *Phys. Chem. Chem. Phys.* **19** 6313–29
- [141] Jogender, Mandeep and Rita Kakkar 2020 Recent Advances on Graphene-Based Gas Sensors *Russ. J. Phys. Chem. A* **94** 2115–20
- [142] Defects T I 2021 Thermally Induced Defects 1–8
- [143] Ben Aziza Z, Zhang Q and Baillargeat D 2014 Graphene/mica based ammonia gas sensors *Appl. Phys. Lett.* **105**
- [144] Cadore A R et al 2018 Enhancing the response of NH₃ graphene-sensors by using devices with different graphene-substrate distances *Sensors Actuators, B Chem.* **266** 438–46
- [145] Liang R, Luo A, Zhang Z, Li Z, Han C and Wu W 2020 Research progress of graphene-based flexible humidity sensor *Sensors (Switzerland)* **20** 1–17
- [146] Lv C et al 2019 Recent advances in graphene-based humidity sensors *Nanomaterials* **9**
- [147] Kasirga T S 2020 Thermal Conductivity Measurements in 2D Materials *Thermal Conductivity Measurements in Atomically Thin Materials and Devices* pp 11–27
- [148] Rogers B, Pennathur S and Adams J 2008 *Nanotechnology: Understanding small systems* ed CRC/Taylor & Francis
- [149] Song H, Liu J, Liu B, Wu J, Cheng H and Kang F 2018 Two-Dimensional Materials for Thermal Management Applications *Joule* **2** 442–63
- [150] Tovee P, Pumarol M, Zeze D, Kjoller K and Kolosov O 2012 Nanoscale spatial resolution probes for scanning thermal microscopy of solid state materials *J. Appl. Phys.* **112** 114317
- [151] Zhang Y, Zhu W, Hui F, Lanza M, Borca-tasciuc T and Rojo M M 2020 A Review on Principles and Applications of Scanning Thermal Microscopy (SThM) **1900892**
- [152] Liu J, Choi G M and Cahill D G 2014 Measurement of the anisotropic thermal conductivity of molybdenum disulfide by the time-resolved magneto-optic Kerr effect *J. Appl. Phys.* **116**

- [153] Fugalto G, Cepellotti A, Paulatto L, Lazzeri M, Marzari N and Mauri F 2014 Thermal conductivity of graphene and graphite: Collective excitations and mean free paths *Nano Lett.* **14** 6109–14
- [154] Lindsay L and Broido D A 2011 Enhanced thermal conductivity and isotope effect in single-layer hexagonal boron nitride *Phys. Rev. B - Condens. Matter Mater. Phys.* **84**
- [155] Jo I, Pettes M T, Ou E, Wu W and Shi L 2014 Basal-plane thermal conductivity of few-layer molybdenum disulfide *Appl. Phys. Lett.* **104** 201902
- [156] Sahoo S, Gaur A P S, Ahmadi M, Guinel M J-F and Katiyar R S 2013 Temperature-Dependent Raman Studies and Thermal Conductivity of Few-Layer MoS₂ *J. Phys. Chem. C* **117** 9042–7
- [157] Bell L E 2008 Cooling, heating, generating power, and recovering waste heat with thermoelectric systems *Science (80-.).* **321** 1457–61
- [158] Disalvo F J 1999 Thermoelectric cooling and power generation *Science (80-.).* **285** 703–6
- [159] Stockholm J G 2018 ScienceDirect Applications in thermoelectricity *Mater. Today Proc.* **5** 10257–76
- [160] Yu J, Sun Q and Jena P 2016 Recent advances in 2D thermoelectric materials *Int. Symp. Clust. Nanomater.* **10174** 101740C
- [161] Kanatzidis M G 2014 thermoelectric figure of merit in SnSe crystals *Nature*
- [162] Kanatzidis M G 2012 all-scale hierarchical architectures 0–5
- [163] Kim S Il et al 2015 Dense dislocation arrays embedded in grain boundaries for high-performance bulk thermoelectrics **348** 109–15
- [164] Kim M, Lee W, Cho K, Ahn J and Sung Y 2016 Spinodally Decomposed PbSe-PbTe Nanoparticles for High-Performance Thermoelectrics: Enhanced Phonon Scattering and Unusual Transport Behavior
- [165] Yang L, Chen Z, Dargusch M S and Zou J 2018 High Performance Thermoelectric Materials : Progress and Their Applications **1701797** 1–28
- [166] Hicks L and Dresselhaus M S 1993 Thermoelectric figure of merit of a one-dimensional conductor *Phys. Rev. B* **47** 631–4
- [167] Hicks L D and Dresselhaus M S 1993 Effect of quantum-well structures on the thermoelectric figure of merit *Phys. Rev. B* **47** 727–31
- [168] Wood C 1988 Materials for thermoelectric energy conversion *Reports Prog. Phys.* **51** 459–539
- [169] Lee M-J et al 2016 Thermoelectric materials by using two-dimensional materials with negative correlation between electrical and thermal conductivity *Nat. Commun.* **7** 12011
- [170] Zeng J et al 2018 Experimental Identification of Critical Condition for Drastically Enhancing Thermoelectric Power Factor of Two-Dimensional Layered Materials *Nano Lett.* **18** 7538–45
- [171] Grosse K L, Bae M H, Lian F, Pop E and King W P 2011 Nanoscale Joule heating, Peltier cooling and current crowding at graphene-metal contacts *Nat. Nanotechnol.* **6** 287–90
- [172] Boyd R et al 2010 Two-Dimensional Phonon Transport **328** 213–7
- [173] Wei P, Bao W, Pu Y, Lau C N and Shi J 2009 Anomalous thermoelectric transport of dirac particles in graphene *Phys. Rev. Lett.* **102** 1–4
- [174] Mahapatra P S, Sarkar K, Krishnamurthy H R, Mukerjee S and Ghosh A 2017 Seebeck Coefficient of a Single van der Waals Junction in Twisted Bilayer Graphene *Nano Lett.* **17** 6822–7
- [175] Buscema M, Barkelid M, Zwiller V, Van Der Zant H S J, Steele G A and Castellanos-Gomez A 2013 Large and tunable photothermoelectric effect in single-layer MoS₂ *Nano Lett.* **13** 358–63
- [176] Saito Y, Iizuka T, Koretsune T, Arita R, Shimizu S and Iwasa Y 2016 Gate-Tuned Thermoelectric Power in Black Phosphorus *Nano Lett.* **16** 4819–24

- [177] Rogers B, Pennathur S and Adams J 2008 Nanomechanics *Understanding small systems* (CRC Press) pp 127–91
- [178] Binnig G, Rohrer H, Gerber C and Weibel E 1982 Tunneling through a controllable vacuum gap *Appl. Phys. Lett.* **40** 178–80
- [179] Binnig G, Rohrer H, Gerber C and Weibel E 1982 Surface Studies by Scanning Tunneling Microscopy *Phys. Rev. Lett.* **49** 57–61
- [180] Meyer E, Josef Hug H and Bennewitz R 2004 *Scanning Probe Microscopy: The Lab on a tip* (Springer Berlin Heidelberg)
- [181] Rosenberger M R, Chuang H J, McCreary K M, Hanbicki A T, Sivaram S V. and Jonker B T 2018 Nano-"Squeegee" for the Creation of Clean 2D Material Interfaces *ACS Appl. Mater. Interfaces* **10** 10379–87
- [182] García R and Pérez R 2002 *Dynamic atomic force microscopy methods* vol 47
- [183] Nonnenmacher M, O'Boyle M P and Wickramasinghe H K 1991 Kelvin probe force microscopy *Appl. Phys. Lett.* **58** 2921–3
- [184] Sommerhalter C, Matthes T W, Glatzel T, Jäger-Waldau A and Lux-Steiner M C 1999 High-sensitivity quantitative Kelvin probe microscopy by noncontact ultra-high-vacuum atomic force microscopy *Appl. Phys. Lett.* **75** 286–8
- [185] Glatzel T, Sadewasser S and Lux-Steiner M C 2003 Amplitude or frequency modulation-detection in Kelvin probe force microscopy *Appl. Surf. Sci.* **210** 84–9
- [186] Burke S A, Ledue J M, Miyahara Y, Topple J M, Fostner S and Grütter P 2009 Determination of the local contact potential difference of PTCDA on NaCl: A comparison of techniques *Nanotechnology* **20**
- [187] Zerweck U, Loppacher C, Otto T, Grafström S and Eng L M 2005 Accuracy and resolution limits of Kelvin probe force microscopy *Phys. Rev. B - Condens. Matter Mater. Phys.* **71** 1–9
- [188] Ma J Y, Ding J, Yan H J, Wang D and Hu J S 2019 Temperature-Dependent Local Electrical Properties of Organic-Inorganic Halide Perovskites: In Situ KPFM and c-AFM Investigation *ACS Appl. Mater. Interfaces* **11** 21627–33
- [189] Baumgart C, Helm M and Schmidt H 2009 Quantitative dopant profiling in semiconductors: A Kelvin probe force microscopy model *Phys. Rev. B - Condens. Matter Mater. Phys.* **80** 1–5
- [190] Ochedowski O, Marinov K, Scheuschner N, Poloczek A, Bussmann B K, Maultzsch J and Schleberger M 2014 Effect of contaminations and surface preparation on the work function of single layer MoS₂ *Beilstein J. Nanotechnol.* **5** 291–7
- [191] Tran T-H, Rodriguez R D, Salerno M, Matković A, Teichert C and Sheremet E 2021 Twisted graphene in graphite: Impact on surface potential and chemical stability *Carbon N. Y.* **176** 431–9
- [192] Shvartsman V V., Kiselev D A, Solnyshkin A V., Lupascu D C and Silibin M V. 2018 Evolution of poled state in P(VDF-TrFE)/(Pb,Ba)(Zr,Ti)O₃ composites probed by temperature dependent Piezoresponse and Kelvin Probe Force Microscopy *Sci. Rep.* **8** 1–6
- [193] Williams C C and Wickramasinghe H K 1986 Scanning thermal profiler *Microelectron. Eng.* **5** 509–13
- [194] Menges F, Mensch P, Schmid H, Riel H, Stemmer A and Gotsmann B 2016 Temperature mapping of operating nanoscale devices by scanning probe thermometry *Nat. Commun.* **7** 1–6
- [195] Majumdar A 1999 *Scanning Thermal Source*
- [196] Assy A, Lefèvre S, Chapuis P O and Gomès S 2014 Analysis of heat transfer in the water meniscus at the tip-sample contact in scanning thermal microscopy *J. Phys. D. Appl. Phys.* **47**
- [197] Assy A and Gomès S 2015 Temperature-dependent capillary forces at nano-contacts for estimating the heat conduction through a water meniscus *Nanotechnology* **26**

- [198] Zhang Y, Zhu W, Hui F, Lanza M, Borca-Tasciuc T and Muñoz Rojo M 2020 A Review on Principles and Applications of Scanning Thermal Microscopy (SThM) *Adv. Funct. Mater.* **30**
- [199] Metzke C, Kühnel F, Weber J and Benstetter G 2021 Scanning thermal microscopy of ultrathin films: Numerical studies regarding cantilever displacement, thermal contact areas, heat fluxes, and heat distribution *Nanomaterials* **11** 1–21
- [200] Lee J, Wright T L, Abel M R, Sunden E O, Marchenkov A, Graham S and King W P 2007 Thermal conduction from microcantilever heaters in partial vacuum *J. Appl. Phys.* **101**
- [201] Gomès S, Assy A and Chapuis P O 2015 Scanning thermal microscopy: A review *Phys. Status Solidi Appl. Mater. Sci.* **212** 477–94
- [202] Shi L, Plyasunov S, Bachtold A, McEuen and Majumdar A 2000 Scanning thermal microscopy of carbon nanotubes using batch-fabricated probes **4295** 1998–2001
- [203] Evangeli C, Spiece J, Sangtarash S, Molina-Mendoza A J, Mucientes M, Mueller T, Lambert C, Sadeghi H and Kolosov O 2019 Nanoscale Thermal Transport in 2D Nanostructures from Cryogenic to Room Temperature *Adv. Electron. Mater.* **5** 1–10
- [204] Kolosov O V., Pumarol M E, Tovee P, Rosamond M C, Petty M C, Zeze D A and Falko V 2012 Direct nanoscale imaging of ballistic and diffusive thermal transport in graphene nanostructures *Tech. Proc. 2012 NSTI Nanotechnol. Conf. Expo, NSTI-Nanotech 2012* 206–9
- [205] Blake P, Hill E W, Castro Neto A H, Novoselov K S, Jiang D, Yang R, Booth T J and Geim A K 2007 Making graphene visible *Appl. Phys. Lett.* **91**
- [206] Abergel D S L, Russell A and Fal'Ko V I 2007 Visibility of graphene flakes on a dielectric substrate *Appl. Phys. Lett.* **91**
- [207] Ding D, Hibino H and Ago H 2018 Grain Boundaries and Gas Barrier Property of Graphene Revealed by Dark-Field Optical Microscopy *J. Phys. Chem. C* **122** 902–10
- [208] Kong X H, Ji H X, Piner R D, Li H F, Magnuson C W, Tan C, Ismach A, Chou H and Ruoff R S 2013 Non-destructive and rapid evaluation of chemical vapor deposition graphene by dark field optical microscopy *Appl. Phys. Lett.* **103**
- [209] Terry D J et al 2018 Infrared-to-violet tunable optical activity in atomic films of GaSe, InSe, and their heterostructures *2D Mater.* **5**
- [210] Malard L M, Pimenta M A, Dresselhaus G and Dresselhaus M S 2009 Raman spectroscopy in graphene *Phys. Rep.* **473** 51–87
- [211] Iqbal M W, Shahzad K, Akbar R and Hussain G 2020 A review on Raman finger prints of doping and strain effect in TMDCs *Microelectron. Eng.* **219**
- [212] Casiraghi C 2009 Doping dependence of the Raman peaks intensity of graphene close to the Dirac point *Phys. Rev. B - Condens. Matter Mater. Phys.* **80** 2–4
- [213] Jorio, A., Dresselhaus M S, Saito R and Dresselhaus G 2011 *Raman spectroscopy in graphene related systems* (Wiley-VCH)
- [214] Group I and R discussion Infrared and Raman spectra of solids
- [215] Wiki A P Basics of Raman Spectroscopy
- [216] Ferrari A C and Basko D M 2013 Raman spectroscopy as a versatile tool for studying the properties of graphene *Nat. Nanotechnol.* **8** 235–46
- [217] Kazakova O, Panchal V and Burnett T L 2013 Epitaxial graphene and graphene-based devices studied by ESPM *Crystals* **3** 191–233
- [218] Eckmann A, Felten A, Mishchenko A, Britnell L, Krupke R, Novoselov K S and Casiraghi C 2012 Probing the nature of defects in graphene by Raman spectroscopy *Nano Lett.* **12** 3925–30
- [219] Ramsteiner M and Wagner J 1987 Resonant Raman scattering of hydrogenated amorphous carbon:

- Evidence for π -bonded carbon clusters *Appl. Phys. Lett.* **51** 1355–7
- [220] Reich S and Thomsen C 2004 Raman spectroscopy of graphite *Philos. Trans. R. Soc. A Math. Phys. Eng. Sci.* **362** 2271–88
- [221] Basko D M, Piscanec S and Ferrari A C 2009 Electron-electron interactions and doping dependence of the two-phonon Raman intensity in graphene 1–10
- [222] You A, Be M A Y and In I 2011 Raman spectra of epitaxial graphene on SiC (0001) **201918** 20–3
- [223] Ni Z H, Chen W, Fan X F, Kuo J L, Yu T, Wee A T S and Shen Z X 2008 Raman spectroscopy of epitaxial graphene on a SiC substrate 1–6
- [224] SEPnet South Eastern Physics network
- [225] Withers F et al 2015 Light-emitting diodes by band-structure engineering in van der Waals heterostructures *Nat. Mater.* **14** 301–6
- [226] Ribeiro-Palau R, Zhang C, Watanabe K, Taniguchi T, Hone J and Dean C R 2018 Twistable electronics with dynamically rotatable heterostructures *Science (80-.).* **361** 690–3
- [227] Frisenda R, Navarro-Moratalla E, Gant P, Perez de Lara D, Jarrillo-Herrero P, Gorbachev R V and Castellanos-Gomez A 2018 Recent progress in the assembly of nanodevices and Van der Waals heterostructures by deterministic placement of 2D materials *Chem. Soc. Rev.*
- [228] Uwannu T, Hattori Y, Taniguchi T, Watanabe K and Nagashio K 2015 Fully dry PMMA transfer of graphene on h-BN using a heating/ cooling system *2D Mater.* **2**
- [229] Castellanos-Gomez A, Buscema M, Molenaar R, Singh V, Janssen L, Van Der Zant H S J and Steele G A 2014 Deterministic transfer of two-dimensional materials by all-dry viscoelastic stamping *2D Mater.* **1**
- [230] Jain A, Bharadwaj P, Heeg S, Parzefall M, Taniguchi T, Watanabe K and Novotny L 2018 Minimizing Residues in Transfer of 2D Materials from PDMS *Arxiv*
- [231] Haigh S J et al 2012 Cross-sectional imaging of individual layers and buried interfaces of graphene-based heterostructures and superlattices *Nat. Mater.* **11** 764–7
- [232] Gasparutti I, Song S H, Neumann M, Wei X, Watanabe K, Taniguchi T and Lee Y H 2020 How Clean Is Clean? Recipes for van der Waals Heterostructure Cleanliness Assessment *ACS Appl. Mater. Interfaces* **12** 7701–9
- [233] Vasu K S et al 2016 Van der Waals pressure and its effect on trapped interlayer molecules *Nat. Commun.* **7** 1–6
- [234] Mayorov A S et al 2011 Micrometer-scale ballistic transport in encapsulated graphene at room temperature *Nano Lett.* **11** 2396–9
- [235] Kim Y, Herlinger P, Taniguchi T, Watanabe K and Smet J H 2019 Reliable Postprocessing Improvement of van der Waals Heterostructures *ACS Nano* **13** 14182–90
- [236] Melios C, Centeno A, Zurutuza A, Panchal V, Giusca C E, Spencer S, Silva S R P and Kazakova O 2016 Effects of humidity on the electronic properties of graphene prepared by chemical vapour deposition *Carbon N. Y.* **103** 273–80
- [237] Panchal V, Giusca C E, Lartsev A, Martin N A, Cassidy N, Myers-Ward R L, Gaskill D K and Kazakova O 2018 Atmospheric doping effects in epitaxial graphene: correlation of local and global electrical measurements *arXiv*
- [238] Wood J D et al 2014 Effective passivation of exfoliated black phosphorus transistors against ambient degradation *Nano Lett.* **14** 6964–70
- [239] Island J O, Steele G A, Zant H S J van der and Castellanos-Gomez A 2015 Environmental instability of few-layer black phosphorus *2D Mater.* **2** 011002
- [240] Castellanos-Gomez A et al 2014 Isolation and characterization of few-layer black phosphorus *2D*

- [241] Wang J I J, Yang Y, Chen Y A, Watanabe K, Taniguchi T, Churchill H O H and Jarillo-Herrero P 2015 Electronic transport of encapsulated graphene and WSe₂ devices fabricated by pick-up of prepatterned hBN *Nano Lett.* **15** 1898–903
- [242] Jin C et al 2017 Interlayer electron-phonon coupling in WSe₂/hBN heterostructures *Nat. Phys.* **13** 127–31
- [243] Petrone N, Chari T, Meric I, Wang L, Shepard K L and Hone J 2015 Flexible Graphene Field-Effect Transistors Encapsulated in Hexagonal Boron Nitride *ACS Nano* **9** 8953–9
- [244] Li Q, Lee C, Carpick R W and Hone J 2010 Substrate effect on thickness-dependent friction on graphene *Phys. Status Solidi Basic Res.* **247** 2909–14
- [245] Robinson B J, Giusca C E, Gonzalez Y T, DKay N, Kazakova O and Kolosov O V. 2015 Structural, optical and electrostatic properties of single and fewlayers MoS₂: Effect of substrate *2D Mater.* **2**
- [246] Ghita R, Logofatu C, Negrila C-C, Ungureanu F, Cotirlan C, Manea A-S, Lazarescu M-F and Ghic C 2011 Study of SiO₂/Si Interface by Surface Techniques *Crystalline Silicon - Properties and Uses* (InTech)
- [247] Huang Y, Sutter E, Shi N N, Zheng J, Yang T, Englund D, Gao H J and Sutter P 2015 Reliable Exfoliation of Large-Area High-Quality Flakes of Graphene and Other Two-Dimensional Materials *ACS Nano* **9** 10612–20
- [248] Ebnesajjad S and Landrock A H 2015 Material surface preparation techniques *Material surface preparation techniques* (Elsevier Inc.) pp 35–66
- [249] Scientific F Acetone
- [250] Scientific F Isopropanol
- [251] Electronics D FEMTO plasma asher model E
- [252] Electronic Diener Cleaning with plasma
- [253] Blake P, Hill E W, Castro Neto A H, Novoselov K S, Jiang D, Yang R, Booth T J and Geim A K 2007 Making graphene visible *Appl. Phys. Lett.* **91** 2007–9
- [254] Ni Z H, Wang H M, Kasim J, Fan H M, Yu T, Wu Y H, Feng Y P and Shen Z X 2007 Graphene thickness determination using reflection and contrast spectroscopy *Nano Lett.* **7** 2758–63
- [255] Teo G, Wang H, Wu Y, Guo Z, Zhang J, Ni Z and Shen Z 2008 Visibility study of graphene multilayer structures *J. Appl. Phys.* **103**
- [256] Brotons-Gisbert M, Sánchez-Royo J F and Martínez-Pastor J P 2015 Thickness identification of atomically thin InSe nanoflakes on SiO₂/Si substrates by optical contrast analysis *Appl. Surf. Sci.* **354** 453–8
- [257] Li H, Wu J, Huang X, Lu G, Yang J, Lu X, Xiong Q and Zhang H 2013 Rapid and reliable thickness identification of two-dimensional nanosheets using optical microscopy *ACS Nano* **7** 10344–53
- [258] Song C, Huang S, Wang C, Luo J and Yan H 2020 The optical properties of few-layer InSe *J. Appl. Phys.* **128**
- [259] Yu V and Hilke M 2009 Large contrast enhancement of graphene monolayers by angle detection *Appl. Phys. Lett.* **95**
- [260] Bing D, Wang Y, Bai J, Du R, Wu G and Liu L 2018 Optical contrast for identifying the thickness of two-dimensional materials *Opt. Commun.* **406** 128–38
- [261] Jessen B S, Whelan P R, Mackenzie D M A, Luo B, Thomsen J D, Gammelgaard L, Booth T J and Bøggild P 2018 Quantitative optical mapping of two-dimensional materials *Sci. Rep.* **8** 2–9
- [262] Masubuchi S, Watanabe E, Seo Y, Okazaki S, Sasagawa T, Watanabe K, Taniguchi T and Machida T

- 2020 Deep-learning-based image segmentation integrated with optical microscopy for automatically searching for two-dimensional materials *npj 2D Mater. Appl.* **4** 4–6
- [263] Masubuchi S, Morimoto M, Morikawa S, Onodera M, Asakawa Y, Watanabe K, Taniguchi T and Machida T 2018 Autonomous robotic searching and assembly of two-dimensional crystals to build van der Waals superlattices *Nat. Commun.* **9** 4–6
- [264] Liu H and Jezek K C 2004 Automated extraction of coastline from satellite imagery by integrating Canny edge detection and locally adaptive thresholding methods *Int. J. Remote Sens.* **25** 937–58
- [265] Dai W, Na J, Huang N, Hu G, Yang X, Tang G, Xiong L and Li F 2020 Integrated edge detection and terrain analysis for agricultural terrace delineation from remote sensing images *Int. J. Geogr. Inf. Sci.* **34** 484–503
- [266] Bharodiya A K and Gonsai A M 2019 An improved edge detection algorithm for X-Ray images based on the statistical range *Heliyon* **5** e02743
- [267] Dorafshan S, Thomas R J and Maguire M 2018 Comparison of deep convolutional neural networks and edge detectors for image-based crack detection in concrete *Constr. Build. Mater.* **186** 1031–45
- [268] Öztürk Ş and Akdemir B 2015 Comparison of Edge Detection Algorithms for Texture Analysis on Glass Production *Procedia - Soc. Behav. Sci.* **195** 2675–82
- [269] Prajapati N, Kumar Nandanwar A and Prajapati G S 2016 Edge Histogram Descriptor, Geometric Moment and Sobel Edge Detector Combined Features Based Object Recognition and Retrieval System *Int. J. Comput. Sci. Inf. Technol.* **7** 407–12
- [270] Law T, Itoh H and Seki H 1996 Image filtering, edge detection, and edge tracing using fuzzy reasoning *IEEE Trans. Pattern Anal. Mach. Intell.* **18** 481–91
- [271] Hsiao P Y, Chen C H, Chou S S, Li L T and Chen S J 2006 A parameterizable digital-approximated 2D Gaussian smoothing filter for edge detection in noisy image *Proc. - IEEE Int. Symp. Circuits Syst.* 3189–92
- [272] Orphology M 2012 E Dge D Etection and D Enoising M Edical I Mage Using *Int. J. Eng. Sci. Emerg. Technol.* **2** 66–72
- [273] Simbulan K B C, Chen P C, Lin Y Y and Lan Y W 2018 A standard and reliable method to fabricate two-dimensional nanoelectronics *J. Vis. Exp.* **2018** 1–8
- [274] Mitutoyo Corporation Micrometer head n148-801
- [275] Pizzocchero F, Gammelgaard L, Jessen B S, Caridad J M, Wang L, Hone J, Bøggild P and Booth T J 2016 The hot pick-up technique for batch assembly of van der Waals heterostructures *Nat. Commun.*
- [276] Sigma-Aldrich Poly(propylene carbonate)
- [277] Vincent T, Panchal V, Booth T, Power S R, Jauho A P, Antonov V and Kazakova O 2018 Probing the nanoscale origin of strain and doping in graphene-hBN heterostructures *arXiv*
- [278] Juspertor GmbH Layout Editor
- [279] Wang L et al 2013 One-dimensional electrical contact to a two-dimensional material *Science (80-.).* **342** 614–7
- [280] Guimarães M H D, Gao H, Han Y, Kang K, Xie S, Kim C J, Muller D A, Ralph D C and Park J 2016 Atomically Thin Ohmic Edge Contacts between Two-Dimensional Materials *ACS Nano* **10** 6392–9
- [281] Zheng C et al 2017 Direct Observation of 2D Electrostatics and Ohmic Contacts in Template-Grown Graphene/WS₂ Heterostructures *ACS Nano* **11** 2785–93
- [282] Sensors B ElectriMulti75-G
- [283] Zhao Q, Wang T, Ryu Y K, Frisenda R and Castellanos-Gomez A 2020 An inexpensive system for the deterministic transfer of 2D materials *arXiv*

- [284] Brown K, Vincent T, Castanon E G, Rus F S, Melios C, Kazakova O and Giusca C E 2020 Contactless probing of graphene charge density variation in a controlled humidity environment *Carbon N. Y.* **163** 408–16
- [285] Lee J E, Ahn G, Shim J, Lee Y S and Ryu S 2012 Optical separation of mechanical strain from charge doping in graphene *Nat. Commun.* **3**
- [286] Mueller N S et al 2018 Evaluating arbitrary strain configurations and doping in graphene with Raman spectroscopy *2D Mater.* **5**
- [287] Melios C, Panchal V, Edmonds K, Lartsev A, Yakimova R and Kazakova O 2018 Detection of Ultralow Concentration NO₂ in Complex Environment Using Epitaxial Graphene Sensors *ACS Sensors* **3** 1666–74
- [288] Panchal V, Giusca C E, Lartsev A, Martin N A and Cassidy N 2016 Atmospheric doping effects in epitaxial graphene : correlation of local and global electrical studies *2D Mater.* **3** 15006
- [289] Buckley D, Black N C G, Castanon E, Melios C, Hardman M and Kazakova O 2020 Frontiers of graphene and 2D material-based gas sensors for environmental monitoring *2D Mater.*
- [290] Miao X, Tongay S, Petterson M K, Berke K, Rinzler A G, Appleton B R and Hebard A F 2012 High efficiency graphene solar cells by chemical doping *Nano Lett.* **12** 2745–50
- [291] Liu Z, Li J and Yan F 2013 Package-free flexible organic solar cells with graphene top electrodes *Adv. Mater.* **25** 4296–301
- [292] Quesnel E et al 2015 Graphene-based technologies for energy applications, challenges and perspectives *2D Mater.* **2**
- [293] Adetayo A and Runsewe D 2019 Synthesis and Fabrication of Graphene and Graphene Oxide: A Review *Open J. Compos. Mater.* **09** 207–29
- [294] Kim C H, Yoo S W, Nam D W, Seo S and Lee J H 2012 Effect of temperature and humidity on NO₂ and NH₃ gas sensitivity of bottom-gate graphene FETs prepared by ICP-CVD *IEEE Electron Device Lett.* **33** 1084–6
- [295] Quellmalz A, Smith A D, Elgammal K, Fan X, Delin A, Östling M, Lemme M, Gylfason K B and Niklaus F 2018 Influence of Humidity on Contact Resistance in Graphene Devices *ACS Appl. Mater. Interfaces* **10** 41738–46
- [296] Yavari F, Kritzinger C, Gaire C, Song L, Gulapalli H, Borca-Tasciuc T, Ajayan P M and Koratkar N 2010 Tunable bandgap in graphene by the controlled adsorption of water molecules *Small* **6** 2535–8
- [297] Wehling T O, Katsnelson M I and Lichtenstein A I 2009 Adsorbates on graphene: Impurity states and electron scattering *Chem. Phys. Lett.* **476** 125–34
- [298] Leenaerts O, Partoens B and Peeters F M 2020 Adsorption of H₂O, NH₃, CO, NO₂, and NO on graphene: A first-principles study 1–6
- [299] Nyakiti L O, Wheeler V D, Garces N Y, Myers-Ward R L, Eddy C R and Gaskill D K 2012 Enabling graphene-based technologies: Toward wafer-scale production of epitaxial graphene *MRS Bull.* **37** 1149–57
- [300] Instruments L S Temperature and environmental stage for Raman measurements
- [301] Instruments L S RH95
- [302] BOC N2 research grade
- [303] Chen J, Shi T, Cai T, Xu T, Sun L, Wu X and Yu D 2013 Self healing of defected graphene *Appl. Phys. Lett.* **102**
- [304] Bruker Corporation PFQNE-AL
- [305] Melios C, Centeno A, Zurutuza A, Panchal V, Giusca C E, Spencer S, Silva S R P and Kazakova O 2016

- Effects of humidity on the electronic properties of graphene prepared by chemical vapour deposition *Carbon N. Y.* **103** 273–80
- [306] Melios C, Winters M, Strupiński W, Panchal V, Giusca C E, Imalka Jayawardena K D G, Rorsman N, Silva S R P and Kazakova O 2017 Tuning epitaxial graphene sensitivity to water by hydrogen intercalation *Nanoscale* **9** 3440–8
- [307] Das A et al 2008 Monitoring dopants by Raman scattering in an electrochemically top-gated graphene transistor *Nat. Nanotechnol.* **3** 210–5
- [308] Basko D M, Piscanec S and Ferrari A C 2009 Electron-electron interactions and doping dependence of the two-phonon Raman intensity in graphene G peak D peak D peak D peak 1–10
- [309] Casiraghi C, Pisana S, Novoselov K S, Geim A K and Ferrari A C 2007 Raman fingerprint of charged impurities in graphene *Appl. Phys. Lett.* **91** 2007–9
- [310] Ferrari A C et al 2006 Raman spectrum of graphene and graphene layers *Phys. Rev. Lett.* **97** 1–4
- [311] Gupta A, Chen G, Joshi P, Tadigadapa S and Eklund P C 2006 Raman scattering from high-frequency phonons in supported n-graphene layer films *Nano Lett.* **6** 2667–73
- [312] Neumann C et al 2015 Raman spectroscopy as probe of nanometre-scale strain variations in graphene *Nat. Commun.* **6** 1–7
- [313] Couto N J G, Costanzo D, Engels S, Ki D K, Watanabe K, Taniguchi T, Stampfer C, Guinea F and Morpurgo A F 2014 Random strain fluctuations as dominant disorder source for high-quality on-substrate graphene devices *Phys. Rev. X* **4** 1–13
- [314] Ishigami M, Chen J H, Cullen W G, Fuhrer M S and Williams E D 2007 Atomic structure of graphene on SiO₂ *Nano Lett.* **7** 1643–8
- [315] Chen C C, Bao W, Theiss J, Dames C, Lau C N and Cronin S B 2009 Raman spectroscopy of ripple formation in suspended graphene *Nano Lett.* **9** 4172–6
- [316] Ni Z H, Wang H M, Ma Y, Kasim J, Wu Y H and Shen Z X 2008 Tunable stress and controlled thickness modification in graphene by annealing *ACS Nano* **2** 1033–9
- [317] Woods C R et al 2014 Commensurate-incommensurate transition in graphene on hexagonal boron nitride *Nat. Phys.* **10** 451–6
- [318] Ahn G, Kim H R, Ko T Y, Choi K, Watanabe K, Taniguchi T, Hong B H and Ryu S 2013 Optical probing of the electronic interaction between graphene and hexagonal boron nitride *ACS Nano* **7** 1533–41
- [319] Pisana S, Lazzeri M, Casiraghi C, Novoselov K S, Geim A K, Ferrari A C and Mauri F 2007 Breakdown of the adiabatic Born – Oppenheimer approximation in graphene **6** 3–6
- [320] Komínková Z and Kalbáč M 2013 Raman spectroscopy of strongly doped CVD-graphene *Phys. Status Solidi Basic Res.* **250** 2659–61
- [321] Yang R, Huang Q S, Chen X L, Zhang G Y and Gao H J 2010 Substrate doping effects on Raman spectrum of epitaxial graphene on SiC *J. Appl. Phys.* **107**
- [322] Lee J E, Ahn G, Shim J, Lee Y S and Ryu S 2012 Optical separation of mechanical strain from charge doping in graphene *Nat. Commun.* **3** 1024–8
- [323] Bao W, Miao F, Chen Z, Zhang H, Jang W, Dames C and Lau C N 2009 Controlled ripple texturing of suspended graphene and ultrathin graphite membranes *Nat. Nanotechnol.* **4** 562–6
- [324] Froehlicher G and Berciaud S 2015 Raman spectroscopy of electrochemically gated graphene transistors: Geometrical capacitance, electron-phonon, electron-electron, and electron-defect scattering *Phys. Rev. B* **91** 1–17
- [325] Bruna M, Ott A K, Ijäs M, Yoon D, Sassi U and Ferrari A C 2014 Doping dependence of the Raman spectrum of defected graphene *ACS Nano* **8** 7432–41
- [326] Vincent T, Hamer M, Grigorieva I, Antonov V, Tzalenchuk A and Kazakova O 2020 Strongly

- Absorbing Nanoscale Infrared Domains within Strained Bubbles at hBN-Graphene Interfaces *ACS Appl. Mater. Interfaces* **12** 57638–48
- [327] Castanon E, Fernández Scarioni A, Schumacher H W, Spencer S, Perry R, Vicary J A, Clifford C A and Corte-León H 2020 Calibrated Kelvin-probe force microscopy of 2D materials using Pt-coated probes *J. Phys. Commun.* **4** 042001
- [328] Xu J, Li D, Chen D, Li W and Xu J 2018 Nanoscale Characterization of Active Doping Concentration in Boron-Doped Individual Si Nanocrystals *Phys. Status Solidi Appl. Mater. Sci.* **215** 1–7
- [329] Zhang Y, Zuo J, Gao Y, Li P, He W and Zheng Z 2019 Investigation on the nanoscale electric performance of NiO thin films by C-AFM and KPFM: The effect of Cu doping *J. Phys. Chem. Solids* **131** 27–33
- [330] Guinane L et al 2020 Nanoscale topography, surface charge variation and defect correlation in 2–8 nm thick functional alumina films *Appl. Surf. Sci.* **528**
- [331] Panchal V, Lartsev A, Manzin A, Yakimova R, Tzalenchuk A and Kazakova O 2014 Visualisation of edge effects in side-gated graphene nanodevices *Sci. Rep.* **4**
- [332] Lan F, Jiang M and Li G 2017 Fei Lan , Minlin Jiang and Guangyong Li 379–82
- [333] Liu Y, Bag M, Renna L A, Page Z A, Kim P, Emrick T, Venkataraman D and Russell T P 2016 Understanding interface engineering for high-performance fullerene/perovskite planar heterojunction solar cells *Adv. Energy Mater.* **6** 1–7
- [334] Nabhan W, Equer B, Broniatowski A and De Rosny G 1997 A high-resolution scanning Kelvin probe microscope for contact potential measurements on the 100 nm scale *Rev. Sci. Instrum.* **68** 3108–11
- [335] Michaelson H B 1977 The work function of the elements and its periodicity *J. Appl. Phys.* **48** 4729–33
- [336] Kasap S O *Electronic materials and devices* (McGrawHill Education)
- [337] Kim J S, Lägél B, Moons E, Johansson N, Baikie I D, Salaneck W R, Friend R H and Cacialli F 2000 Kelvin probe and ultraviolet photoemission measurements of indium tin oxide work function: a comparison *Synth. Met.* **111** 311–4
- [338] Kikukawa A, Hosaka S and Imura R 1995 Silicon pn junction imaging and characterizations using sensitivity enhanced Kelvin probe force microscopy *Appl. Phys. Lett.* **66** 3510–2
- [339] Ahmad M, Agarwal K, Kumari N and Mehta B R 2018 KPFM based investigation on the nature interfaces and its effect on the electrical and thermoelectric properties **023904**
- [340] Kang Z, Si H, Shi M, Xu C, Fan W and Ma S 2019 Kelvin probe force microscopy for perovskite solar cells **62** 776–89
- [341] Shikler R, Meoded T, Fried N, Mishori B and Rosenwaks Y 1999 Two-dimensional surface band structure of operating light emitting devices *J. Appl. Phys.* **86** 107–13
- [342] Filleter T, Emtsev K V., Seyller T and Bennewitz R 2008 Local work function measurements of epitaxial graphene *Appl. Phys. Lett.* **93**
- [343] Almadori Y, Bendiab N and Grévin B 2018 Multimodal Kelvin Probe Force Microscopy Investigations of a Photovoltaic WSe₂/MoS₂ Type-II Interface *ACS Appl. Mater. Interfaces* **10** 1363–73
- [344] Sharma I and Mehta B R 2017 Enhanced charge separation at 2D MoS₂/ZnS heterojunction: KPFM based study of interface photovoltage *Appl. Phys. Lett.* **110**
- [345] Ahmad M, Varandani D and Mehta B R 2018 Large surface charge accumulation in 2D MoS₂/Sb₂Te₃ junction and its effect on junction properties: KPFM based study *Appl. Phys. Lett.* **113**
- [346] Wang X et al 2019 Defect Heterogeneity in Monolayer WS₂ Unveiled by Work Function Variance *Chem. Mater.* **31** 7970–8

- [347] Melios C, Panchal V, Giusca C E, Strupiński W, Silva S R P and Kazakova O 2015 Carrier type inversion in quasi-free standing graphene: Studies of local electronic and structural properties *Sci. Rep.* **5** 1–8
- [348] Sadewasser S, Glatzel T, Shikler R, Rosenwaks Y and Lux-Steiner M C 2003 Resolution of Kelvin probe force microscopy in ultrahigh vacuum: Comparison of experiment and simulation *Appl. Surf. Sci.* **210** 32–6
- [349] TipsNano NSG03
- [350] Bruker Corporation PFQNE-AL
- [351] NuNano SPARK 350 Pt
- [352] Santos S and Verdaguer A 2016 Imaging water thin films in ambient conditions using Atomic Force Microscopy *Materials (Basel)*. **9** 1–16
- [353] Liscio A, Palermo V, Müllen K and Samorì P 2008 Tip - Sample interactions in Kelvin probe force microscopy: Quantitative measurement of the local surface potential *J. Phys. Chem. C* **112** 17368–77
- [354] Jacobs H O, Leuchtman P, Homan O J and Stemmer A 1998 Resolution and contrast in Kelvin probe force microscopy *J. Appl. Phys.* **84** 1168–73
- [355] Fujihira M 1994 Structural study of Langmuir–Blodgett films by scanning surface potential microscopy *J. Vac. Sci. Technol. B Microelectron. Nanom. Struct.* **12** 1604
- [356] Barbet S, Popoff M, Diesinger H, Deresmes D, Théron D and Mélin T 2014 Cross-talk artefacts in Kelvin probe force microscopy imaging: A comprehensive study *J. Appl. Phys.* **115**
- [357] Jacobs H O, Knapp H F and Stemmer A 2018 Practical aspects of kelvin probe force microscopy *Rev. Sci. Instrum.* **70** 101–18
- [358] Melitz W, Shen J, Kummel A C and Lee S 2011 Kelvin probe force microscopy and its application *Surf. Sci. Rep.* **66** 1–27
- [359] Lawless K R 1974 The oxidation of metals *Reports Prog. Phys.* **37** 231–316
- [360] Parsons P and Dixon G 2013 *The periodic table: a field guide to the elements* (Quercus)
- [361] Challonder J 2019 *The periodic table: the new guide to the building blocks of our universe* ed SevenOaks
- [362] Sebastian A, Salapaka M V. and Cleveland J P 2003 Robust Control Approach to Atomic Force Microscopy *Proc. IEEE Conf. Decis. Control* **4** 3443–4
- [363] Xue B, Yan Y, Hu Z and Zhao X 2014 Study on effects of scan parameters on the image quality and tip wear in AFM tapping mode *Scanning* **36** 263–9
- [364] Sadewasser S, Leendertz C, Streicher F and Lux-Steiner M C 2009 The influence of surface topography on Kelvin probe force microscopy *Nanotechnology* **20** 505503
- [365] Wu Y and Shannon M A 2006 ac driving amplitude dependent systematic error in scanning Kelvin probe microscope measurements: Detection and correction *Rev. Sci. Instrum.* **77**
- [366] Saraf S, Schwarzman A, Dvash Y, Cohen S, Ritter D and Rosenwaks Y 2006 Nanoscale measurement of the energy distribution of semiconductor surface states *Phys. Rev. B - Condens. Matter Mater. Phys.* **73** 1–7
- [367] Hudlet S, Saint Jean M, Roulet B, Berger J and Guthmann C 1995 Electrostatic forces between metallic tip and semiconductor surfaces *J. Appl. Phys.* **77** 3308–14
- [368] Kalinin S V. and Bonnell D A 2001 Local potential and polarization screening on ferroelectric surfaces *Phys. Rev. B - Condens. Matter Mater. Phys.* **63** 1–13
- [369] Collins L, Kilpatrick J I, Weber S A L, Tselev A, Vlassioux I V., Ivanov I N, Jesse S, Kalinin S V. and

- Rodriguez B J 2013 Open loop Kelvin probe force microscopy with single and multi-frequency excitation *Nanotechnology* **24**
- [370] Boehmisch M, Burmeister F, Rettenberger A, Zimmermann J, Boneberg J and Leiderer P 1997 Atomic force microscope based Kelvin probe measurements: Application to an electrochemical reaction *J. Phys. Chem. B* **101** 10162–5
- [371] Hansen W N and Hansen G J 2001 Standard reference surfaces for work function measurements in air *Surf. Sci.* **481** 172–84
- [372] Panchal V et al 2018 Confocal laser scanning microscopy: A tool for rapid optical characterization of 2D materials *arXiv Mesoscale Nanoscale Phys.*
- [373] McMurray H N and Williams G 2002 Probe diameter and probe-specimen distance dependence in the lateral resolution of a scanning Kelvin probe *J. Appl. Phys.* **91** 1673–9
- [374] Senoner M and Unger W E S 2013 Summary of ISO/TC 201 Technical Report: ISO/TR 19319:2013 - Surface chemical analysis - Fundamental approaches to determination of lateral resolution and sharpness in beam-based methods *Surf. Interface Anal.* **45** 1313–6
- [375] Wang R, Wang S, Zhang D, Li Z, Fang Y and Qiu X 2011 Control of carrier type and density in exfoliated graphene by interface engineering *ACS Nano* **5** 408–12
- [376] Hibino H, Kageshima H, Kotsugi M, Maeda F, Guo F-Z and Watanabe Y 2009 Dependence of electronic properties of epitaxial few-layer graphene on the number of layers investigated by photoelectron emission microscopy *Phys. Rev. B* **79** 125437
- [377] Duch J, Kubisiak P, Adolfsson K H, Hakkarainen M, Golda-Cepa M and Kotarba A 2017 Work function modifications of graphite surface via oxygen plasma treatment *Appl. Surf. Sci.* **419** 439–46
- [378] Datta S S, Strachan D R, Mele E J and Johnson A T C 2009 Surface Potentials and layer charge distributions in Few-Layer Graphene films *Nano Lett.* **9** 7–11
- [379] Silvestrov P G and Efetov K B 2008 Charge accumulation at the boundaries of a graphene strip induced by a gate voltage: Electrostatic approach *Phys. Rev. B - Condens. Matter Mater. Phys.* **77** 1–5
- [380] Caridad J M, Power S R, Shylau A A, Gammelgaard L, Jauho A P and Bøggild P 2019 Gate electrostatics and quantum capacitance in ballistic graphene devices *Phys. Rev. B* **99**
- [381] Caridad J M, Power S R, Lotz M R, Shylau A A, Thomsen J D, Gammelgaard L, Booth T J, Jauho A P and Bøggild P 2018 Conductance quantization suppression in the quantum Hall regime *Nat. Commun.* **9** 1–6
- [382] Bischoff D, Krähenmann S, Dröscher M A, Gruner C, Barraud C, Ihn T and Ensslin K 2012 Reactive-ion-etched graphene nanoribbons on a hexagonal boron nitride substrate *Appl. Phys. Lett.* **203103** 2–6
- [383] Phys J A 2015 Graphene nanoribbons : Relevance of etching process **184303**
- [384] Yang G, Li L, Lee W B and Ng M C 2018 Structure of graphene and its disorders: a review *Sci. Technol. Adv. Mater.* **19** 613–48
- [385] Latychevskaia T, Wicki F, Escher C and Fink H W 2017 Imaging the potential distribution of individual charged impurities on graphene by low-energy electron holography *Ultramicroscopy* **182** 276–82
- [386] Liang F, Xu H, Wu X, Wang C, Luo C and Zhang J 2018 Raman spectroscopy characterization of two-dimensional materials *Chinese Phys. B* **27**
- [387] National Physical Laboratory 2020 Quantum materials and sensors group
- [388] Peng Z, Yang R, Kim M A, Li L and Liu H 2017 Influence of O₂, H₂O and airborne hydrocarbons on the properties of selected 2D materials *RSC Adv.* **7** 27048–57
- [389] Frisenda R, Navarro-Moratalla E, Gant P, Pérez De Lara D, Jarillo-Herrero P, Gorbachev R V. and

- Castellanos-Gomez A 2018 Recent progress in the assembly of nanodevices and van der Waals heterostructures by deterministic placement of 2D materials *Chem. Soc. Rev.* **47** 53–68
- [390] Hicks L D and Dresselhaus M S 1993 Effect of quantum-well structures on the thermoelectric figure of merit *Phys. Rev. B* **47** 12727–31
- [391] Hicks L D and Dresselhaus M S 1993 Thermoelectric figure of merit of a one-dimensional conductor *Phys. Rev. B* **47** 16631–4
- [392] Vineis C J, Shakouri A, Majumdar A and Kanatzidis M G 2010 Nanostructured thermoelectrics: Big efficiency gains from small features *Adv. Mater.* **22** 3970–80
- [393] Chen Z G, Hana G, Yanga L, Cheng L and Zou J 2012 Nanostructured thermoelectric materials: Current research and future challenge *Prog. Nat. Sci. Mater. Int.* **22** 535–49
- [394] He J and Tritt T M 2017 Advances in thermoelectric materials research: Looking back and moving forward *Science (80-.).* **357**
- [395] Han G, Chen Z G, Drennan J and Zou J 2014 Indium selenides: Structural characteristics, synthesis and their thermoelectric performances *Small* **10** 2747–65
- [396] Hung N T, Nugraha A R T and Saito R 2017 Two-dimensional InSe as a potential thermoelectric material *Appl. Phys. Lett.* **111**
- [397] Harzheim A et al 2018 Geometrically Enhanced Thermoelectric Effects in Graphene Nanoconstrictions *Nano Lett.* **18** 7719–25
- [398] Harzheim A, Evangeli C, Kolosov O V. and Gehring P 2020 Direct mapping of local Seebeck coefficient in 2D material nanostructures via scanning thermal gate microscopy *2D Mater.* **7** 041004
- [399] Tovee P, Pumarol M, Zeze D, Kjoller K and Kolosov O 2012 Nanoscale spatial resolution probes for scanning thermal microscopy of solid state materials *J. Appl. Phys.* **112**
- [400] ANASYS Instruments 2018 ThermaLever probes
- [401] Kelvin Nanotechnology KNT-SThM-2an
- [402] TEKTRONIX INC. 2021 Keithley 3390 Arbitrary Waveform Generator
- [403] Stanford Research Systems SR650 Programmable filter
- [404] Stanford Research Systems Lock-in Amplifier SR830
- [405] TEKTRONIX INC. 2021 Keithley 6430 Sourcemeter
- [406] Wickramaratne D, Zahid F and Lake R K 2015 Electronic and thermoelectric properties of van der Waals materials with ring-shaped valence bands *J. Appl. Phys.* **118**
- [407] Shafique A and Shin Y H 2020 The effect of non-analytical corrections on the phononic thermal transport in InX (X = S, Se, Te) monolayers *Sci. Rep.* **10** 1–10
- [408] National Academy of sciences of Ukraine Frantsevich Institute for problems of materials science (IPMS)
- [409] Li Y, Mehra N, Ji T and Zhu J 2018 Realizing the nanoscale quantitative thermal mapping of scanning thermal microscopy by resilient tip-surface contact resistance models *Nanoscale Horizons* **3** 505–16
- [410] Nazarenko M, Rosamond M C, Gallant A J, Kolosov O V., Dubrovskii V G and Zeze D A 2017 A simplified model to estimate thermal resistance between carbon nanotube and sample in scanning thermal microscopy *J. Phys. D: Appl. Phys.* **50**
- [411] Jin J S, Lee J S and Kwon O 2008 Electron effective mean free path and thermal conductivity predictions of metallic thin films *Appl. Phys. Lett.* **92** 2–5
- [412] Botcha V D, Zhang M, Li K, Gu H, Huang Z, Cai J, Lu Y, Yu W and Liu X 2018 High-K substrate effect

- on thermal properties of 2D InSe few layer *J. Alloys Compd.* **735** 594–9
- [413] Rai A, Sangwan V K, Gish J T, Hersam M C and Cahill D G 2021 Anisotropic thermal conductivity of layered indium selenide *Appl. Phys. Lett.* **118**
- [414] Sun D, Aivazian G, Jones A M, Ross J S, Yao W, Cobden D and Xu X 2012 Ultrafast hot-carrier-dominated photocurrent in graphene *Nat. Nanotechnol.* **7** 114–8
- [415] Zuev Y M, Chang W and Kim P 2009 Thermoelectric and magnetothermoelectric transport measurements of graphene *Phys. Rev. Lett.* **102** 1–4
- [416] Duan J, Wang X, Lai X, Li G, Watanabe K, Taniguchi T, Zebarjadi M and Andrei E Y 2016 High thermoelectric power factor in graphene/hBN devices *Proc. Natl. Acad. Sci. U. S. A.* **113** 14272–6
- [417] Kockert M, Mitdank R, Zykov A, Kowarik S and Fischer S F 2019 Absolute Seebeck coefficient of thin platinum films *J. Appl. Phys.* **126**
- [418] Zolotavin P, Evans C I and Natelson D 2017 Substantial local variation of the Seebeck coefficient in gold nanowires *Nanoscale* **9** 9160–6
- [419] Epoxy Technology INC EPO-TEK H21D
- [420] Karak S, Paul S, Negi D, Poojitha B, Srivastav S K, Das A and Saha S 2021 Hexagonal boron nitride–graphene heterostructures with enhanced interfacial thermal conductance for thermal management applications *ACS Appl. Nano Mater.*
- [421] Langer G, Hartmann J and Reichling M 1997 Thermal conductivity of thin metallic films measured by photothermal profile analysis *Rev. Sci. Instrum.* **68** 1510–3
- [422] Zhu W, Zheng G, Cao S and He H 2018 Thermal conductivity of amorphous SiO₂ thin film: A molecular dynamics study *Sci. Rep.* **8** 1–9
- [423] Banszerus L, Schmitz M, Engels S, Goldsche M, Watanabe K, Taniguchi T, Beschoten B and Stampfer C 2016 Ballistic Transport Exceeding 28 μm in CVD Grown Graphene *Nano Lett.* **16** 1387–91
- [424] Hochbaum A I, Chen R, Delgado R D, Liang W, Garnett E C, Najarian M, Majumdar A and Yang P 2008 Enhanced thermoelectric performance of rough silicon nanowires *Nature* **451** 163–7
- [425] Sun W, Liu H, Gong W, Peng L M and Xu S Y 2011 Unexpected size effect in the thermopower of thin-film stripes *J. Appl. Phys.* **110**
- [426] Harzheim A, Könemann F, Gotsmann B, van der Zant H and Gehring P 2020 Single-Material Graphene Thermocouples *Adv. Funct. Mater.* **30** 1–5
- [427] Xu X, Gabor N M, Alden J S, Van Der Zande A M and McEuen P L 2010 Photo-thermoelectric effect at a graphene interface junction *Nano Lett.* **10** 562–6
- [428] Woessner A et al 2016 Near-field photocurrent nanoscopy on bare and encapsulated graphene *Nat. Commun.* **7** 1–7
- [429] Graphenea McKinsey estimates a \$70 billion market for graphene semiconductors in 2030
- [430] Ribeiro-Palau R, Zhang C, Watanabe K, Taniguchi T, Hone J and Dean C R 2018 Twistable electronics with dynamically rotatable heterostructures *arXiv* **693** 690–3
- [431] Carr S, Massatt D, Fang S, Cazeaux P, Luskin M and Kaxiras E 2017 Twistrionics: Manipulating the electronic properties of two-dimensional layered structures through their twist angle *Phys. Rev. B* **95** 1–6
- [432] Masubuchi S and Machida T 2019 Classifying optical microscope images of exfoliated graphene flakes by data-driven machine learning *npj 2D Mater. Appl.* **3** 4–6
- [433] Orji N G et al 2018 Metrology for the next generation of semiconductor devices *Nat. Electron.* **1** 532–47
- [434] Hui F and Lanza M 2019 Scanning probe microscopy for advanced nanoelectronics *Nat. Electron.* **2**

- [435] Kolosov O V, Grishin I and Jones R 2011 Material sensitive scanning probe microscopy of subsurface semiconductor nanostructures via beam exit Ar ion
- [436] San M and Mucientes J 2020 Nanoscale Mechanical and Electrical Properties of Structures
- [437] Cao Y, Fatemi V, Fang S, Watanabe K, Taniguchi T, Kaxiras E and Jarillo-Herrero P 2018 Unconventional superconductivity in magic-angle graphene superlattices *Nature* **556** 43–50
- [438] Ouyang W, Qin H, Urbakh M and Hod O 2020 Controllable Thermal Conductivity in Twisted Homogeneous Interfaces of Graphene and Hexagonal Boron Nitride *Nano Lett.* **20** 7513–8
- [439] Zhao X 2019 *Gate electrostatics in narrow graphene devices* (Denmark Technical University)